Optical and Semiconductor Devices Group

Department of Electrical and Electronic Engineering

Imperial College London

Near Field Communication and Localisation with Slow Waves

Artem Voronov

Supervised by Prof. Richard R. A. Syms and Dr Oleksiy Sydoruk

A thesis submitted for the degree of

Doctor of Philosophy

September 2023

Abstract

The capture volume of near field communication (NFC) systems is limited by adverse scaling laws, antenna perimeter restrictions, and hardware overhead costs. Here, we develop complete, modular, and easily scalable NFC communication and localisation systems based on slow wave antennas.

A review of conventional NFC is conducted, the history of radio-frequency identification discussed, and modern capture volume enhancement techniques considered. New methods for power flow modelling in periodic waveguides with complex characteristic impedance are developed and used to design directional filters for receiver isolation and carrier suppression. The tuneable filters comprise coupled sections of magneto-inductive (MI) waveguides and enable infinite carrier rejection and multiple-passband responses.

We then develop a novel bistatic tag localisation method for slow wave MI antennas. ISO/IEC 14443 Type-A queries are injected as MI waves and corresponding tag signatures extracted from either antenna end via matched filter-couplers. Pair-wise cross-correlation of tag identifiers is used to calculate the differential TOF, which is converted to a position estimate using the antenna group velocity. Accurate localisation is demonstrated using a planar MI antenna, a custom reader, and off-the-shelf tags. We then design flexible antennas with distributed sensors by periodically loading coaxial cable with field-generating nodes. Various sensor topologies are considered and used in experimental antennas up to 48.5 metres long. Accurate one- and quasi-two-dimensional bistatic localisation is demonstrated, and the feasibility of longer antennas discussed.

Finally, we develop monostatic localisation, whereby tag location is achieved with a single receiver using the absolute TOF variation in the delay between the injected reader query and the tag response. Response characteristics of multiple tag classes are characterised, and the effects of carrier power, phase, and sensor-tag separation measured. Accurate one-dimensional positioning is achieved using a flexible loaded transmission line antenna. Conclusions are drawn and the outlook and limitations of slow wave NFC considered.

Declaration of Originality

I declare that the research contained in this thesis is the product of my own work. The use of supporting literature by other Authors has been clearly indicated and appropriately referenced. This work or parts thereof have not been previously submitted for any academic or professional qualification.

Artem Voronov

Declaration of Copyright

List of Publications

This thesis is supported by the following publications:

A. Voronov, O. Sydoruk, and R. R. A. Syms, "Power waves and scattering parameters in magneto-inductive systems," *AIP Advances*, vol. 11, no. 4, pp. 045327–045327, Apr. 2021.

A. Voronov, R. R. A. Syms, and O. Sydoruk, "High-Performance Magnetoinductive Directional Filters," *Electronics*, vol. 11, no. 6, p. 845, Mar. 2022.

R. R. A. Syms, A. Voronov, and O. Sydoruk, "HF RFID Tag Location Using Magneto-Inductive Waves," *IEEE Journal of Radio Frequency Identification*, vol. 71, no. 6, pp. 347–354, 2022.

A. Voronov, O. Sydoruk, and R. R. A. Syms, "Waveguide Antenna Topologies for Distributed High-Frequency Near field Communication and Localization," *IEEE Transactions on Antennas and Propagation*, vol. 71, no. 6, pp. 5026–5035, Jun. 2023.

A. Voronov, R. R. A. Syms and O. Sydoruk, "Monostatic Near Field Tag Localization with Distributed Slow-Wave Antennas," *IEEE Transactions on Instrumentation and Measurement*. (Under revision).

Acknowledgements

I would like to express my sincere gratitude to Prof. Richard R. A. Syms and Dr Oleksiy Sydoruk for their unwavering support, invaluable counsel, and wholehearted dedication. I am forever thankful for the imparted knowledge and skills, as well as the lessons on creativity and perseverance.

I would further like to thank the Optical and Semiconductor Devices Group, the Department of Electrical and Electronic Engineering, and Imperial College London for my PhD scholarship and the wonderful opportunity to conduct my research.

I am also forever grateful for the love and support of my parents Oleg Voronov and Irina Voronova, who made this possible and worthwhile.

Contents

Chapter 1: Introduction

1.1 History of radio-frequency identification

Contrary to popular belief, the concept of radio-frequency identification (RFID) is approximately a century old and was developed concurrently with radar. For both technologies, the fundamental objective was to identify passive targets by their unique signatures, albeit the interpretation of "target" differed. In radar, successful identification often resulted in its destruction, meaning targets were uncooperative. In RFID, identification was done to establish a reliable communication channel to the target, typically comprising a passive transponder. Since RFID was employed in civilian applications, systems needed to become cost-effective and compact to justify their deployment, which required multiple decades of technological and industrial progress. In this Section, we briefly discuss the historical development of RFID systems.

While the existence of radio waves was experimentally verified in 1887 by Herz, and wireless transatlantic communication demonstrated in 1901 by Marconi, no significant progress on radar technology was made until the 1930s due to the limitations of contemporary technology. Nonetheless, the concept of radar can be traced to Hülsmeyer's 1904 German patent for a ship detection and angular localisation system based on the reflection of radio waves [1]. Similarly, a 1925 U.S. patent for a radiotelegraphic system introduced the concept of bi-directional communication between an active transceiver and a passive transponder by load modulation using resonant inductively-coupled antennas – a fundamental principle employed by modern RFID systems [2]. Significant advances in military radar technology were made before and during World War II, such as the development of identification friend or foe (IFF) transponders for British and German aircraft, and the invention of the cavity magnetron by British engineers in 1940. The latter enabled the production of portable, short-wavelength and high-power radar sets, which further fuelled the development of radar technology.

In 1945, to commemorate the alliance between the US and USSR during the Second World War, the American ambassador was gifted an intricate carved replica of the Great Seal of the United States by the Young Pioneers of the Soviet Union [3]. The present raised no suspicion and was subsequently placed in the library of the US ambassador's residence. Unbeknownst to the Americans, imbedded within the Seal was a covert listening device (subsequently nicknamed 'The

Thing') weighing only 31 grams, and consisting of a monopole antenna connected to a sound-sensitive cavity resonator. Sound waves from conversations taking place in the library generated vibrations in the resonator membrane, which modulated the antenna load. The transponder was then interrogated by an incident carrier signal originating from a nearby parked van, and the voice-modulated backscatter signal picked up by a receiver tuned to the cavity's resonant frequency. The novelty and simplicity of the transponder enabled its successful exploitation for years, despite extensive investigations commissioned by the US and Great Britain, until its discovery in 1952. Independently, a 1948 periodical by Harry Stockman defined and demonstrated a similar communication framework, described as "communication by means of reflected power" [4]. The systems comprised a generic high directivity transmitter and a modulated reflector. The transmitter illuminated the target reflector with an unmodulated microwave, ultrasound, or infrared carrier waveform. A physical property of the reflector could then be varied in real time to modulate the backscatter. It was also suggested that the modulating signal could be used to transmit information, such as voice messages, or employed as a unique identifier of the interrogated target. The work is often credited as the first publication on RFID. Still, over twenty years would pass before practical applications emerged.

Between 1968 and 1971 several patents for electronic article surveillance (EAS) systems for monitoring and theft prevention of goods were filed, marking some of the first commercial applications of RFID [5]–[8]. The systems comprised transmitters which generated electromagnetic fields at a fundamental frequency and disposable resonant tags. The resonators were fitted with non-linear impedances such as ferrite film or diodes, designed to re-transmit a distinguishable signature at harmonic frequencies upon interrogation. The tags could be permanently deactivated by triggering a magnetic switch, a fusible link, or by saturating the ferrite layer with an external field. Such tags are often referred to as "1-bit" tags and are still employed today. In addition to EAS, RFID technology generated significant interest in automatic vehicle identification (AVI) applications, mostly for motor vehicles and trains [9]. Extensive field tests of AVI systems were conducted in the U.S. [10], [11]. Despite calls for regulation and standardisation of AVI systems, no agreement between industry and government officials was reached due to contradictory interests and a low technological readiness level. Consequently, a set of functional yet technologically incompatible AVI solutions were developed, such as the fixed-frequency Fairchild system using encapsulated transponders, or the swept-frequency Siemens system employing shorted aluminium waveguides with switchable cavity resonators.

By the mid-1970s the widespread availability of inexpensive logic chips allowed for enhanced load modulation schemes which supported the exchange of digital identification codes. Electronic license plates with CMOS logic modulators were proposed for remote identification of motor vehicles at X-band frequencies [12]. A sophisticated livestock monitoring system operating in the 1 GHz band was deployed, with each transponder containing a pre-programmed 3-digit memory bank [13]. The design introduced novel features commonly used by modern RFID such as unique digital identifiers, subcarrier modulation, and an error detection system for transmitted codes. Additionally, the tags carried a built-in sensor which encoded the animal's temperature in the subcarrier frequency. Similar systems were being tested on experimental farms in the United Kingdom, the Netherlands, Germany, and the United States [14]. One of the earliest uses of the term "radio frequency identification" can also be found in 1975 patent describing a primitive anticollision algorithm [15]. Another patent filed in 1979 described a portable personal identification device with a programmable identification code [16]. A follow-up patent 1980 patent spoke of a "portable identifier, preferably shaped like a credit card", which could be used in business transactions and financial exchanges [17]. A need for personal identification to be performed very quickly and accurately was also noted.

By the 1980s, technological advances in microelectronics and communication technology made AVI toll collection economically viable [18], with multiple systems deployed in the United States and Europe . Solutions included near field inductive systems with carrier frequencies below 200 MHz, as well as microwave systems spanning 900 MHz to 4.2 GHz [19]. Similarly, miniature cost-effective tags for animal identification were being deployed. The tags used low-frequency inductive coupling in the 125 kHz frequency range, which is still true for modern animal identification systems [20], [21]. In retail, passive tags began to be regarded as viable alternatives to the barcode due to their programmable nature and their ability to be read without a direct line of sight [22]. The robustness of RFID systems in rugged and demanding maritime, rail, and highway environments made the technology suitable for logistics applications. Experimental testing in intermodal container shipping was initiated [23]. The acronym "RFID", became adopted by industry professionals, appearing in a 1989 patent for an inventory control system [24], as well as a research publication [18]. By the 1990s the use of the acronym was commonplace.

The 1990s saw a significant increase in RFID commercialisation and scientific research, triggering an exponential growth in the number of available systems, market players, and manufacturers. Mass adoption of RFID technology, however, was still being impeded by the lack of compatibility between available solutions, which kept the industry competition low and the system cost high [25]. The need to standardise was particularly evident in the AVI sector [26], since the technologies used in different regions were incompatible. Naturally, the 90s marked the beginning of RFID standardisation in all application fields. Specialist RFID divisions were being established in global technology companies such as Philips, Bosch, Alcatel, Texas Instruments, and Mikron [25]. Notably, Texas Instruments developed the TIRIS system [27] which became adopted for ski-pass ticketing and vehicle access control, while Philips introduced the Mifare 1K chips [28] for automatic fare collection. By the mid-90s smart cards had gained widespread acceptance in Europe and Asia, with an estimated 1 billion cards produced in 1998 [29]. Smart cards were particularly popular in France, where the technology was uses to reduce telecommunication transaction costs and successfully lower credit card fraud by 75% over a five year period [30]. Owing to the wide range of communication protocols and card types already in use, three sets of standards were developed by the International Organisation for Standardisation (ISO) which all operated in the high-frequency (HF) band. ISO/IEC 10536 [31] was published in 1992 for close-coupling smart cards, with support for both inductive and capacitive coupling. ISO/IEC 14443 [32] for proximity-coupling and ISO/IEC 15693 [33] for vicinity-coupling smart cards were published in tandem in 2000 after 13 years of development. Both card types exclusively utilise magnetic near fields, with vicinity cards operating at increased range at the cost of reduced communication security and lower data rates. ISO/IEC 14443 is inherently less vulnerable to malicious attacks and primarily used in data-sensitive applications such as contactless payments [34], [35], biometric passports [36], [37], electronic keys [38], and ticketing [39].

In 1999, the Auto-ID Center was established at the Massachusetts Institute of Technology in partnership with the Uniform Code Council (UCC), Gilette, and Procter & Gamble, and tasked with developing automated identification technologies and applications [40]. To design a global and standardised identification system for all traded physical objects, the Auto-ID Center introduced the Electronic Product Code (EPC). The Center would subsequently split into Auto-ID Labs and EPCglobal in 2003, with the former remaining a research centre, while the latter became the de-facto standardisation body for ultra-high frequency (UHF) RFID systems [41]. EPCglobal developed the passive backscatter air-interface protocol “Class-1 Generation-2 UHF RFID” in 2004, which operated in the 860 – 960 MHz Industrial, Scientific, and Medical (ISM) band. The protocol was ratified by the International Organization of Standardization as ISO 18000 - 6 [42], intended to facilitate compatibility amidst strict international radio licensing regulations.

The growing deployment of contactless smart card technology in ticketing, electronic identification, and access control was taking place alongside an equally booming mobile phone industry. Naturally, the potential benefits of integrating smart card technology and mobile devices were quickly noted by industry. In 2002, Sony and Philips entered a partnership to jointly develop near field communication (NFC) technology, incorporating smart-key and smartcard reader functionality into NFC enabled devices such as mobile phones, digital cameras, and personal computers, enabling contactless payments and short-range data transfer [43]. Later that year the ECMA-340 Near Field Communication protocol was published [44] and subsequently ratified by the ISO and International Electrotechnical Commission as ISO/IEC 18092 in 2004 [45]. To further promote NFC technology, Sony, Philips, and Nokia founded the NFC Forum in 2004, with the Nokia 3220 mobile phone shipping with an optional NFC shell add-on the following year [46].

The ubiquitous integration of RFID in industry and everyday life, combined with the proliferation of mobile computing, wireless networks, and Internet technology created new opportunities, applications, and problems for RFID. The continued reduction in tag costs meant it became feasible to affix tags to individual objects, which was particularly useful in logistics. Naturally, this produced a demand for methods and systems capable of locating such items in physical space. Localisation functionality was unsupported by contemporary RFID systems in any frequency band, which could only detect the presence or absence of a tag within the antenna capture volume. The issue was recognised by academia, with some early solutions to tag localisation appearing around 2000 [47]. The research was mostly restricted to UHF frequency systems often employing multiple readers and reference tags, with tag position estimated using relative signal strength indicators. System performance was generally dependent on environmental parameters and was vulnerable to local disturbances and multipath effects. Subsequent UHF systems employed more advanced positioning techniques based on backscatter phase, time-of-arrival, environment fingerprinting, and statistical methods [48]. Tag localisation in the HF band, however, remained underdeveloped in comparison to UHF due to its shorter achievable read range and lack of signal phase information, with the few available methods limited to multiple readers [49] or multiplexed antenna arrays [50].

Despite its short range, the potential of NFC technology was starting to be recognised for its utility in the Internet of Things; nowadays a popular academic research field and a hot topic in industry, which coincidentally has its roots in RFID [51]. The NFC framework offers a convenient means to design and integrate inexpensive, yet functionally sophisticated battery-less sensors [52], which can be powered and interrogated with a single tap from a smartphone. The continued reductions in tag costs and advances in fabrication techniques have further served to promote the technology [53], with notable sensing applications in healthcare and food quality monitoring. Examples of NFC sensors include miniaturised flexible skin-adhesive patches for heart rate and blood oxygenation monitoring [54], [55] and electrochemical fluid analysis [56], card-sized Hepatitis B virus detectors [57], subdermal implants for local tissue oximetry [58], and flexible cellulose water-soluble gas sensors embedded within food packaging for food quality monitoring [59]. Methods of interconnecting the various sensors into a single system using field-generating metamaterial waveguides have also been proposed in the context of body-area networks [60]. NFC technology could also be used to control context-aware smart spaces populated with NFC-enabled devices [61].

Today, radio-frequency identification has become a prominent and established technology. The global RFID market is estimated to be worth \$12.8 billion, with 39 billion passive tags sold in 2023, valued at \$7.9 billion [62]. Approximately 84% of tags sold operated in the UHF frequency band, 13% operated in the HF band, and only 3% were LF tags. In terms of market share, however, HF tags accounted for 67% of the total value, UHF accounted for 25%, and LF tags were responsible for 8%. The dominant market value share of HF tags arises from the added cost of enhanced security features required for contactless payments, access control, storage, and transmission of sensitive data. Most NFC tags are employed in smart card and fob packages (61%), with the most popular applications being financial transactions and security. The global RFID market is expected to sustain its expansion, with a projected market value of approximately \$19 billion in 2028.

The operating frequencies of modern RFID systems are tightly regulated and range from 135 kHz at LF to 5.8 GHz at super high frequency (SHF). Figure 1.1 presents a summary of prominent RFID standards and their corresponding position in the frequency spectrum, with NFC-enabled standards highlighted by a dashed red outline.

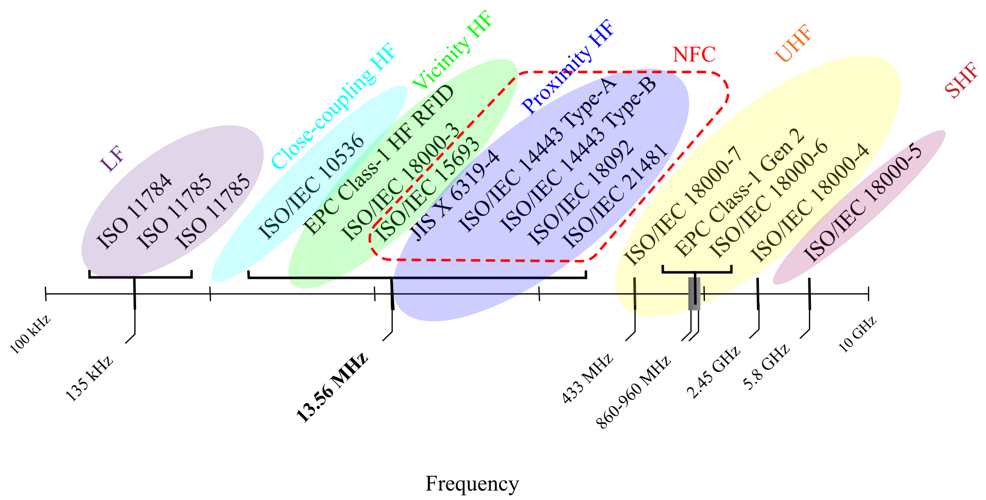

Figure 1.1. Overview of prominent RFID communication standards spanning from LF (low frequency) to SHF (super high frequency). The dashed red outline highlights NFC-compliant standards.

1.2 Near field communication

1.2.1 *Overview*

Near field communication (NFC) is a high-frequency (HF) short-range wireless communication technology which operates in the 13.56 MHz industrial, scientific, and medical (ISM) band [63], [64]. NFC employs magnetic near fields for bi-directional data transmission between NFC-enabled devices, which include readers, passive and active tags, and smartphones. NFC was jointly developed by Sony and Philips, with the protocol first published in 2002 as the ECMA – 340 standard “Near Field Communication Interface and Protocol (NFCIP-1)” [44]. Both manufacturers had already invested heavily in HF RFID technology, with Philips owning the globally successful Mifare ® contactless product line, while Sony had developed the Felica® card systems which were widely deployed in Japan. The NFC protocol was designed to market the functionality of contactless smart cards to the booming portable consumer electronics market (particularly mobile phones), and thus included a new active communication mode in addition to the established reader-writer mode. The NFC Forum consortium was shortly founded by Sony, Philips, and Nokia in 2004 to lobby the adoption of near field communication technology to industry and develop system specifications and communication protocols on top of NFCIP-1 [65]. Although the original NFC standard was based exclusively on the Mifare ® and Felica® protocols, the NFC Forum specifications have been continuously evolving, with current protocols being compliant with all modern HF RFID standards for both proximity and vicinity tags [66]. As such, the lines between HF RFID, NFC, and ‘contactless’ have become blurred, with the three terms often used interchangeably.

Near field communication has become ubiquitous, with most modern smartphones and tablets equipped with an NFC transceiver module for tag emulation and peer-to-peer communication, while most credit and debit cards support contactless payments [67]. Most countries now issue electronic passports [36], with the holder’s biometric data stored on an NFC tag embedded in the passport cover or data page. The use of NFC smartcards and smartphones in ticketing is also widespread [39]. The short operating range of NFC naturally appeals to high-security applications involving the transmission of sensitive data, as it makes eavesdropping more difficult for attackers [68], [69]. Furthermore, high magnetic coupling between the device antennas provides sufficient power for passive tags to include a cryptographical module for enhanced security [70]. Other established applications include access control [38], animal identification [71], and logistics [72]. Recently, the technology has also been used to power and communicate with battery-less sensors [53]. Since NFC employs alternating magnetic fields as a communication medium, the framework can also be used for wireless inductive charging, with native support added to the NFC specifications in 2020. As such, NFC supports multiple operating modes as shown in Figure 1.2, each compatible with multiple communication standards and data rates.

- *Reader-Writer mode:* an active reader uses its external magnetic field to power and interrogate a passive transponder in vicinity. Reader commands are transmitted by modulating the RF field using amplitude-shift keying (ASK), while the tag responds by load modulation. Communication can only be initiated by the reader. This is the classic operating mode of HF RFID systems.
- *Tag emulation mode:* communication is established between a pair of active devices, with one operating as a reader, and the other mimicking a passive tag. Only the reader can act as initiator and uses ASK to modulate its RF field, while the listening device responds by load modulation. From the reader's perspective, the emulator device functions a passive tag.
- *Peer-to-Peer mode:* two active devices exchange data by alternately modulating their RF fields using ASK. Either device may act as the communication initiator, and both devices have their own power supplies.
- *Wireless charging mode:* An NFC device continuously generates an external magnetic field to inductively charge another NFC device.

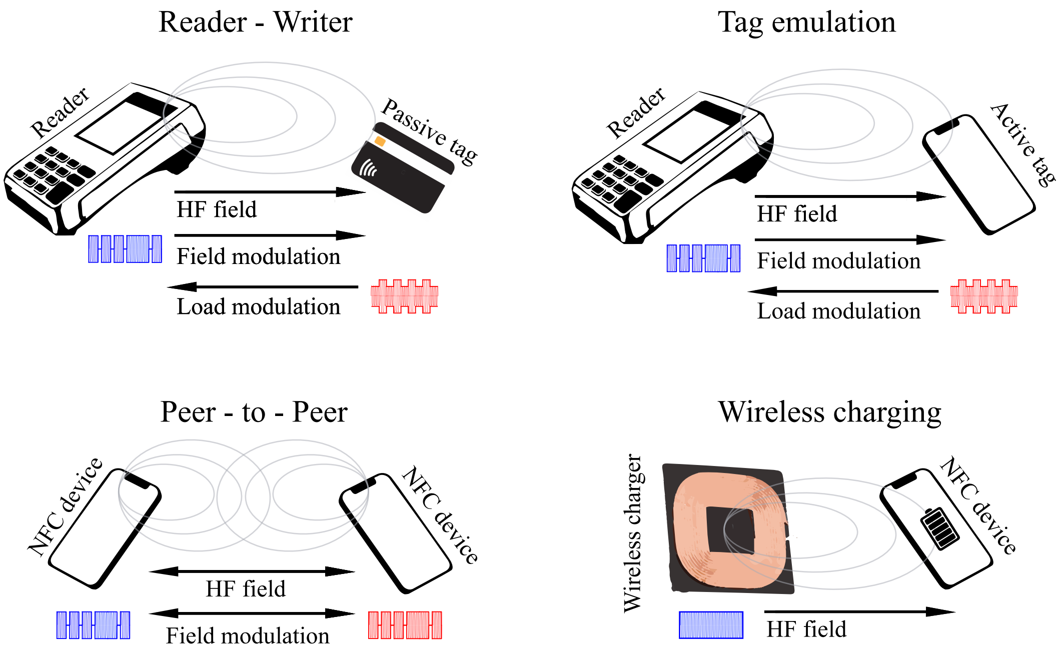

Figure 1.2. Near field communication operating modes.

It is important to note that an NFC device may be able to function in one, several, or all operating modes [73]. For example, an NFC payment terminal might only act as a reader, while the integrated NFC transceiver modules of modern smartphones can support all four modes.

1.2.2 *NFC standards*

NFC specifications are unwieldy and convoluted, mainly due to the number of competing contactless communication standards. The specifications are based on and compatible with three proximity and one vicinity HF RFID standards. The primary difference between proximity and vicinity tags is the latter's reduced minimum field strength requirement, resulting in a roughly ten-fold increase in maximum operating range when compared to proximity tags. The increased range, however, constrains the power transmitted to vicinity tags, meaning tag architectures are less complex and operate at reduced data rates in comparison to proximity tags.

NFC-supported proximity standards include the ISO/IEC 14443 standard [74]–[77], which itself contains competing and independent Type-A and Type B interfaces, the JIS X 6319-4 standard [78]–[81], which is a Japanese standard based on Sony Felica®, and the ISO/IEC 18092 [82], which is a ratified version of the ECMA-340. NFC also supports the ISO/IEC 15693 vicinity tag standard [83]–[85]. These technologies are classified by the NFC Forum as

Table 1.1. HF RFID standards supported by NFC.

Standard	ISO/IEC 14443 Type-A	ISO/IEC 14443 Type-B	JIS X 6319-4	ISO/IEC 15693	ISO/IEC 18092
NFC Forum technology	NFC-A	NFC-B	NFC-F	NFC-V	NFCIP-1
Carrier frequency	13.56 MHz				
Data rate (kb/s)	106	106	212, 424	26.48	As in NFC-A or NFC-F In P2P mode both devices operate as in Polling mode
Approx. range (cm)	10	10	10	100	
Modulation (polling to listening)	100% ASK	10% ASK	10% ASK	100% ASK	
Bit coding (polling to listening)	Modified Miller	NRZ-L	Manchester	'1 out of 4' PPC	
Modulation (listening to polling)	OOK subcarrier load modulation	PSK subcarrier load modulation	OOK load modulation	OOK subcarrier load modulation	
Bit coding (listening to polling)	Manchester	NRZ-L	Manchester	Manchester	
Subcarrier frequency (kHz)	847.5	847.5	None	423.75	
Mode support	Reader-Writer Tag emulation Peer-to-Peer	Reader-Writer Tag emulation	Reader-Writer Tag emulation Peer-to-Peer	Reader-Writer	Reader-Writer Tag emulation Peer-to-Peer
Based on	Philips Mifare®	Innovatron®	Sony Felica®	-	ISO/IEC 14443 Type-A JIS X 6319-4
Prominent applications	Contactless payment cards Key cards for access control Ticketing Inventory management			Inventory management Access control	Contactless payment Ticketing Digital wallets

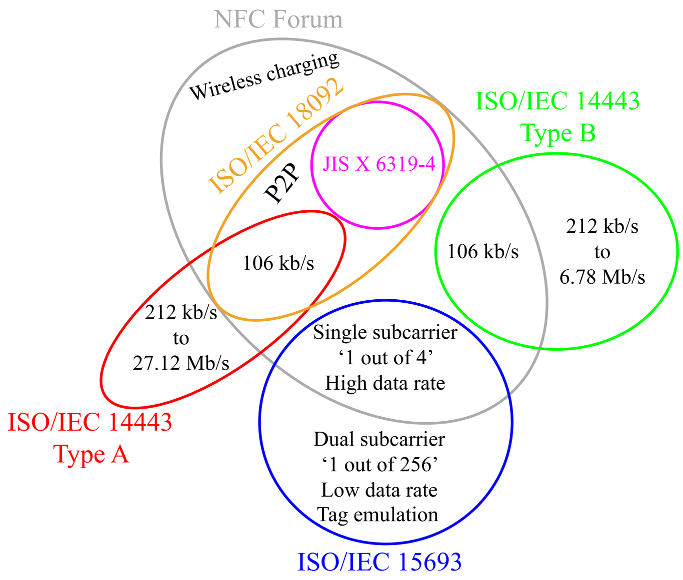

Figure 1.3. Venn diagram comparing NFC Forum specifications with their corresponding HF RFID standards.

NFC-A, NFC-B, NFC-F, NFC-V, and NFCIP-1, respectively. Table 1.1 provides an overview based on the NFC Forum's "Analog" [86] and "Digital" [87] technical specifications. All technologies operate at 13.56 MHz using the half-duplex method, such that data is alternately transmitted between a polling and listening device. A polling device acts to initiate communication and employs ASK field modulation, with the modulation index varying between 10% and 100% across technologies. Data bit coding includes modified Miller, non-return to zero-level (NRZ-L), Manchester, and pulse position coding (PPC). Listening devices reply by modulating their antenna load, which creates time-varying disturbances in the RF field of the polling device. The only exception occurs when operating in P2P mode, in which case both devices alternately generate and modulate their own fields. For load modulation, either Manchester or NRZ-L coding is used. In all technologies except NFC-F the load is modulated using a subcarrier, derived from the RF field of the polling device. The subcarrier serves to separate the typically weak load modulation signal sidebands from the high-powered RF carrier in frequency. All technologies can operate in the Reader-Writer mode, which is also the only supported mode for vicinity tags.

It is important to note that while NFC complies with current HF RFID standards, the scope of NFC specifications is limited and does not include all their features. Figure 1.3 shows a Venn diagram comparing NFC specifications with the HF RFID standards they are based on. Key differences include native NFC support of just the lowest data rate (106 kb/s) for ISO/IEC 14443 Type-A and Type-B, namely 212 kb/s to 27.12 Mb/s data rates for Type-A, and 212 kb/s to 6.78 Mb/s data rates for Type B. For ISO/IEC 15693, only the single subcarrier mode at the highest data rate is supported and vicinity tag emulation by an NFC device is unavailable. The

JIS X 6319 - 4 is the only standard fully supported by NFC, but it is not commonly employed outside of Japan. ISO/IEC 14443 – on the other hand – is used worldwide, with all Mastercard® and Visa® contactless cards [34] and machine-readable travel documents [36] (such as biometric passports) in compliance with the standard. For all practical purposes, the ISO/IEC 14443 Type-A standard (specifically the 106 kb/s data rate), is the key contactless protocol owing to its compliance with NFC-A, support of all NFC communication modes, and its current use in billions of passive tags and active devices worldwide.

1.2.3 *Reader-writer operating mode*

The Reader-Writer operating mode is supported by most NFC-enabled active devices [73]. It is also the classic operating mode of all HF RFID systems. In this mode, a reader device continuously generates an external magnetic field at the carrier frequency $f_c = 13.56$ MHz, which is used to power a passive tag. Reader-writer systems typically operate under the 'reader talks first' principle, meaning only the reader may act as the communication initiator. Both the reader and tag comprise three blocks: a resonant inductive antenna, an HF analogue interface, and a digital processing and control section. Figure 1.4 shows a simplified block diagram depicting the system architecture of a high-power NFC reader and a passive tag.

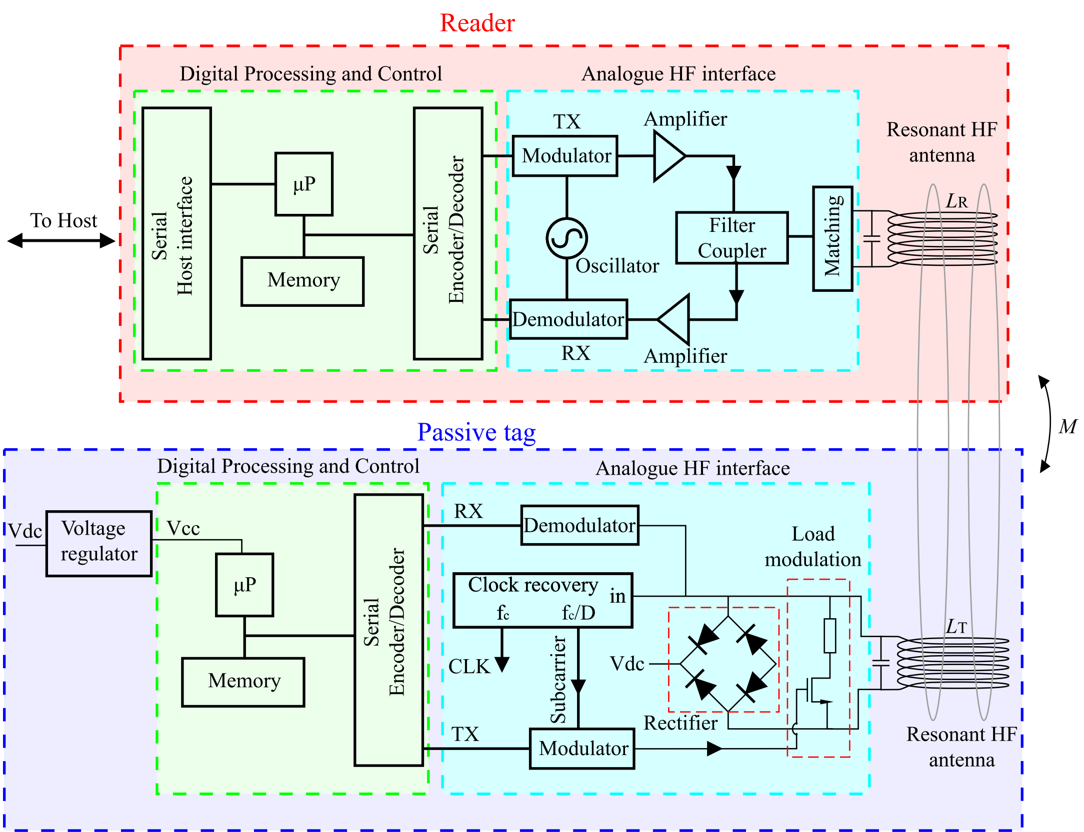

Figure 1.4. Simplified system block diagram depicting the architecture of a high-power NFC reader and a passive tag.

For the reader, the digital processing and control block is responsible for facilitating the bi-directional data flow between the host application software and the analogue HF interface. This includes processing incoming host commands and converting them into NFC-compliant data frames with appropriate bit-level coding, which are then supplied to the contactless interface via serial. Equally, received tag data frames must be decoded, checked for transmission errors, and relayed back to the host. The digital controller is also responsible for ensuring the correct timing of data frames. The analogue HF interface contains separate transmit (TX) and receive (RX) signal paths, which connect to a resonant inductive antenna via a matching circuit [88]. An HF carrier is generated by a precision crystal oscillator and supplied to the TX modulator, which up-converts the baseband reader message signal and applies the appropriate ASK modulation scheme based on the NFC technology used. Finally, the modulated signal is amplified to achieve the required field strength and supplied to the antenna. The tag response signal power typically constitutes only a fraction of the carrier power, especially if the tag is far away or the reader and tag coils are misaligned. Incoming tag responses thus need to be amplified before demodulation. For OOK load modulation, the RX demodulator may simply consist of a rectifier and low-pass filter, but for PSK demodulation a reference carrier signal is needed.

Since the external RF field must be continuous to power the tag, the receiver cannot be isolated from the transmitter with a duplexer. In many conventional systems, the TX and RX are connected directly to the antenna [89], [90]. For high power readers, however, this is not possible, since the TX signal would cause non-linearity in the receiver or obscure the tag response. As such, the RX must be protected from the TX signal at the carrier frequency. Possible solutions have included attenuators [91], band-stop filters in the RX path [92], or separate TX and RX antennas [93]. An elegant solution, however, is to employ a frequency-selective passive coupler functioning as a form of circulator [94]. The reader antenna is typically formed by an inductive loop with multiple turns to increase the magnetic field strength and is often implemented as a planar spiral for compactness. The antenna is made resonant at f_c by a tuning capacitance and matched to the reader interface. Step-down matching is often employed to boost the antenna current and increase the external field strength.

NFC tags are available in a wide range of form factors, with dimensions ranging from the size of a passport cover to 1.6 mm x 1.9 mm x 0.5 mm coil-on-chip packages [95]. The antenna is typically the largest component, with all tag electronics contained in miniature application-specific integrated circuits. Tags magnetically couple to the reader and the reader signal is induced in the tag antenna. A diode bridge is used to rectify the induced voltage and feed a regulator circuit which provides a stable voltage supply to all tag systems. To ensure the correct timing of the half-duplex communication protocol, the tag system clock is synchronised to the HF carrier using a clock recovery circuit [63]. The circuit also includes binary frequency division stages which are used to generate the subcarrier for load modulation (unless NFC-F technology is used). Similarly to the reader, the analogue front end includes separate TX and RX signal paths. ASK-modulated frames are demodulated using envelope detection and decoded by the digital processor. During transmission, the encoded baseband tag message is modulated onto the square-wave subcarrier waveform, and the resultant signal used to dynamically modulate the tag antenna load. This creates corresponding disturbances in the reader antenna, modulating the voltage across it with the tag message. The magnitude of coupling coefficients must be kept high to ensure the output of the tag voltage rectifier is sufficient to power tag circuits, as well as to ensure the tag response is detectable.

1.2.4 *ISO/IEC 14443 Type-A*

The ISO/IEC 14443 standard comprises four parts (Part1 – Part 4) and contains two independent communication signal interfaces: Type-A and Type-B. Originally, the data rates of both interfaces were limited to $f_c/128$ b/s and employed different bit coding and modulation schemes. Following two decades of development and multiple revisions, Type-A now includes eleven data rates spanning $f_c/128$ to $2f_c$ b/s, while Type-B includes seven data rates spanning $f_c/128$ to $f_c/2$ b/s. An attempt to equalise the competing interfaces was also made with both types using the same modulation scheme and bit coding for data rates from $f_c/64$ to $f_c/2$ b/s. Nonetheless, the lowest data rate must be supported by all ISO/IEC 14443 compliant devices for anticollision, and is the only data rate native to NFC-A or NFC-B. Since the NFC-A technology is fundamental to near field communication, we will restrict ourselves to the 106 kb/s data rate of ISO/IEC 14443 Type-A.

Part 1 of the Standard [74] describes the physical characteristics of compliant tags and defines six tag classes (Class 1 – Class 6) based on tag and antenna dimensions. Nonetheless, the tag packaging is not restricted to these classes, and a tag may constitute "an object of any other dimension". Tag antenna dimensions are, however, restricted to 86 mm x 54 mm x 3 mm, which correspond to the dimensions of an ID-1 banking or identification card as per ISO/IEC 7810 [96].

Part 2 of the Standard [75] describes the RF power requirements and the signal interface including bit rates, bit modulation, bit representation and coding. To communicate, the reader produces an HF alternating magnetic field at the carrier frequency $f_c = 13.56$ MHz $\pm$ 7 kHz. The minimum reader field strength requirements vary, ranging from $H_{min} = 1.5$ A/m to $H_{max} = 8.5$

A/m for tag classes with mandatory support (Class 1 – Class 3), with maximum permissible field strength reaching $H_{\max} = 18$ A/m for the optional Class 6.

To communicate with the tag at a data rate of $f_{\mathrm{b}} = f_{\mathrm{c}}/128 \approx 106$ kb/s, the reader uses ASK modulation with a modulation index of 100%. The modulation data signal comprises a stream of Modified Miller encoded data with a bit duration of $T_{\mathrm{b}} = 128/f_{\mathrm{c}} \approx 9.44$ μs. The coding scheme is shown in Figure 1.5 (a) and consists of three symbols: X, Y, and Z, differentiated by the position of a pause of duration T_1 during which the signal value is 0 or equal to 1 otherwise. The pause duration is such that $28/f_{\mathrm{c}} \leq T_1 \leq 40.5/f_{\mathrm{c}}$, with the start of pause located at $T_{\mathrm{b}}/2$ s for symbol X and at the start of symbol Z. No pause is present for symbol Y, resulting in a continuous RF field. Symbol X always represents a logic '1', while symbols Y and Z both represent logic '0'. Priority is given to symbol Y, with Z used from the second contiguous '0' onwards. The symbols are chained together and used to modulate the carrier, amounting to OOK of the reader field. Symbol Z is used to signify the start of communication, while a logic '0' followed by symbol Y is used to indicate the end of communication.

The tag responds at the same data rate and bit duration. During its response, the tag generates a subcarrier with frequency $f_{\mathrm{s}} = f_{\mathrm{c}}/16 \approx 847.5$ kHz, which is modulated with the encoded tag data stream. The data bits are encoded using Manchester code, with a 1-0 transition representing a logic '1' (symbol D), and a 0-1 transition representing a logic '0' (symbol E), as shown in Figure 1.5 (b), with the edge transitions occurring at $T_{\mathrm{b}}/2$ intervals. Symbol D is also used as the start of communication, while symbol F (no subcarrier) is used to signify the end of communication.

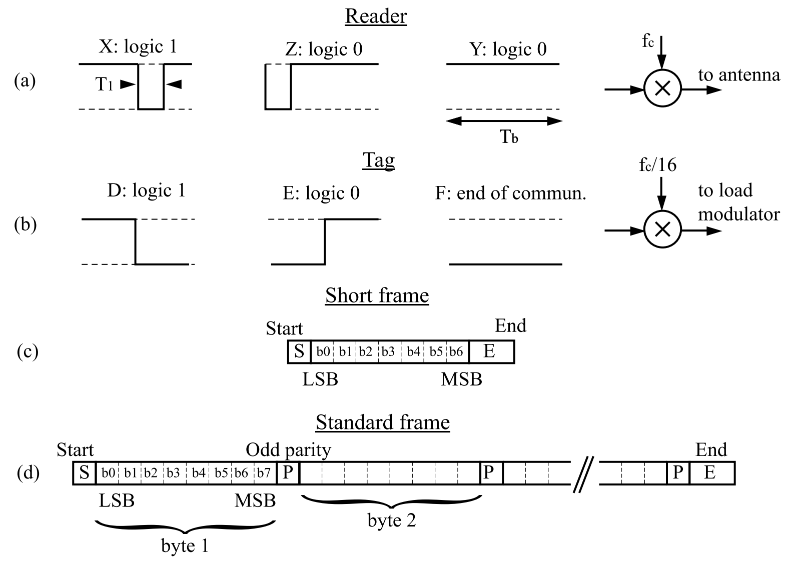

Figure 1.5. Overview of the ISO/IEC 14443 Type-A communication interface: (a) reader to tag logic bit coding; (b) tag to reader logic bit coding; (c) a short data frame; (d) a standard data frame.

Part 3 of the Standard [76] describes how the bit streams are formatted in data frames during communication, the tag initialisation procedure, and the anticollision routine to differentiate between multiple tags. During the communication initialisation, the reader uses a short frame comprising a start bit, 7 data bits, and two end of communication bits as shown in Figure 1.5 (c). The data bits are chained such that the least significant bit (LSB) is transmitted first. In all other cases, the standard frame is used, as shown in Figure 1.5 (d). The standard frame consists of a variable number of data bytes, each transmitted LSB first. Each byte is followed by an odd parity bit, with the entire frame bounded by start and end of communication symbols. Standard frames are used in both communication directions.

Figure 1.6 shows the simplified state diagram for a tag during communication on the left side and the anticollision loop diagram on the right side. In the absence of a sufficiently strong reader field, the tags remain in the "Power-off" state. Following the application of a compliant HF field for a minimum period of 5 ms, any tags in vicinity transition to the "Idle" state. In this state, the tag listens for a request command (REQA) or a wake-up command (WUPA) from the reader. Both commands are transmitted using short frames and both are used to probe the field for Type-A tags. Upon receipt of either command, all tags in the "Idle" state respond with an answer to query (ATQA) containing information about the tag such as the unique identifier (UID) size. The ATQA is transmitted using a two-byte standard frame with the least significant byte sent first. Following transmission, the tags enter the "Ready" state. Tags are now ready to enter the anticollision routine, intended to acquire the unique identifier (UID) of each transponder and enable the reader to differentiate between tags and select a particular tag for further communication. Tag UIDs are

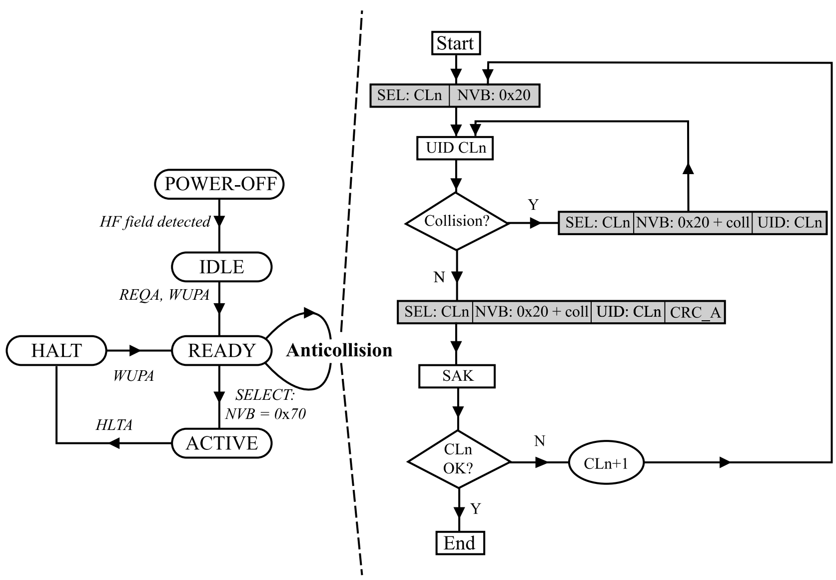

Figure 1.6. State transition diagram of an ISO/IEC 14443 Type-A compliant tag and corresponding anticollision loop diagram.

reminiscent of serial numbers and are usually stored in read only memory, with manufacturers responsible for their uniqueness. However, temporary randomised UIDs may be permitted under special circumstances for single-size UIDs.

The reader initiates the anticollision loop by issuing a "select" (SEL) command byte, followed by a "number of valid bits" (NVB) byte. The coding of SEL defines the cascade level CLn, where n specifies the number of anticollision loop iterations necessary to acquire the complete UID. UIDs have three possible sizes: single, double or triple, which contain 4, 7, or 10 bytes, respectively. The CLn equals the UID size (for example $n = 3$ for a triple-size UID). The NVB specifies the number of all valid data bits which have been transmitted by the reader in the "Select" frame. Initially, the reader specifies CL1 and NVB = 0x20, to which all tags synchronously respond with the first four bytes of their UID (or complete UID if single-sized) followed by a block check characters (BCC) byte, calculated as exclusive-or over the four previous bytes. If multiple tags were present and a collision was detected by the reader, the reader increments the NVB by the position of the first collision bit and transmits the "Select" frame, the updated NVB, and a part of the valid UID bits which were received before the collision occurred. Upon receipt of the updated "Select" frame, tags with UIDs matching the valid bits transmitted by the reader respond with the remainder of the first four UID bytes. This loop continues until the first four UID bytes have been acquired for all tags, with the maximum number of iterations equal to 32.

The reader can now select a particular tag by transmitting a "Select" frame, NVB = 0x70, the four UID bytes, and a cyclic redundancy check error detection code (CRC_A). The selected tag replies with a select acknowledge (SAK) byte, specifying whether the full UID had been received by the tag. If the UID was complete, the tag enters the "active" state and becomes available for higher-level communication. Otherwise, the CL is increased and the anticollision routine is repeated. Tags may transition into the "Halt" state from the "Active" state when issued with a valid HLTA command.

The delay between the end of a reader data frame and the start of a tag response data frame is strictly regulated to ensure synchronous operation of the half-duplex communication protocol. The delay is referred to as the frame delay time (FDT) T_{D}, which varies depending on the command type issued by the reader and the value of the last transmitted bit prior to the end of communication. The FDT is measured between the end of the last pause transmitted by the reader and the first modulation edge of the start bit of the tag response, as shown in Figure 1.7. For the "REQA", "WUPA", or "SEL" commands, the FDT $= 1236/f_{\mathrm{c}} \approx 91.15$ µs if the value of the last data bit is '1', or FDT $= 1172/f_{\mathrm{c}} \approx 86.43$ µs if the last data bit was '0'. For all other command types, the

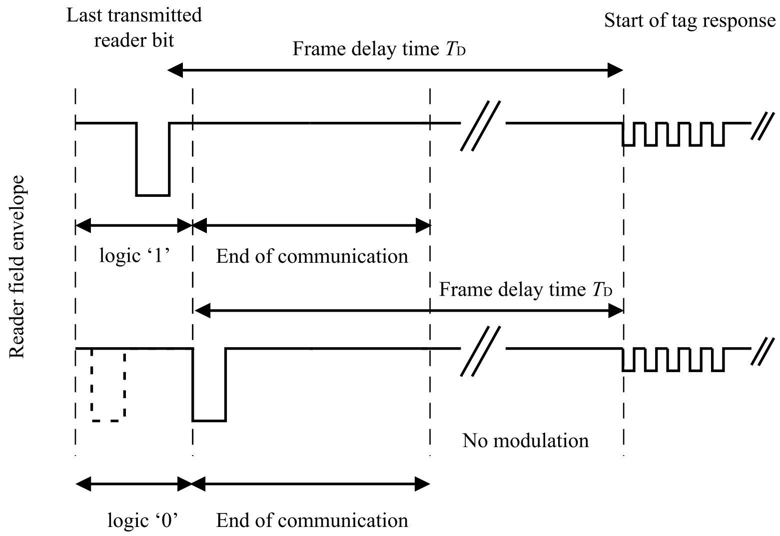

Figure 1.7. Frame delay timing between reader and tag data frames for ISO/IEC 14443 Type-A.

duration of the FDT also depends on the number of data bytes transmitted by the reader within a standard frame.

Part 4 of the Standard [77] describes the transmission of application protocol data units (APDUs) containing arbitrary data. Part 4 is beyond the scope of this thesis.

1.2.5 *Signal characteristics*

The topology of the NFC analogue interfaces, as well as the antenna design parameters are determined by the characteristics of the RF interface signals. Figure 1.8 (a) shows the time-domain field variation of an REQA command issued by a reader (highlighted in red) and a corresponding ATQA tag response (highlighted in green). The plot was obtained by measuring the HF field between a reader and an NFC-A smart card using a small inductive probe connected to an oscilloscope. The field is completely dominated by the HF carrier, with weak reader and tag modulation signals separated in time by frame delay pauses.

Figure 1.8 (b) shows the power spectrum of the reader signal, normalised by the HF carrier power at f_c. The modulation signal sidebands are at least 15 dB below the carrier signal and mostly obscured by it. The minimum forward-link bandwidth BW_R (highlighted in red) required for communication is determined by the minimum bit code feature width in the modified-Miller encoded symbols. This is defined by the minimum permitted value of T_1 [Figure 1.5 (a)], given by $T_{1_{min}} = 28/f_c$. The minimum approximate bandwidth which is required is thus $BW_R = 2/T_{1_{min}} = 2 \cdot f_c/28 \approx 969$ kHz.

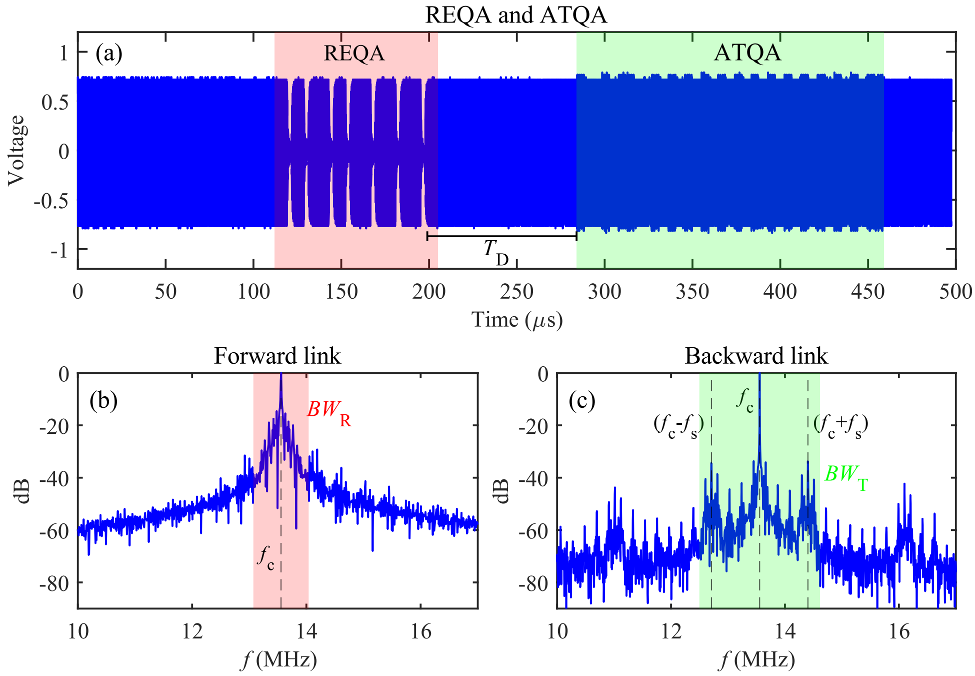

Figure 1.8. Measured ISO/IEC 14443 Type-A RF interface signals; (a) HF field modulation during tag initialisation; (b) energy spectral density of the reader signal (forward link); (c) energy spectral density of the tag response (backward link). Dashed lines show the carrier and subcarrier frequencies f_c and $f_\mathrm{c} \pm f_\mathrm{s}$.

Figure 1.8 (c) shows the power spectrum of the tag response signals, also normalised by the reader carrier power. The modulating signal sidebands are centred around $f_\mathrm{c} \pm f_\mathrm{s}$, with the subcarrier power at least 30 dB below the carrier, while subcarrier harmonics remain below -40 dB. The minimum backward-link bandwidth (highlighted in green) is $BW_\mathrm{T} = 2f_\mathrm{s} + 4f_\mathrm{b} = 2f_\mathrm{c}/16 + 4f_\mathrm{c}/128 = 5f_\mathrm{c}/32 \approx 2.12$ MHz, where the first term is the subcarrier separation, while the second term is the minimum bandwidth required by the Manchester-encoded tag modulation signals. The minimum required NFC-A bandwidth is thus determined by the backward link due to the presence of subcarriers.

1.2.6 *RF interface*

NFC devices communicate by modulating the magnetic near field using resonant inductive antennas, designed to maximise field strength, power transmission, and range. Figure 1.9 shows a simplified lumped-element equivalent circuit of the reader and tag antennas [63]. The reader antenna has an inductance L_1 and resistance R_1, with an additional in-series load resistor R_{L1}. The antenna is fed by the reader front-end, represented by a voltage source of power P_R and output impedance Z_S. To maximise power transmission, the antenna is matched to the source impedance at f_c using an L-section with capacitors C_{M1} and C_{M2}, which also make the antenna resonant [97].

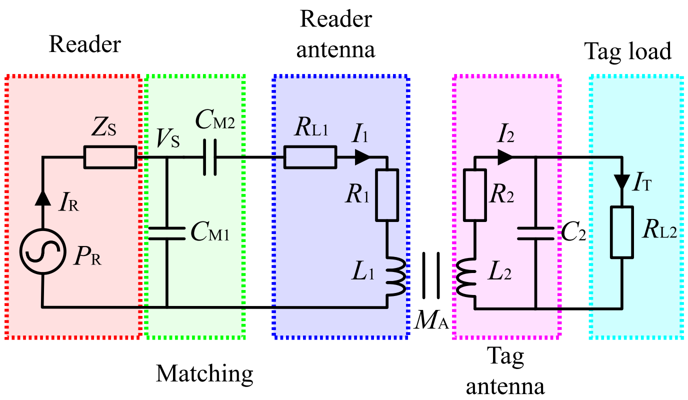

Figure 1.9. Simplified equivalent circuit of an NFC reader and tag.

The tag antenna has inductance L_2 and resistance R_2, with a parallel capacitance C_2 tuned to resonate with L_2 at f_c. The tag load is represented by resistance R_{L2}. The reader and tag antennas are coupled by mutual inductance M_A with a coupling coefficient $k_A = M_A/\sqrt{L_1 L_2}$.

For practical systems, the value of k_A is variable, so reader antennas are matched under the assumption $k_A = 0$. Denoting $R_{A1} = R_{L1} + R_1$, the matching conditions at $\omega_c = 2\pi f_c$ are as follows, provided Z_s is real and $Z_s > R_{A1}$.

$$
\begin{aligned}
C_{M1} &= \frac{1}{\omega_c Z_s}\sqrt{\frac{Z_s}{R_{A1}} - 1} \\
C_{M2} &= \left\{\omega_c\left[L_1\omega_c - \sqrt{R_{A1}(Z_s - R_{A1})}\right]\right\}^{-1}
\end{aligned}
\tag{1.1}
$$

At the carrier frequency, $V_s = \sqrt{Z_s P_r}$ and the current flowing through the reader antenna is given by

$$
I_1 = \frac{\sqrt{Z_s P_r}}{R_{A1} + j\sqrt{R_{A1}(Z_s - R_{A1})}}. \tag{1.2}
$$

The absolute value of the current $|I_1| = \sqrt{P_r/R_{A1}}$, meaning the maximum reader antenna current is limited by antenna resistance, while the power dissipated in the antenna is $P_R = |I_1|^2 R_{A1}$. Since the magnetic field strength is proportional to the current flowing through the antenna, it appears desirable to minimise antenna resistance and set $R_{L1} \to 0$. However, the antenna bandwidth must be sufficiently high to accommodate the reader and tag modulation sidebands. Consequently, conventional systems require reader and tag antenna Q-factors to approximately remain between 10 and 30 [88]. The 3dB reader antenna bandwidth BW_1 is determined by the loaded antenna Q-factor Q_{A1}, typically an order of magnitude below the unloaded Q-factor Q_1 ($R_{\mathrm{L1}} = 0$).

$$Q_{A1} = \frac{f_{\mathrm{c}}}{BW_1} = \frac{\omega_c L_1}{(R_{\mathrm{L1}} + R_1)} \tag{1.3}$$

Figure 1.10 shows the S21 scattering parameters for the equivalent circuit in Figure 1.9, which have been numerically simulated using Matlab®. The reader source is across Port 1 and the tag load is across Port 2, with $L_1 = 2$ µH, $L_2 = 4$ µH, $k_{\mathrm{A}} = 0.01$, $Q_1 = 200$, $R_{\mathrm{L2}} = 3.6$ kΩ, $C_2 = 34.4$ pF, while C_{M1} and C_{M2} were set according to (1.1). The blue line shows the S21 parameters for the unloaded reader antenna ($Q_{\mathrm{A1}} = Q_1$), while for the red line the reader antenna Q-factor has been lowered to $Q_{\mathrm{A1}} = 10$ using R_{L1}. The artificial loading results in a transmitted power reduction at the carrier frequency by ΔP_{c} (12 dB), but an increase of ΔP_{s} (5.5 dB) at the sideband frequencies $f_{\mathrm{c}} \pm f_{\mathrm{s}}$. Similarly, the difference in transmission between carrier and subcarrier frequencies is substantially reduced for the loaded case. In practice, the value of R_{L1} must be optimised to enable sufficiently high carrier transmission for tag powering, while also minimising attenuation of the modulation signal sidebands. The lost carrier power P_{D} dissipated by the loading resistor typically accounts for most of the antenna loss and is easily calculated when $k_{\mathrm{A}} = 0$.

$$P_{\mathrm{D}} = P_{\mathrm{R}} \left(1 - \frac{Q_{\mathrm{A1}}}{Q_1}\right) \tag{1.4}$$

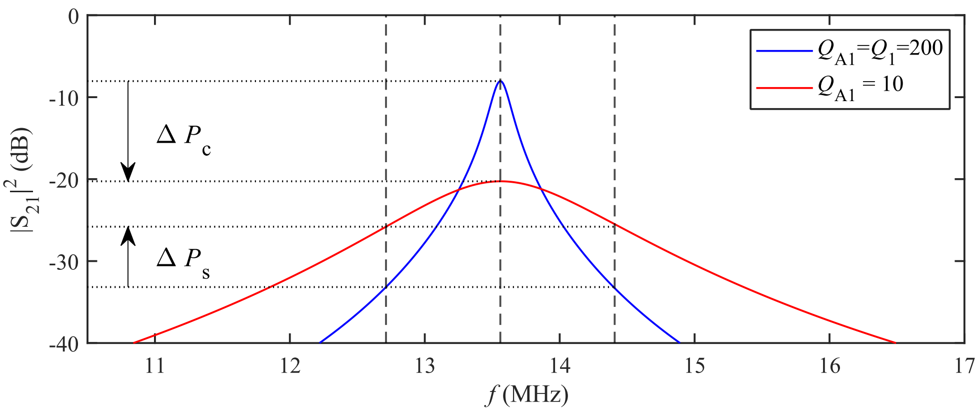

Figure 1.10. Simulated variation of scattering parameters between the reader source and tag load with reader antenna Q-factor. Dashed lines show the carrier and subcarrier frequencies.

1.2.7 *Antenna field scaling*

The reader's magnetic near field can be enhanced by increasing the antenna current I_1, as well as optimising the antenna geometry. Typical antenna geometries include circular, square, rectangular, and spirals thereof. NFC systems generally operate at very short range due to the inherently adverse scaling of magnetic near fields and the need to transmit sufficient power to ensure tag power-up. [98]. Operating range is strongly dependent on reader and tag antenna orientations, requiring axial alignment for optimal performance [99]. For a circular loop lying in the x-y plane with diameter $2b$, the axial z-component of the magnetic field is given by

$$H_{\mathrm{z}} = \frac{I_1 b^2}{2(b^2 + z^2)^{3/2}}. \tag{1.5}$$

At small range such that $z \ll b$, the field H_{z} is approximately constant, but for $z \gg b$, the field $H_{\mathrm{z}} \propto 1/z^3$. Although the inverse cubic decay is already poor, the implications for reader power are more drastic. To achieve a minimum axial field strength $H_{\mathrm{z_{min}}}$, the required reader power is

$$P_{\mathrm{R}} = \frac{2\omega_{\mathrm{c}} L_1 H_{\mathrm{z_{min}}}^2 (b^2 + z^2)^3}{Q_{\mathrm{A1}} b^4}. \tag{1.6}$$

For $z \gg b$, we have $P_{\mathrm{R}} \propto z^6$, implying that the reader power must increase by a factor of 64 to achieve a field strength of $H_{\mathrm{z_{min}}}$ at twice the range. The field and power scaling can be improved by employing alternative antenna geometries. For example, the centreline magnetic field of two parallel conductors with opposing currents separated by $2b$ and parallel to the x-axis is given by

$$H_{\mathrm{z}} = \frac{I_1 b}{\pi(b^2 + z^2)}. \tag{1.7}$$

The range scaling of the parallel conductor pair is preferable to a circular loop with the same diameter as the conductor separation, since the field decays as $1/z^2$ for the former. Similarly, reader power scaling is also improved for the parallel conductors, with $P_r \propto z^4$ in (1.8).

$$P_r = \frac{\omega_{\mathrm{c}} L_1 H_{\mathrm{z_{min}}}^2 (b^2 + z^2)^2}{2Q_{\mathrm{A1}} b^2}. \tag{1.8}$$

Naturally, the fields from (1.7) cannot be realised in practice since conductors of infinite length are needed. A good approximation is provided by a rectangular current loop with a high aspect ratio. Similarly, the field scaling of a square current loop is similar to that of a circular loop (1.5). The z-component of the magnetic field of a rectangular current loop lying in the x-y plane and centred around the origin with width $2a$ and height $2b$ in the x- and y-directions, respectively, may be calculated using well-known analytic expressions [100], [101].

$$
\begin{aligned}
H_z &= \frac{I_1}{4\pi}\sum_{n=1}^{4}\left[\frac{(-1)^n d_n}{r_n[r_n+(-1)^{n+1}c_n]}-\frac{c_n}{r_n[r_n+d_n]}\right] \\
c_1 &= -c_4 = a+x, \qquad d_1 = d_2 = y+b \\
c_2 &= -c_3 = a-x, \qquad d_3 = d_4 = y-b \\
r_1 &= \sqrt{(a+x)^2+(y+b)^2+z^2} \qquad r_2 = \sqrt{(a-x)^2+(y+b)^2+z^2} \\
r_3 &= \sqrt{(a-x)^2+(y-b)^2+z^2}, \qquad r_4 = \sqrt{(a+x)^2+(y-b)^2+z^2}
\end{aligned}
\tag{1.9}
$$

Figure 1.11 (a) compares the axial field of the circular loop (1.5), parallel conductor pair (1.7) and rectangular loop (1.9), with $b = 0.35$ m in all cases. For the rectangular loop, the aspect ratio $A = a/b$ is varied from $A = 1$ (square) to $A = 4$, approximating a parallel conductor pair (1.7). At short range ($z < b$), the strongest field is produced by the circular loop followed by the square loop, which closely approximates it. The field is reduced as A increases and becomes weakest for the parallel conductors. This happens because magnetic fields are strongest in the immediate vicinity of the conductors. The opposite outcome is observed at long range ($z > b$), with the parallel conductor field decaying the slowest. Figure 1.11 (b) compares the reader power required to achieve a minimum field strength $H_{z_{\min}} = 1.5$ A/m at axial distance z for the same antenna geometries. As A increases, the reader power requirement for rectangular antennas approach those of parallel conductors but depart for large z. Rectangular loops thus offer improved performance at intermediate range.

The above arguments suggest that if physical restrictions on reader antenna dimensions exist (for example, b is fixed), then a rectangular antenna may provide the highest capture volume. The achievable aspect ratio is, however, limited by the need to keep the loop perimeter length below $\lambda_c/2 \approx 11$ m to prevent radiation, where λ_c is the wavelength at f_c. Additionally, for loop

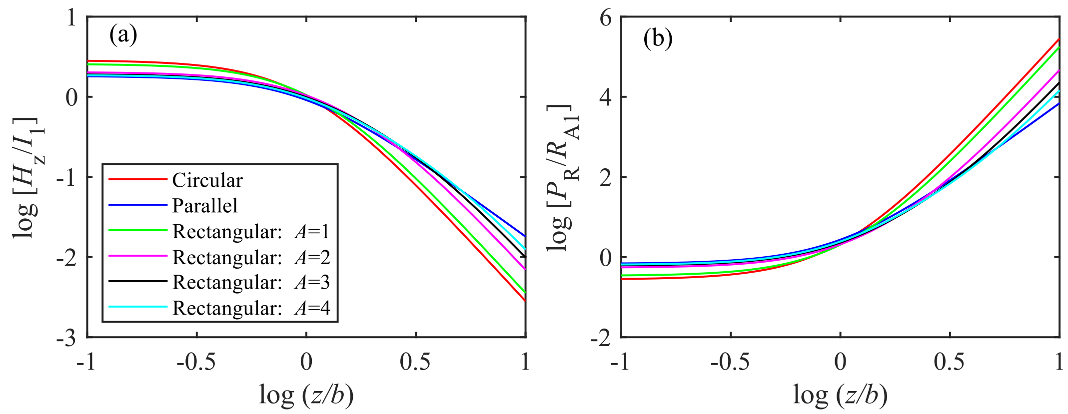

Figure 1.11. Theoretical variation of the (a) axial magnetic field component and (b) required reader power to achieve $H_{z_{\min}} = 1.5$ A/m with range for a range of antenna geometries.

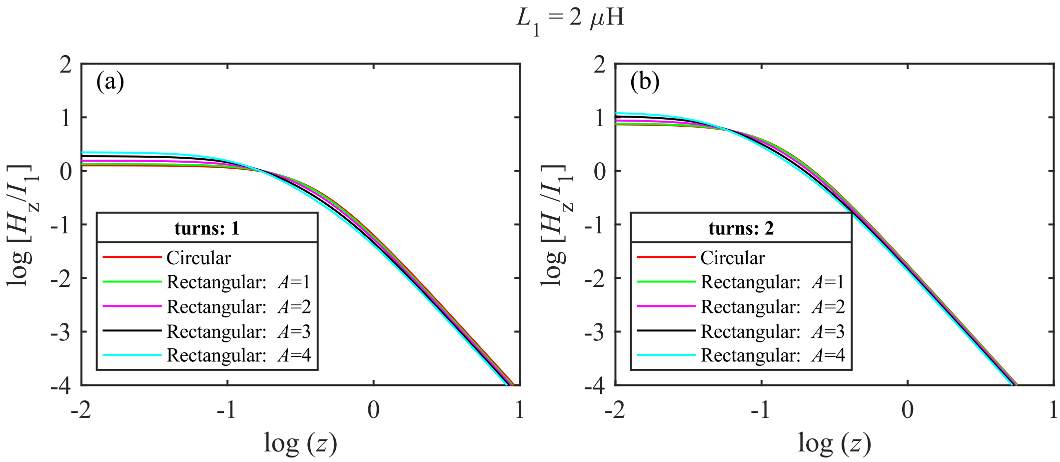

Figure 1.12. Theoretical variation of the axial magnetic field component for a range of antenna geometries, with antenna inductance fixed at 2 μH using (a) one and (b) two turns.

perimeters in excess of $\sim\lambda_c/10$, the achievable magnetic field strength becomes reduced due to phase differences along the antenna conductors, which are not accounted for by (1.5), (1.7) or (1.9). Furthermore, the tag must physically remain in the reactive near field of the reader antenna for communication to occur, such that $z \ll \lambda_c/(2\pi) \approx 4$ m [98], [102]. Consequently, increasing the antenna perimeter may in fact reduce the axial range, meaning the capture volume of a single antenna is fundamentally limited. We also note that the antennas in Figure 1.11 have different inductances, which may be restricted in practice by matching requirements. A fairer comparison would be to compute the axial antenna fields with the inductance fixed for all geometries.

Figure 1.12 (a) compares H_z for circular and rectangular loop antennas, with the additional restriction that $L_1 = 2$ μH. Under this condition, the range scaling is the opposite to Figure 1.11, with the circular loop achieving the lowest field strength at short range and the highest field strength at long range. Likewise, the rectangular loop with $A = 4$ has the poorest scaling at long range, but the highest field strength at short range due to the short conductor separation required to achieve the desired inductance. Furthermore, in contrast to Figure 1.11, the field scaling at range is less pronounced, with all antennas exhibiting similar performance. Due to the adversity and limitations imposed by near field scaling, conventional readers typically favour small-perimeter loops with multiple turns, sacrificing long-range performance for strong fields in the immediate vicinity as illustrated by Figure 1.12 (b), which depicts the axial fields of antennas with two turns.

1.2.8 *Capture volume limitations*

As discussed in the previous Section, the capture volume of NFC reader antennas is fundamentally limited in the transverse direction by extremely poor field scaling, as well as longitudinally by restrictions on maximum antenna perimeter. A trivial enhancement method is to increase the reader carrier power for a minor increase in transverse range. This method, however, requires non-trivial receiver isolation techniques and may generate fields exceeding permissible safety regulations. Another solution is to employ physically large antennas with optimal loop geometry [98]. Both methods are usually employed in conjunction, with [91] achieving a 25 cm NFC-A tag activation range using a circular loop antenna with a diameter of 40 cm and a 12-V battery-powered reader, while in [93] a range of 40 cm was achieved using a 50 cm x 50 cm square loop antenna and a 60 W reader. The drawbacks of these methods are apparent from the latter work: "While increasing the amplification, the matching components necessary (to adapt the antenna impedance to a 50 Ω regime for maximum power transfer) heated up to 120 °C within two minutes and resulted in a mismatch that eventually broke the antenna and the reader". Other methods of increasing transverse range include artificially lowering the minimum operating field strength requirements by using active tags [103], or detecting higher tag response harmonics [93], [104].

A more efficient means for capture volume enhancement is to employ reader antenna arrays [105], which enables lateral scaling of the capture volume and bypasses the perimeter restrictions imposed on individual antenna elements. Arrangements allowing arbitrary tag orientations [106], [107], and arrays with null zone compensation [108] have been demonstrated. Common array feeding methods include multiplexing [50], [109], with the reader sequentially powering each antenna element to scan for tags in vicinity [110]. The hardware complexity of multiplexed systems, however, scales poorly with the number of antenna elements. The hardware overhead is most significant for arrays with direct element addressing but can be substantially reduced by employing active matrix arrays [111]. For example, given an N-by-M antenna array, the number of reader channels is $N \cdot M$ for direct addressing, but reduces to $N + M$ for active matrix implementations. It must also be noted that multiplexed arrays generally cannot power multiple antennas simultaneously, which makes communication with multiple distributed tags problematic.

Clearly, more efficient and practical methods of increasing capture volume are required. An alternative has been suggested in a recent study [94], which employs multiple-element travelling-wave antennas to increase lateral capture volume with no added cost to reader complexity, while also powering all the constituent antenna elements simultaneously. The antenna comprised a periodic arrangement of low-loss field-generating resonant loops, capable of supporting band-limited wave propagation over the NFC frequency band. Although multiple travelling-wave antenna topologies exist, the study employed a magneto-inductive (MI) waveguide antenna owing to its continuous axial magnetic fields. A reader was placed at one end of the antenna, with the other end terminated with a high-power absorptive load. The reader could then inject Type-A-compliant queries, powering and interrogating all tags in vicinity. The background theory on MI waveguides and the study in question are reviewed in the following Section.

1.3 Magneto-inductive waveguides

1.3.1 *Overview*

Magneto-inductive waveguides comprise a metamaterial formed by periodic arrays of magnetically coupled resonators, which can support the propagation of forward or backward magneto-inductive waves. Despite the recent attention, neither concept is entirely new. The propagation and filtering properties of periodic materials (both naturally occurring and artificial), including those comprising electrical circuits, have been known in the 1940s [112]. The recent proposition regarding the existence of media with simultaneously negative permittivity and permeability [113] which founded the metamaterial field can be traced back to 1968 [114]. One-dimensional MI waveguides were formally defined in 2002 [115], shortly after the first experimental verification of negative refraction index metamaterials [116]. It was suggested that MI waveguides were both dispersive and band-limited, with MI waves identified as a type of slow wave. The theoretical models were extended to two- and three-dimensional MI waveguides [117] and shown to agree with experimental results [118], [119]. MI waves have been observed at frequencies ranging from RF to optical, with resonators formed by split-rings, Swiss rolls, lumped-elements, and capacitor grids [120]–[126]. Sophisticated theoretical models accounting for the effects of retardation [127], radiation [128], higher-order non-nearest neighbour coupling [129], refraction [130], and loss [131] have been developed. MI waveguides with non-trivial characteristics have also been proposed and methods of tailoring their properties using dispersion engineering were discussed [132]. MI waveguides with multiple frequency passbands have been implemented as well as coupled waveguide pairs, ring resonators, and waveguides comprising doubly resonant elements.

Multiple applications of MI waveguides have been developed, which vary in terms of their practical usefulness. Since the waveguide dispersion characteristics can be tailored by simply changing the relative physical positioning of constituent resonators, the waveguides are capable of internally filtering MI waves. MI equivalents of mirrors, Fabry-Perot resonators, Bragg gratings, power couplers, splitters, phase shifters, and delay lines have all been proposed [133]–[136]. The latter have been applied in chip-less RFID tags, since the slow wave nature of MI waveguides allows long delays to be implemented using short waveguide sections. MI waveguides have been employed as communication channels [137], [138], with performance generally inferior to conventional systems owing to signal dispersion, susceptibility to external interference, limited bandwidth, and substantial loss per unit length. MI communication systems can, however, outperform conventional systems in RF-challenged environments, such as underwater [139], underground [140], or inside oil reservoirs and mine tunnels [141]. Naturally, the external magnetic fields inherent to all MI waveguides make them suitable candidates for wireless power transfer [142]–[146], with MI relay elements used to improve the efficiency and range of wireless power delivery systems. Near field imaging applications are also abundant, with MI slabs employed as lenses [147]–[151]. Perhaps the most promising applications, however, are in magnetic resonance imaging (MRI) systems, with MI waveguides employed as both flux guides and detectors [152]–[155]. The use is justified by improved patient safety owing to the lack of direct connections between MI waveguide elements, which eliminates the risk of overheating in the presence of strong MRI fields. Furthermore, flexible thin-film MI waveguides may be employed in catheters for high-precision patient imaging [156]–[158]. Finally, MI systems can be employed for capture volume enhancement in near field communication systems [94], which is the focus of the following Sections. Before proceeding, however, we review key theory on MI waveguides.

1.3.2 *One-dimensional MI waveguides*

The simplest magneto-inductive waveguide topology is that of a uniform one-dimensional waveguide. Provided the element dimensions are substantially smaller than the operating wavelength, the waveguide may be accurately modelled by a lumped-element equivalent circuit. Such a circuit is shown in Figure 1.13, which consists of magnetically coupled resonators with inductance L, capacitance C, equivalent resistance R, physical length a, and nearest neighbour mutual inductance M. Although non-nearest neighbour coupling is a common problem, the effect can be minimised by appropriate element spacing. Here, we assume the unwanted coupling is

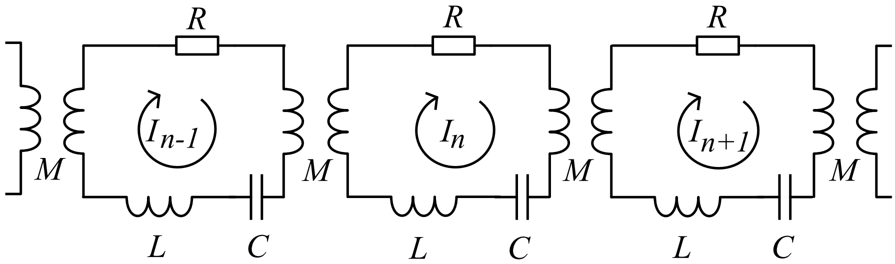

Figure 1.13. Equivalent circuit of a lossy one-dimensional magneto-inductive waveguide.

negligible. If the loop current in resonator n is I_n, we can obtain a circuit equation relating the currents in adjacent elements at angular frequency ω.

$$I_n\left(j\omega L + \frac{1}{j\omega C} + R\right) + j\omega M(I_{n-1} + I_{n+1}) = 0 \tag{1.10}$$

The series inductance and capacitance form a resonator with angular resonant frequency ω_0.

$$\omega_0 = \frac{1}{\sqrt{LC}} \tag{1.11}$$

The resistance R can also be related to the unloaded element Q-factor Q.

$$Q = \frac{\omega_0 L}{R} \tag{1.12}$$

Finally, we define the nearest-neighbour coupling coefficient κ.

$$\kappa = \frac{2M}{L} \tag{1.13}$$

The coupling coefficient is positive for axial resonator orientations and negative for planar configurations [132]. The value range is fundamentally limited by $-2 < \kappa < 2$. Typical values, however, fall within the range $-0.2 < \kappa < 0.7$, with inherently weaker coupling in the planar configuration [159].

We now assume a travelling-wave solution propagating from the left of the form $I_n = I_0 e^{-jkna}$, where I_0 is the current amplitude at $n = 0$ and $k = k' - jk''$ is the complex propagation constant, where both k' and k'' are purely real quantities. The assumed solutions for I_n, as well as equations (1.11) – (1.13) can be substituted into (1.10), which yields the dispersion equation (1.14).

$$\cos(ka) = \frac{1}{\kappa}\left(\frac{\omega_0^2}{\omega^2} + j\frac{\omega_0}{\omega Q} - 1\right) \tag{1.14}$$

For lossless waveguides, the Q-factor is infinite, and the right-hand side of (1.14) is purely real. Wave propagation is then permitted when $|\cos(ka)| < 1$. The ideal frequency passband is thus given by

$$\frac{1}{\sqrt{1+|\kappa|}} \leq \frac{\omega}{\omega_0} \leq \frac{1}{\sqrt{1-|\kappa|}}. \tag{1.15}$$

The propagation constant is purely real in the passband and purely imaginary in the stopbands. In lossy waveguides, however, attenuated out-of-band propagation is allowed. For lossy, high Q-factor waveguides, the real and imaginary parts of (1.14) can be simplified, yielding useful approximations for $k'a$ and $k''a$.

$$\cos(k'a) \approx \frac{1}{\kappa}\left(\frac{\omega_0^2}{\omega^2} - 1\right) \tag{1.16}$$

$$k''a \approx \frac{1}{\kappa Q sin(k'a)}. \tag{1.17}$$

Equation (1.16) suggests that $k'a$ can be approximated by the ideal dispersion relation for low-loss waveguides. Equation (1.17) suggests that the wave attenuation is inversely proportional to the product of κQ. All practical MI systems should thus maximise nearest-neighbour coupling, as well as element Q-factors (as opposed to conventional NFC readers). It has also been shown that the presence of non-nearest neighbour coupling may significantly hinder performance [129].

Figure 1.14 shows the theoretical frequency variation of $k'a$ and $k''a$ obtained using (1.14) for lossy waveguides with $\kappa = \{\pm 0.3, \pm 0.6\}$ and $Q = 200$. It is well-known that the dispersion equations for periodic media have periodic solutions [112]. In (1.14), for example, $k'a + 2\pi v$ are all valid propagation constants, where v is an integer. It is also well-known that such media may be right- or left-handed, characterised by codirectional group and phase velocities for the former, and opposite for the latter [160]. We choose to restrict the solutions for ka such that $\pi \leq k'a \leq \pi$, for which the group velocity $v_g = \frac{d\omega}{dk'} \geq 0$. Waveguides with positive κ support the propagation of forward waves, while negative κ results in backwards waves. Wave propagation is both band-limited and dispersive, with $k'a = \pm\pi/2$ at resonance, depending on κ polarity. The effect of loss

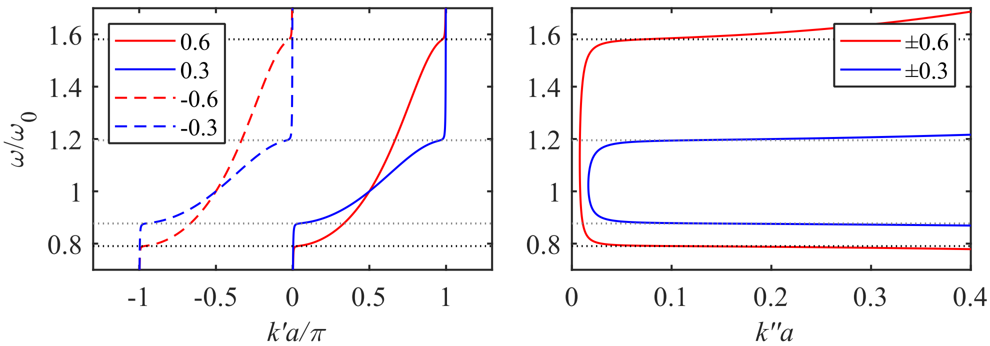

Figure 1.14. Theoretical variation of $k'a$ and $k''a$ with frequency for lossy one-dimensional MI waveguides with $\kappa = \{\pm 0.3, \pm 0.6\}$ and $Q = 200$. Dotted lines indicate the frequency passband edges for lossless waveguides.

is to increase the passband width beyond the constraints of (1.15), with higher attenuation for smaller κ values as suggested by (1.17).

1.3.3 *Characteristic impedance and matching*

Infinitely long lines cannot be implemented in practice, but reflections can still be eliminated by terminating the waveguide with its characteristic impedance Z_0. For an MI waveguide, Z_0 is given as follows [117].

$$Z_0 = j\omega M e^{-jka} \,. \tag{1.18}$$

The MI characteristic impedance is frequency-dependent and complex, both in the passbands and in the stopbands. This is true even if the waveguide is lossless, in contrast to the characteristic impedance of ideal transmission lines and RF instruments, which is both constant and real. This makes matching MI waveguides to conventional systems difficult. Such properties also complicate the modelling of internal power flow, with conventional models often generating seemingly anomalous scattering parameters, as will be shown in Chapter 2.

At resonance, $k'a = \pm\pi/2$, and the characteristic impedance becomes purely real such that $Z_0(\omega_0) = Z_{0\mathrm{M}} = \omega_0|M|e^{-k''a}$. For high Q-factors, $Z_{0\mathrm{M}} \approx \omega_0 M$, which means MI waveguides can always be matched to a real load R_L at ω_0. It has also been shown that broadband matching can be achieved at two or three frequencies simultaneously [161], [162]. Examples of possible

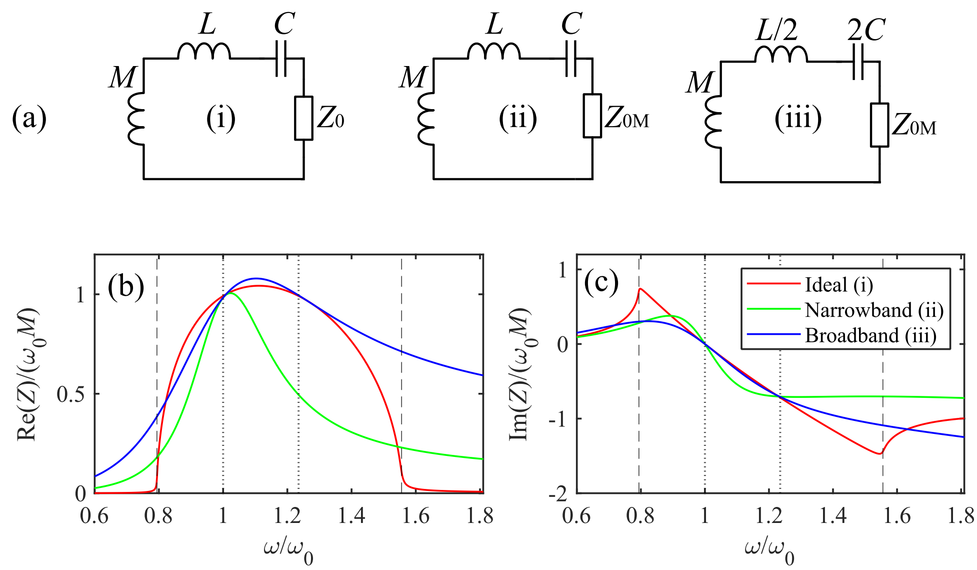

Figure 1.15. (a) Possible candidates for MI waveguide termination impedances, including ideal (i), narrowband, and broadband (iii). Real (b) and imaginary (c) parts of impedances (i)-(iii) for a waveguide with $L = 2\ \mu\mathrm{H}$, $Q = 200$, $Z_{0\mathrm{M}} = 50\ \Omega$, and $\omega_0 = 2\pi f_c$.

termination impedances Z are shown in Figure 1.15 (a). Termination (i) corresponds to the ideal characteristic impedance, which is not realisable in practice but useful for numerical and analytic calculations. Impedance (ii) is for narrowband matching at ω_0, which is often sufficient. It consists of a standard waveguide element with an in-series $Z_{0\mathrm{M}}$ load. Lastly, termination (iii) may be employed for broadband matching at two frequencies, namely ω_0 and $\omega_0/\sqrt{1-\kappa^2}$, achieved by halving the self-inductance and doubling the capacitance of the terminating element.

Figure 1.15 (b) shows the real parts of impedances (i)-(iii) and Figure 1.15 (c) shows their imaginary parts, given a waveguide with $L = 2\ \mu\mathrm{H}$, $Q = 200$, $\omega_0 = 2\pi f_c$, and $Z_{0\mathrm{M}} = 50\ \Omega$. Dashed lines indicate the waveguide frequency passband according to (1.15), while the dotted lines show the matching frequencies. The real part of characteristic impedance (i) is approximately zero outside of the passband, while its imaginary part is zero at resonance. The narrowband termination (ii) offers good matching around ω_0, but its real part quickly diverges from Z_0. Termination (ii) provides excellent matching throughout most of the passband and can be employed in high-performance MI systems.

The terminations in Figure 1.15 (a) can only be used at the end elements of otherwise uniform MI waveguides. It may, however, be desirable to perform internal matching within a waveguide, or seamlessly join a pair of MI waveguides with minimal internal reflections. An example of such a problem is shown in Figure 1.16. The first semi-infinite uniform waveguide has an element inductance L_1, capacitance C_1, mutual inductance M_1, resonant frequency ω_{01}, and stretches from $n = -\infty$ to $n = 0$. The second waveguide has an inductance L_2, capacitance C_2, mutual inductance M_2, resonant frequency ω_{02}, and stretches from $n = 1$ to $n = +\infty$. The mutual inductance at the interface between the waveguides is M. Standard physics suggests that an incident MI wave from the left side should be partially reflected at the discontinuity, with the remaining power appearing as a transmitted travelling wave in the second waveguide. We thus assume the following solutions for the current I_n, with the amplitudes of the incident, reflected, and transmitted waves are given by I_0, R_0 and T_1, respectively. The propagation constants are $k_1 a_1$ and $k_2 a_2$.

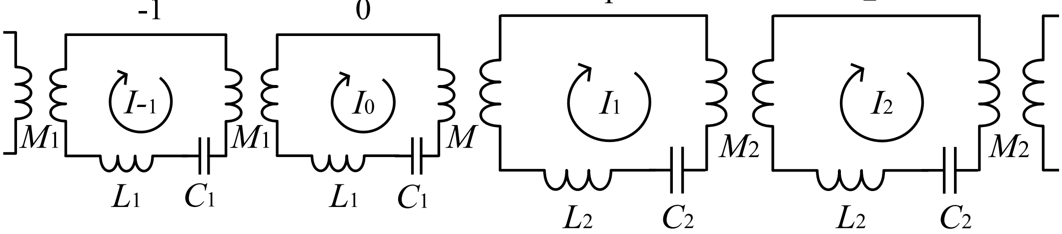

Figure 1.16. Internal matching of an MI waveguide pair.

$$I_n = \begin{cases} I_0 e^{-jk_1 n a_1} + R_0 e^{jk_1 n a_1}, & n \leq 0 \\ T_1 e^{-jk_2 n a_2}, & n \geq 1 \end{cases} \tag{1.19}$$

The currents at the junction can be found by summing the voltages at elements 0 and 1.

$$\begin{aligned} I_0 \left(j\omega L_1 + \frac{1}{j\omega C_1} \right) + j\omega M_1 I_{-1} + j\omega M I_1 &= 0 \\ I_1 \left(j\omega L_2 + \frac{1}{j\omega C_2} \right) + j\omega M I_0 + j\omega M_2 I_2 &= 0 \end{aligned} \tag{1.20}$$

Equations (1.19) can then be substituted into (1.20). The element self-impedances may also be related to the propagation constants by their respective dispersion relations. The resultant equations may be solved for the wave reflection (Γ) and transmission (T) coefficients.

$$\Gamma = \frac{R_0}{I_0} = -\frac{M^2 e^{-jk_2 a_2} - M_1 M_2 e^{-jk_1 a_1}}{M^2 e^{-jk_2 a_2} - M_1 M_2 e^{jk_1 a_1}} \tag{1.21}$$

$$T = \frac{T_1}{I_0} = -\frac{M M_1 \left(e^{jk_1 a_1} - e^{-jk_1 a_1} \right)}{M^2 e^{-jk_2 a_2} - M_1 M_2 e^{jk_1 a_1}} \tag{1.22}$$

In practical systems, the waveguides are likely to have the same resonant frequency $\omega_{01} = \omega_{02} = \omega_0$. Furthermore, we assume that the coupling coefficients may be equalised, such that $\kappa = \frac{2M_1}{L_1} = \frac{2M_2}{L_2} = \frac{2M}{\sqrt{L_1 L_2}}$. Under these conditions, (1.21) simplifies to $\Gamma = 0$ at all frequencies. Similarly, T simplifies to

$$T = \frac{T_1}{I_0} = \sqrt{\frac{M_1}{M_2}} = \sqrt{\frac{L_1}{L_2}}. \tag{1.23}$$

The above observations imply that perfect internal matching may be achieved, provided that the coupling coefficient is constant throughout the combined waveguide. Equation (1.23) also suggests that the loop current amplitudes scale according to the square root of the mutual inductance ratio between the matched sections. Furthermore, the impedance transition may be abrupt (such as in Figure 1.16) or occur gradually over multiple elements. The latter approach is more practical for large impedance steps.

1.3.4 MI antennas for NFC

Magneto-inductive waveguides have been employed as field guides or antennas in several NFC applications. One example is the use flexible textile-integrated MI waveguides to interconnect wearable or implantable passive NFC sensors in body-area networks [60], [163]. Another application used two-dimensional MI grids in commercial NFC-compliant wireless charging stations for mobile devices [164]. Lastly, travelling-wave MI antennas have been used in high capture volume NFC readers for communicating with off-the-shelf NFC-A tags [94]. A system block diagram of the latter application is shown in Figure 1.17.

The system employed a low-loss antenna with rectangular resonators of width $w = 1$ m, height $h = 0.35$ m, inductance $L = 2$ μH, and $Q > 300$. The resonators were arranged in a quasi-axial formation with nearest neighbours overlapping each other, resulting in positive κ values. The nearest-neighbour coupling coefficients could then be tuned to achieve $Z_{0\mathrm{M}} = 50\ \Omega$ by adjusting the separation distance s, resulting in $\kappa \approx 0.59$. The high coupling, combined with high quality factors meant $k'a \approx 1/(300 \cdot 0.59) \approx 0.006$ at ω_0 according to (1.17), amounting to a modest power loss of 0.05 dB per element. A transmitter injected NFC-A queries into the left end, which propagated along the antenna as MI waves. End reflections were minimised by broadband matching. A frequency-selective filter could be placed at either end, which was used to suppress the HF carrier and extract either the reflected, or transmitted tag response signals.

The operating principle of the antenna can be explained by a simple theoretical model. Assuming a tag was magnetically coupled to element 0, the load modulation may be described as a time-varying element resistance $R'(t)$.

$$R'(t) = R + \Delta R_0 + \Delta R_1 \cos(\omega_s t) \tag{1.24}$$

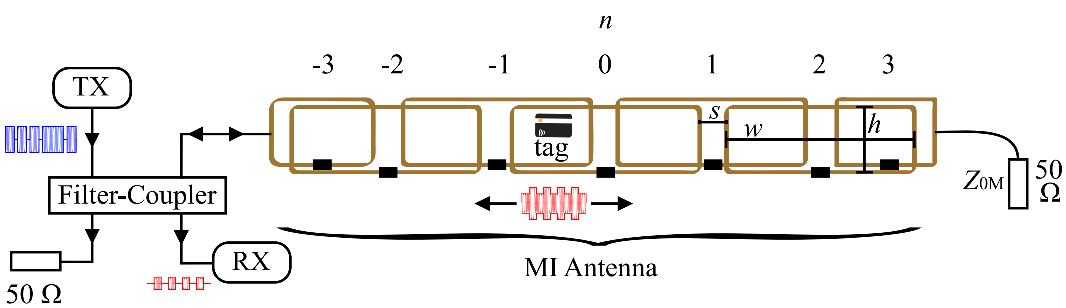

Figure 1.17. High capture volume NFC system using a magneto-inductive travelling-wave antenna. Tag responses may be acquired by reflection or transmission at either end.

ΔR_0 and ΔR_1 represent the DC and AC load modulation amplitudes, with the DC term ensuring modulation is always lossy, and $\omega_s = 2\pi f_s$ is the load modulation frequency. The circuit equation for the loaded element is

$$L\frac{dI_0}{dt} + R'(t)I_0 + \frac{1}{C}\int I_0 dt + M\left(\frac{dI_{-1}}{dt} + \frac{dI_1}{dt}\right) = 0\,. \tag{1.25}$$

For the other resonators, the circuit equation is as follows.

$$L\frac{dI_\mathrm{n}}{dt} + RI_n + \frac{1}{C}\int I_n dt + M\left(\frac{dI_{n-1}}{dt} + \frac{dI_{n+1}}{dt}\right) = 0 \tag{1.26}$$

The carrier signal may be modelled as an incident travelling wave from the left side. The load modulation should result in transmitted and reflected MI waves at element 0, both at the carrier frequency and modulation sidebands $\omega_+ = \omega_\mathrm{c} + \omega_\mathrm{s}$ and $\omega_- = \omega_\mathrm{c} - \omega_\mathrm{s}$. This may be summarised by the following travelling-wave solutions for I_n.

$$\begin{aligned} I_n(t) &= \frac{1}{2}\begin{Bmatrix} \left[A_\mathrm{I}e^{j\omega t}e^{-jnka} + \mathrm{cc}\right] + \left[A_{\mathrm{R}\_}e^{j\omega_- t}e^{jnk_- a} + \mathrm{cc}\right] \\ \left[A_\mathrm{R}e^{j\omega t}e^{jnka} + \mathrm{cc}\right] + \left[A_{\mathrm{R}_+}e^{j\omega_+ t}e^{jnk_+ a} + \mathrm{cc}\right] \end{Bmatrix}, \quad n \le 0 \\ I_n(t) &= \frac{1}{2}\begin{Bmatrix} \left[A_\mathrm{T}e^{j\omega t}e^{-jnka} + \mathrm{cc}\right] + \left[A_{\mathrm{T}\_}e^{j\omega_- t}e^{-jnk_- a} + \mathrm{cc}\right] \\ +\left[A_{\mathrm{T}_+}e^{j\omega_+ t}e^{-jnk_+ a} + \mathrm{cc}\right] \end{Bmatrix}, \quad n > 0 \end{aligned} \tag{1.27}$$

A_I, A_R, A_{R_-}, and A_{R_+} are the incident and reflected waves at ω_c, ω_-, and ω_+, respectively. A_T, A_{T_-}, and $A_{\mathrm{T}_+}$are the amplitudes of the transmitted carrier and modulation sidebands, respectively, while cc represents the complex conjugate of the preceding term. Finally, k, k_-, and k_+ are the propagation constants at ω_c and $\omega_\mathrm{c} \pm \omega_\mathrm{s}$. The assumed solutions and the dispersion relation (1.14) may be substituted into (1.25) and (1.26), and the resultant simultaneous equations solved for the reflection and transmission coefficients at carrier and load modulation frequencies.

$$\begin{aligned} \frac{A_\mathrm{R}}{A_\mathrm{I}} &= \frac{-\Delta R_0}{\Delta R_0 + 2\omega M\sin(ka)} \\ \frac{A_{\mathrm{R}_\pm}}{A_\mathrm{I}} = \frac{A_{\mathrm{T}_\pm}}{A_\mathrm{I}} &= \frac{-\Delta R_1}{2[\Delta R_0 + 2\omega_\pm M\sin(k_\pm a)]} \end{aligned} \tag{1.28}$$

Equations (1.28) describe the effects of load modulation on the waveguide antenna. For static load modulation (tag is silent), some of the carrier becomes reflected back to the reader from the loaded resonator. The effect of time-varying load modulation (tag is responding) is to induce harmonic waves at the loaded element, which propagate away from the element in both directions. The receivers may thus be placed at either antenna end, or at both ends for improved signal-to-noise ratio. The magnitude of the reflection and transmission coefficients (1.28) is dependent on the coupling strength between the tag and antenna resonator, with stronger signals induced at smaller antenna-tag separations.

1.3.5 *Magneto-inductive antenna fields*

Like conventional NFC antennas, the external magnetic field strength of travelling-wave MI antennas is dependent on the resonator geometry and loop currents. In contrast to conventional antennas, however, the MI antenna layout is restricted by the need to achieve high $|\kappa|$ for low loss propagation and adequate NFC bandwidth, while simultaneously minimising non-nearest neighbour coupling and satisfying matching constraints. A good compromise can be achieved with high-aspect ratio rectangular resonators [159].

Figure 1.18 shows the magnitude of the H_z component of the external magnetic field at resonance for a quasi-axial MI antenna with $w = 1$ m, $h = 0.35$ m, $L = 2$ μH, and $Z_{0M} = 50\ \Omega$. The Figure also includes a schematic representation of the antenna resonators, which lie in the x – y plane. The fields have been analytically calculated using (1.9), while the element currents were obtained using (1.10). The resonator separation s (as indicated in Figure 1.17) can be used to adjust M between nearest neighbours to satisfy the matching constraint $M = 50/\omega_c$. The field is strongest in regions where the neighbouring loops overlap due to the partial addition of their individual fields, which are $\pi/2$ out of phase at resonance. It should be noted that the magnitude of the H_x component (not shown) from the vertical conductors is also significant.

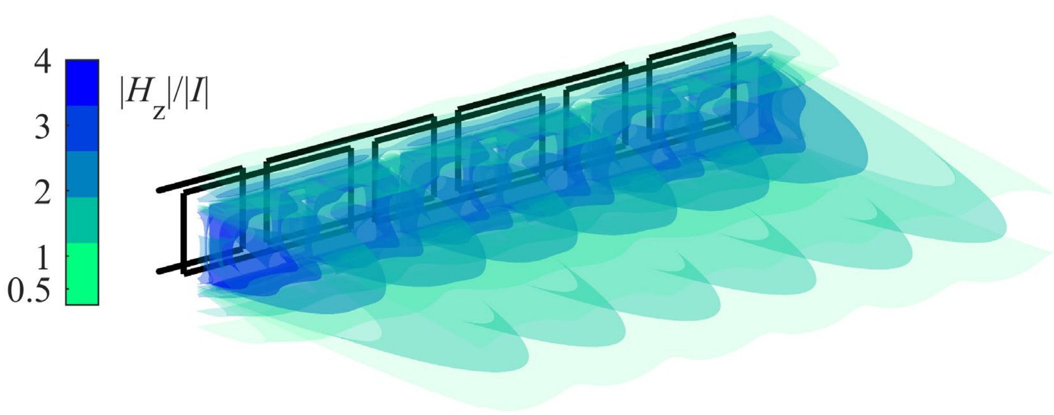

Figure 1.18. Magnitude of the H_z magnetic field component for uniform quasi-axial MI waveguide antenna, with $w = 1$ m, $h = 0.35$ m, and $L = 2$ μH.

As previously discussed, the characteristic impedance of MI waveguide antennas may be internally scaled with no reflections, provided κ and ω_0 are constant throughout. Figure 1.19 shows a field plot for a 9-element waveguide, with resonator self-inductances scaled from $L_0 = 2$ μH to $L_8 = 4$ μH in uniform steps of 0.25 μH by adjusting loop dimensions accordingly. The

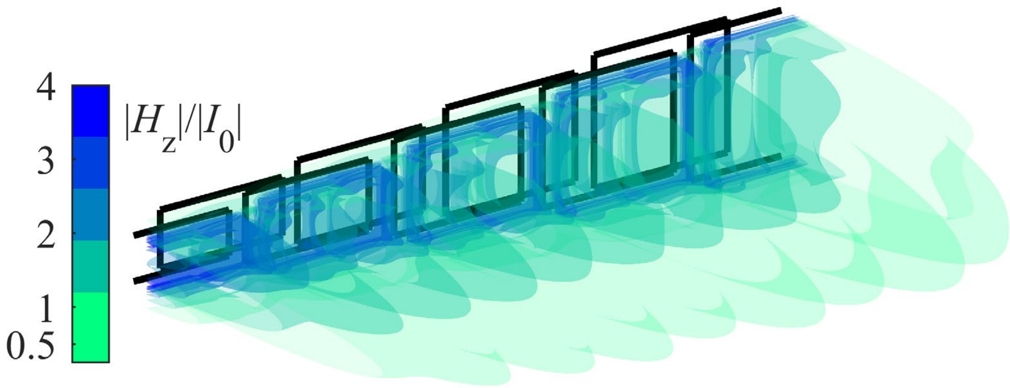

Figure 1.19. Magnitude of the H_z magnetic field component for a non-uniform MI waveguide antenna, with loop inductances scaled from 2 μH to 4 μH in steps of 0.25 μH.

resonator currents have also been scaled according to (1.23) such that $I_8 = 1/\sqrt{2} \cdot I_0$, and the resonator separation adjusted to achieve a uniform κ. While the capture volume of each resonator is incremented by the perimeter scaling, loop currents become weaker, such that no meaningful increase in transverse range is obtained. Nonetheless, the technique offers a convenient means to shape the lateral capture volume in the x-y plane.

1.3.6 *Power scaling*

We now draw a performance comparison between NFC readers employing conventional antennas (Figure 1.9) and readers using MI travelling-wave antennas (Figure 1.17) in the context of high-capture volume systems. Conventional reader antennas must be artificially loaded to lower their Q-factor, which accounts for most of the dissipated reader power. The antennas may be assembled into arrays, but each element must still be powered individually. In contrast, the resonators in MI antennas can maximise their Q-factors, with most of the reader power dissipated in the terminating resistive load. Furthermore, the reader signal need only be injected at a single antenna end to simultaneously power all elements. This has significant implications the scaling of reader power with antenna capture volume.

Figure 1.20 compares the reader power required to produce a minimum current of 0.1 A (rms) in N identical antenna elements with inductance 2 μH and unloaded Q-factor of 200 at $f_c = 13.56$ MHz using conventional and magneto-inductive antenna arrays. For conventional arrays

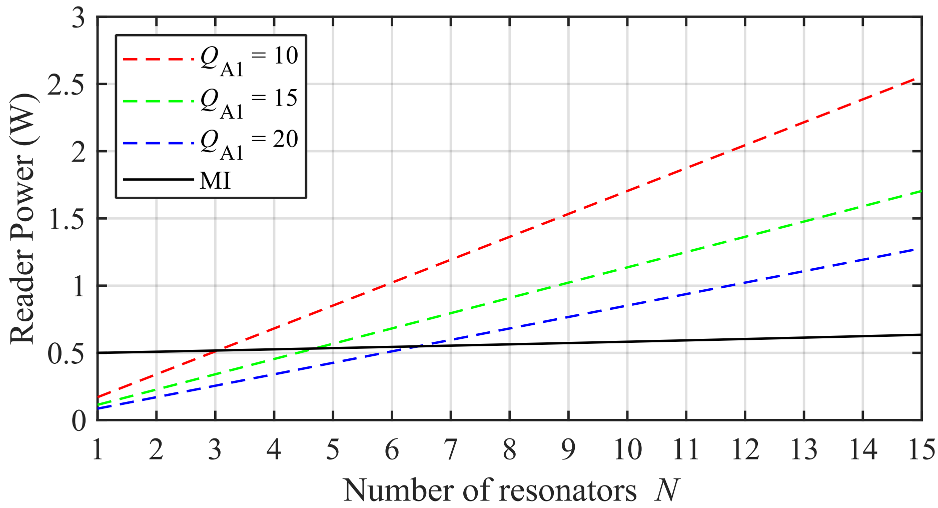

Figure 1.20. Reader power required to achieve a minimum loop current of 0.1 A (rms) in N elements simultaneously using a conventional NFC reader array (dashed lines) and magneto-inductive antenna array (solid line). The elements have an inductance of 2 μH and unloaded Q-factor of 200 at f_c.

(dashed lines), the resonator Q-factors have been artificially reduced to 10 (red), 15 (green) and 20 (blue). For the MI antenna, $\kappa \approx 0.59$, such that $Z_{0M} = 50\ \Omega$. In conventional arrays, the total reader power scales linearly with the number of elements, with the slope determined by the loaded Q-factor value. For MI antennas, the scaling is approximately constant, particularly so for low N. For high N, increases in reader power are required to offset propagation losses (1.17). Clearly, MI antennas are preferable if high antenna capture volume is required. For example, if $Q_{A1} = 10$, MI antennas with more than 3 elements require less power to achieve the same element current, and thus the same field strength. In addition to superior power scaling, the hardware overhead of MI systems is also reduced.

1.4 Summary and thesis overview

In this Chapter, we briefly reviewed the history of radio-frequency identification, discussed the operating principles and limitations of near field communication, and examined capture volume enhancement methods using travelling-wave antennas. We first explained how the development of RFID systems was influenced by contemporary technological advances and applications. NFC was then identified as a recent extension of RFID in the high-frequency regime, and the complex relationships between established HF RFID standards and NFC specifications were examined. The NFC-A technology based on ISO/IEC 14443 Type-A was then identified as the pivotal NFC protocol due to compatibility with prominent smart card systems and its widespread adoption. We then discussed the architecture and operating principles of generic readers and tags, reviewed the NFC-A protocol, and analysed the signal characteristics of forward- and backward-link communication. The need to artificially load reader and tag antennas for bandwidth expansion was explained and its implications for reader power dissipation noted. The range and power scaling of magnetic near fields for various antenna shapes and dimensions were then examined. Fundamental limitations in antenna capture volume due to adverse power scaling and antenna perimeter constraints were discussed.

We then examined capture volume enhancement methods using travelling-wave magneto-inductive antennas. First, we reviewed basic theory on MI waveguides including design equations, dispersion relation, characteristic impedance, and waveguide matching techniques. It was then shown that the longitudinal capture volume can be increased with no hardware overhead by propagating reader signals as travelling current waves along a magneto-inductive antenna. The system architecture was described, and antenna operating principles were reviewed. The external magnetic fields of quasi-axial antennas were then simulated for both uniform and non-uniform waveguides. Finally, the scaling of capture volume with input power was compared between conventional antenna arrays and MI antennas, with the former shown to be linear and the latter approximately constant. These observations suggested a few obvious new directions for the development of MI-based NFC systems. The arrangement of the remainder of the thesis is therefore as follows.

In Chapter 2 we develop novel discrete power-wave definitions for MI waveguides which address the ambiguities arising during power flow modelling using conventional MI waves due to the complex characteristic impedance. We then show how power waves can be used to extract scattering parameters at internal junctions and discontinuities in integrated MI devices.

Although the signal-carrying sidebands in an NFC system can always be extracted by filtering in software, the effect of residual carrier can be damaging to front-end electronics, especially at the high RF powers needed for range extension. The new power-wave theory is therefore used in Chapter 3 to develop a family of MI filter-couplers for receiver protection in high-power MI NFC systems. The filters are experimentally characterised and advanced functionality such as infinite carrier rejection and multiple-passband responses is demonstrated.

NFC systems are conventionally concerned with secure communication between a pair of devices and are deliberately designed to minimise the possibility of eavesdropping. However, additional functionality - for example, the ability to monitor the presence of an item or attendance of a user at a given location - might be possible in less secure systems if the tag position could also be determined. Localisation has been the subject of much attention in UHF RFID but is considerably more difficult in the HF band because of the lack of radiating fields. In Chapter 4 we therefore develop a novel bistatic NFC tag localisation method, which estimates tag position from the time-of-flight (TOF) difference in the UID response extracted from either end of a one-dimensional MI antenna via a pair of matched filter-couplers. A complete experimental system is implemented, including a custom NFC-A compliant reader, a planar transformer-coupled slow wave MI antenna, and a digital framework for TOF estimation using cross-correlation.

System practicality is then vastly improved in Chapter 5, where we develop flexible slow wave loaded transmission line (LTL) antenna topologies with distributed and modular sensor nodes to address the intrinsic limitations of MI waveguides. LTL antennas up to 50 metres in length are constructed, and accurate tag localisation is demonstrated.

In Chapter 6, we minimise the hardware complexity of bistatic positioning by developing a monostatic localisation method based on absolute TOF estimates using a single receiver. A monostatic slow wave system devoid of return signal cables is then constructed, and accurate positioning is again demonstrated. Finally, Chapter 7 draws conclusions and summarises potential directions for future research.

Chapter 2:
Magneto-Inductive Power Waves

In this Chapter, we consider the internal power flow in magneto-inductive systems – a fundamental aspect of MI wave propagation that might be expected to be well understood by now. However, serious anomalies in existing theory were found to arise when designing the new passive filter components needed for a MI-based NFC system. Here, discrete power waves are defined for magneto-inductive systems; metamaterials based on chains of magnetically coupled resonators. These waves are shown to satisfy the discrete power conservation equation for MI waves and are used to calculate the scattering parameters for multi-port MI devices without the anomalous predictions of conventional methods. These results will enable the correct evaluation of internal scattering parameters in MI systems but may also be relevant to other discrete metamaterials with band-limited propagation and complex characteristic impedance.

2.1 Overview

First, we consider power flow modelling in conventional waveguides. Scattering parameters are a standard method of characterisation, design, and analysis of electrical networks and electromagnetic media, particularly at high frequencies [165]–[167]. The method involves the decomposition of currents and voltages into incident and reflected waves at specific ports, allowing the computation of reflection and transmission coefficients. For lossless transmission lines and RF equipment with real characteristic and port impedances, the method is straightforward. Complications arise when the port impedances become complex – for example due to loss, sometimes yielding seemingly anomalous results such as reflection coefficients greater than unity for a passive load [168], [169]. This a well-understood, but not well-known consequence of the existence of multiple scattering wave definitions, which are identical for real port impedances, but possess fundamentally different properties otherwise. Namely, these are based on pseudo-waves and power waves [170]. The incident (a) and reflected (b) pseudo-waves for a port with characteristic impedance Z_0, port voltage difference V, and incoming current I are defined as

$$a = \frac{V + Z_0 I}{2\sqrt{\mathrm{Re}(Z_0)}} \qquad b = \frac{V - Z_0 I}{2\sqrt{\mathrm{Re}(Z_0)}}. \tag{2.1}$$

Conveniently, $V = \sqrt{\mathrm{Re}(Z_0)} \cdot (a + b)$ and $I = [\sqrt{\mathrm{Re}(Z_0)}/Z_0] \cdot (a - b)$. Furthermore, standard transmission line theory suggests that $V = V^+ + V^-$ and $I = (V^+ - V^-)/Z_0$, where V^+ and V^- are the incident and reflected travelling voltage waves at the port interface. Thus, the pseudo-waves can also be expressed as $a = V^+/\sqrt{\mathrm{Re}(Z_0)}$ and $b = V^-/\sqrt{\mathrm{Re}(Z_0)}$, meaning pseudo-waves are impedance-normalised mathematical abstractions of physical travelling waves at the port interface. The apparent simplicity of pseudo-waves conceals a pitfall, which may be illustrated with an example. Suppose that a port with $Z_0 = R_0 + jX_0$ is terminated by a passive load Z_L. Let us also assume that the load is perfectly matched, such that $Z_\mathrm{L} = Z_0^* = R_0 - jX_0$. The reflection coefficient $S_{11} = b/a = V^-/V^+$ is then given by

$$S_{11} = \frac{Z_L - Z_0}{Z_L + Z_0} = \frac{-jX_0}{R_0}. \tag{2.2}$$

Clearly, S_{11} is non-zero for a conjugate-matched load. Furthermore, $|S_{11}| > 1$ when $X_0 > R_0$. Since most RF systems have $\mathrm{Im}(Z_0) \approx 0$, such occurrences are misunderstood and misinterpreted by many. A good example of this is a recent article which identified ambiguous reflection coefficients as a novel discovery [171]. Such results are not anomalous, but a mathematical artifact of the pseudo-wave model, which may be explained by examining the power flow $P = \mathrm{Re}(VI^*)$.

$$P = |a|^2 - |b|^2 + 2\,\mathrm{Im}(ab^*)\frac{\mathrm{Im}(Z_0)}{\mathrm{Re}(Z_0)}. \tag{2.3}$$

It is well-known that while voltages and currents obey the principle of superposition, powers do not. A peculiar exception occurs when $\mathrm{Im}(Z_0) = 0$ and the third term on the right-hand side of (2.3) vanishes. In this special case, the net power flow is conveniently equal to the difference between individual powers of the incident and reflected pseudo-waves. Clearly, this is not true for the general case and pseudo-waves are unsuitable for power flow analysis. To address this issue, power-wave definitions were developed by Kurokawa in 1964 [172] and investigated by others [173]–[175].

$$a_\mathrm{p} = \frac{V + Z_0 I}{2\sqrt{\mathrm{Re}(Z_0)}} \qquad\qquad b_\mathrm{p} = \frac{V - Z_0^* I}{2\sqrt{\mathrm{Re}(Z_0)}}. \tag{2.4}$$

The power waves are no longer directly related to travelling voltage waves but satisfy $P = |a_\mathrm{p}|^2 - |b_\mathrm{p}|^2$, even if Z_0 is complex. They also ensure the scattering parameter magnitude may never exceed unity in a passive system. Interestingly, if Z_0 is real, (2.1) and (2.4) are the same.

These arguments also stand for magneto-inductive transmission lines, which (until now) have been analysed by travelling MI wave models. Similar to (2.1), standard theory yields valid but practically meaningless results, such as larger-than-unity reflection and transmission coefficients. Further difficulties arise from the more complicated characteristic impedance of MI waveguides in comparison to conventional transmission lines. For the former, Z_0 is complex even in the lossless case, as well as frequency dependent. The properties of Z_0 also differ in the passband and stopband frequency regions. As a result, internal MI wave scattering parameters are ambiguous even for lossless waveguides. Equivalent power-wave definitions for the increasingly complex MI systems are clearly required. Unfortunately, (2.4) are not applicable, since MI waveguides are a discrete medium. Neither can the voltage V be unambiguously defined for the constituent resonators, which comprise closed conductive loops.

The aim of this Chapter is to develop a power wave formulation for a periodic system supporting MI waves that can be used to extract the scattering parameters at junctions between media in addition to terminations. Important differences from Kurokawa's work are introduced by the discrete nature of the system and lack of voltages at internal elements. In Section 2.2, we derive the power conservation relation for MI waves. In Section 2.3, we prove that discrete variants of power waves satisfy this relation and show how they may be used to find scattering parameters in MI systems. In Section 2.4, we illustrate the process with simple examples for N-port MI devices where conventional methods break down. Conclusions are drawn in Section 2.5.

2.2 Power conservation in MI systems

We first consider the internal power flow in an infinite MI waveguide formed from magnetically coupled, lossy resonant loops, as shown in Figure 2.1 (a). We begin by multiplying the characteristic circuit equation (1.10) by I_n^*.

$$(R + j\omega L + 1/j\omega C)I_n I_n^* + j\omega M(I_{n-1}I_n^* + I_n^* I_{n+1}) = 0 \tag{2.5}$$

Adding (2.5) to its own complex conjugate, dividing by 4 and re-arranging, we then get:

$$\frac{1}{2}RI_n I_n^* + \left(\frac{j\omega M}{4}\right)(I_n^* I_{n+1} - I_n I_{n+1}^*) = \left(\frac{j\omega M}{4}\right)(I_{n-1}^* I_n - I_{n-1}I_n^*) \tag{2.6}$$

Since the first term in (2.6) is the power P_d dissipated in element n, (2.6) is a power conservation relation, with the second and third terms representing the powers P_{n+1} and P_n flowing into element $n+1$ from element n, and into n from $n-1$, respectively. Figure 2.2 shows the variation of P_d, P_n and P_{n+1} with n for a very lossy MI waveguide with parameters $\kappa = 0.6$ and $Q = 10$, assuming that $L = 100$ nH and $\omega/\omega_0 = 1$. Figure 2.2 (a) shows the results obtained when there is only a forward-going wave present, so that $I_n = I_\mathrm{F}e^{-jnka}$, with $I_\mathrm{F} = 1$ mA.

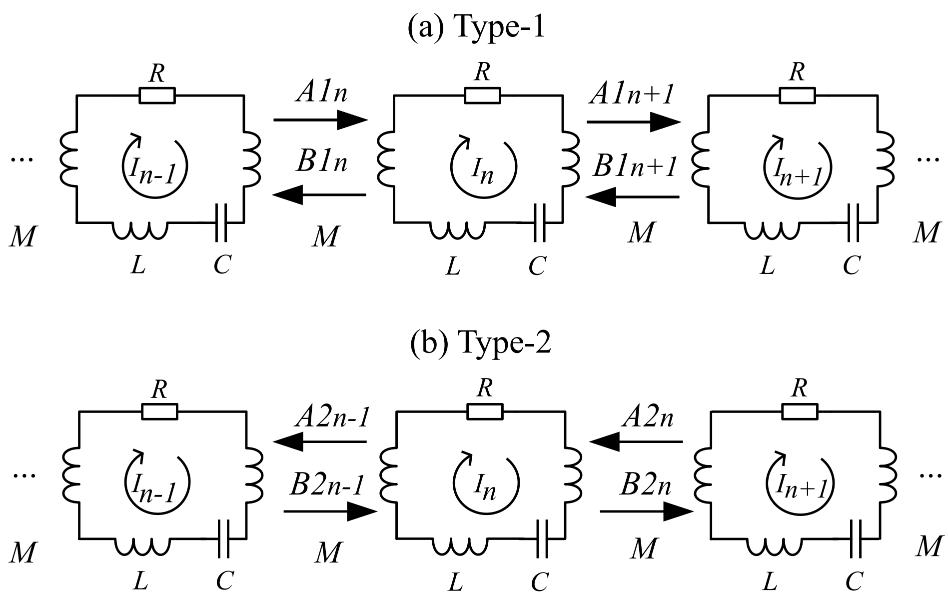

Fig. 2.1. MI waveguide, showing the direction of power flow for Type 1 (a) and Type 2 (b) power waves.

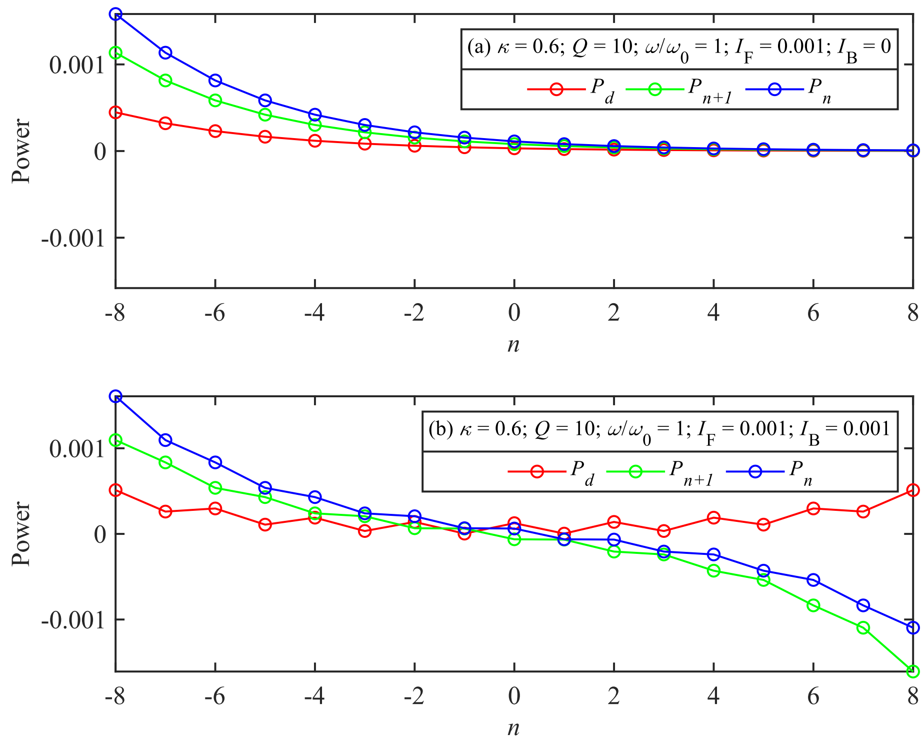

Fig. 2.2. Variation of P_d, P_n and P_{n+1} with n, for an MI waveguide with $\kappa = 0.6$, $Q = 10$, assuming $L = 100$ nH, $\omega/\omega_0 = 1$ and (a) $I_\mathrm{F} = 1$ mA, $I_\mathrm{B} = 0$, (b) $I_\mathrm{F} = I_\mathrm{B} = 1$ mA.

In this case, all three variations decrease exponentially with n as expected. Figure 2.2 (b) shows the results when both forward- and backward-going waves are present, so that $I_n = I_\mathrm{F}\, e^{-jnka} + I_\mathrm{B}\, e^{jnka}$, with $I_\mathrm{F} = I_\mathrm{B} = 1$ mA. In this case, P_d, P_n and P_{n+1} are not (as might initially be expected) sums or differences of exponentials; there is additional oscillation caused by beating. In both cases we have verified that the power conservation relation (2.6) is satisfied.

2.3 Discrete power waves and scattering parameters

We now seek to express power flow for the discrete current waves that exist in MI systems. To do so we introduce a discrete form of power wave. We will need two types. For lines extending to the left we define Type 1 waves with amplitudes $A1_n$ and $B1_n$ at element n as:

$$\begin{aligned} A1_n &= (-j\omega M I_{n-1} + Z_0 I_n)/\left\{2\sqrt{Re(Z_0)}\right\} \\ B1_n &= (-j\omega M I_{n-1} - Z_0^* I_n)/\left\{2\sqrt{Re(Z_0)}\right\} \end{aligned} \tag{2.7}$$

Note that these expressions contain no voltages. However, analogies with Kurokawa's a_p and b_p coefficients follow from the fact that $-j\omega M I_{n-1}$ is the voltage induced in element n by element $n-1$. Multiplying out, we get:

$$\begin{aligned} |A1_n|^2 &= \begin{Bmatrix} \omega^2 M^2 I_{n-1} I_{n-1}^* + j\omega M Z_0 I_{n-1}^* I_n \\ -j\omega M Z_0^* I_{n-1} I_n^* + Z_0 Z_0^* I_n I_n^* \end{Bmatrix} / \{4Re(Z_0)\} \\ |B1_n|^2 &= \begin{Bmatrix} \omega^2 M^2 I_{n-1} I_{n-1}^* - j\omega M Z_0^* I_{n-1}^* I_n \\ +j\omega M Z_0 I_{n-1} I_n^* + Z_0 Z_0^* I_n I_n^* \end{Bmatrix} / \{4Re(Z_0)\} \end{aligned} \tag{2.8}$$

Subtracting these equations from each other and dividing by 2 we then get:

$$\frac{1}{2}\{|A1_n|^2 - |B1_n|^2\} = \left(\frac{j\omega M}{4}\right)(I_{n-1}^* I_n - I_{n-1} I_n^*) \tag{2.9}$$

In a similar way, we can obtain:

$$\frac{1}{2}\{|A1_{n+1}|^2 - |B1_{n+1}|^2\} = \left(\frac{j\omega M}{4}\right)(I_n^* I_{n+1} - I_n I_{n+1}^*) \tag{2.10}$$

Equations (2.9) and (2.10) may then be recognised as P_n and P_{n+1}, respectively. Substituting into (2.6) and re-arranging the Equation so that all terms are positive, the result is:

$$\frac{1}{2}R|I_n|^2 + \frac{1}{2}\{|A1_{n+1}|^2 + |B1_n|^2\} = \frac{1}{2}\{|A1_n|^2 + |B1_{n+1}|^2\} \tag{2.11}$$

Equation (2.11) then allows the direction of the separate power flows carried by each power wave to be identified as shown in Figure 2.1 (a).

Before proceeding, we briefly consider some properties of these waves, namely when k is real and the current consists of the sum of a forward-going wave of amplitude I_{F} and a backward wave of amplitude I_{B}, so that I_n can be written as:

$$I_n = I_{\mathrm{F}}\, e^{-jnka} + I_{\mathrm{B}}\, e^{jnka} \tag{2.12}$$

Direct substitution shows that:

$$\begin{aligned} A1_n &= +\sqrt{Re(Z_0)}\, I_{\mathrm{F}}\, e^{-jnka} \\ B1_n &= -\sqrt{Re(Z_0)}\, I_{\mathrm{B}}\, e^{jnka} \end{aligned} \tag{2.13}$$

Clearly $A1_n$ is only dependent on I_{F} in this case, while $B1_n$ is only dependent on I_{B}. The forward and backward power flows are then:

$$\begin{aligned} \frac{1}{2}|A1_n|^2 &= \frac{1}{2}\mathrm{Re}(Z_0)|I_F|^2 \\ \frac{1}{2}|B1_n|^2 &= \frac{1}{2}\mathrm{Re}(Z_0)|I_B|^2 \end{aligned} \tag{2.14}$$

These results imply that for real k there will be no difference between calculations based on power waves and on the moduli squared of the separate current amplitudes. However, differences are to be expected when k is complex (such as when Q is finite or within the stopband regions).

We now consider the second type of discrete power wave for lines extending to the right, as shown in Figure 2.1 (b). For consistency with Kurokawa's direction of current flow as 'inward', we define Type 2 amplitudes $A2_n$ and $B2_n$ at element n as:

$$\begin{aligned} A2_n &= (j\omega M I_{n+1} - Z_0 I_n)\Big/\Big\{2\sqrt{Re(Z_0)}\Big\} \\ B2_n &= (j\omega M I_{n+1} + Z_0^* I_n)\Big/\Big\{2\sqrt{Re(Z_0)}\Big\} \end{aligned} \tag{2.15}$$

Here $j\omega M I_{n+1}$ is the voltage induced in element n by element $n+1$. Carrying out similar manipulations, it is simple to show that:

$$\frac{1}{2}R|I_n|^2 + \frac{1}{2}\{|A2_{n-1}|^2 + |B2_n|^2\} = \frac{1}{2}\{|A2_n|^2 + |B2_{n-1}|^2\}. \tag{2.16}$$

This power conservation relation is in a similar form to (2.11), but the terms are different. The two types of discrete power wave allow sources at different locations, and both are needed to compute the full set of scattering parameters. For example, Figure 2.3 shows a two-port MI device extending from element m to element n; here the scattering parameters are:

$$\begin{aligned} S_{11} &= B1_m/A1_m \qquad & S_{21} &= B2_n/A1_m \\ S_{12} &= B1_m/A2_n \qquad & S_{22} &= B2_n/A2_n \end{aligned} \tag{2.17}$$

As expected, these expressions are analogous to Kurokawa's scattering parameters. Simple conclusions may be drawn immediately. For example, if k is purely imaginary, which occurs out-of-band in lossless systems, the conjugate impedance is $Z_0^* = -Z_0$. In this case, $B1_m = A1_m$ and $B2_n = A2_n$ so S_{11} and S_{22} are unity for any k.

Before presenting examples, we show how Kurokawa's scattering parameters can be found for terminated MI circuits; we term this the 'Kurokawa' method. Figure 2.4 (a) shows the arrangement of a 2-port device, using his notation for the voltages v_1 and v_2 and the currents i_1 and i_2 at Ports 1 and 2.

In this case, the power wave scattering parameters are:

$$\begin{aligned} S_{11} &= (v_1 - z_{01}^* i_1)/(v_1 + z_{01} i_1) \\ S_{21} &= \sqrt{\{\mathrm{Re}(z_{01})/\mathrm{Re}(z_{02})\}}\,(v_2 - z_{02}^* i_2)/(v_1 + z_{01} i_1). \end{aligned} \tag{2.18}$$

If v_1 is derived from a source at Port 1 with voltage v_{01}, then $v_1 = v_{01} - z_{01} i_1$. Similarly, in the absence of a source at Port 2, $v_2 = -z_{02} i_2$. These results may therefore be written as:

$$\begin{aligned} S_{11} &= 1 - 2\mathrm{Re}(z_1) i_1/v_{01} \\ S_{21} &= -2\sqrt{\{\mathrm{Re}(z_1)\mathrm{Re}(z_2)\}}\, i_2/v_{01} \end{aligned} \tag{2.19}$$

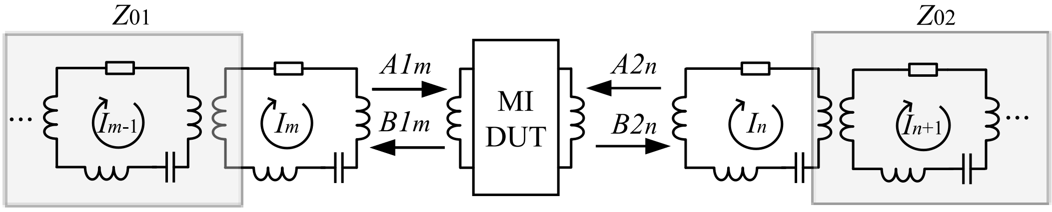

Fig. 2.3. Type 1 and Type 2 power waves used to find the scattering parameters of a two-port MI device.

These expressions allow the power wave scattering parameters at the terminations to be found from a numerical solution of the circuit equations, which can yield i_1 and i_2 for a given v_{01}.

2.4 Examples

We illustrate the use of the discrete power waves with examples chosen to demonstrate anomalous predictions of increasing severity using conventional methods, first involving two-ports with equal and unequal port impedances and then a three-port device.

2.4.1 *Two-port device with equal port impedances*

We begin with the case shown in Figure 2.4 (b), namely an MI waveguide discontinuity caused by a local variation in the mutual inductance from M to $M' = \mu M$ between two elements. We follow the approach used in Section 1.3.3 and [134] of finding reflection and transmission coefficients at the junction. The governing equations are as (1.10) for all elements except at the discontinuity, where:

$$\begin{aligned}(R + j\omega L + 1/j\omega C)I_{-1} + j\omega M(I_{-2} + \mu I_0) = 0 \\ (R + j\omega L + 1/j\omega C)I_0 + j\omega M(\mu I_{-1} + I_1) = 0\end{aligned} \tag{2.20}$$

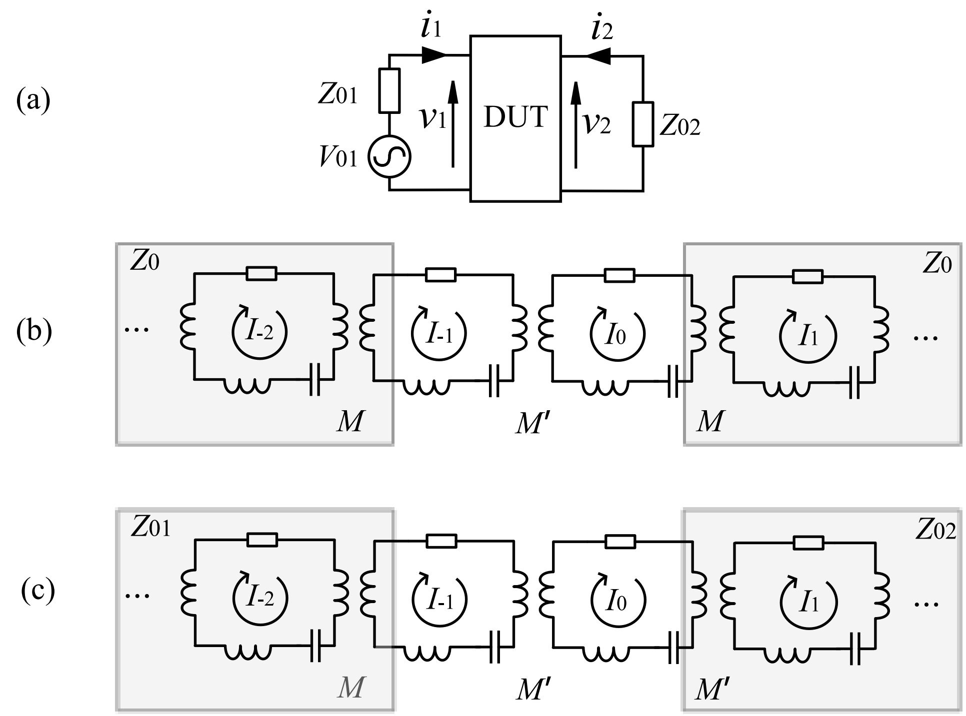

Fig. 2.4. (a) General 2-port device, and example 2-port MI systems with (b) equal and (c) unequal port impedances.

Solutions may be found for incidence from $n = -\infty$ by assuming incident and reflected waves before the discontinuity and a transmitted wave after it, so that:

$$I_n = \begin{cases} I_\mathrm{I}\, e^{-jnka} + I_\mathrm{R} e^{jnka}, & n < 0 \\ I_\mathrm{T}\, e^{-jnka}, & n \geq 0 \end{cases} \tag{2.21}$$

Away from the discontinuity, (2.21) satisfies the characteristic equation (1.10). Substitution of (2.21) into (2.20) yields the reflection and transmission coefficients $\Gamma = I_\mathrm{R}/I_\mathrm{I}$ and $\mathrm{T} = I_\mathrm{T}/I_\mathrm{I}$:

$$\Gamma = \frac{(\mu^2 - 1)e^{jka}}{\{e^{jka} - \mu^2 e^{-jka}\}}$$
$$\mathrm{T} = \frac{\mu\{e^{jka} - e^{-jka}\}}{\{e^{jka} - \mu^2 e^{-jka}\}} \tag{2.22}$$

As expected, $\Gamma = 0$ and $\mathrm{T} = 1$ when $\mu = 1$. For lossless systems and in-band operation, these expressions allow the calculation of $|S_{11}|^2$ and $|S_{21}|^2$ as $|\Gamma|^2$ and $|\mathrm{T}|^2$; we refer to this approach as the 'travelling-wave' method. However, for lossy systems and/or out-of-band operation, the results can be anomalous. We illustrate this by comparison with results obtained by 1) using the Kurokawa method (2.19) with an equivalent circuit model of the system in Figure 2.4 (a), and 2) substituting (2.22) into the expressions (2.7) and (2.15) for discrete MI power waves and then

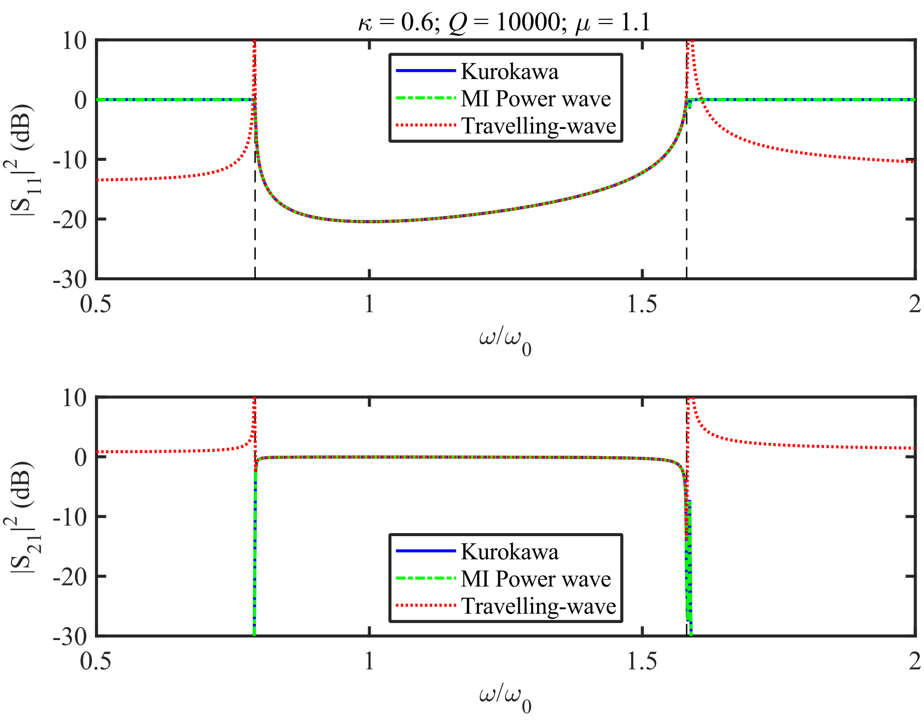

Fig. 2.5. Frequency dependence of $|S_{11}|^2$ and $|S_{21}|^2$, for a weak MI reflector with $\kappa = 0.6, Q = 10{,}000$ and $\mu = 1.1$, as predicted using three different methods. Dashed lines indicate the frequency passband for a lossless waveguide.

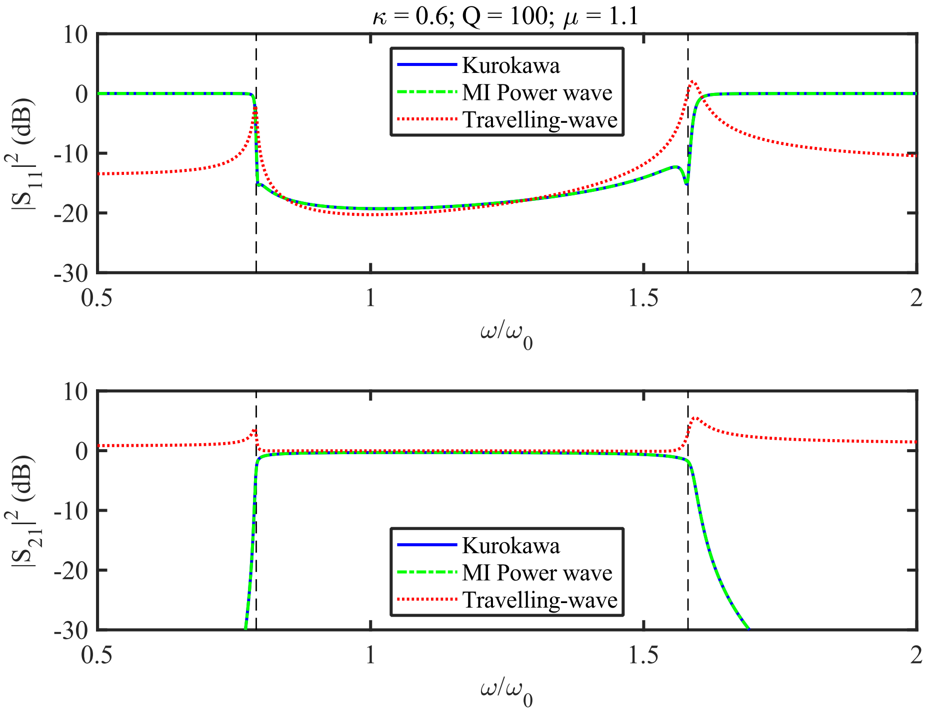

Fig. 2.6. Frequency dependence of $|S_{11}|^2$ and $|S_{21}|^2$, for a weak MI reflector with $\kappa = 0.6$, $Q = 100$ and $\mu = 1.1$, as predicted using three different methods. Dashed lines indicate the frequency passband for a lossless waveguide.

evaluating the scattering parameters using (2.17). In each case, Port 1 is located at $n = -1$, Port 2 is at $n = 0$, and both ports have the same characteristic impedance Z_0.

As a numerical example, we first assume parameters of $\kappa = 0.6$, $Q = 10{,}000$ and $\mu = 1.1$, constituting a weak reflector in a strongly coupled system with unfeasibly low loss. Figure 2.5 shows the variations with frequency of $|S_{11}|^2$ and $|S_{21}|^2$ on a dB scale obtained using the three methods. The results are qualitatively similar in each case. Expectedly, all three methods agree in-band, where there is high transmission. Expectedly, the Kurokawa and MI power wave methods agree out-of-band and show high reflection in this range. However, the travelling-wave method predicts a reflection coefficient greater than unity here.

Figure 2.6 shows similar results for $|S_{11}|^2$ and $|S_{21}|^2$ obtained with more realistic losses ($Q = 100$). The Kurokawa and MI power wave calculations again agree exactly over the whole range. However, the predictions of the travelling wave method are now incorrect in-band as well as out-of-band, due to the non-zero imaginary component of the propagation constant.

2.4.2 *Two-port device with unequal port impedances*

We now consider the case shown in Figure 2.4 (c), namely a discontinuity caused by a global variation in the mutual inductance from M to $M' = \mu M$ between elements -1 and 0 and thereafter,

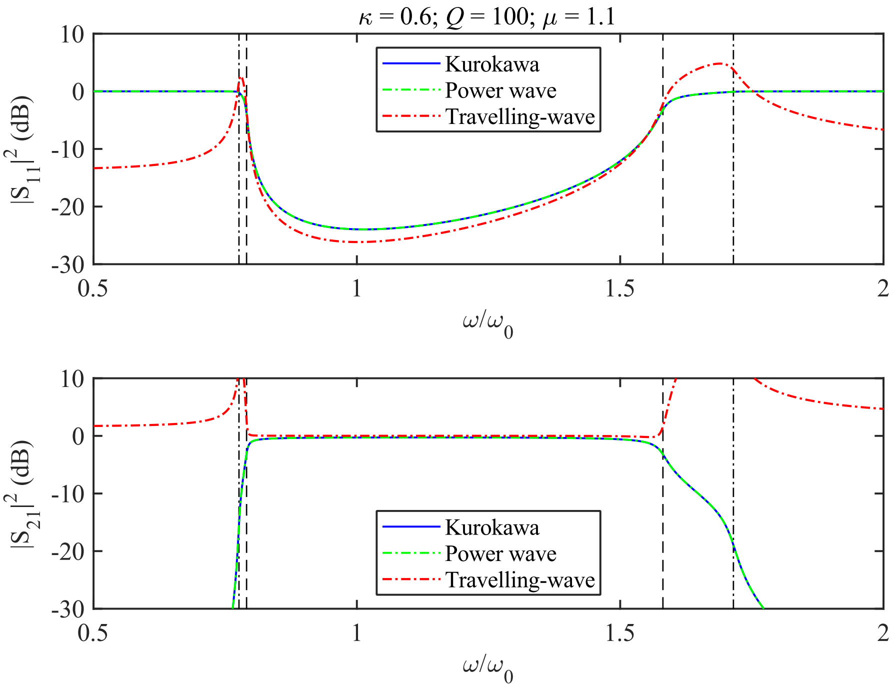

Fig. 2.7. Frequency variation of $|S_{11}|^2$and $|S_{21}|^2$ for a junction between two MI waveguides with $\kappa = 0.6, Q = 100$ and $\mu = 1.1$ as predicted using three different methods. Dashed and dot-dashed black lines show the frequency passbands of the respective waveguides.

so the system consists of two interconnected MI waveguides with different propagation constants k_1 and k_2. There are now two dispersion equations:

$$\begin{aligned} &R + j\omega L + 1/j\omega C + 2j\omega M\cos(k_1 a) = 0 \qquad && n < -1 \\ &R + j\omega L + 1/j\omega C + 2j\omega\mu M\cos(k_2 a) = 0 \qquad && n > 0 \end{aligned} \tag{2.23}$$

These equations lead to characteristic impedances $Z_{01} = j\omega M\, e^{-jk_1 a}$ and $Z_{02} = j\omega\mu M\, e^{-jk_2 a}$ for the two lines. At the junction, the governing equations are:

$$\begin{aligned} &(R + j\omega L + 1/j\omega C)I_{-1} + j\omega M(I_{-2} + \mu I_0) = 0 \\ &(R + j\omega L + 1/j\omega C)I_0 + j\omega\mu M(I_{-1} + I_1) = 0 \end{aligned} \tag{2.24}$$

Assuming a solution in the form of incident, reflected and transmitted waves, namely:

$$I_n = \begin{cases} I_{\mathrm{I}}\, e^{-jnk_1 a} + I_{\mathrm{R}}\, e^{jnk_1 a}, & n < 0 \\ I_{\mathrm{T}}\, e^{-jnk_2 a}, & n \geq 0 \end{cases} \tag{2.25}$$

The reflection and transmission coefficients may be found as:

$$\Gamma = \frac{\mu e^{jk_1 a} - e^{jk_2 a}}{e^{jk_2 a} - \mu e^{jk_1 a}}$$

$$T = \frac{e^{jk_1a} - e^{-jk_1a}}{e^{jk_2a} - \mu e^{jk_1a}}. \tag{2.26}$$

Once again, as expected, $\Gamma = 0$ and $T = 1$ when $\mu = 1$ and $k_1 = k_2$ (uniform waveguide). Scattering parameters for ports located at $n = -1$ and $n = 0$ may again be calculated by all three methods. For example, we may again assume the parameters $\kappa = 0.6$, $Q = 100$, and take $\mu = 1.1$ so that the right-hand line has a larger bandwidth than the left-hand line and $|Z_{02}| > |Z_{01}|$. Figure 2.7 shows the frequency variation of $|S_{11}|^2$ and $|S_{21}|^2$ calculated by all three methods on a dB scale, with the cut-off frequencies of the two lossless bands marked using black dotted and dot-dashed lines. Once again, the Kurokawa and MI power wave methods agree exactly. The travelling-wave method agrees reasonably inside the smaller band, when k_1 and k_2 are both approximately real. However, it predicts ambiguous results when either or both of k_1 and k_2 have significantly large imaginary parts.

2.4.3 *Three-port device with equal port impedances*

We now consider the three-port splitter shown in Figure 2.8 (b) and formed from three MI waveguides with identical characteristics. These support currents I_n, K_n and J_n, as indicated in the Figure. Line 1 extends from $n = -\infty$ to $n = -1$, and lines 2 and 3 from $n = 1$ to $n = +\infty$. The three lines are coupled together at element 0, which has mutual inductance $M_i = \mu_i M$ to line i. Elsewhere, the three lines have parameters R, L, C and M, while the dispersion equation is analogous to (1.10). The equations that must be solved at the junction are:

$$\begin{aligned}
&(R + j\omega L + 1/j\omega C)I_{-1} + j\omega M(I_{-2} + \mu_1 I_0) = 0 \\
&(R + j\omega L + 1/j\omega C)I_0 + j\omega M(\mu_1 I_{-1} + \mu_2 K_1 + \mu_3 J_1) = 0 \\
&(R + j\omega L + 1/j\omega C)K_1 + j\omega M(K_2 + \mu_2 I_0) = 0 \\
&(R + j\omega L + 1/j\omega C)J_1 + j\omega M(J_2 + \mu_3 I_0) = 0
\end{aligned} \tag{2.27}$$

Here, I_0 is the current at the connecting loop, a separate unknown. For incidence from line 1, solutions are assumed as:

$$\begin{aligned}
&I_n = I_\mathrm{I}\, e^{-jnka} + I_\mathrm{R}\, e^{jnka} && n < 0 \\
&K_n = K_\mathrm{T2}\, e^{-jnka} && n > 0 \\
&J_n = J_\mathrm{T3}\, e^{-jnka} && n > 0
\end{aligned} \tag{2.28}$$

Substituting and making use of the dispersion equation, solutions can be obtained as in [134].

$$\Gamma = \frac{I_R}{I_I} = \frac{(1-\mu_1^2)e^{jka} - (\mu_2^2+\mu_3^2-1)e^{-jka}}{(\mu_1^2+\mu_2^2+\mu_3^2-1)e^{-jka} - e^{jka}}$$

$$T_2 = \frac{K_{\mathrm{T2}}}{I_I} = \frac{\mu_1\mu_2\{e^{-jka} - e^{jka}\}}{(\mu_1^2+\mu_2^2+\mu_3^2-1)e^{-jka} - e^{jka}} \tag{2.29}$$

$$T_3 = \frac{J_{\mathrm{T2}}}{I_I} = \frac{\mu_1\mu_3\{e^{-jka} - e^{jka}\}}{(\mu_1^2+\mu_2^2+\mu_3^2-1)e^{-jka} - e^{jka}}$$

Here, we focus on the case when $\mu_1 = 1$ and $\mu_2^2 + \mu_3^2 = 1$ such that (2.29) reduces to $\Gamma = 0$, $T_2 = \mu_2$ and $T_3 = \mu_3$, implying that the splitter is matched and has a constant splitting ratio. Using the Kurokawa method, equations are solved for the four loops, assuming a voltage source with output impedance Z_0 at Port 1 and terminations Z_0 at Ports 2 and 3 as shown in Figure 2.8 (a). Using discrete power waves, A and B coefficients are found for each line in turn. Figure 2.9 shows the frequency response on a dB scale of $|S_{11}|^2$ and $|S_{21}|^2$ thus obtained, with parameter values $\kappa = 0.6, Q = 100, \mu_1 = 1$ and $\mu_2 = \mu_3 = 1/\sqrt{2}$ so the device operates as a 3dB splitter. As usual, the black dashed lines show the lossless band edges. The predictions of the travelling wave method

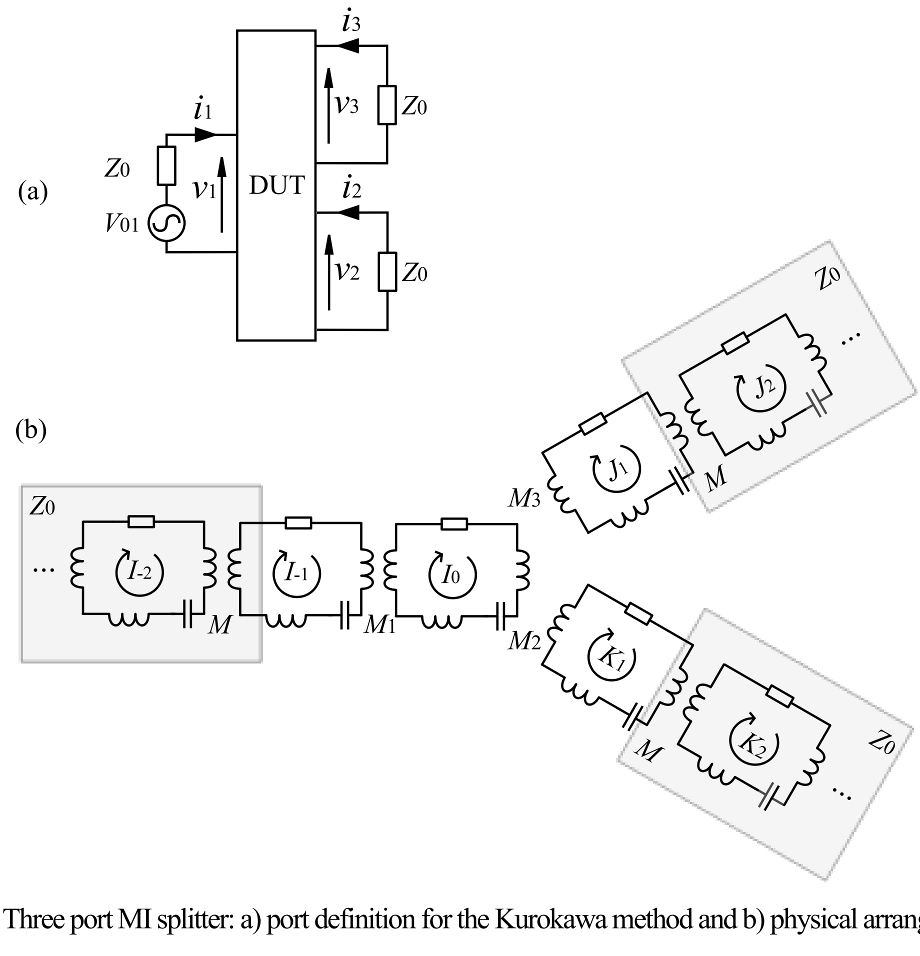

Fig. 2.8. Three port MI splitter: a) port definition for the Kurokawa method and b) physical arrangement.

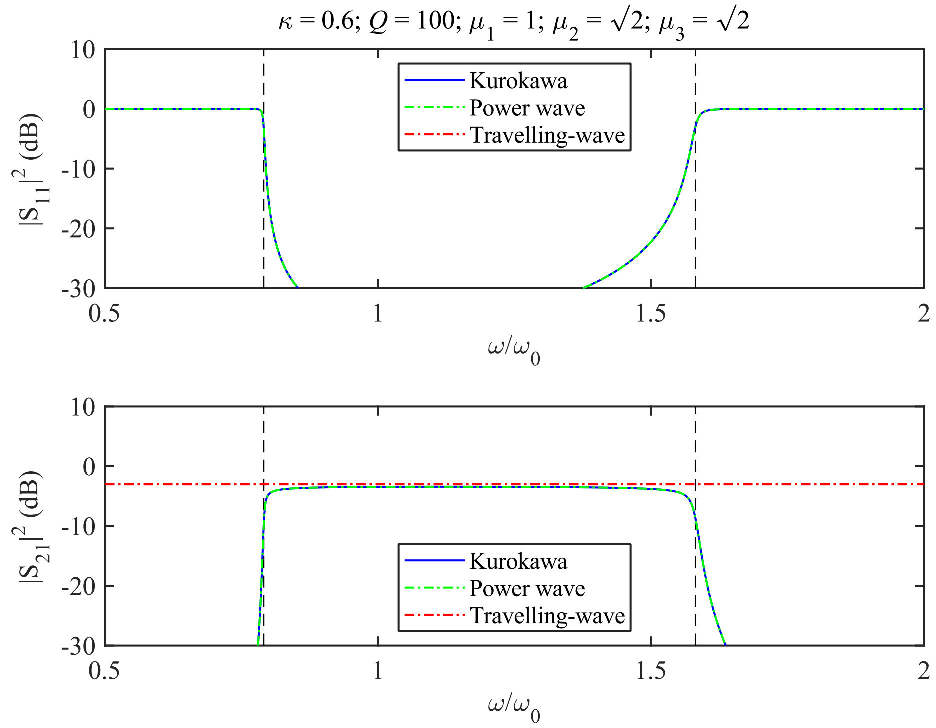

Fig. 2.9. Frequency dependence of $|S_{11}|^2$ and $|S_{21}|^2$, for a 3-dB MI splitter with parameters $\kappa = 0.6, Q = 100, \mu_1 = 1$ and $\mu_2 = \mu_3 = 1/\sqrt{2}$, as predicted using three different methods. Black dashed lines show the lossless band edges.

are entirely incorrect for $|S_{11}|^2$, since the reflection coefficient is $\Gamma = 0$. Although the predictions for $|S_{21}|^2$ (and $|S_{31}|^2$, since this is identical) are qualitatively correct in-band, only the Kurokawa and MI power wave methods show the expected band-limited performance.

These results highlight the need for meaningful and unambiguous estimates of power flow in MI waveguide systems, particularly in the presence of loss or out-of-band operation. For terminated ports, Kurokawa's wave formulations may be used to numerically calculate power flows using (2.19). However, the proposed discrete power wave method also allows scattering parameters to be found when there is no immediately adjacent port, for example at junctions between semi-infinite media. Furthermore, the new method allows meaningful analytic solutions for power flow to be extracted from the ambiguous travelling-wave solutions of boundary matching problems. This can be done by direct substitution of analytic travelling wave reflection and transmission coefficients into the MI power wave expressions; a technique which will be employed in practice for the design of high-power NFC filter-couplers in the next Chapter.

2.5 Conclusions

A discrete formulation of power waves has been developed for magneto-inductive waveguides. These waves are analogous to the continuous power waves introduced by Kurokawa for transmission-line systems, satisfy the power conservation relation and avoid the physical anomalies seen in scattering parameters found using travelling-wave formulations for passive MI systems. They are applicable to a system supporting pure current waves and allow determination of intermediate scattering parameters, for example at junctions between semi-infinite media. This is demonstrated in the next Chapter, where we employ power wave theory for the development of novel passive MI devices needed for NFC systems.

The importance of the power wave approach has been demonstrated using examples involving multi-port MI devices, that show how analytic solutions can be correctly converted to scattering parameters. Consequently, this approach should assist in designing systems that involve connected MI devices (for example, containing splitting or filtering components as well as simple propagation pathways). Since an analogous power conservation relation may be constructed for MI waves in 2D, assuming mutual inductances M_x and M_y in the two perpendicular directions, it may be useful for calculating power flow in devices based on metasurfaces. Furthermore, it is likely to be relevant to other periodic metamaterials, such as electro-inductive waveguides, for which discrete power waves may also be constructed.

Chapter 3:
Magneto-Inductive Filter-Couplers

In this Chapter, we develop a new class of high-performance frequency-selective filter-couplers based on magneto-inductive waveguides. The filter-couplers are directional filters, which have been optimised for carrier suppression and receiver isolation in high-power near field communication applications. Design equations are developed and solved using wave analysis and dispersion theory, and it is shown that filter-couplers can be designed for use both in MI systems with complex, frequency-dependent impedance as well as in conventional systems with real impedance. Wave analysis is used to reduce the complexity of circuit equations. High performance MI structures combining directional and infinite rejection filtering are demonstrated, as well as multiple-passband high-rejection filtering. A new method for improving filtering performance through multipath loss compensation is described. Methods for constructing tuneable devices using custom ferrite-cored transformers are proposed and demonstrated, and experimental results are shown to agree with theoretical models. Limitations are explored and high-power handling capability for NFC is demonstrated, despite the use of ferrite materials.

3.1 Overview

Directional filters are four-port couplers with frequency filtering capability [176]–[179]. They can remove band-limited noise and unwanted signals at specific frequencies, or be arranged in cascade for frequency-division multiplexing [180]–[182]. Lumped element, transmission-line, and waveguide formats have been developed for frequencies ranging from very-high frequency (VHF) to millimetre-wave [183]–[190]. Two-port filters with high attenuation have also been developed and use multipath cancellation, reflection, or absorption to achieve infinite rejection [191]–[197]. Applications include transmit/receive modules, multiplexers in ultra-wide-band antennas and superheterodyne receivers [198]–[202]. Apart from rare cases [203], development has involved systems with real impedance. Directional filter operation is best explained by example. Figure 3.1 shows an equivalent circuit of the lumped-element version of Cohn's transmission line directional filter [176].

The circuit has four ports and comprises two coupled ladder sections, namely a right-handed LC pi-section (blue) and a left-handed LC t-section (red). Component parameters are chosen such that the sections have complementary phase shifts of $\pm\pi/2$ at angular frequency $\omega_0 = 1/\sqrt{LC}$,

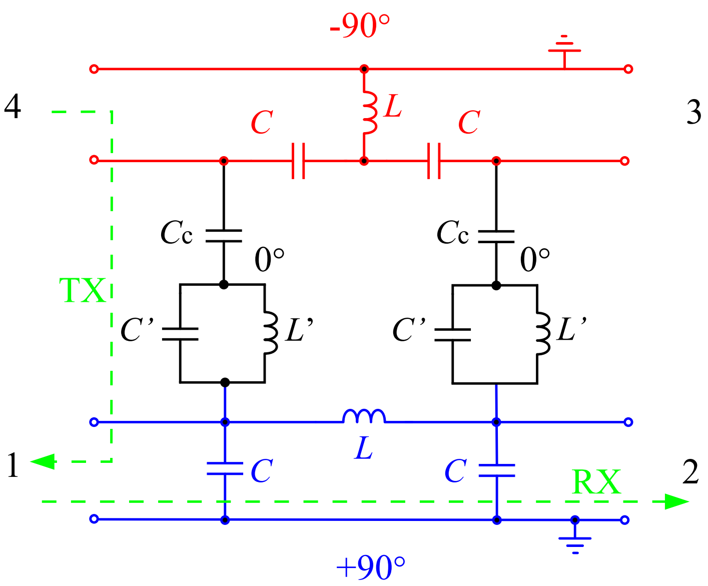

Figure 3.1. Equivalent circuit of a lumped-element directional filter.

while matching to a port impedance Z_0 requires $L = Z_0/\omega_0$, meaning $C = 1/(\omega_0^2 L)$. The sections are joined by a pair of identical coupling networks, comprising an in-series connection between a capacitor C_c and a parallel resonator with inductance L' and capacitance C'. The coupling network impedance Z_c at frequency ω is given by

$$Z_c = \frac{1 - \omega^2 L'(C_c + C')}{j\omega C_c(1 - \omega^2 L'C')}. \tag{3.1}$$

Component parameters are chosen such that $Z_c = 0$ at ω_0, which requires $C' = 1/(4\omega_0^2 L')$ and $C_c = 3C'$, resulting in a direct connection between the complementary ladders at $\omega = \omega_0$ with zero phase shift. Let us assume that all ports are matched, the filter components are lossless, and Port 1 is the input. In this case, Ports 2 and 3 become fully isolated at ω_0 due to phase cancellation, with the input signal emerging from Port 4. Away from the resonant frequency, Z_c acts to block signal propagation and the input emerges from Port 2. If the inductors are lossy, some leakage into isolated ports is expected due to slight differences in amplitude between out-of-phase signals during cancellation. Since the device is symmetric, the input port position may be reconfigured with equivalent results. The filter may thus be used as a frequency-selective circulator.

Figure 3.2 shows the simulated scattering parameters for the filter-coupler from Figure 3.1 with ω_0 tuned to the NFC-A carrier frequency such that $L = 0.587$ µH, $C = 235$ pF, $L' = 3$ µH, $C' = 11.5$ pF and $C_c = 34.4$ pF. The inductances are assumed to be lossy, with the Q-factors of L and L' such that $Q_L = Q_{L'} = 150$. All parameters apart from S41 are lowest at f_c, with the minimal

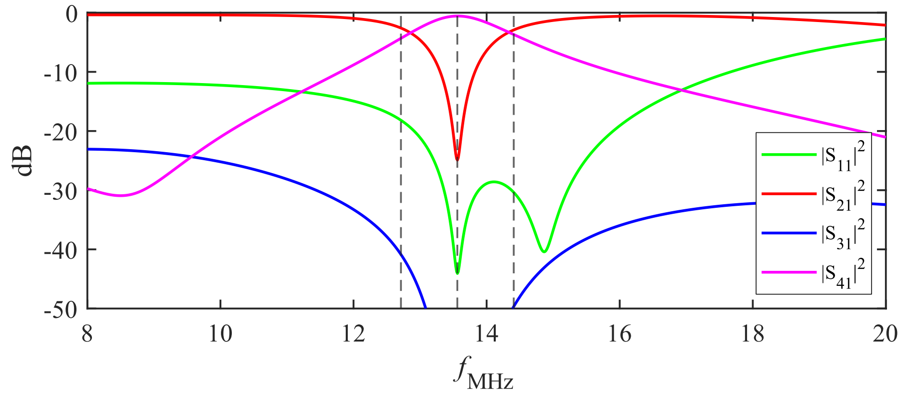

Figure 3.2. Scattering parameters of lumped-element directional filter tuned to $\omega_0 = \omega_c$ with $L = 0.587$ μH, $C = 235$ pF, $L' = 3$ μH, $C' = 11.5$ pF, $C_c = 34.4$ pF, and $Q_L = Q_{L'} = 150$. Dashed lines show NFC-A carrier and sideband frequencies.

value determined by inductor losses. The S21 and S41 parameters have complementary band-pass and band-stop responses, with response bandwidth determined by inductance L'. Such characteristics may be employed for carrier suppression and sideband extraction in high-power NFC. For example, the filter-coupler may be placed at the feed end of a travelling-wave antenna (Figure 1.17), with the transmitter TX connected to Port 4, the antenna input connected to Port 1, the receiver RX connected Port 2, while Port 3 is terminated in a matched load. Alternatively, the transmitter may feed one antenna end directly, with the opposite end connected to Port 1 of the filter coupler, the receiver connected to Port 2, and the remaining ports terminated in matched loads. Tag responses are thus acquired by reflection in the former configuration and by transmission in the latter.

We now show that a pair of coupled right- and left-handed MI waveguides can form a directional filter and investigate its potential for signal blocking in MI-based NFC. The filters are designed to effectively operate at high RF power, since operation is based on complementary outputs rather than absorption, and to ensure effective blocking, frequency selectivity is tunable. Furthermore, a new method for implementing four-port directional filters with tunable infinite-rejection responses is presented. Wave theory is developed to explain the principle of multipath loss compensation and high attenuation is confirmed by experiment. Designs are extended to allow multiple stopbands with improved rejection. Three-port directional filters are also shown to be feasible and can be made using a section of MI waveguide with the addition of as few as three resonators. In each case wave theory is used to reduce the complexity of the circuit equations. Simple multiplexers can be implemented by cascading directional filters. Together, these features can introduce additional functionality and complexity in magneto-inductive systems, since the filter components can be integrated directly with MI waveguides. Additionally, such devices can be successfully used in conventional systems.

3.2 Magneto-inductive directional filters

We now develop the analysis of MI directional filters, consider their frequency response, bandwidth, and tuneability. Figure 3.3 shows the equivalent circuit of a filter based on a pair of infinite horizontal MI waveguides consisting of identical resonators with inductance L, capacitance C, resonant frequency ω_0, and width a, but with opposite coupling polarity so that the lower guide is right-handed (blue) and the upper guide left-handed (red). The mutual inductances are equal in magnitude, with $M > 0$, so the coupling coefficients are $\kappa_\mathrm{f} = 2M/L$ and $\kappa_\mathrm{b} = -2M/L$. The waveguides are weakly coupled using a pair of resonators, which connect the waveguides via mutual inductances M_c and coupling coefficients $\kappa_\mathrm{c} = 2M_c/L$, such that $\kappa_\mathrm{f} > \kappa_\mathrm{c}$. The network has four ports 1 – 4 formed by sections of MI waveguide. The lower line supports currents I_n and the top line supports currents J_n, while the two coupling resonators have currents K and P. Note that the waveguide terminations can also be represented by lumped impedances as shown in Figure 1.15. There are three main possibilities: (i) an infinite MI waveguide represented by its characteristic impedance Z_0, (ii) a resistive termination represented by the mid-band impedance $Z_{0\mathrm{M}}$, and (iii) a broad-band termination to $Z_{0\mathrm{M}}$, achieved by halving the inductance and doubling the capacitance in the resonator.

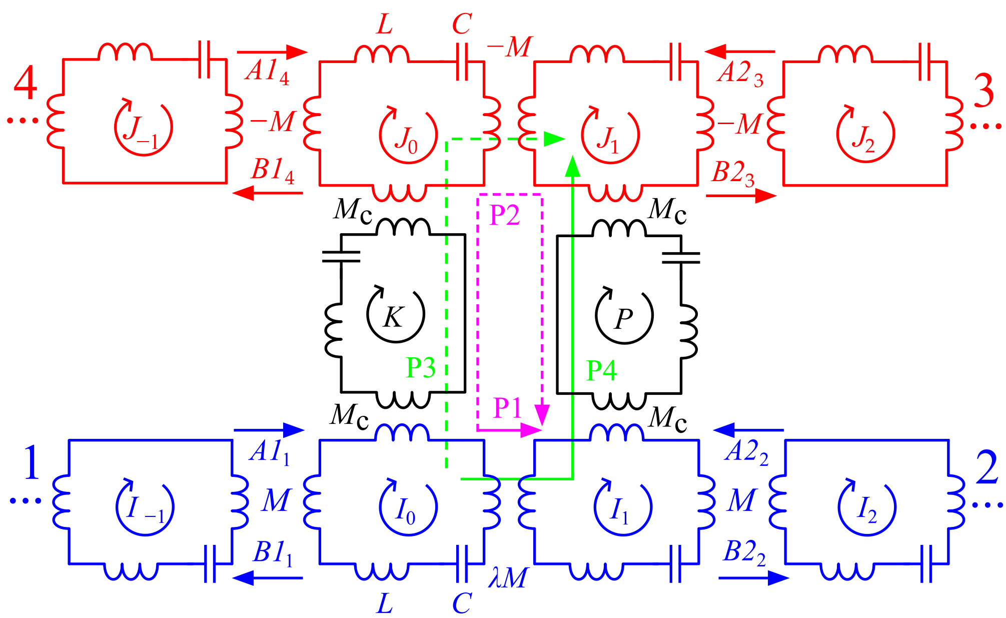

Figure 3.3. Equivalent circuit of a magneto-inductive directional filter comprising identical resonators.

For now, we assume Type (i) terminations and suppose that an MI wave is incident at Port 1 from the left. Experience suggests that this wave will be partially reflected at $n = 0$ due to the discontinuity caused by the coupling resonator, and that the remaining power, less any loss, will emerge as MI waves from Ports 2-4. We write expressions for the currents I_n and J_n in terms of the incident, reflected and transmitted MI waves.

$$I_n = \begin{cases} I_{\mathrm{I}} e^{-jk_{\mathrm{f}}na} + I_{\mathrm{R}} e^{jk_{\mathrm{f}}na}, & n \leq 0 \\ T_2\, e^{-jnk_{\mathrm{f}}a}, & n \geq 1 \end{cases}$$
$$J_n = \begin{cases} T_3 e^{-j\kappa_{\mathrm{b}}na}, & n \geq 1 \\ T_4 e^{j\kappa_{\mathrm{b}}na}, & n \leq 0 \end{cases} \tag{3.2}$$

Here I_{I} and I_{R} are the amplitudes of the incident and reflected waves at Port 1. T_2, T_3, T_4 are the wave amplitudes from Ports 2, 3, and 4. For the forward-wave guide, the propagation constant is $k_{\mathrm{f}} = k_{\mathrm{f}}' - jk_{\mathrm{f}}''$, while $k_{\mathrm{b}} = k_{\mathrm{b}}' - jk_{\mathrm{b}}''$ is the propagation constant of the backward one. From Figure 1.14 and the dispersion relation (1.10) we can deduce a relationship between κ_{f} and κ_{b}.

$$k_{\mathrm{b}}a = k_{\mathrm{f}}a - \pi \tag{3.3}$$

We may now combine the characteristic equations for the MI waveguides with the circuit equations for the coupling elements with currents K and P. For convenience, we define the element self-impedance $Z = j\omega L + \frac{1}{j\omega C} + R$ and the mutual impedances $Z_{\mathrm{m}} = j\omega M$ and $Z_{\mathrm{mc}} = j\omega M_{\mathrm{c}}$. A set of six coupled equations is obtained.

$$\begin{aligned} ZI_0 + Z_{\mathrm{m}}(I_{-1} + I_1) + Z_{\mathrm{mc}}K &= 0 \\ ZI_1 + Z_{\mathrm{m}}(I_0 + I_2) + Z_{\mathrm{mc}}P &= 0 \\ ZK + Z_{\mathrm{mc}}(I_0 + J_0) &= 0 \\ ZP + Z_{\mathrm{mc}}(I_1 + J_1) &= 0 \\ ZJ_0 - Z_{\mathrm{m}}(J_{-1} + J_1) + Z_{\mathrm{mc}}K &= 0 \\ ZJ_1 - Z_{\mathrm{m}}(J_0 + J_2) + Z_{\mathrm{mc}}P &= 0 \end{aligned} \tag{3.4}$$

Substituting the assumed solutions (3.2) into (3.4), using the dispersion equation (1.10) and the propagation constant relation (3.3), the currents K and P may be eliminated, and the system solved for the travelling-wave reflection and transmission coefficients.

$$
\begin{aligned}
\frac{I_{\mathrm{R}}}{I_{\mathrm{I}}} &= \frac{-\left(e^{j2k_{\mathrm{f}}a}+1\right)\mu^2}{1+2\mu^2 e^{j2k_{\mathrm{f}}a}-e^{j4k_{\mathrm{f}}a}} \\
\frac{T_2}{I_{\mathrm{I}}} &= \frac{1-e^{j4k_{\mathrm{f}}a}}{1+2\mu^2 e^{j2k_{f}a}-e^{j4k_{\mathrm{f}}a}} \\
\frac{T_3}{I_{\mathrm{I}}} &= 0 \\
\frac{T_4}{I_{\mathrm{I}}} &= \frac{\left(1-e^{j2k_{\mathrm{f}}a}\right)\mu^2}{1+2\mu^2 e^{j2k_{\mathrm{f}}a}-e^{j4k_{\mathrm{f}}a}}
\end{aligned}
\tag{3.5}
$$

Here, $\mu = M_{\mathrm{c}}/M$ is the mutual inductance ratio. Note that the coefficients (3.5) are complex-valued and frequency-dependent. They are expressed only in terms of μ and the propagation constant k_{f}, which may be computed from (1.10). However, care must be taken to choose the appropriate solution such that $k_{\mathrm{f}}'' \geq 0$ and $0 \leq k_{\mathrm{f}}' \leq \pi$. The results imply that no signal leaves Port 2 at resonance, provided the guides are lossless. Similarly, the transmission from Port 4 is maximum at resonance while the reflectance at Port 1 is zero. Port 3 is isolated at all frequencies, both within and outside of the MI passbands. This behaviour is inherent in the way signals are combined. The phase shift at resonance along path P1 in Figure 3.2 (a) is $\pi/2$, while the phase shift along path P2 is $3\pi/2$. If the device is lossless, the signal from Port 2 is zeroed by cancellation. If the element Q-factors are finite, the losses along P1 and P2 are different, such that only partial signal cancellation occurs. The two signal paths P3 and P4 to Port 3 are in antiphase for all frequencies.

Although the results above provide valid amplitude reflection and transmission coefficients, they offer no insight on power flow in devices that are either lossy or operating out-of-band. We therefore define three sets of discrete power wave pairs $\{A1_1, B1_1\}$, $\{A2_2, B2_2\}$, $\{A1_4, B1_4\}$ for Ports 1, 2, and 4, respectively, at positions as shown in Figure 3.3.

$$
\begin{aligned}
A1_1 &= \frac{-Z_{\mathrm{m}}I_{-1}+Z_{0\mathrm{f}}I_0}{2\sqrt{\mathrm{Re}(Z_{0f})}} & B1_1 &= \frac{-Z_{\mathrm{m}}I_{-1}-Z_{0\mathrm{f}}^*I_0}{2\sqrt{\mathrm{Re}(Z_{0\mathrm{f}})}} \\
A2_2 &= \frac{Z_{\mathrm{m}}I_2-Z_{0\mathrm{f}}I_1}{2\sqrt{\mathrm{Re}(Z_{0\mathrm{f}})}} & B2_2 &= \frac{Z_{\mathrm{m}}I_2+Z_{0\mathrm{f}}^*I_1}{2\sqrt{\mathrm{Re}(Z_{0\mathrm{f}})}} \\
A1_4 &= \frac{Z_{\mathrm{m}}I_{-1}+Z_{0\mathrm{b}}I_0}{2\sqrt{\mathrm{Re}(Z_{0\mathrm{b}})}} & B1_4 &= \frac{Z_{\mathrm{m}}I_{-1}-Z_{0\mathrm{b}}^*I_0}{2\sqrt{\mathrm{Re}(Z_{0\mathrm{b}})}}
\end{aligned}
\tag{3.6}
$$

Here, $Z_{0\mathrm{f}} = j\omega M e^{-jk_{\mathrm{f}}a}$ and $Z_{0\mathrm{b}} = -j\omega M e^{-jk_{\mathrm{b}}a}$ are the characteristic impedances of the forward and backward waveguides. In fact, $Z_{0\mathrm{f}} = Z_{0\mathrm{b}}$ whenever (3.3) applies. Power wave scattering parameters with respect to Port 1 may then be found.

$$S_{11} = \frac{B1_1}{A1_1}$$
$$S_{21} = \frac{B2_2}{A1_1} \tag{3.7}$$
$$S_{41} = \frac{B1_4}{A1_1}$$

We may obtain analytic expressions for the scattering parameters of a directional filter with MI line terminations by substituting the travelling wave coefficients (3.5) into the MI power-wave definitions (3.6) and applying the ratios (3.7).

$$S_{11} = \left(1 - e^{2k_\mathrm{f}''a}\right)\left\{e^{j2k_\mathrm{f}'a} + e^{2(k_\mathrm{f}''+j2k_\mathrm{f}')a}\right\} + \mu^2\left(1 + 2e^{2(k_\mathrm{f}''+jk_\mathrm{f}')a} - e^{j2k_\mathrm{f}'a}\right)/d$$
$$S_{21} = e^{(k_\mathrm{f}''+jk_\mathrm{f}')a} - e^{(k_\mathrm{f}''+j3k_\mathrm{f}')a} + e^{-(k_\mathrm{f}''+jk_\mathrm{f}')a} - e^{(-k_\mathrm{f}''+jk_\mathrm{f}')a}/d$$
$$S_{41} = \mu^2(e^{j2k_\mathrm{f}'a} - 1)/d \tag{3.8}$$
$$d = 1 + 2\mu^2 e^{2(k_\mathrm{f}''+jk_\mathrm{f}')a} - e^{4(k_\mathrm{f}''+jk_\mathrm{f}')a}$$

Moduli squared of the power-wave coefficients (3.8) are equal to the moduli squared of the travelling-wave coefficients (3.5) whenever $k_\mathrm{f}'' = k_\mathrm{b}'' = 0$, as expected from the arguments expressed in Chapter 2.

3.2.1 *Frequency response*

To illustrate the above, Figure 3.4 shows the frequency dependence of power-wave scattering parameters for different terminations, with $L = 1$ μH, κ_f =0.6, and κ_c=0.3 (so that $\mu = 1/2$). Results for lossless and lossy elements with magneto-inductive terminations Figures 3.4 (a)-(b) are obtained using equations (3.8), and results for lossy elements with narrowband [Figure 3.4 (c)] and broadband [Figures 3.4 (d)] resistive terminations were obtained by the numerical solution of circuit equations, which were substituted into expressions of the type (2.19).

In each case, frequencies near ω_0 are diverted into Port 4, while the remaining power is sent to Port 2. Port 4 therefore has a band-pass response while Port 2 has a band-stop one. The MI passband is as estimated from previous arguments. The isolation of Port 3 is unaffected by loss, but the power emerging from Port 4 is reduced and Port 2 rejection diminished. Since losses are inversely proportional to κQ and $\kappa_\mathrm{c}Q$, both high coupling coefficients and Q-factors are required to minimise loss. The effect of narrowband resistive terminations is to reduce the effective

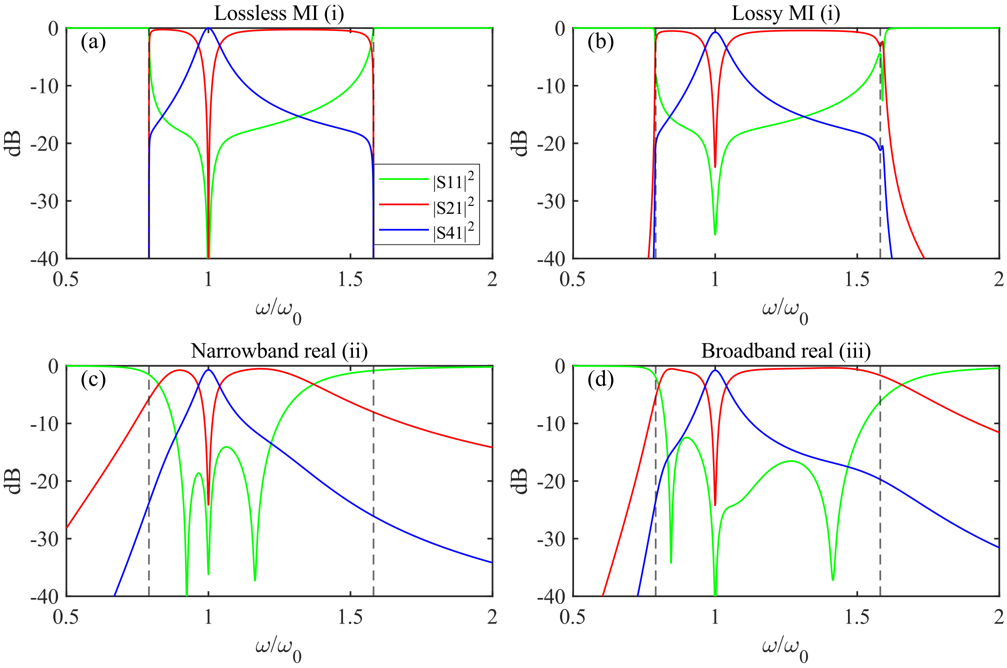

Figure 3.4. Theoretical power-wave scattering parameters of an MI filter-coupler with $\kappa_{\mathrm{f}} = 0.6$ and $\kappa_{\mathrm{c}} = 0.3$. (a) Lossless infinite MI waveguide terminations; (b) lossy infinite waveguide terminations with $Q = 200$; (c) lossy narrowband terminations with $Z_{0\mathrm{M}} = 50\ \Omega$; (d) lossy broadband terminations with $Z_{0\mathrm{M}} = 50\ \Omega$. Dashed lines indicate the passband of a lossless waveguide with $\kappa = 0.6$.

bandwidth. However, this can be partly restored by using a broad-band termination. Unsurprisingly, the best performance is exhibited by magneto-inductive terminations.

3.2.2 *Filter bandwidth*

An analytic expression for the 3-dB bandwidth of the bandpass channel $|S_{41}|^2$ may be obtained in the lossless case for MI waveguide terminations. The bandwidth may be found by computing the half-power frequencies of $|S_{41}|^2$ within the filter passband with k'' set to zero using (3.9).

$$|S_{41}|^2_{k''=0} = \frac{\mu^4 e^{j2k'_f a}\left(e^{j2k'_f a} - 1\right)^2}{1 - e^{j4k'_f a}(4\mu^4 + 2 - e^{j4k'_f a})} = \frac{1}{2} \tag{3.9}$$

Equation (3.9) has two solutions for k'_{f} within the waveguide passband, and thus two solutions for ω. These may be expressed in terms of κ_{f}, μ, and ω_0, and used to compute the angular bandwidth B.

$$\begin{gathered} B = \omega_0 \left(\sqrt{\frac{1}{1-\kappa_f p}} - \sqrt{\frac{1}{1+\kappa_f p}} \right) \\ p = \frac{1}{2}\sqrt{\mu^4 - \sqrt{\mu^8 + 4} + 2} \end{gathered} \tag{3.10}$$

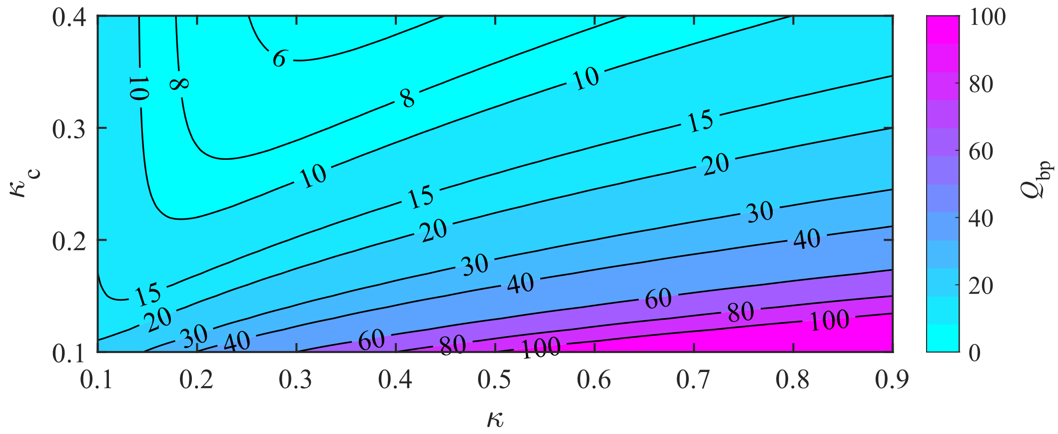

Figure 3.5. Variation of Q_{bp} with κ and κ_{c} for a lossless filter with MI terminations with $\kappa_{\mathrm{f}} = 0.6$ and $\kappa_{\mathrm{c}} = 0.3$.

The bandpass quality factor is related to the bandwidth by $Q_{\mathrm{bp}} = \omega_0/B$ and is easily computed. Figure 3.5 shows a contour map of the variation of Q_{bp} with κ and κ_c. High filter Q-factors require high values of κ and low values of κ_{c}. However, the achievable Q-factor is limited, since propagation losses may become unacceptable if κ_{c} were too low according to (1.17).

3.2.3 *Frequency tuning*

So far, the filter centre frequency has been determined by ω_0, which is the resonant frequency of the MI waveguide resonators. It would clearly be beneficial to introduce centre frequency tuning capability within the MI passband. Figure 3.6 shows the effect of tuning the resonant frequency of the coupling resonators ω_0' to different values, namely 1) $\omega_0' = 0.9\omega_0$, 2) $\omega_0' = \omega_0$ and 3) $\omega_0' = 1.1\omega_0$, assuming lossless resonators and lossless MI terminations. Although the best performance is obtained when $\omega_0' = \omega_0$, tuning around ω_0 is practically feasible for the variations in ω_0' shown. The resonant frequency ω_0' may be adjusted using variable capacitors in practice.

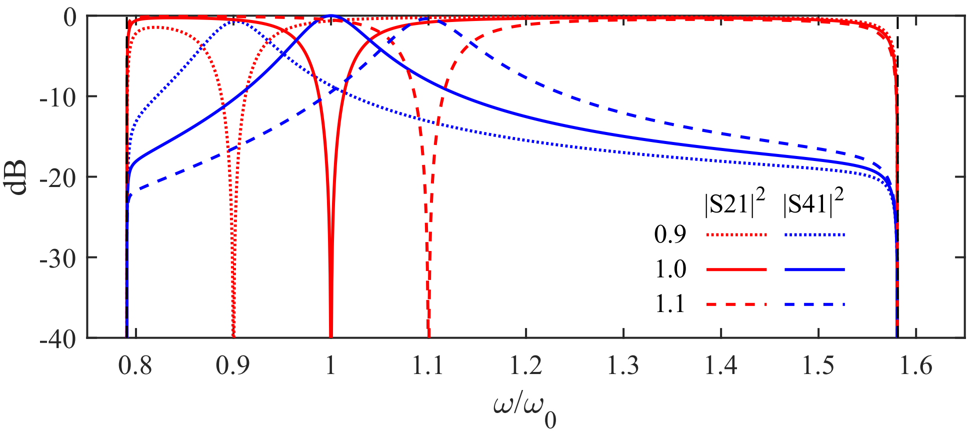

Figure 3.6. Centre frequency tuning of MI directional filter with $\kappa_{\mathrm{f}} = 0.6$ and $\kappa_{\mathrm{c}} = 0.3$. Black dotted lines indicate the filter frequency passband. The tuning frequencies are $\omega_0' = \omega_0\,\{0.9, 1.0, \text{and } 1.1\}$.

3.3 Advanced filters

In this Section, we consider the properties of more advanced filters, namely single-notch filters with infinite rejection at the centre frequency even if components are lossy, as well as filters with multiple band-stop frequencies.

3.3.1 *MI directional filters with multiple rejection*

In the absence of loss, infinite signal rejection occurs at ω_0 at Port 2 when Port 1 is used as an input. However, for finite Q-factors, the two signal paths P1 and P2 from Port 1 to Port 2 in Figure 3.3 incur unequal losses, and some leakage into Port 2 still occurs at resonance. To equalise the signal amplitudes along the two paths, the magnetic coupling strength between resonators 0 and 1 in the forward waveguide (blue) may be adjusted. We define a new magnetic coupling coefficient $\kappa_f' = \lambda\kappa_f$ between these elements, such that $0 \leq \lambda \leq 1$ and re-consider the port reflection and transmission coefficients. The circuit equations must be modified to:

$$\begin{aligned} ZI_0 + Z_\mathrm{m}(I_{-1} + \lambda I_1) + Z_\mathrm{mc}K &= 0 \\ ZI_1 + Z_\mathrm{m}(\lambda I_0 + I_2) + Z_\mathrm{mc}P &= 0 \\ ZK + Z_\mathrm{mc}(I_0 + J_0) &= 0 \\ ZP + Z_\mathrm{mc}(I_1 + J_1) &= 0 \\ ZJ_0 - Z_\mathrm{m}(J_{-1} + J_1) + Z_\mathrm{mc}K &= 0 \\ ZJ_1 - Z_\mathrm{m}(J_0 + J_2) + Z_\mathrm{mc}P &= 0 \end{aligned} \tag{3.11}$$

As before, we may substitute the assumed solutions (3.2) into (3.11) and use the respective dispersion relations to extract modified reflection and transmission coefficients. The transmission from Port 2 may then be expressed as a rational polynomial in λ as follows:

$$\frac{T_2}{I_\mathrm{I}} = \frac{p_0 + \lambda p_1}{q_0 + 2\mu^4 e^{j2k_\mathrm{f}a}\lambda + q_2\lambda^2},$$

$$\begin{aligned} p_0 &= \mu^4 e^{j2k_\mathrm{f}a}\left(1 - e^{j2k_\mathrm{f}a}\right) \\ p_1 &= \left(e^{j4k_\mathrm{f}a} - 1\right)^2 + \mu^2 e^{j2k_\mathrm{f}a}\left(2 - 2e^{j4k_\mathrm{f}a} + \mu^2\left(e^{j2k_\mathrm{f}a} - 1\right)\right) \\ q_0 &= e^{j2k_\mathrm{f}a}\left(e^{j6k_\mathrm{f}a} + e^{j4k_\mathrm{f}a} - e^{j2k_\mathrm{f}a} - 1\right) \\ &\quad + \mu^2 e^{j2k_\mathrm{f}a}\left(2 - 2e^{j2k_\mathrm{f}a} - 4e^{j4k_\mathrm{f}a} + 4\mu^2 e^{j2k_\mathrm{f}a} - \mu^2\right) \\ q_2 &= 1 + e^{j2k_\mathrm{f}a} - e^{j4k_\mathrm{f}a} - e^{j6k_\mathrm{f}a} + \mu^2 e^{j2k_\mathrm{f}a}\left(2 + 2e^{j2k_\mathrm{f}a} - \mu^2\right). \end{aligned} \tag{3.12}$$

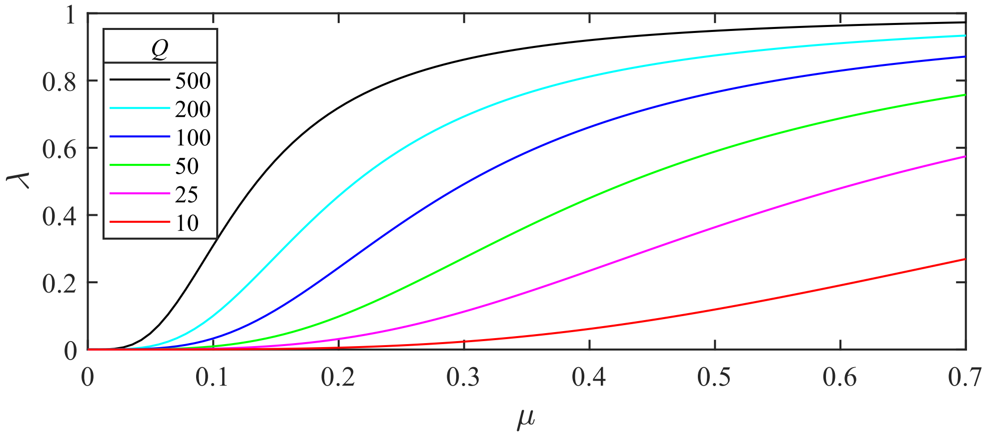

Figure 3.7. Variation of λ with μ for different resonator Q-factors for the single-notch filter with $\kappa_{\mathrm{f}} = 0.6$.

For infinite rejection at resonance, the numerator of the transmission coefficient must be equal to zero, which requires

$$\lambda = -\frac{p_0}{p_1}. \tag{3.13}$$

The dispersion relation (1.10) may be simplified at $\omega = \omega_0$, and the corresponding propagation constant expressed analytically in terms of κ_{f} and Q alone.

$$k_f a|_{\omega_0} = \frac{\pi}{2} + j\ln\left(\sqrt{1+\frac{1}{\kappa^2 Q^2}} - \frac{1}{\kappa Q}\right) \tag{3.14}$$

The expression (3.14) may then be substituted into (3.13) and an analytic expression for λ extracted in terms of filter parameters.

$$\lambda = \frac{\mu^4\rho^4}{\mu^4\rho^4 - 2\mu^2\rho^4 + 2\mu^2\rho^2 + \rho^6 - \rho^4 - \rho^2 + 1}$$
$$\rho = \sqrt{1+\frac{1}{\kappa^2 Q^2}} - \frac{1}{\kappa Q} \tag{3.15}$$

Figure 3.7 shows the variation of λ with μ for a selection of resonator Q-factors. Lower values of λ are required for higher losses, as well as for smaller μ. In each case, λ tends to unity as μ increases, with sharper increases for lower losses. When λ is set according to (3.15), Port 2 is fully isolated from Port 1 at resonance. There are, however, side effects on filter performance, namely some leakage into Port 3 now occurs due to asymmetry and the frequency passband of Port 2 is reduced, although reflectivity at Port 1 is improved. Figure 3.8 shows the theoretical frequency variation of scattering parameters for filters with lossy magneto-inductive (i) and resistive narrowband (ii) terminations, using $\kappa = 0.6$, $\kappa_{\mathrm{c}} = 0.3$, $Q = 200$ and $\lambda = 0.8746$ according to

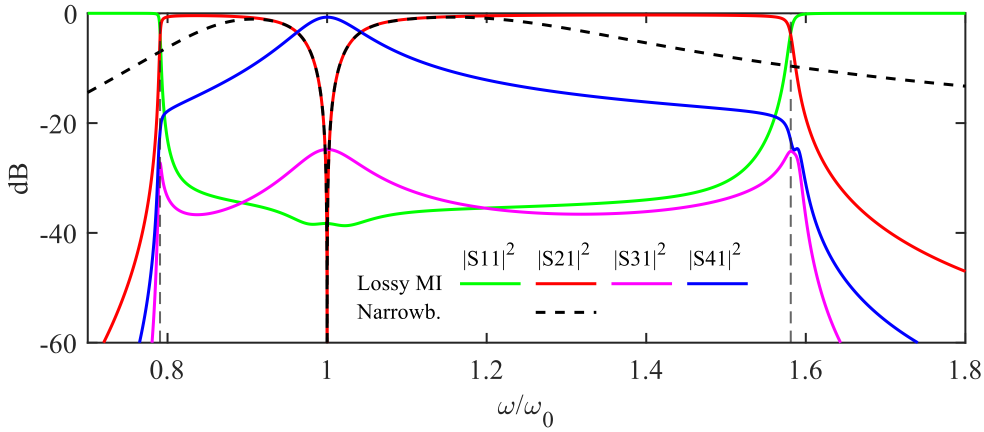

Figure 3.8. Frequency variation of scattering parameters for an infinite rejection MI directional filter with lossy MI or resistive narrowband terminations, using $\kappa_\mathrm{f} = 0.6$, $\kappa_\mathrm{c} = 0.3$, $Q = 200$.

(3.15). Both termination types perform well with S11 mostly below -30 dB within the passband, while S21 is zero at resonance. If port isolation is important, λ may be adjusted to balance rejection with leakage into Port 3. The mutual inductance discontinuity generated by tuning λ implies that the complementary waveguide pair is no longer symmetrical, and the ports may no longer be used interchangeably. Only the two ports immediately adjacent to the λ-tuned resonator pair would yield an infinite-rejection response. The remaining two ports would exhibit diminished performance characteristics if used as inputs.

3.3.2 *Multiple band-stop filters*

A directional filter with N complementary band-stop and band-pass responses can be implemented by increasing the number of coupling resonators from 1 to N as shown in Figure 3.9. Again, a pair of forward- and backward-wave MI waveguides with coupling coefficients $\kappa_\mathrm{f} = \kappa$ and $\kappa_\mathrm{b} = -\kappa$ are connected using vertical lines containing N weakly-coupled resonators with magnetic coupling coefficient κ_c. The resonator rows are labelled from 0 (bottom) to $N-1$ (top) and have currents K_m and P_m flowing in the left and right columns, respectively. The lines of coupling resonators may be considered as two identical uniform MI waveguides, with a passband of $1/\sqrt{1+|\kappa_c|} \leq \omega/\omega_0 \leq 1/\sqrt{1-|\kappa_c|}$ and dispersion relation $Z + Z_\mathrm{mc}\left(e^{-jk_\mathrm{c}a} + e^{jk_\mathrm{c}a}\right) = 0$, where k_c is the propagation constant. The currents P_m and K_m may thus be expressed in terms of reflected and transmitted waves. The reflected wave amplitudes are P_R and K_R, while the transmitted wave amplitudes are P_T and K_T.

$$
\begin{aligned}
P_m &= P_\mathrm{T} e^{-jk_\mathrm{c}ma} + P_\mathrm{R} e^{jk_\mathrm{c}ma} \\
K_m &= K_\mathrm{T} e^{-jk_\mathrm{c}ma} + K_\mathrm{R} e^{jk_\mathrm{c}ma}
\end{aligned}
\tag{3.16}
$$

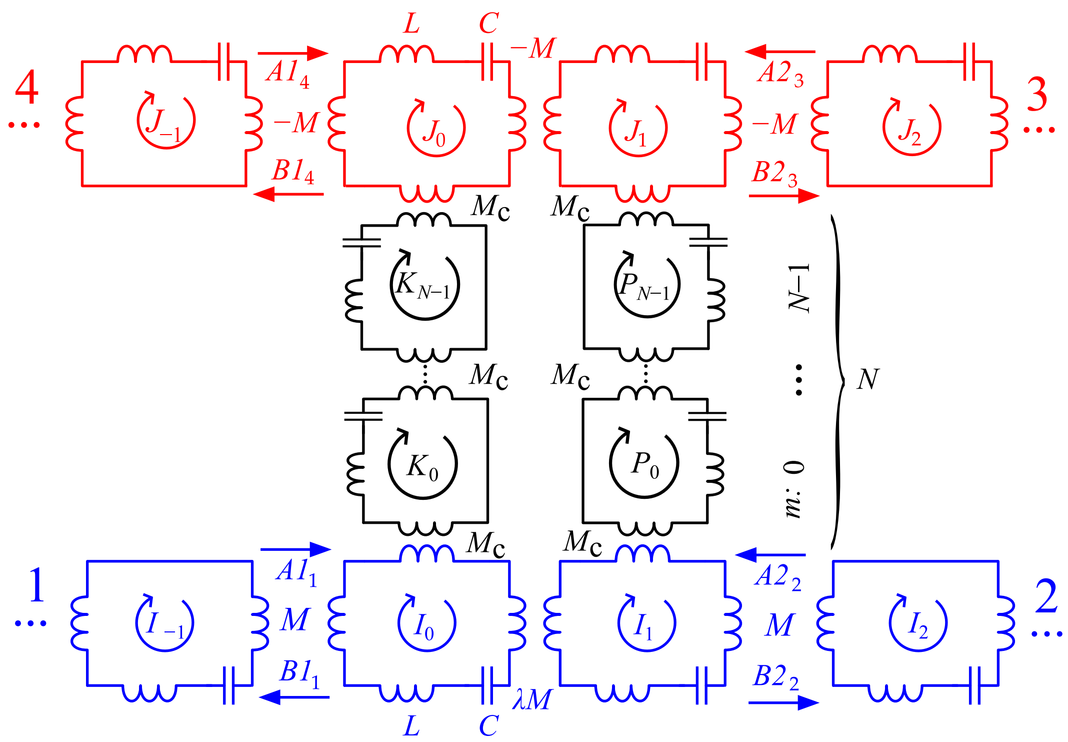

Figure 3.9. Equivalent circuit of a multiple band-stop MI directional filter.

The travelling wave assumptions for currents I_n and J_n remain unchanged from (3.2). Once again, we may write down the circuit equations at the junctions between the waveguides.

$$\begin{aligned}
ZI_0 + Z_\mathrm{m}(I_{-1} + I_1) + Z_\mathrm{mc}K_0 &= 0 \\
ZI_1 + Z_\mathrm{m}(I_0 + I_2) + Z_\mathrm{mc}P_0 &= 0 \\
ZK_0 + Z_\mathrm{mc}(I_0 + K_1) &= 0 \\
ZP_0 + Z_\mathrm{mc}(I_1 + P_1) &= 0 \\
ZK_{N-1} + Z_\mathrm{mc}(K_{N-2} + J_0) &= 0 \\
ZP_{N-1} + Z_\mathrm{mc}(P_{N-2} + J_1) &= 0 \\
ZJ_0 - Z_\mathrm{m}(J_{-1} + J_1) + Z_\mathrm{mc}K_{N-1} &= 0 \\
ZJ_1 - Z_\mathrm{m}(J_0 + J_2) + Z_\mathrm{mc}P_{N-1} &= 0
\end{aligned} \tag{3.17}$$

The eight coupled equations (3.17) can once again be solved for the travelling-wave reflection coefficient at Port 1 and transmission coefficients at Ports 2-4 by substituting the respective dispersion relations and eliminating the terms P_T,P_R, and K_T,K_R.

$$\begin{aligned}
\frac{I_\mathrm{R}}{I_\mathrm{I}} = {} & \left(e^{j2k_\mathrm{c}a(N+1)} - 1\right)\left\{e^{j2k_\mathrm{c}a}\left(1 + e^{j2k_\mathrm{f}a}\right) - \mu e^{j(k_\mathrm{f}+k_\mathrm{c})a}\left(1 + e^{j2k_\mathrm{c}a}\right)\right. \\
& \left. + \mu^2 e^{j2(k_\mathrm{f}+k_\mathrm{c})a}\right\} / D \\
\frac{T_2}{I} = {} & \left(1 - e^{j2(N+1)k_\mathrm{c}a}\right)\left\{2e^{j2(k_\mathrm{f}+k_\mathrm{c})a} - \mu e^{j(3k_\mathrm{f}+k_\mathrm{c})a}\left(1 + e^{j2k_\mathrm{c}a}\right)\right\}/D
\end{aligned}$$

$$\frac{T_4}{I} = \mu e^{j(N+1)k_c a}\{2e^{j(k_f+k_c)a}(1-e^{j2k_c a}) - \mu e^{j2k_f a}(1-e^{j4k_c a})\}/D$$
$$D = (e^{j2ka}-1)e^{j2k_c a}(1-e^{j2k_c a(N+1)}) + 2\mu e^{j(k_f+k_c)a}(1-e^{j2k_c a(N+2)}) - \mu^2 e^{j2ka}(1-e^{j2k_c(N+3)a}) \quad (3.18)$$

The coefficients can be converted to scattering parameters as before. Figure 3.10 shows their frequency variation for $N = 2$ and $N = 5$. The additional coupling resonators generate multiple bandpass responses in S41 and complementary notches in S21. The value of κ_c determines the sharpness of the peaks in S41, as well as the notch frequencies, with larger separation between peaks for higher values. The quality factors of individual peaks increase for higher N, while the effect of loss is to diminish rejection in S21 and increase insertion loss in S41. The number of band-stop and band-pass frequencies is given by N.

The frequencies of peaks and notches can be found by computing the maxima of S_{21} or the minima of S21 within the MI passband. The central frequencies ω_v simplify to:

$$\omega_v = \omega_0 \sqrt{\frac{1}{1+\kappa_c \cos\left(\frac{v\pi}{N+1}\right)}}, \quad (3.19)$$

where $v = 1 \ldots N$. The notch spacing is non-uniform and can be adjusted by varying ω_0 or κ_c. The frequency locations of ω_v are independent of κ, provided $\kappa > \kappa_c$. When N is odd there is always a peak at the resonant frequency ω_0. As previously shown, infinite rejection can be achieved at resonance when $N = 1$. However, since path losses are frequency-dependent, infinite rejection cannot be obtained at multiple central frequencies simultaneously when $N > 1$. However,

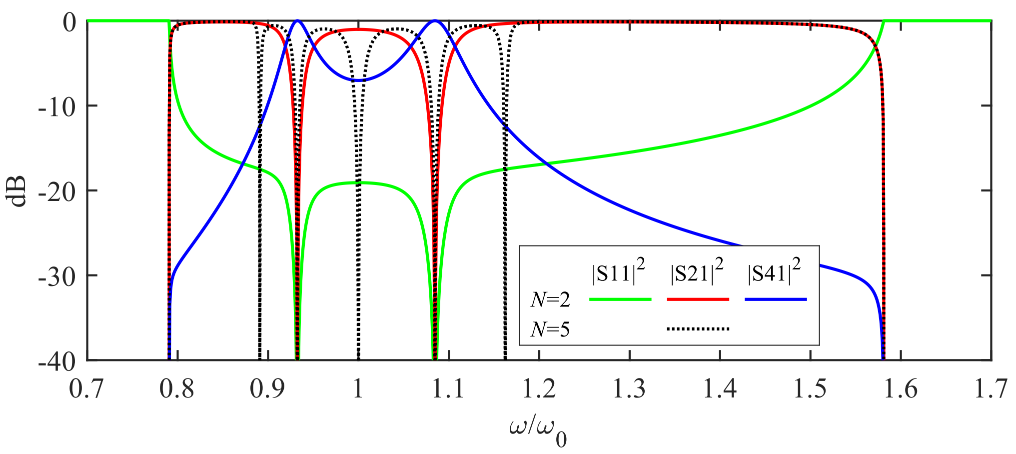

Figure 3.10. Frequency variation of scattering parameters for a multiple-bandstop MI directional filter with lossless MI terminations with $\kappa_f = 0.6$ and $\kappa_c = 0.3$. Parameters are obtained for $N = 2$ and $N = 5$ using (3.18).

simulations show that it is possible to improve performance by optimising the value of the tuning coefficient λ.

3.3.3 *Three-port filters and multiplexers*

In the absence of infinite or improved rejection ($\lambda = 1$), the current in Port 3 is exactly zero at all frequencies when Port 1 is used as an input. This implies that Port 3 can be physically removed from either the single- or multiple-notch devices, along with the resonator at $n = 1$ in the backward-wave guide in Figure 3.3 or Figure 3.9. Specifically, resonators with currents $J_{n\geq 1}$ can be eliminated. Hence, a three-port directional filter can be obtained by loading a uniform MI waveguide with just 3 weakly-coupled resonators and a suitable termination impedance for Port 4. Infinite or improved rejection, however, is then not possible owing to the lack of a secondary signal path for loss compensation (for example, P2 in Figure 3.3). Otherwise, if $\lambda = 1$, the characteristics of three- and four-port filters are indistinguishable. Multiplexers may also be implemented by cascading Ports 1-2 of the directional filters, with central frequency tuning methods (Section 3.2.3) used to specify the channel frequencies, and the individual frequency components obtained at Port 4 of the constituent filters.

3.4 Experimental verification

In this Section, we present experimental results for MI directional filters intended for carrier suppression and receiver isolation in high-power NFC-A applications. As such, the filters have been designed to operate at $\omega_0 = 2\pi f_c$, where $f_c = 13.56$ MHz. The designs have been developed to be tuneable to allow the demonstration of filter operation and extension to advanced filter topologies.

3.4.1 *Single-notch filter*

The overall design was as shown in Figure 3.3; however, resistive terminations were used, and ports were floated using paired capacitors. The equivalent circuit diagram of the experimental filter is shown in Figure 3.11. To allow frequency tunability, all resonators included a variable capacitor. To confine magnetic fields and prevent non-nearest neighbour coupling, all inductors employed low-loss ferrimagnetic toroidal cores with inner and outer diameters of 13.2 mm and 21 mm (Fair-Rite 5967000601, based on "67" Ni-Zn ferrite material with a cutoff at 50 MHz). The initial relative permeability was $\mu_r \approx 40$; implying that most of the magnetic flux was contained within the core. Two windings (with inductances L_C and L_T, such that $L = L_C + L_T$) were used for the

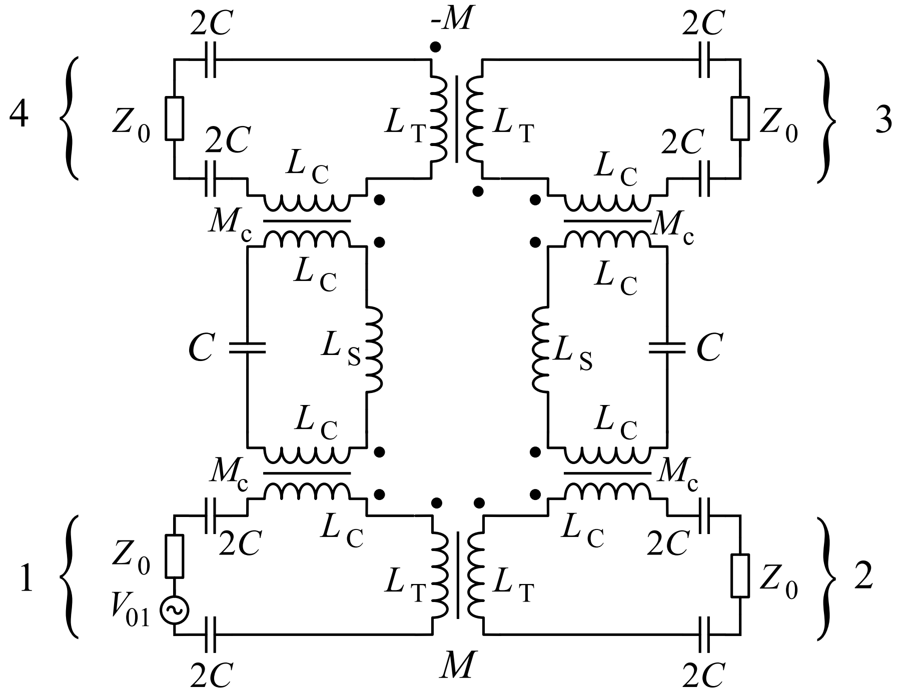

Figure 3.11. Equivalent circuit of the experimental single-notch MI directional filter with real narrowband (ii) terminations.

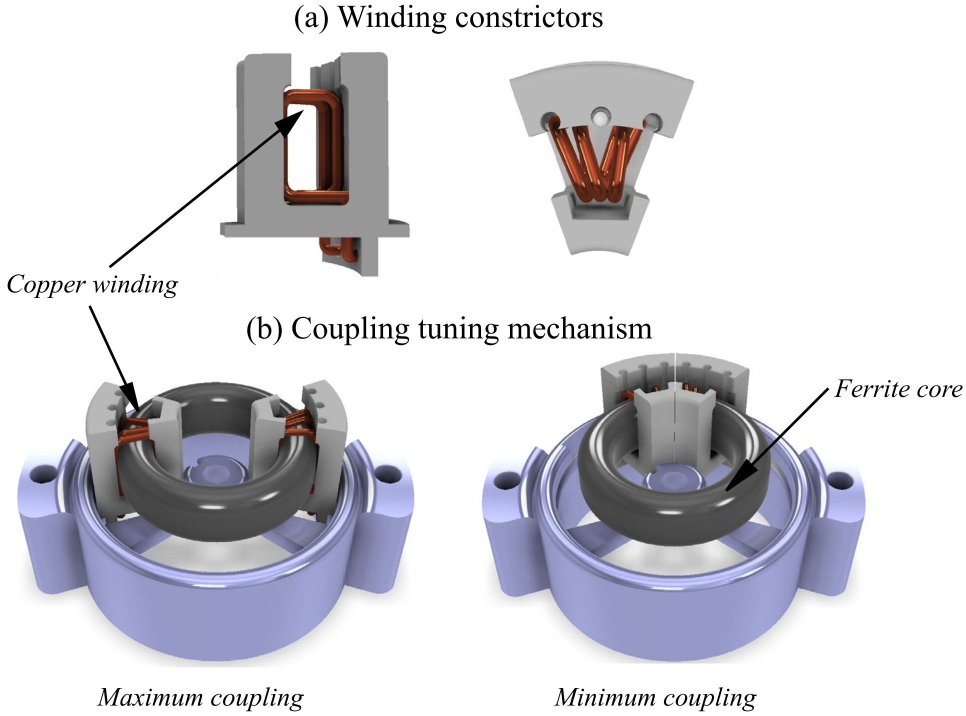

Figure 3.12. Drawing of the mechanism used for mutual inductance tuning between nearest neighbours. (a) Constrictors used to prevent deformation of the inductor windings; (b) custom frame for winding position adjustment along the toroid circumference.

waveguide elements, and three (with inductances L_C, L_C and L_S, such that $L = 2L_C + L_S$) for the coupling resonators. Adjacent windings were reversed to obtain negative coupling coefficients in the backward-wave section. In addition to resonant frequency tuning, a method was developed to enable the tuning of mutual inductance between resonators, using components constructed by 3D-printing with polycarbonate filament. Figure 3.12 shows this mechanism, allowing control over the relative position of two copper windings. The coupling coefficient was a non-linear function of the winding separation, with minimum separation yielding maximum coupling. The mechanism comprised a pair of winding constrictors [Figure 3.12 (a)], used to prevent deformations to the winding shape during tuning, which were inserted into a custom frame below the toroidal core [Figure 3.12 (b)]. The windings could then be re-positioned along the toroid circumference. Since μ_r was fairly low, a wide range of mutual inductance adjustment could be achieved.

Figure 3.13 (a) shows a photograph of the completed filter, constructed on a copper clad printed circuit board using low-loss mica capacitors. Mechanical tuning was provided for all mutual inductances. The value of M needed for impedance matching to a 50Ω load at resonance was first identified. Inductors L_S were then chosen to equalise the self-inductance of all resonators, and capacitances were tuned to achieve resonance at f_c for all resonators. Table 3.1 shows the values of key parameters and adjustment ranges.

Four-port scattering parameters were measured using an electronic network analyser (Agilent E5061B). To begin with, λ was set to unity, so that the response magnitudes were independent of which port was used as the input. Figure 3.14 compares the frequency dependence of S-parameters

(a) Single-notch filter (a) Double-notch filter

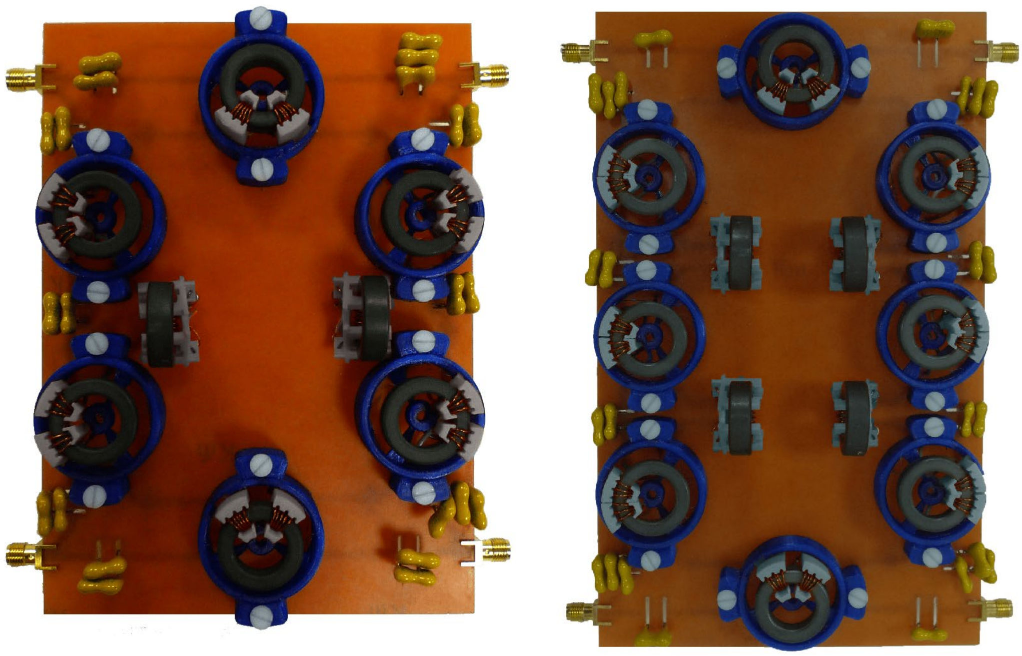

Figure 3.13. Photographs of experimental MI directional filters; (a) single-notch, $N = 1$; (b) Double-notch, $N = 2$. Tuning mechanisms are clearly visible in blue.

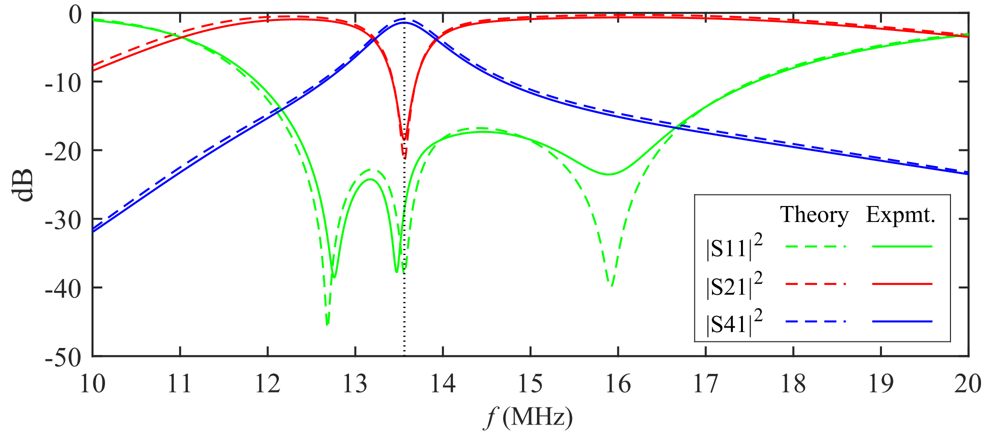

Figure 3.14. Comparison between experimental (solid) and theoretical (dashed) frequency variation of the scattering parameters for the single-notch MI directional filter with no infinite rejection ($\lambda = 1$). The filter has $f_0 = 13.56$ MHz, $Q = 200, Z_{0M} = 50\ \Omega, \kappa_c = 0.28$.

with the predictions of the theoretical model for $\kappa_c = 0.28$. Excellent agreement with experimental results can be seen. Larger values of μ were investigated and found to reduce losses and increase the passband of the bandpass channel and improve the notch depth. Port 2 had -18.5 dB rejection at the central frequency, while the bandpass insertion loss was -1.4 dB.

Table 3.1. Experimental filter parameter values.

Parameter	Value	Adjustment Range
L_T	1.16 μH	N/A
L_C	460 nH	
L_S	710 nH	
κ_f	0.725	0.51 - 0.92
κ_c	0.28	0.19 - 0.34
ω_0	13.56 MHz	DC to 50 MHz
Q	200±10%	N/A

3.4.2 *Single-notch filter with infinite rejection*

Stopband rejection can be greatly improved by fine tuning λ according to (3.15). For parameters in Table 3.1, the value of λ required for infinite rejection is 0.79, well within range for the coupling tuning mechanism. Figure 3.15 compares the simulated and measured scattering parameters obtained in this case. A performance improvement of over 50 dB is achieved compared to Figure 3.14, with over 70 dB rejection at Port 2. This improvement comes at the expense of reduced isolation of Port 3, with a minimum attenuation of 18 dB at the central frequency between Ports 1 and 3. However, sideband losses in S21 are still very low. Infinite rejection filters are particularly well-suited for extracting tag responses by transmission, i.e. when the filter-coupler is

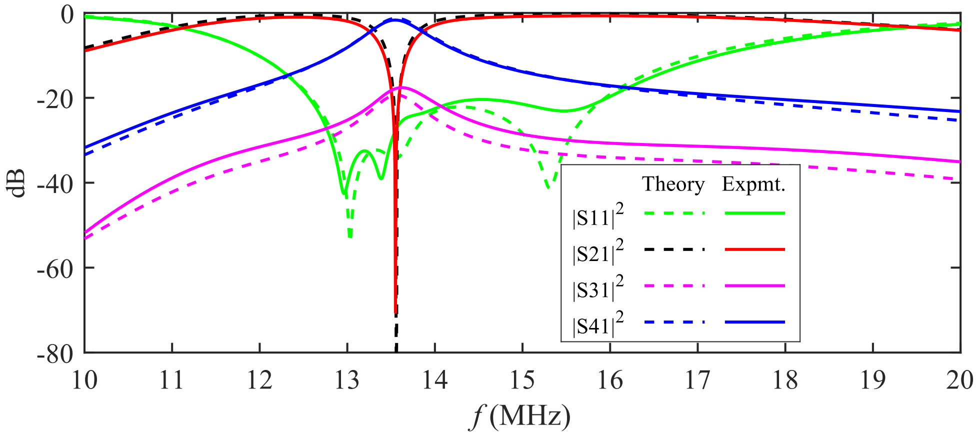

Figure 3.15. Comparison between experimental (solid) and theoretical (dashed) frequency variation of the scattering parameters for the single-notch MI directional filter with infinite rejection ($\lambda = 0.79$). The filter has $f_0 = 13.56$ MHz, $Q = 200, Z_{0M} = 50\ \Omega, \kappa_c = 0.25$.

placed at the opposite antenna end to the transmitter, since the carrier may be eliminated at no detriment to port isolation.

3.4.3 *Double-notch filters*

A two-notch directional filter with parameter values of Table 3.1 was implemented in the same way by increasing the number of coupling resonators in each vertical branch from one to two. A photograph of the two-notch filter is shown in Figure 3.13 (b). The magnitude of κ_c determines the frequency locations of the notches in S21 according to (3.19). However, smaller values of κ_c also increase propagation losses through the coupling resonators, reducing notch depth and increasing losses in the bandpass channel. Figure 3.16 compares theoretical and experimental results for $\kappa_c = 0.28$. The agreement between simulation and experimental results is again

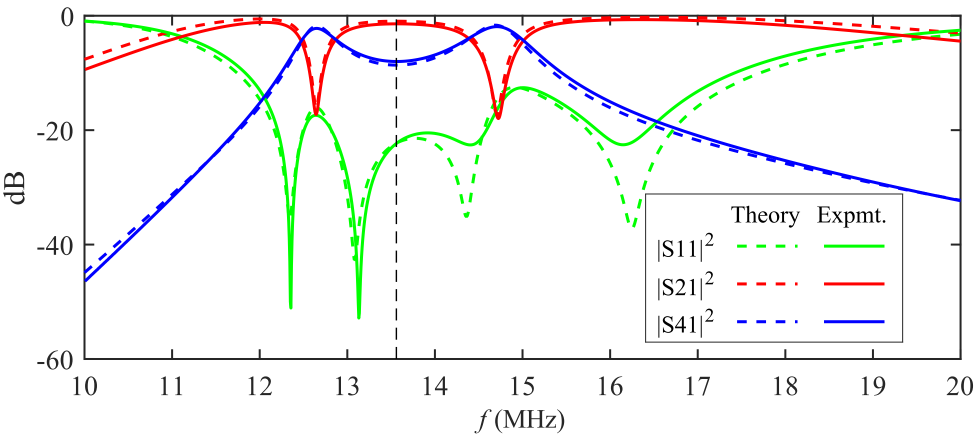

Figure 3.16. Comparison between experimental (solid) and theoretical (dashed) frequency variation of the scattering parameters for the two-notch MI directional filter with no improved rejection ($\lambda = 1$). The filter has $f_0 = 13.56$ MHz, $Q = 200, Z_{0M} = 50\ \Omega, \kappa_c = 0.30$.

excellent. Attenuation in S21 is the same as for the single-notch filter, implying that two channel frequencies can be extracted simultaneously without hindering performance.

3.4.4 *Double-notch filters with improved rejection*

Although infinite rejection does not appear to be possible in multiple-notch filters, rejection can still be improved by adjusting λ. Figure 3.17 compares theoretical and measured S-parameters for a two-notch filter with $\kappa_c = 0.3$ and $\lambda = 0.64$, chosen to equalise rejection at the two notches. A significant performance improvement in rejection of over 15 dB is obtained, once again at the expense of Port 3 isolation. As for single-notch filters, lower values of λ are needed for higher values of μ. Low insertion loss is observed around the resonance frequency but increases elsewhere as matching between the guides and load deteriorates.

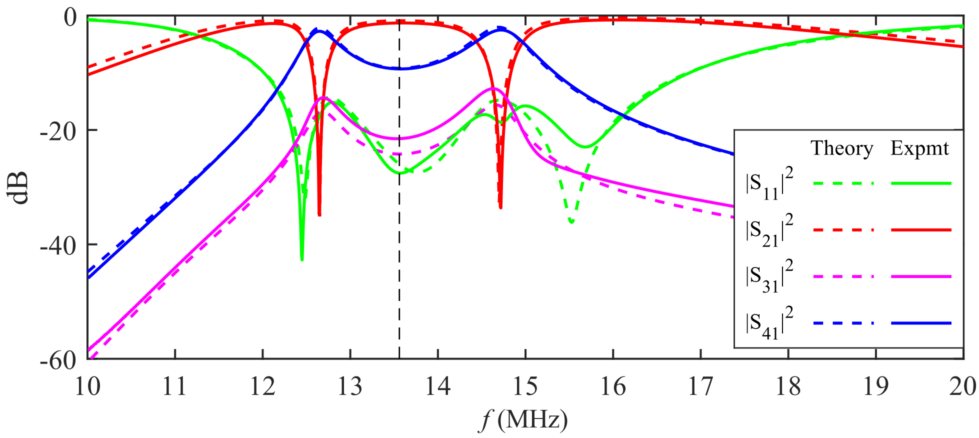

Figure 3.17. Comparison between experimental (solid) and theoretical (dashed) frequency variation of the scattering parameters for the two-notch MI directional filter with improved rejection ($\lambda = 0.64$). The filter has $f_0 = 13.56$ MHz, $Q = 200$, $Z_{0M} = 50\ \Omega$, $\kappa_c = 0.30$.

3.4.4 *Near field communication applications*

Toroidal transformers based on soft ferrites allow magneto-inductive designs to be realised with minimal non-nearest neighbour coupling. However, core materials must have low loss and high linearity, especially in applications which require high power handling capability. In NFC-A, the carrier power can be orders of magnitude greater than that of the sidebands, meaning the receiver must remain isolated at the carrier frequency to improve sensitivity and prevent damage. The single-notch filter presented here can be integrated into existing MI systems via direct connection to the waveguides, has high rejection at resonance, and may be used to dump residual carrier signal into a matched absorptive load. However, the filter must be effective at representative

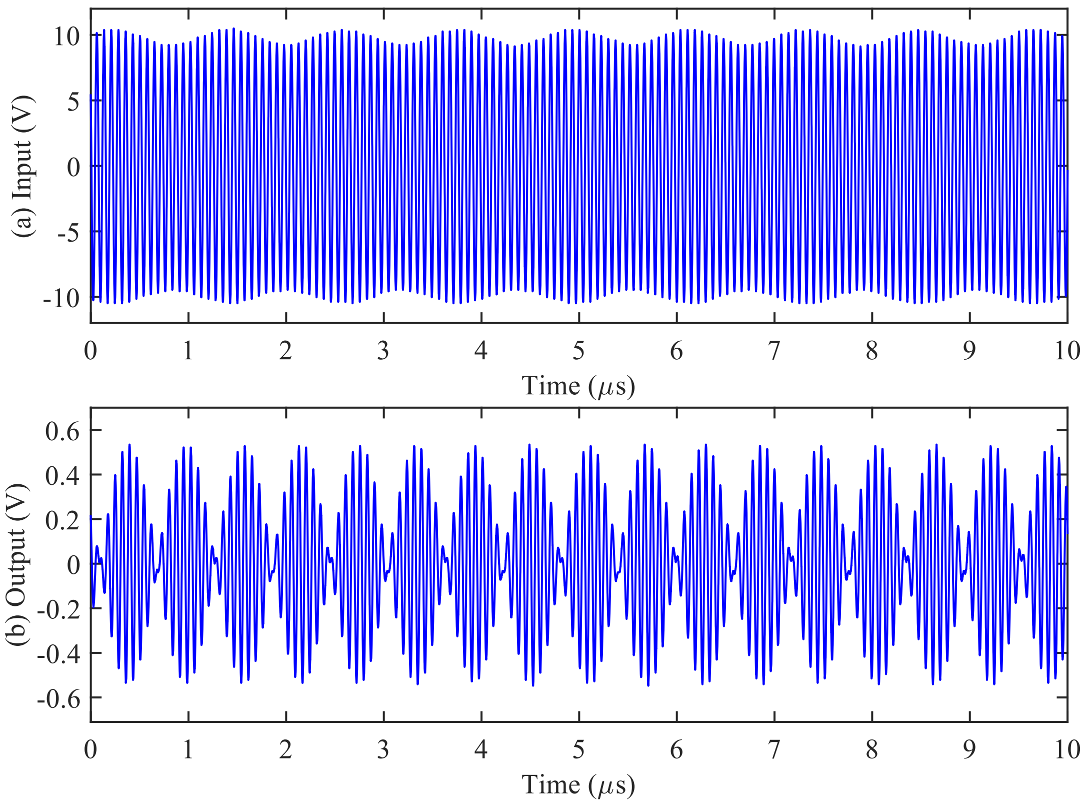

Figure 3.18. (a) measured Port 1 input signal $s(t)$ with $P_c = 1$ W and the corresponding (b) output signal from Port 2. The input signal power has been compensated for the 30 dB attenuation incurred during measurement.

carrier powers, despite potential non-linearities introduced by ferrite cores. We may emulate compliant NFC-A signals by modulating a high-power carrier with frequency f_c with a sinusoidal message signal at the subcarrier frequency f_s. The resultant signal is identical to the practical waveforms generated during the tag response sequence but lacks any subcarrier modulation. The waveform of the input signal $s(t)$ may be modelled as follows.

$$s(t) = [A_c + A_m \cos(2\pi f_m t)] \cos(2\pi f_c t) \tag{3.20}$$

Here A_c and A_m are the carrier and message amplitudes. The message signal was derived from one signal generator (Agilent E4433B) and carrier modulated by a second signal generator (Agilent N5181A), followed by amplification using a 30 dB power amplifier (Minicircuits ZHL-32A+). Carrier amplitude A_c was adjusted to produce a specific carrier power P_c, while a modulation index $A_m/A_c \approx 0.1$ was chosen to generate typically small sidebands. The signal $s(t)$ was then injected into Port 1 of a single-notch MI directional filter with infinite rejection, while the output was measured at Port 2. Ports 3 and 4 were terminated by 50 Ω loads. Detection was performed using a digital storage oscilloscope (Keysight InfiniiVision DSOX3024T). To measure the input $s(t)$ without damaging the oscilloscope, a 30 dB attenuator was employed. Figure 3.18

shows the time-domain input (a) and output (b) waveforms into Port 1 and out of Port 2, respectively. The filter has clearly extracted virtually all the carrier signal while keeping the weak subcarrier signal intact. We may analyse the filter characteristics further using frequency-domain analysis of the waveforms.

Figure 3.19 (a) shows the measured power spectral density (PSD) of the input signal $s(t)$ for P_c = 1 W, normalised by the carrier power. Amplifier non-linearities have resulted in minor harmonics of the AM spectrum, which have been partially suppressed at high frequencies with a low-pass filter. Figure 3.19 (b) shows the PSD of the output signal at Port 2 (the stopband channel). The output signal exhibits an attenuation of 73 dB at the carrier frequency and 1.2 dB attenuation at the sideband frequencies. In fact, the only significant difference between frequency content of the input and output signals appeared to be the carrier rejection. No additional harmonics have

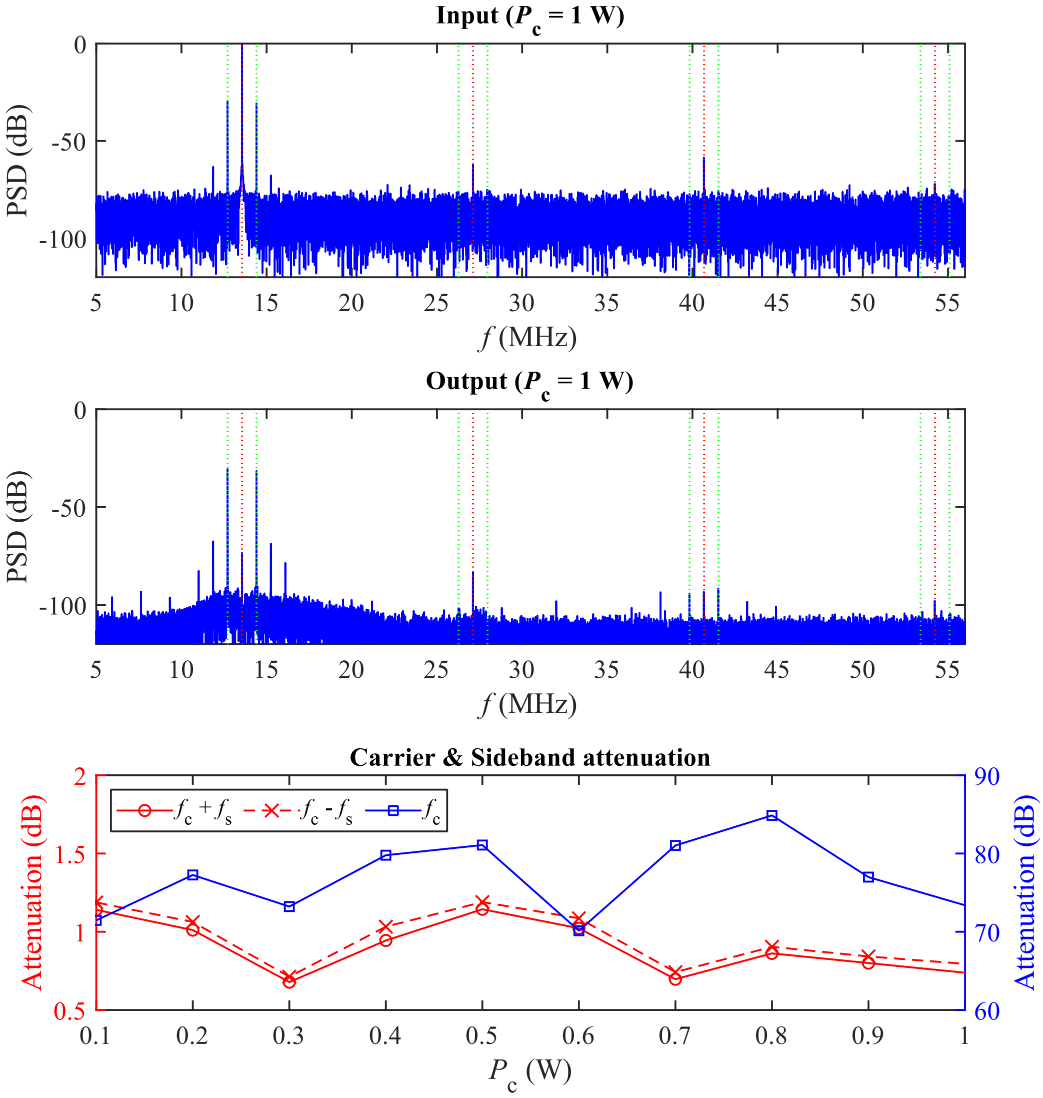

Figure 3.19. Power spectral densities of (a) the input signal $s(t)$ into Port 1 and (b) the output signal at Port 2, both normalised by the input carrier power P_c. Dashed lines, red: carrier harmonics, green: subcarrier harmonics. (c) Filter attenuations at carrier (f_c), upper sideband ($f_c + f_s$) and lower sideband ($f_c + f_s$) frequencies.

been introduced, implying the filter was operating linearly, despite use of ferrite cores. Figure 3.19 (c) shows the signal attenuation at the carrier and subcarrier (upper and lower) frequencies, over an input carrier power between 0.1 W and 1 W. Attenuation is almost independent of P_c, suggesting effective power handling capability and overall performance.

3.4.5 *Frequency scaling*

The potential for scaling to higher frequencies is largely determined by ferrite performance. Table 3.2 shows some performance parameters of low-cost Ni-Zn soft ceramic ferrite materials and toroidal cores designed for RF applications such as EMI suppression (upper group) and broadband transformers and baluns (lower group), including their initial relative permeability μ_i, the Curie temperature 'TC' and the loss factor. The main difference between the groups is the maximum usable frequency F_{max}. According to Snoeks' limit [204], a fundamental property of ferrite materials is the inverse relationship between μ_i and F_{max}. High-frequency performance is therefore accompanied by a reduction in magnetic field confinement capacity and an increase in material loss. Physically smaller cores may be used to minimise the volume of magnetic material. However, careful design is required to optimise performance. Power handling would likely be reduced, and automated coil winding may be required for construction [205]. Despite this, the data suggest that the central frequencies may be extended to the low UHF band. Above this, air-cored inductors should be used, but non-nearest neighbour coupling and radiation will inevitably complicate design and hinder performance.

Table 3.2. Performance parameters for a selection of ferrite materials and toroidal cores.

Manufacturer	Model	Outside diameter (mm)	Inside diameter (mm)	Height (mm)	μ_i	F_{max} (MHz)	Curie Temperature (°C)	Material	Loss factor
Ferroxcube	-	-	-	-	125	20	>350	4C65	130 at 10 MHz
Fair-rite	5961001801	22.10	13.70	6.35	125	25	>300	61	10 at 10 MHz
Ferroxcube	_	_	_	_	25	100	>400	4E2	_
Fair-Rite	5968001801	22..10	13.70	6.35	16	150	>500	68	300 at 100 MHz
National Magnetics	_	-	-	-	7.5	400	>320	M5	<3500 at 100 MHz

3.5 Conclusions

New configurations of magneto-inductive devices with directional filter characteristics have been developed, comprising magnetically coupled LC resonators. Design rules have been established, and methods of calculating scattering parameters when filters are used in MI systems (which have complex, frequency-dependent impedance) or conventional systems (with real impedance) have been developed. The circuit equations have been simplified and solved using wave analysis. Analytic expressions have been developed for the power scattering parameters, bandwidth, infinite and improved rejection conditions, and centre frequencies of multiple-notch filters. A simple method for central frequency tuning has been proposed, and advanced filters allowing infinite rejection at a chosen frequency or improved rejection at several frequencies have been proposed.

MI directional filter operation has been verified in the high-frequency range. Ceramic ferrite cores have been used to eliminate non-nearest neighbour coupling within a compact layout, and simple methods for tuning the element resonant frequencies and nearest neighbour coupling coefficients have been proposed and experimentally demonstrated. Experimental results for tuneable filters, filters with infinite rejection, and filters with multiple band-stop frequencies have all been shown to agree with theoretical models. Sufficient power handling capability for use in near field communication systems for HF carrier suppression has been demonstrated, with linear filter characteristics despite the use of ferrite cores.

MI directional filters can also be designed for use at UHF. Potential research could concentrate on counteracting ferrite losses, or alternatively, minimization of non-nearest neighbour coupling and radiation in open-loop designs. Furthermore, the wave operating principles can be extended to other metamaterial types, such as elastic or acoustic. For example, it has already been shown that MEMS could be used to generate high-performance two-port notch and comb filters. But, most importantly, the new MI filter-couplers may be employed in high-performance slow wave near field communication and localisation systems, as shown in the following Chapters.

Chapter 4:
Near Field Localisation with Magneto-Inductive Waveguide Antennas

In this Chapter we develop, simulate, and experimentally verify a novel bistatic NFC tag localisation method, which employs time-of-flight differences in tag response for accurate positioning. Localisation of passive tags in the high-frequency regime is well-known to be problematic, mainly due to the extremely poor range scaling of magnetic near fields. Here we present a solution for one-dimensional localisation based on MI waves. Passive NFC-A compliant tags are interrogated using a travelling wave antenna formed by a planar MI waveguide. Load modulation signals generated by the tag during its unique identifier response are coupled into the waveguide and travel to either antenna end at low group velocity. Time-of-arrival differences are calculated by pair-wise cross-correlation of the responses, and the tag position is estimated to the nearest antenna element. Correlation detection is demonstrated using a system simulation model, and theoretical predictions are validated by an experimental system comprising eleven transformer-coupled resonators operating at 13.56 MHz frequency. Accurate localisation is obtained up to the tag reading limit using less than 1W carrier power.

4.1 Overview

The problem of tag localisation in RFID systems has attracted significant interest in both industry and academia [47], [48], [206]–[209]. While modern commercial readers can identify and communicate with numerous transponders located within their capture volume, they are typically unable to differentiate between tags based on their position in physical space, with localisation potential limited to detecting their presence or absence. Accurate localisation capability could significantly enhance system functionality and is particularly appealing for large-scale logistics applications, inventory management, and animal tracking. The argument is further strengthened by the wide availability of low-cost tags and the existing worldwide adoption of RFID technology [62]. Consequently, multiple tag localisation schemes have been developed, most of which operate in the UHF regime [210]–[217] owing to its long operating range and prevalence in logistics. Most of the current methods use relative signal strength (RSSI) or backscatter phase indicators for tag positioning. Learning algorithms and statistical environment fingerprinting techniques have also

Table 4.1. UHF RFID tag localisation methods.

Located object	Reference system	Method	Reference
Tag	Multiple fixed readers	Signal strength	[211]
Reader	Multiple fixed tags	Signal strength	[213]
Tag	Mobile reader antenna	Signal phase	[215], [216]
Tag	Fixed reader antennas	Signal phase	[210], [212], [214], [217]

Table 4.2. NFC tag localisation methods.

Ref.	Located object	Antenna type	Number of readers	Transverse range	Hardware complexity scaling	Reader power
[218]	Books	1 mobile antenna	1, with probabilistic localisation	N/A	Shelf layout	High
[219]	Books	2 mobile antennas	1, with probabilistic localisation	N/A	Room layout	High
[109]	Vicinity tag	2 x 2 flexible antenna array	1, with multiplexer	11.1 cm	Element number	2 W
[110]	Encapsulated tag	21 element antenna array	1, with cascaded multiplexers	4 cm	Element number	1-5 W
[50]	Encapsulated tag	6x5 antenna array	2, with 16 channels each	10 cm	Element number	0.5-8 W
[111]	NFC Speedtap tags	5 x5 antenna array	1, but antenna elements have individual oscillators	3 cm	Element number	280 mW
This Chapter	ID1 tags	11-element travelling-wave MI antenna	1, with 2 receivers	6 cm	Fixed	1 W

been developed to improve accuracy and mitigate environmental disturbances such as multipath effects [220], [221]. Multiple reference tags or multiple reader antennas are typically required for accurate localisation. A selection of current UHF localisation techniques can be found in Table 4.1.

The HF regime, however, offers limited possibilities for localisation in comparison, owing to the poor range scaling of magnetic near fields and the lack of signal phase information. Current research typically leverages the short NFC transmission range for accurate reader localisation within reference tag grids with known spatial coordinates [222]–[228]. The readers are often affixed to mobile robots for automatic pathfinding, while the reference tag distributions can be uniform or sparse [229]. Similar methods have been applied to identify the location and orientation of furniture [230] and for smartphone geo-localisation in indoor environments [231], [232]. The converse problem of automated tag positioning, however, has fewer solutions, with tracking methods limited to the deployment of numerous standalone readers [49], scanning with mobile readers [218], [219], [233], or multiplexed antenna arrays [50], [109]–[111]. Costly hardware scaling is typically required to increase the capture volume of such methods. It should also be noted that one-dimensional MI waveguides have been employed for localisation of metallic resonators using load position sensing [234], [235], while MI surfaces have been used for targeted wireless charging of NFC devices [236]. Still, tag localisation in the HF regime is underdeveloped in comparison to its UHF counterpart. Table 4.2 compares some existing ISO/IEC 14443 Type-A compliant localisation techniques with the method proposed in this Chapter.

4.2 System architecture

One solution to NFC localisation may be conversion of reader and tag signals to non-radiative travelling waves, such as a magneto-inductive waves, which propagate along a waveguide antenna with low group velocity. As in a bistatic radar, the tag position may then be estimated from the time-of-flight (TOF) difference between the tag responses extracted from either antenna end. Unlike radar, however, tags respond to reader queries with a delay determined by the frame delay time (FDT), which may fluctuate between individual tags by up to 400 ns [76]. Despite this, we show that correlation detection can be employed for accurate localisation using unique identifier (UID) tag responses.

Figure 4.1 shows a block diagram of the proposed system. The antenna comprises a transformer-coupled planar MI waveguide antenna with N elements, such that high nearest-neighbour coupling may be achieved, while minimising non-nearest neighbour coupling effects.

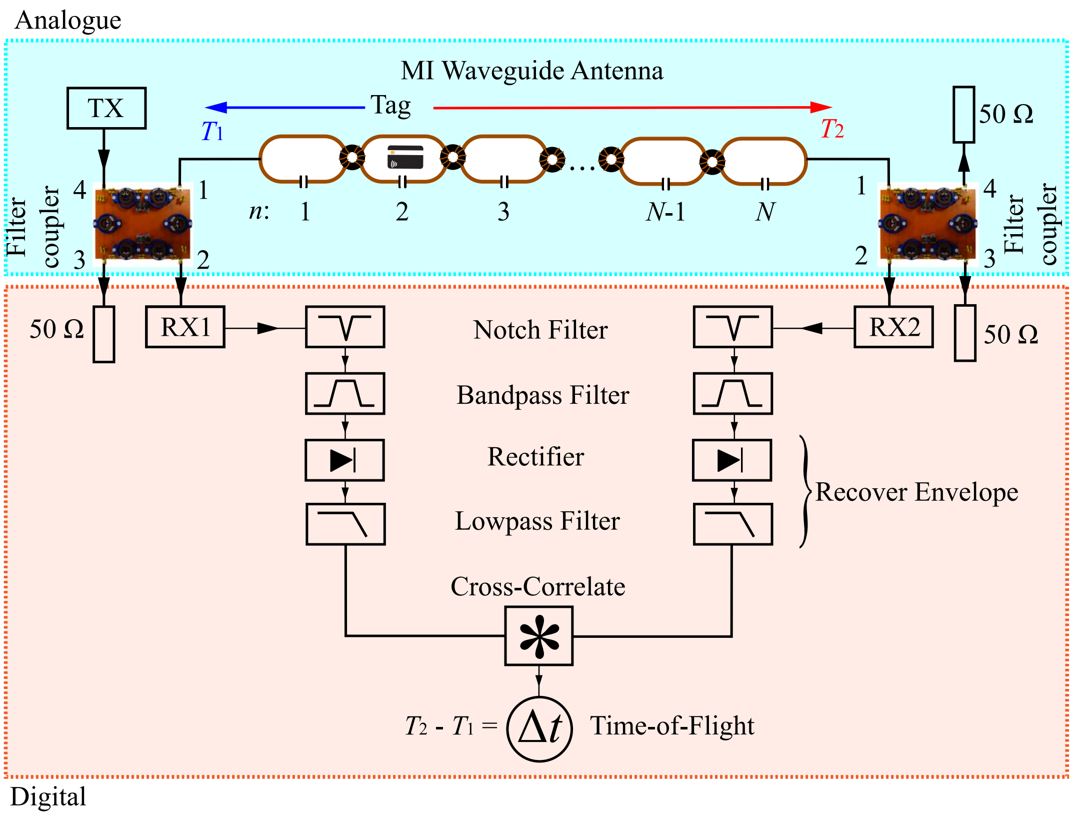

Figure 4.1. System block diagram for tag localisation by cross-correlation of magneto-inductive waves.

The transmit (TX) signal from the reader is injected into the antenna at one end via a MI single-notch filter-coupler (as demonstrated in the previous Chapter) tuned to the carrier frequency f_{c}, with a second filter-coupler used to divert any residual carrier into an absorptive load at the other end. TX signals propagate along the waveguide antenna, generating external magnetic near fields and powering a tag in its vicinity. When interrogated, a tag induces a time-varying load in an antenna element, which results in reflected and transmitted slow waves at carrier and sideband frequencies. The sidebands are separated from the carrier using the filter couplers and detected by two receivers (RX1 and RX2) placed at either end. In the absence of loss, the element magnetic field strength is position-independent, so the antenna can be axially extended to increase capture volume without detriment to efficiency. Digital notch and bandpass pre-filters are then applied to the sampled tag response signals to eliminate any residual carrier and suppress out-of-band noise [237]. Baseband tag responses are recovered using envelope detection, implemented by rectification and low-pass filtering. The tag UID is then decoded, and pair-wise cross correlation of the baseband UID signals is used to estimate the TOF difference $\Delta t = T_2 - T_1$ [238]. Assuming the waveguide group velocity is known, the physical tag position may be obtained from the Δt estimate.

The demands on receiver electronics and sampling rate requirements may be reduced by maximising the slow wave factor of the MI antenna. Slow-wave structures, however, are generally dispersive and the amount of resultant signal distortion increases with slow wave factor. Dispersion is thus expected to be a limiting factor on localisation accuracy, particularly for antennas with large N. Performance must also depend on the signal-to-noise ratio (SNR) and the nature of the noise. Figure 4.2 shows three possible noise sources, which include (A) uncorrelated receiver noise n_{A} originating at antenna outputs, (B) partly correlated noise n_{B} originating at each element which

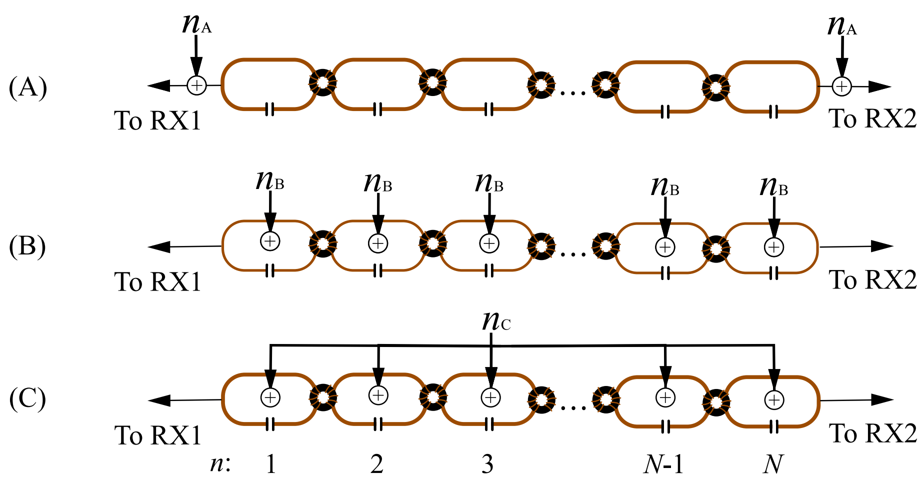

Figure 4.2. Noise sources in a MI waveguide: (A) uncorrelated noise n_{A}, (B) weakly correlated noise n_{B}, and (C) strongly correlated noise n_{C}.

propagates to either antenna end, or (C) ambient RF noise n_{C} induced in all antenna elements simultaneously. Obvious sources of internal noise are thermal and shot noise. External noise sources include switches, motors, vehicle ignition, plasma processing [239] and, increasingly, computers [240]. External noise (C) must generate strongly correlated outputs, which may lead to false correlations at $\Delta t = 0$. We examine such limitations in the following Sections.

4.3 Antenna design

Magneto-inductive waveguides are inherently dispersive. Similarly, MI waves are slow waves owing to their band-limited nature (1.15). The group velocity $v_{\mathrm{g}} = d\omega/dk'$ in the passband of an ideal MI waveguide can be found by differentiating the lossless dispersion relation (1.10).

$$v_g = \frac{\kappa a \sin{(ka)}\omega^3}{2\omega_0^2} \tag{4.1}$$

Similarly, the slow wave factor (SWF) can be found by comparing v_{g} with the free space velocity of an electromagnetic wave c.

$$\mathrm{SWF} = \frac{c}{v_{\mathrm{g}}} \tag{4.2}$$

Figure 4.3 (a) shows the frequency variation of the group velocity, while Figure 4.3 (b) shows the frequency variation of the slow wave factor; both normalised by the element width as v_{g}/a and ac/v_{g}, respectively. Two important observations may be made. Firstly, the slow wave factor and the waveguide bandwidth have an inverse relationship, meaning $|\kappa|$ should be minimised to maximise the per-element group delay. Secondly, the amount of signal distortion is highest for weakly-coupled waveguides owing to the increased group velocity variation within the passband. The coupling coefficient should thus be selected to balance group velocity dispersion with group delay. It should also be noted that $|\kappa|$ must be sufficiently high to accommodate the minimum backward link bandwidth BW_{T} within the antenna passband. Provided the resonant frequency is f_{c}, the limiting value of the coupling coefficient $|\kappa_{\min}|$ is given by the solution to (4.3).

$$BW_{\mathrm{T}} = \left(\frac{1}{\sqrt{1-|\kappa_{\min}|}} - \frac{1}{\sqrt{1+|\kappa_{\min}|}}\right) f_{\mathrm{c}} \tag{4.3}$$

Since $BW_{\mathrm{T}} = 5f_{\mathrm{c}}/32$, the minimum coupling coefficient $|\kappa_{\min}| \approx 0.1539$. Despite the high SWFs, operation around $|\kappa_{\min}|$ may result in unacceptable propagation losses (1.17) and restrict

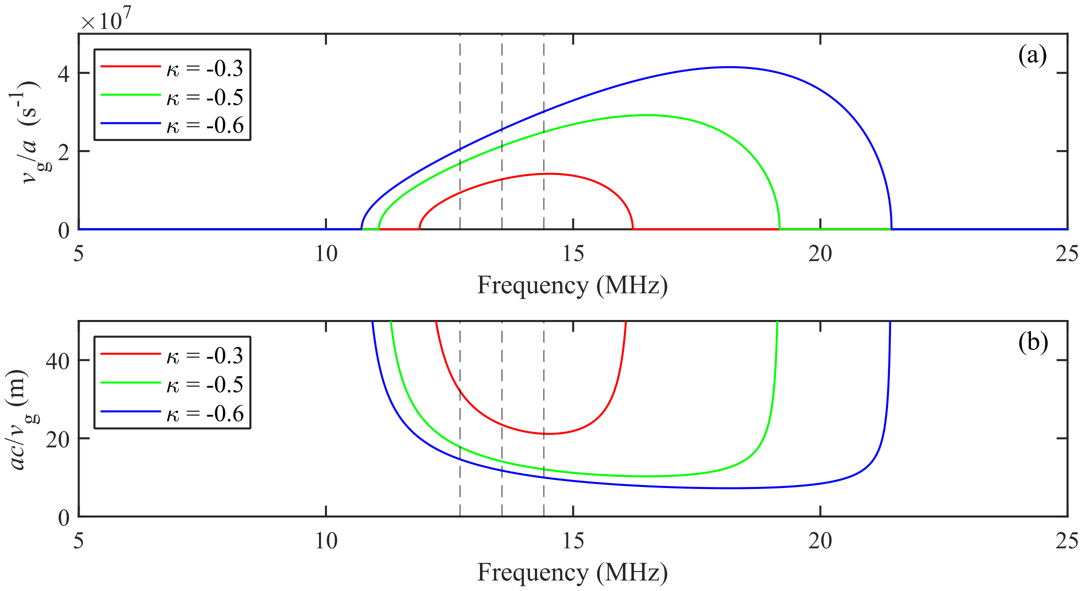

Figure 4.3. (a) Theoretical variation of normalised group velocity v_g/a and (b) normalised slow wave factor ac/v_g with frequency for an ideal MI waveguide with f_0 = 13.56 MHz, $\kappa = -0.3$ (red), $\kappa = -0.5$ (green), and $\kappa = -0.6$ (blue). Dashed lines indicate the carrier and subcarrier frequencies.

maximum antenna length. The group velocity at resonance is $v_{g0} = |\kappa|a\omega_0/2$. The SWF at resonance is then $c/v_{g0} = 2c/(|\kappa|a\omega_0)$. For $a = 15$ cm and $\kappa = -0.5$, say, we then obtain SWF ≈ 94, a relatively large value that improves timing accuracy. For $a = 1.5$ m, the slow wave factor reduces to 9.4. Positioning to the nearest element number, however, must be independent from the element width, since the per-element group delay is the same for all a.

The TOF differences Δt that must be measured to detect distance-of-flight (DOF) differences Δx have the form $\Delta t = \Delta x/v_g$. Since the tag can only be displaced from the waveguide centre by a whole number of elements, $\Delta x = 2\nu a$, where ν is an integer. At resonance, $\Delta t = 4\nu/|\kappa|\omega_0$. In terms of the period $T_0 = 2\pi/\omega_0$, we obtain $\Delta t/T_0 = 2\nu/(|\kappa|\pi)$. For $\kappa = -0.50$, the minimum TOF difference that must be detected is then $\Delta t/T_0 \approx 4/\pi \approx 1.273$. To reduce timing errors below 10%, sampling must be carried out at a frequency $f_{\mathrm{samp}} > 12.73f_0$, or at least 173 MSa/s. Reduced accuracy, however, may be sufficient.

For antennas with low signal distortion, tag position may be accurately estimated from Δt for all antenna elements. However, MI waveguides have considerable dispersion, especially for low $|\kappa|$. Localisation accuracy will thus become degraded by envelope changes to the tag response signals. The effect will be strongest for tags located at the antenna extremes, when the two signals are most dissimilar. The amount of expected distortion may be estimated by the group velocity dispersion of an MI waveguide GVD $= d(1/v_g)/d\omega$.

$$\mathrm{GVD} = \frac{-2\omega_0^2}{\kappa a\omega^4 \sin(ka)}\left\{3 + \frac{2\omega_0^2 \cos(ka)}{\kappa\omega^2 \sin^2(ka)}\right\} \tag{4.4}$$

The GVD is zero when the contents of the curly bracket above vanish, allowing the frequency of zero dispersion ω_Z to be found as:

$$\frac{\omega_Z}{\omega_0} = \frac{1}{\sqrt{2 - \sqrt{1 + 3\kappa^2}}} \tag{4.5}$$

This ratio is unity when $|\kappa|$ is low, but gradually rises as $|\kappa|$ increases. Our studies have shown that operation at ω_Z rather than ω_0 allows some reduction in envelope distortion, but at a price of higher losses; consequently, there is little obvious advantage in operating away from resonance. For a substantial reduction in signal distortion a linear phase response is required throughout most of the passband due to the wide separation between subcarrier sidebands.

4.4 Tag response characteristics

We now consider the autocorrelation properties of the tag unique identifier responses as defined by NFC-A or ISO/IEC 14443 Type-A. Although this protocol was not designed for localisation, suitable autocorrelation envelopes may be obtained for single-size UID frames. Figure 4.4 shows the bit-level formatting, as transmitted by the tag in a standard frame. The response begins with a start bit S, which is always represented by a logic ‘1’. The UID is then split into four bytes, transmitted with the most significant byte first, with each byte followed by a parity bit P. The bit order of individual bytes is least significant bit (LSB) first. The last byte is followed by a block check code BCC, obtained as a bitwise exclusive OR of the four UID bytes, which is again followed by a parity bit. The UID data frame is terminated with the ‘end of communication’ symbol ‘F’, during which no subcarrier modulation occurs. The binary response thus contains 1 + 5 x 9 = 46 bits, while its Manchester-coded response contains 92 chips.

Performance of such responses in a correlation detection system may be assessed as follows. The processing gain G may be estimated as the bandwidth expansion factor, namely $92N_\mathrm{S}$, where N_S is the number of samples per chip. If N_S is only moderate, the processing gain can be large (for

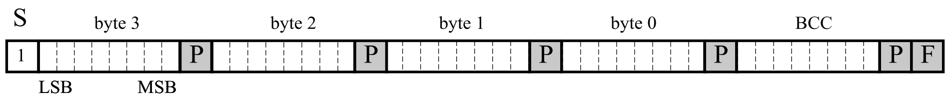

Figure 4.4. Bit formatting of a single-size tag UID, transmitted in a standard frame.

example, $G > 2000$ for $N_S = 48$). Because half of the chips are zero, the peak of each autocorrelation is $46N_S$ times the signal strength. Correlation detection is therefore an intrinsically low noise operation.

In contrast to radar responses, UID autocorrelations are not ideal delta functions. The ability to accurately locate the correlation peak then depends on the sidelobe ratio (SLR). Its value may be estimated by assuming a two-chip offset for binary codes consisting entirely of 'ones' as $SLR = 46/45 = 1.0222$. However, the BCC byte prevents this case arising in practice. For example, Figure 4.5 (a) shows the baseband response and the ideal autocorrelation for UID = '0xFFFFFFFF', where the BCC has introduced discontinuities in the otherwise regular code. These have increased the sidelobe ratio to 46/43 = 1.0698. Despite this, the envelope of the autocorrelation function is still broad.

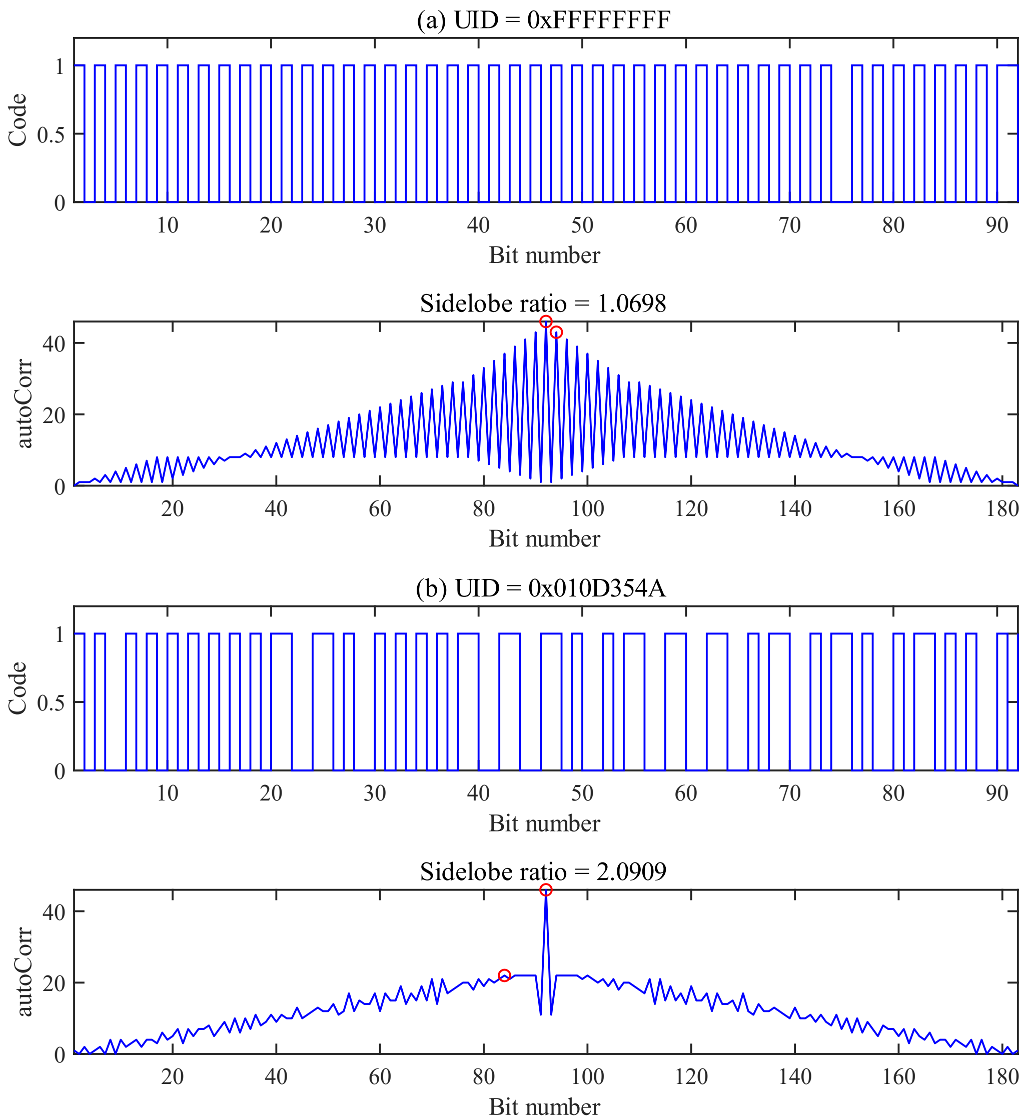

Figure 4.5. Baseband Manchester-coded UID responses (upper diagrams) and their autocorrelations (lower), for UIDs with (a) low and (b) high sidelobe ratios.

The UID above is the worst case we have identified. Using a numerical search of one eighth of all possible UIDs (which number $256^4 = 4.29 \times 10^9$), we have found that SLR does not fall below 1.0698, and that the autocorrelation peak sharpens as the code becomes more random, with a maximum SLR $= 46/22 = 2.0909$. In this case, the autocorrelation consists of a sharp peak generated by the code itself, superimposed on a triangular base arising from its average level. For example, Figure 4.5 (b) shows the baseband response and autocorrelation for UID = '0x010D354A', which possesses the maximum SLR identified. Similar autocorrelations are common, allowing the TOF to be estimated from the location of the sharp central peak, whose shape is largely determined by the autocorrelation of a single bit.

4.5 System simulation

We now describe the simulation model for the system shown in Figure 4.1, implemented in Matlab®, assuming the effects of tag loading on the antenna are negligible. The frequency variation of the propagation constant is first found by solving the MI dispersion equation (1.10) for a uniform waveguide with $f_0 = 13.56$ MHz for sample values of κ and Q. For a given tag position, represented by the integer $P \in [1, N]$, this variation is used to calculate transfer functions for the two counter-propagating waves, in the form $T_\mathrm{R} = e^{-jN_1ka}$ and $T_\mathrm{T} = e^{-jN_2ka}$, where $N_1 = P - 1$ and $N_2 = N - P$. The effects of the filter couplers are ignored due to their similarity to the notch filters. Transfer functions T_FN and T_FB for the notch and bandpass filters are also calculated. The notch filters were used to achieve 60 dB carrier suppression with minimal sideband attenuation, while high-order Butterworth filters were used to reject out-of-band noise. A small trade-off between dispersion- and noise-induced errors was observed by adjusting filter bandwidth.

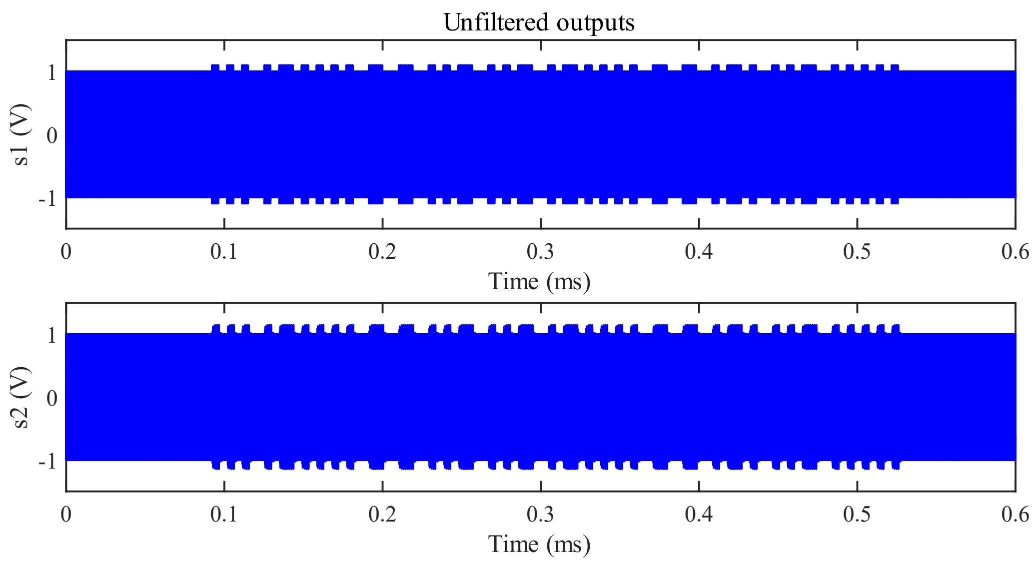

Figure 4.6. Simulated noiseless unfiltered tag load modulation signals $s1$ and $s2$, given $A_\mathrm{m} = 0.1, \kappa = -0.6, Q = 200$, and $N = 11$, with the tag positioned at $P = 1$.

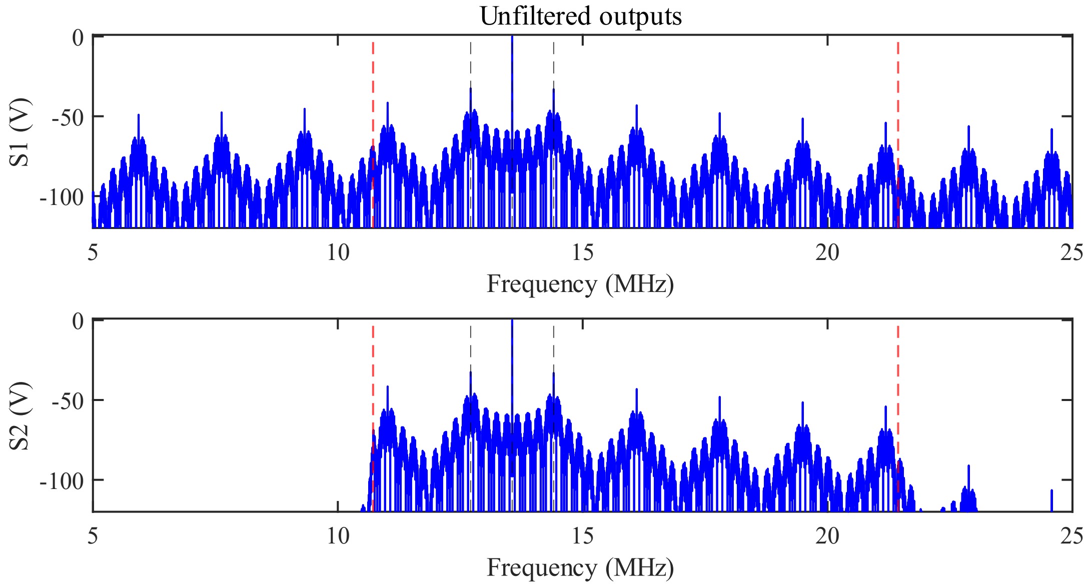

Figure 4.7. Simulated noiseless unfiltered tag modulation signals $S1$ and $S2$ for $A_{\mathrm{m}} = 0.1, \kappa = -0.6$, $Q = 200$, and $N = 11$, with the tag positioned at $P = 1$. Dashed red lines indicate the antenna frequency passband.

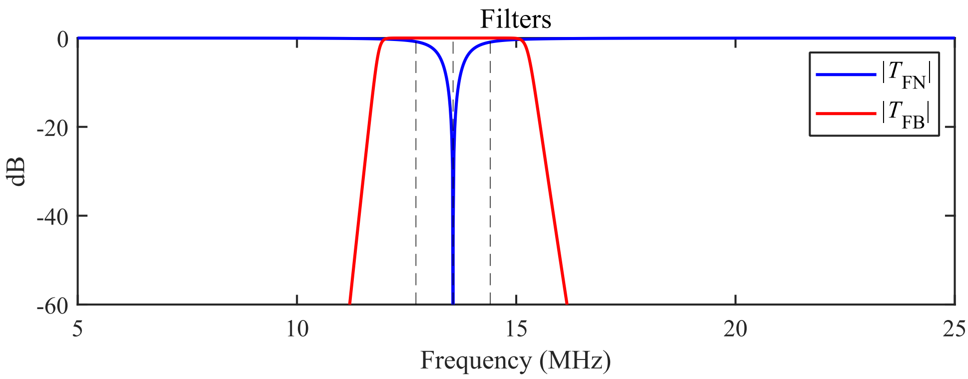

Figure 4.8. Digital notch and bandpass filter transfer functions T_{FN} and T_{FB} for carrier and out-of-band noise suppression.

A baseband Manchester-coded digital message signal s_{T} comprising the tag UID is first constructed and used to modulate a square-wave subcarrier waveform with amplitude A_{m} to generate the tag message signal. The resultant signal is then used to AM-modulate a carrier waveform with a unit amplitude, sampled at $f_{\mathrm{samp}} = 96 f_{\mathrm{c}}$. The resultant vector s_0 is used to represent the load-modulation signal.

$$s_0(t) = (1 + A_{\mathrm{m}} s_{\mathrm{T}} \operatorname{sgn}(\cos(2\pi f_{\mathrm{s}} t)\,) \cos(2\pi f_{\mathrm{c}} t) \tag{4.6}$$

Propagation and filtering are simulated by using the discrete Fourier transform to obtain the frequency domain equivalent S_0, applying the transfer functions of the MI waveguide (T_{R} or T_{T}) to obtain the transformed frequency-domain signals $S1$ and $S2$, and using the inverse Fourier transform to generate time domain signals $s1$ and $s2$, as shown in Figures 4.7 and 4.6, respectively.

The simulated traces were obtained using $A_{\mathrm{m}} = 0.1$, $\kappa = -0.6$, $Q = 200$, with the tag positioned at the left end of an 11-element antenna. As in conventional systems, weak tag response signals are superimposed on the dominant carrier signal. The effects of antenna distortion are evident from the characteristics of $S2$ extracted from the right end, which has become filtered by the antenna passband, unlike $S1$.

Digital filters T_{FN} and T_{FB} (Figure 4.8), are then applied in similar fashion to obtain the filtered time-domain signals $s1_{\mathrm{f}}$ and $s2_{\mathrm{f}}$ (Figure 4.9), and the filtered frequency-domain signals $S1_{\mathrm{f}}$ and

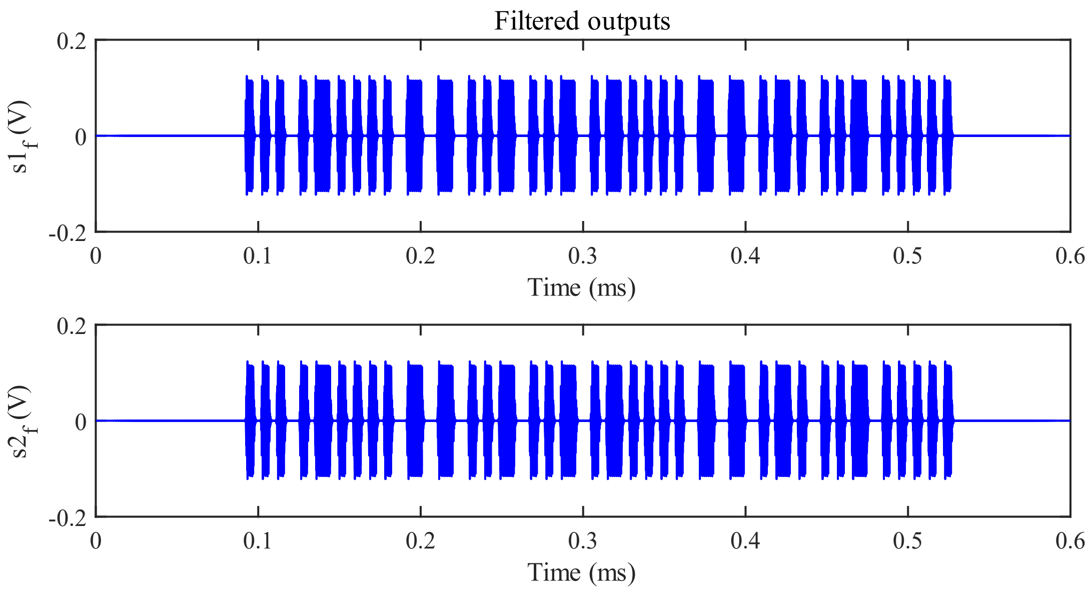

Figure 4.9. Simulated noiseless filtered tag load modulation signals $s1_{\mathrm{f}}$ and $s2_{\mathrm{f}}$, given $A_{\mathrm{m}} = 0.1, \kappa = -0.6, Q = 200$, and $N = 11$, with the tag positioned at $P = 1$.

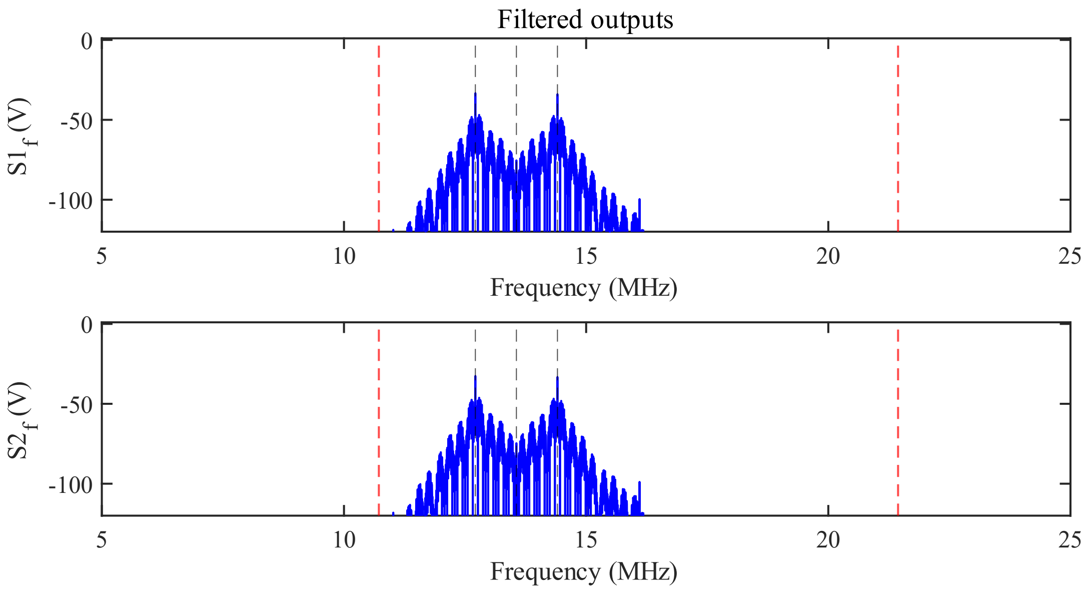

Figure 4.10. Simulated noiseless filtered tag load modulation signals $S1_{\mathrm{f}}$ and $S2_{\mathrm{f}}$, given $A_{\mathrm{m}} = 0.1$, $\kappa = -0.6, Q = 200$, and $N = 11$, with the tag positioned at $P = 1$.

$S2_{\mathrm{f}}$ (Figure 4.10). The effect of the filters is to eliminate the carrier and suppress the tag response harmonics introduced by the square-wave subcarrier, which is employed by real tags. The outputs must now be down-converted for further processing.

Baseband envelopes are recovered by rectification and convolution with a rectangular window for low-pass filtering, and the down-converted signals $s1_{\mathrm{D}}$ and $s2_{\mathrm{D}}$ are obtained, both clearly representative of the binary Manchester-coded tag UID (Figure 4.11). The standard data

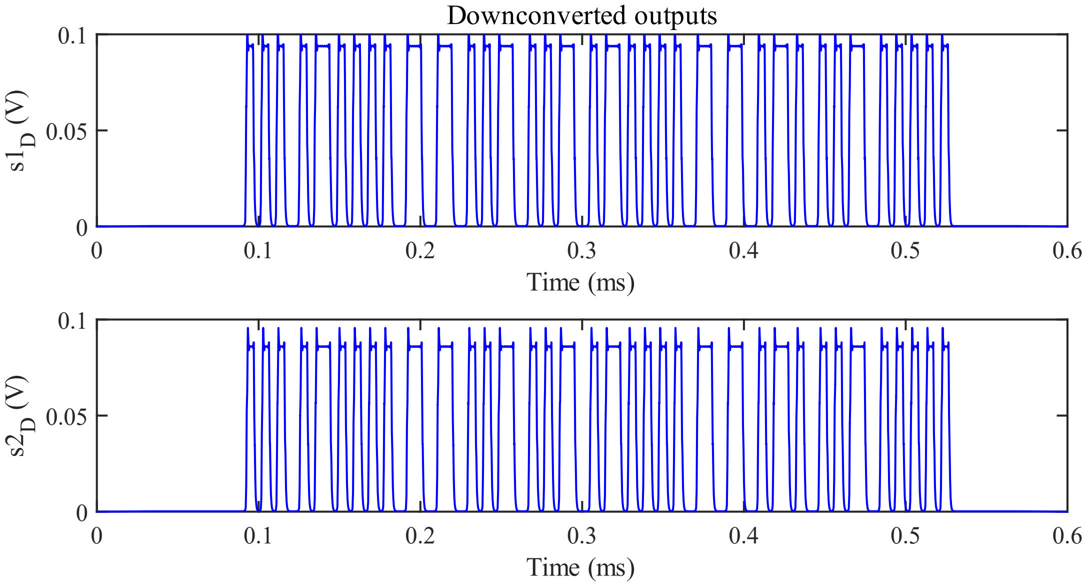

Figure 4.11. Simulated noiseless down-converted load modulation signals $s1_{\mathrm{D}}$ and $s2_{\mathrm{D}}$, given $A_{\mathrm{m}} = 0.1, \kappa = -0.6, Q = 200$, and $N = 11$, with the tag positioned at $P = 1$.

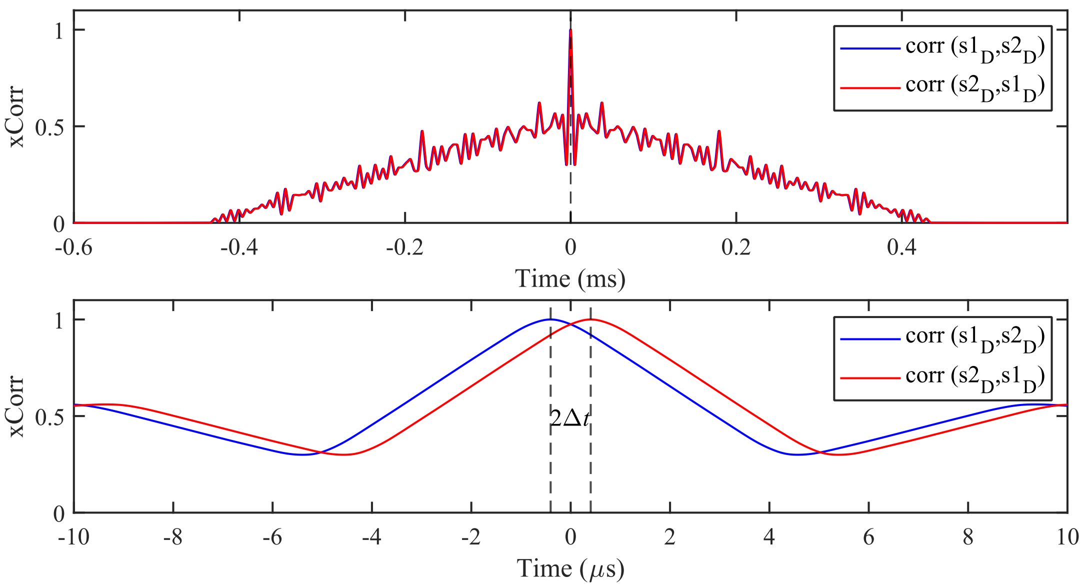

Figure 4.12. Simulated noiseless cross-correlation plots over long (upper diagram) and short (lower diagram) timescales for UID = ‘0xF38AE495’, given $A_{\mathrm{m}} = 0.1, \kappa = -0.6, Q = 200$, and $N = 11$, with the tag positioned at $P = 1$.

frames are recovered by correlation with the backward-link bit code symbols, and UIDs are extracted after checking parity bits and the BCC. The signals $s_{1\mathrm{D}}$ and $s_{2\mathrm{D}}$ are cross-correlated, and Δt is found from the difference in peak times obtained from pair-wise cross-correlation as shown in Figure 4.12. The tag position P_{est} is then estimated from Δt using the group velocity at resonance v_{g0}. Figure 4.13 (a) shows the simulated variation of P_{est} with tag position P for a noiseless system. As expected, the variation is linear, and the slope of the line varies with the antenna coupling coefficient due to group velocity dispersion. Correct localisation is assumed if the position error $e = P_{\mathrm{est}} - P$ satisfies $|e| < 0.5$, meaning $P = \mathrm{round}(P_{\mathrm{est}})$, where 'round()' signifies rounding to the nearest integer.

The effects of dispersion are diminished by stronger coupling. For example, Figure 4.13 (b) shows the variation of e with P, for an 11- element antenna with variable κ. In each case, e varies linearly with P, and the slope is reduced towards zero by increasing $|\kappa|$. Simulations of longer guides with N up to 41 showed similar trends, and localisation with $|e| < 0.5$ was possible provided $|\kappa|$ was large enough. The localisation error is always highest at antenna extremes, due to maximum dissimilarity between the extracted tag responses. Similarly, the error is zero at the

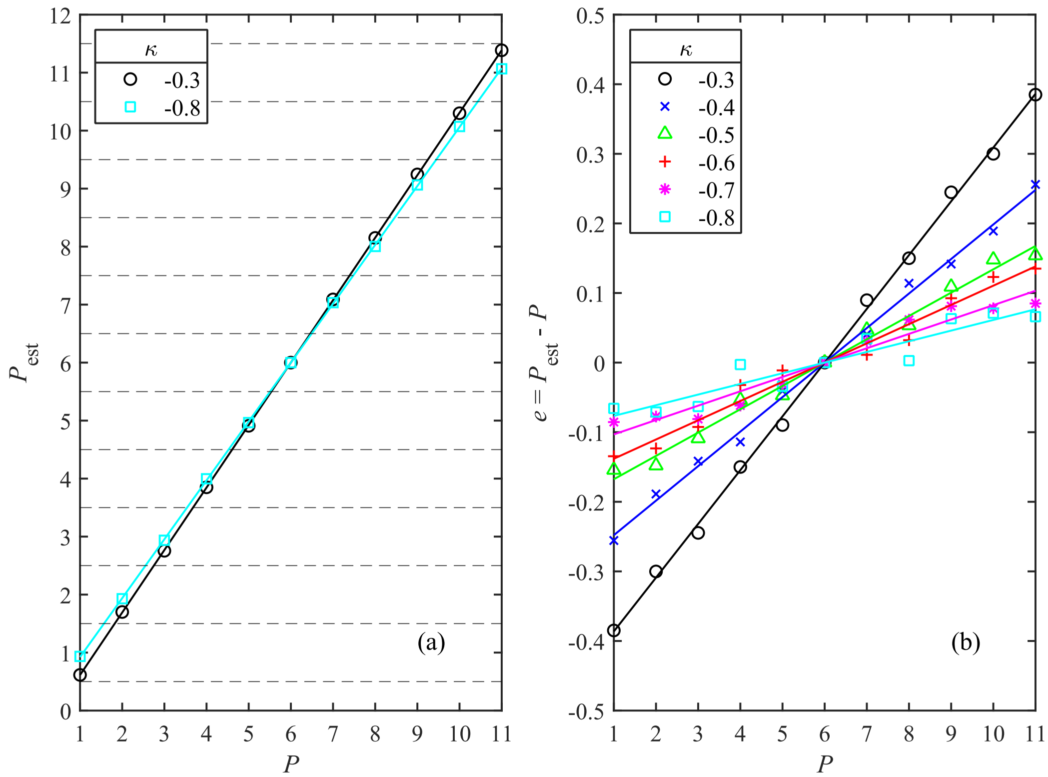

Figure 4.13. (a) Simulated variation of the tag position estimate P_{est} with tag position P for $\kappa = -0.3$ and $\kappa = -0.8$, with dashed lines indicating P_{est} thresholds; (b) simulated variation of position estimation error e with tag position P for a range of κ values as indicated in the legend. Both subfigures assume no noise and $N = 11$.

midpoint element since the signals are identical in the absence of noise. If the tag is laterally offset, especially at non-zero range, load modulation signals may be induced in more than one element. It is simple to modify the model to include signals from a neighbouring element. Their effect is to pull the estimated tag position toward the adjacecent loop.

Naturally, the presence of noise degrades localisation accuracy and limits the maximum antenna length. An initial investigation using the noise models in Figure 4.2 was performed, using data from multiple simulations with the tag positioned at $P = 1$ (worst-case) and a modest sampling rate of $f_{\mathrm{samp}} = 8f_{\mathrm{c}}$. In each case, white Gaussian noise sources with variance σ^2 was introduced (A) before the filters at each end, (B) at each antenna element with no correlation between sources, and (C) at each antenna element with complete correlation between sources. The signal-to-noise ratio within the antenna passband was then varied for noise models (A)-(C), and 100 samples of P_{est} were obtained for each SNR value. The samples were then fitted to Gaussian distributions, and the means and variances for each noise model were plotted in Figure 4.14 (a) and Figure 4.14 (b), respectively. The estimate means and variances were stable and accurate up to a threshold SNR ≈ 10dB for all noise models. As noise levels rose, the standard deviation σ_{A} for receiver noise (A) began to increase geometrically, while the mean μ_{A} remained approximately constant, dipping slightly around 0 dB only to return to original levels. Similar behaviour was

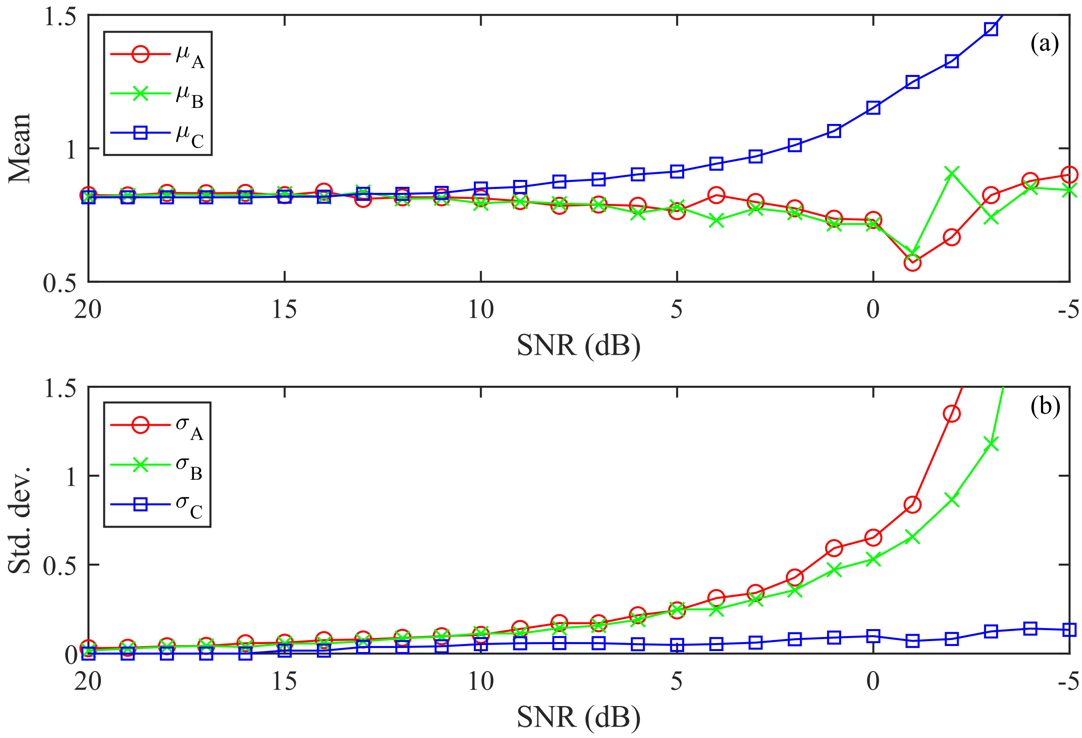

Figure 4.14. Variation of the (a) mean and (b) standard deviation of the tag position estimate P_{est} with SNR for noise models (A), (B), and (C), obtained by simulation for $\kappa = -0.6$, $P = 1$, using a sample size of 100 for each SNR value.

observed for model (B). Ambient correlated noise (C), however had the opposite effect, such that the mean μ_{C} rose for low SNR while the standard deviation σ_{C} remained constant. This behaviour is expected, as the correlated nature of the noise forces the mean position estimate towards the midpoint antenna element.

4.6 Experimental verification

We now present an experimental verification of TOF tag localisation using a demonstration magneto-inductive antenna and a custom NFC-A reader. Experiments were carried out using an 11-element MI antenna with an overall length just below 1.8 m, with antenna photographs shown in Figure 4.15. The number of elements was large enough to demonstrate operation, while the use of an odd number of resonators conveniently provided a midpoint element with zero time of flight difference. Each element was constructed from 1/8” outer diameter copper pipe, bent to shape and held in a planar arrangement using 3D-printed mounts fabricated using polylactic acid with a relative permittivity of approximately 2.5. The horizontal conductor separation was 15 cm, the vertical separation was 6 cm, while adjacent elements were separated by $\sim 1.3\,cm$. This arrangement minimised coupling by free-space fields, reducing the likelihood of a tag being detected simultaneously by two elements. Nearest neighbour magnetic coupling was achieved using transformers based on low-loss ferrite toroidal elements (5967000601, Fair-Rite Products Corp.), with opposite winding directions such that $M < 0$. Neighbour coupling was mechanically adjustable over the range $-0.3 \leq \kappa \leq -0.6$ by using a rapid prototyped mechanism to alter the relative position of the two coil windings, similarly to the coupling tuning mechanisms discussed in the previous Chapter.

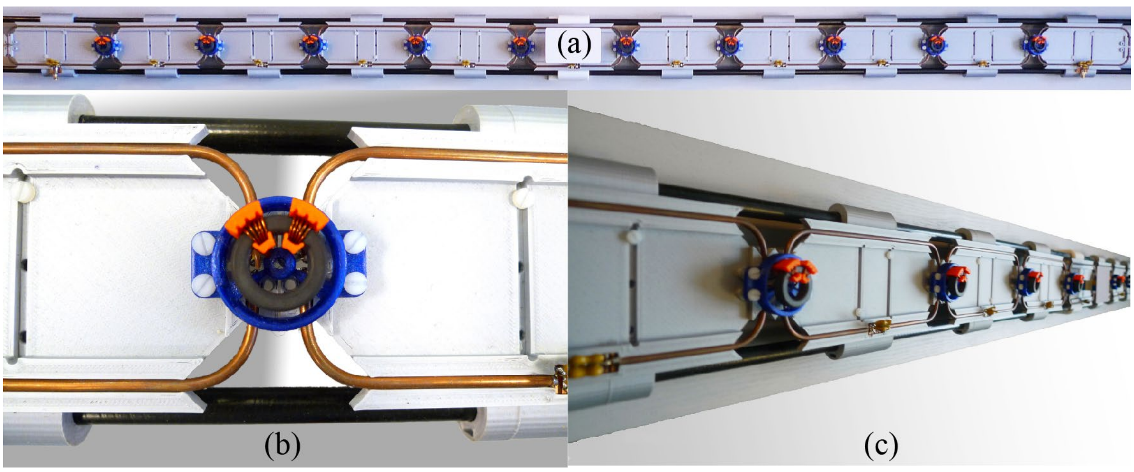

Figure 4.15. Photographs of the prototype MI antenna used for time-of-flight tag localisation. (a) Top view of the antenna with an ID-1 tag at midpoint; (b) tuneable coupling transformers; (c) perspective view of the antenna.

Tuning and matching were carried out using an electronic network analyser (Agilent E5061B). The total element self-inductance was $L = 2.45$ µH, the resonant frequency was set to $f_c = 13.56$ MHz with a quality factor of $Q = 180$ using mica capacitors with $C = 56$ pF. The coupling coefficient was adjusted to give a mid-band characteristic impedance of $Z_{0M} = 50\ \Omega$, which required $\kappa = -0.48$. To minimise unwanted reflections due to antenna imperfections, each resonator was equipped with a variable capacitor for individual tuning, while mutual inductance uniformity was ensured by pair-wise tuning of the coupling transformers between the elements. Figure 4.16 (a) compares the theoretical dispersion characteristic from (1.10) with the measured resonant frequencies of an un-loaded 9-element antenna, which lie at $ka = \nu\pi/10$, where $\nu = -9 \ldots -1$; excellent agreement is observed. Figure 4.16 (b) compares the theoretical frequency variation of the scattering parameters for an 11-element antenna obtained by numerical circuit simulation with the experimental measurements obtained using the electronic network analyser. The results show good matching and low-loss propagation between ~11 MHz and ~18 MHz with a minimum loss of 1.5 dB, which is approximately 0.5 dB below the theoretical estimate.

A transceiver was constructed with the functionality as depicted in Figure 4.1. Digital data frames compliant with NFC-A and ISO/IEC 14443 Type-A were generated using a personal computer and passed via unique serial bus (USB) to a microcontroller (Arduino Uno) acting as a

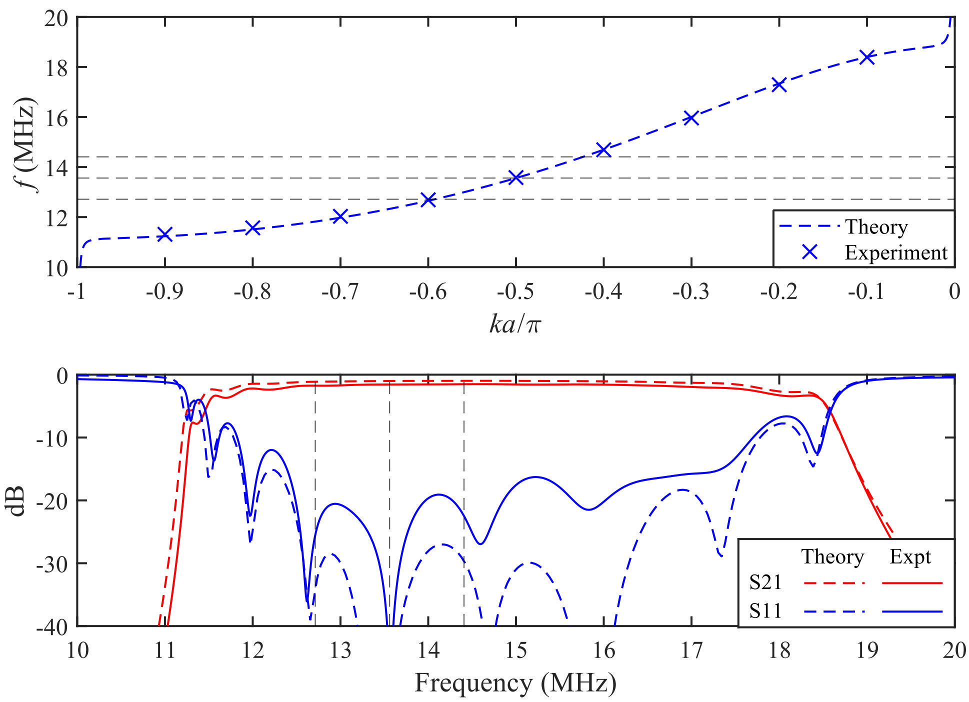

Figure 4.16. (a) Comparison of the theoretical dispersion characteristic (dashed blue) with the experimental measurement (crosses) of antenna resonances; (b) comparison of the theoretical antenna scattering parameters with experimental scattering parameters. Dashed black lines indicate the carrier and subcarrier frequencies.

function generator. The output from the microcontroller was used to modulate a carrier at 13.56 MHz derived from a signal generator (TTi TGR6000) via an RF analogue switch (Minicircuits ZFSWHA-1-20+) to generate 100% ASK at 106 kb/s. A quartz crystal filter was placed at the output of the carrier generator for denoising. The HF carrier was amplified to a maximum power of 1 W using an amplifier (Minicircuits ZHL-32A+), and a low-pass filter with a cutoff at 20 MHz was used to suppress any harmonics in the amplifier response. Signals were transferred into and out of the MI waveguide using matched lumped element filter couplers at each end. Detection of OOK tag responses was done using a digital storage oscilloscope (Keysight InfiniiVision DSOX3024T) with a sampling rate of 1.25 GSa/sec, which acted as a signal acquisition buffer. Two oscilloscope channels were used as receivers RX1 and RX2. The acquired tag response samples were passed back to the PC via USB for further processing in Matlab®. Digital filters from Figure 4.8 were used to suppress carrier and noise, and a Tukey window was used to remove artifacts at signal edges. Unique identifiers were recovered by rectification, filtering, and correlation with Manchester transition templates (like in simulation), while the tag position was estimated by pair-wise cross-correlation. A photograph of the complete tag localisation system is provided in Figure 4.17.

Figure 4.18 shows the reader-tag data exchange during the UID acquisition handshake. The reader first generated an unmodulated HF field for 5 ms to ensure the tag transitioned from the

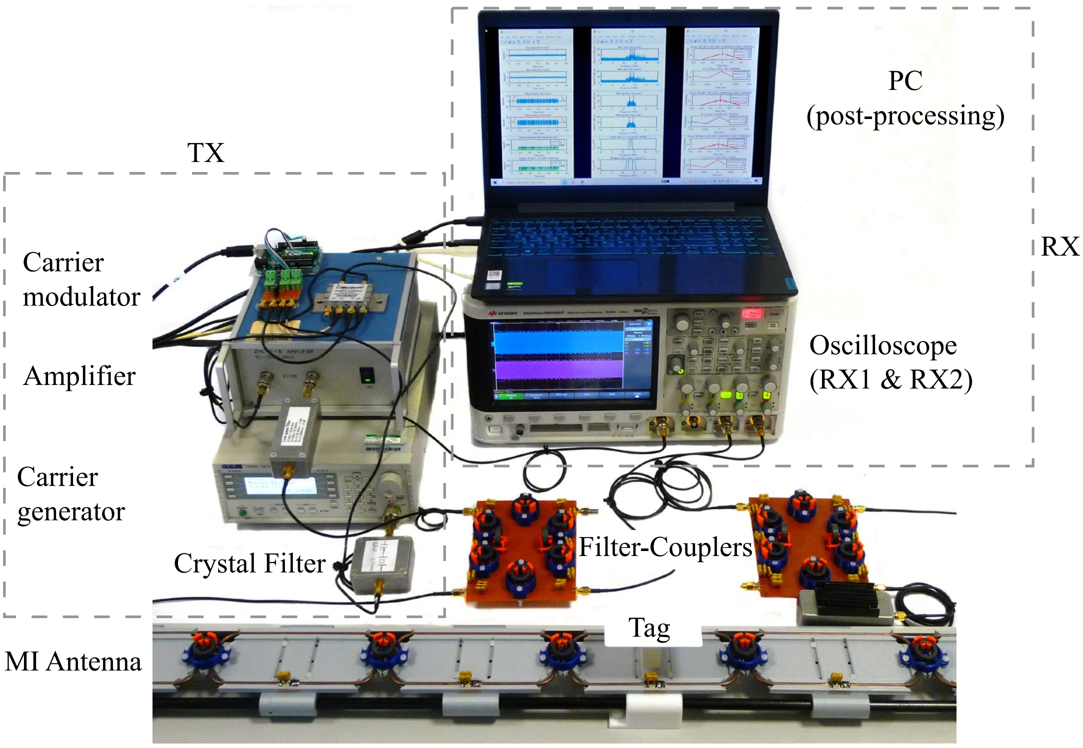

Figure 4.17. NFC tag localisation system in operation with post-processed results displayed on PC screen and raw tag UID traces displayed on the oscilloscope screen.

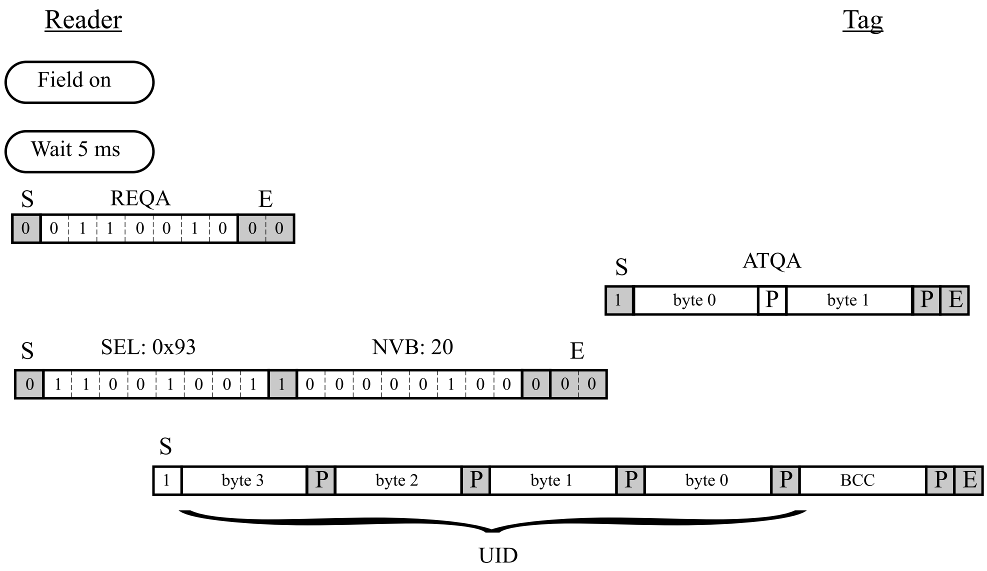

Figure 4.18. Reader-tag 'handshake' compliant with NFC-A used to acquire a single-size tag UID.

'off' state into the 'idle' state. The reader then issued an 'REQA' query using a short data frame, with the tag responding with 'ATQA' and transitioning into the 'ready' state. Afterwards, the reader initiated the anticollision procedure with $\mathrm{CL}n = 1$ and NVB = 0x20, requesting the tag to present its complete unique identifier. The reader field was then disabled after UID acquisition.

Experiments were carried out using an ISO/IEC 14443 Type-A compliant Class-1 tag in an ID-1 smartcard package measuring 85 mm x 54 mm and a tag UID of 0xF38AE495. The tag had a resonant frequency of 14.5 MHz and an unloaded Q-factor of ~ 30 (both measured with the tag in the 'off' state). The tag was placed at the centre of each antenna element, with the tag footprint confined by the resonator conductors. The antenna-tag separation could be regulated using dielectric spacers. Figure 4.19 shows the acquired tag responses $S1$ and $S2$ in the frequency domain for $P = 1$ and 0 cm antenna-tag separation, as measured at RX1 and RX2 prior to digital filtering. A remarkable similarity with the simulated responses from Figure 4.7 is observed, such as the attenuation of out-of-band frequency components in $S2$ by the MI antenna passband as well as the presence of harmonics in the tag response. The spectra also highlight the weak nature of the tag response signals, with subcarrier powers approximately 30 dB below the carrier power, even after ~ 20 dB of carrier attenuation administered by the filter-couplers. Despite this, tag responses were recovered easily. Figure 4.20 shows the recovered response envelopes $s1_{\mathrm{D}}$ and $s2_{\mathrm{D}}$. The latter had a slightly lower amplitude, due to the larger numbers of elements traversed. For both signals, the parity bits, the BCC, and the tag UID were correct.

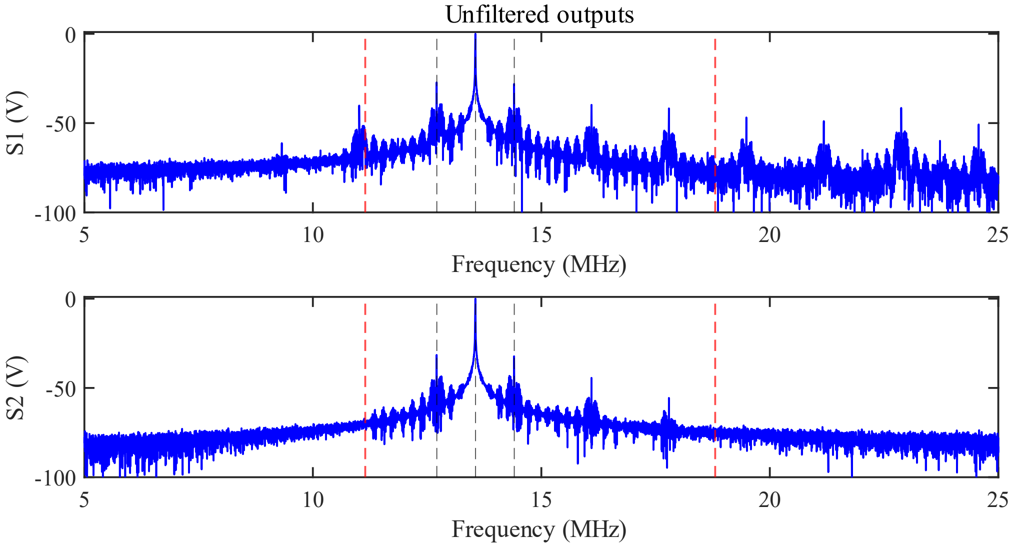

Figure 4.19. Frequency spectrum of the tag response signals as measured by the oscilloscope at RX1 and RX2 for $P = 1$ and UID = 0xF38AE495. Dashed red lines indicate the experimental antenna passbands. Dashed black lines indicate the carrier and subcarrier frequencies.

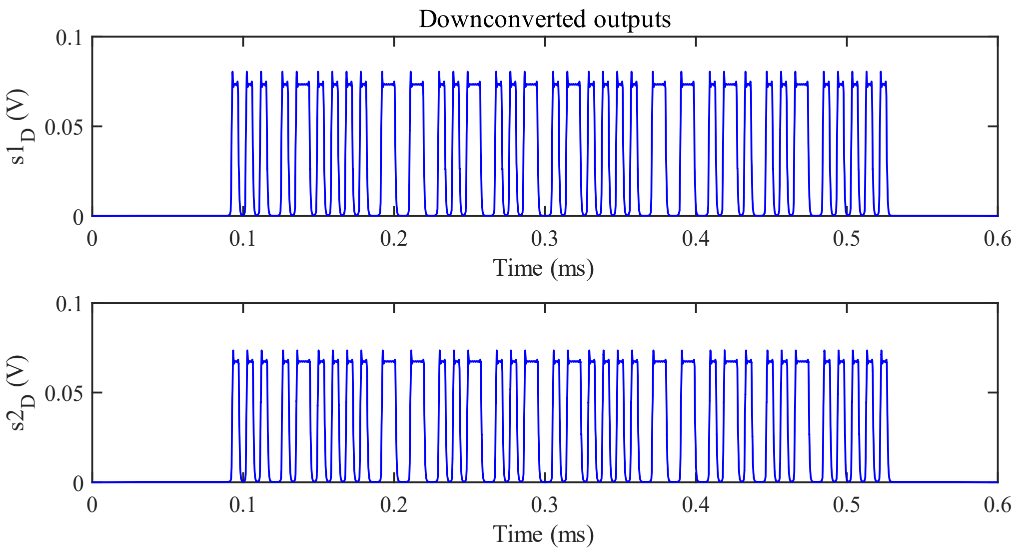

Figure 4.20. Experimental measurement of down-converted signals obtained using the 11-element antenna using a tag with a UID of 0xF38FEA95 at $P = 1$.

The experimental cross-correlations plotted on long and short timescales in Figure 4.21 demonstrate accurate localisation with a small position error (here, $e \approx -0.13$). Rounding of the correlation peaks is insignificant, and substantial agreement with Figure 4.12 validates both the theoretical model and the general approach of timing by cross-correlation of UID responses.

As expected, the time delay between the two signals increased linearly with tag displacement from the array centre, with a peak delay of ~ 1 μs. Figure 4.22 shows the experimental variation of the positioning error e with P, obtained at zero antenna-tag separation over a range of carrier power between 0.05 W and 1 W. In each case, the tag UID was recovered correctly, and the tag

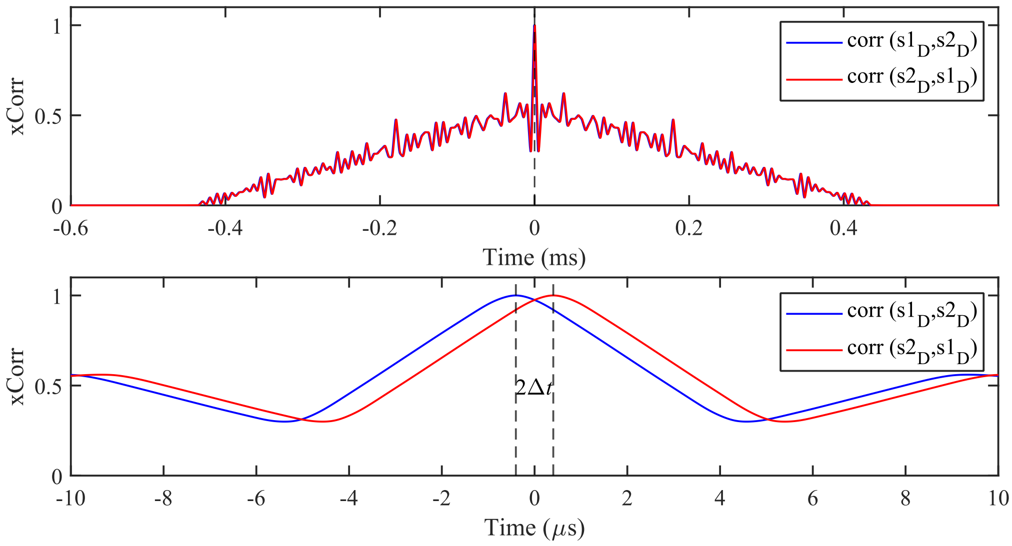

Figure 4.21 Experimental cross-correlation signals over long (upper diagram) and short (lower) timescales obtained using the 11-element antenna, for UID = 0xF38FEA95 and $P = 1$.

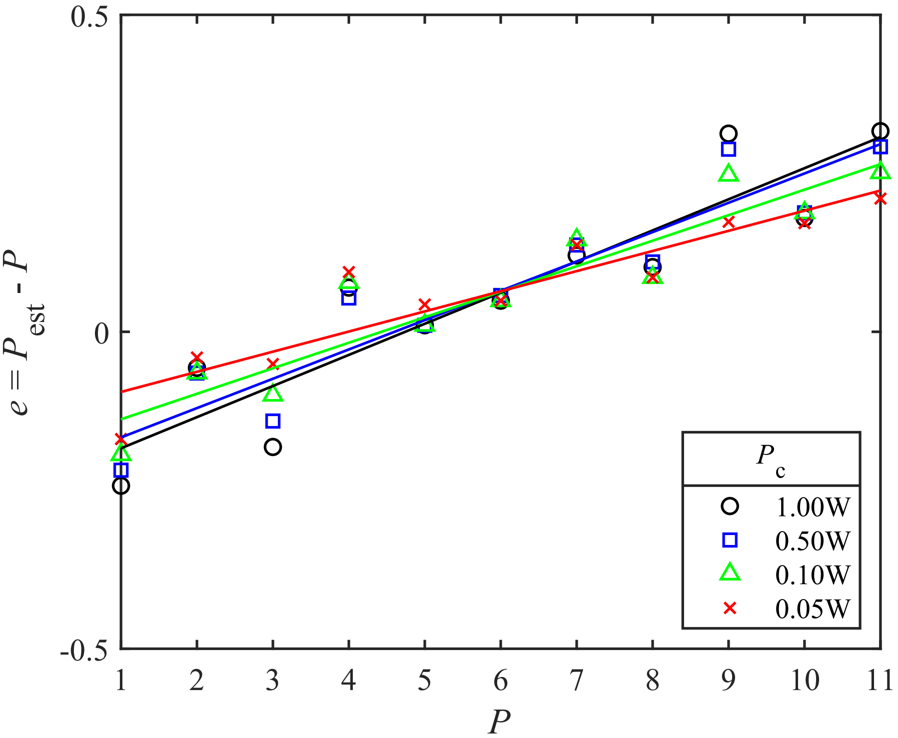

Figure 4.22. Experimental variation of localisation error e with position P obtained using the 11-element MI waveguide at different carrier powers as indicated in the legend. Solid lines are lines of best ft.

position was correctly estimated with $|e| < 0.5$. At higher powers, the slope of the error variation is in good agreement with results in Figure 4.13 (b) for $\kappa = -0.5$; however, the slope reduced slightly as the RF power and SNR reduced.

Figure 4.23 shows Gaussian probability density functions fitted to 100 experimental samples of tag position estimates for varying antenna-tag separations (0cm to 3cm), with the tag at $P = 1$

and using 1 W of carrier power. As the range increases and the SNR deteriorates, the distribution broadens and shifts towards the array centre, implying that the most likely noise source is correlated ambient noise (C) from Figure 4.2. Tags could be correctly located at antenna-tag separations of up to 5 cm, but errors fell outside acceptable limits at 6 cm, the conductor separation, when the UID was no longer recovered correctly. This occurred due to insufficiently high external field strength to power the tag. Carrier powers in excess of 1 W would be required to extend operating range. The results were similar for other tags, including the best and worst unique identifier cases with UID = 0x010D354A and UID = 0xFFFFFFFF identified in Section 4.4. Localisation of small fob-type tags was possible, but only at zero antenna-tag separation using 1 W carrier power. Similar results were obtained by cross-correlation of reconstructed UID templates. Although correlation peaks were sharper, no convincing improvement in the mean or standard distribution of the estimated position were observed.

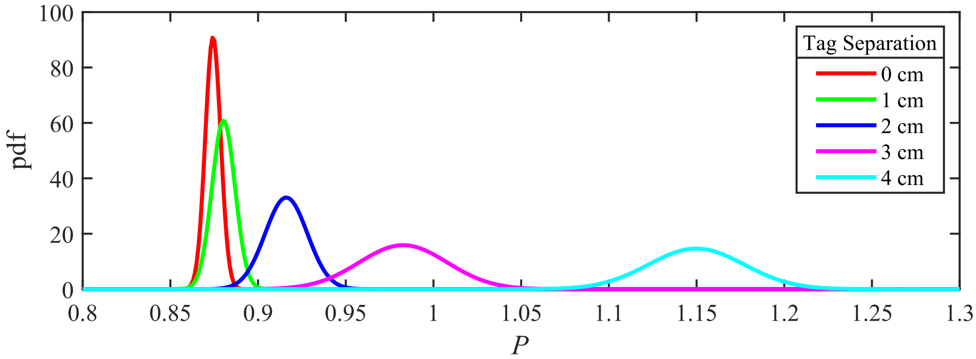

Figure 4.23. Normal probability density functions fitted to 100 experimental position estimate samples for each value of antenna-tag separation, with the tag placed at $P = 1$ using 1 W carrier power.

4.7 Conclusions

A new method of one-dimensional NFC tag localisation based on time-of-flight differences in tag response in a slow wave magneto-inductive antenna has been proposed and demonstrated. The autocorrelations of ISO/IEC 14443 Type-A unique identifier responses have been investigated. A correlation detection scheme has been proposed, and simulations using a transfer function model with practical parameters have shown that flight times may be estimated by correlation of responses from either end of the antenna, provided the magnetic coupling coefficient is sufficiently high. TOF difference may be converted into distance-of-flight difference and thence to a tag position estimate using the MI waveguide group velocity, allowing localisation to be combined with identification despite uncertainty in either the exact nature or the timing of the tag signal. Theoretical predictions have been confirmed experimentally using an 11-element model waveguide with small loop dimensions, and tag positions have been estimated accurately at transverse ranges up to the tag reading limit using RF carrier power levels below 1W.

While highly effective at tag localisation, the current system has several limitations: the travelling wave antenna is rigid and physically small, the maximum number of resonators is bounded by high group velocity dispersion, and both the coupling coefficients and element resonant frequencies must be carefully tuned for accurate performance; all of which make the proposed solution unsuitable for real world applications. Marginal improvements in practicality may be achieved by scaling the resonator dimensions. Flexible printed MI antennas could also be developed to reduce weight and bulk, improve consistency of element resonant frequencies and coupling, and allow more general layouts. Meander waveguide layouts could be implemented to enable quasi-2D tracking, while arrays might enable full 2D tracking based on the propagation of cylindrical waves. Significant improvements, however, require fundamental changes to the antenna topology. In the following Chapter, we develop and implement novel distributed and flexible slow wave antenna topologies, which address all the aforementioned limitations.

Chapter 5:
Slow Wave Antennas for Near Field Communication and Localisation

To improve the practicality, robustness, and performance of the TOF tag localisation system from the previous Chapter, we now develop a novel class of flexible waveguide antennas with distributed read nodes. The antennas comprise sections of coaxial transmission lines which are periodically loaded with field-generating inductive networks. Several topologies were compared to each other theoretically and the best-performing candidate was selected to fabricate antennas between 5 and 48.5 metres long, each containing 15 read nodes. Waveguiding properties of the antennas were measured and agreement with theory was demonstrated. Afterwards, each antenna was integrated with a custom NFC reader and shown to be capable of near field communication with and localisation of commercial off-the-shelf transponders compliant with ISO 14443 Type-A protocol. The transverse detection range was 10 cm using 1 W reader carrier power. Both one-dimensional and quasi two-dimensional configurations were tested. The proposed antennas are flexible, scalable, have low loss, and can be used for near field communication, identification, and tracking of distributed and mobile tags.

5.1 Overview

In the previous Chapter, we introduced an alternative approach to one-dimensional NFC tag localisation, which exploited the slow wave properties of a magneto-inductive travelling-wave antenna. A signal generated by a tag propagated in two opposite directions along the antenna with low group velocity. Receivers placed at both antenna ends detected the signals with a measurable delay, and the transponder position along the antenna was estimated from the time-of-flight difference. While the localisation method was shown to be highly effective, the practicality of the system was limited by magneto-inductive antenna properties and characteristics. Unfortunately, such limitations are inherent to all MI waveguides.

Nearest-neighbour coupling coefficients must be kept high to minimise propagation loss and group velocity dispersion, meaning one must resort to either quasi-axial air-coupled arrangements, or planar MI waveguides with ferrite transformers. The former requires a higher number of resonators per unit length due to the element overlap, which makes non-nearest neighbour coupling an issue and increases losses per unit length. The latter option minimises the unwanted coupling, but the resultant antennas are rigid and bulky. Furthermore, both implementations incur substantial loss per unit length and require careful tuning of element resonances and coupling coefficients to ensure antenna uniformity. Finally, it may be desirable to distribute the capture volume in physical space, as opposed to the inherently continuous fields of MI waveguides.

Fortunately, other waveguide topologies are also capable of supporting slow waves. Well-known examples are left- and right-handed waveguides that contain periodic lumped-element sections [241], [242] or electrically small resonators [243]. Therefore, waveguides that both support slow waves at HF and comprise field-generating inductors that can couple to NFC transponders have potential as antennas. The aim of this Chapter is thus to explore candidate waveguide antennas and experimentally demonstrate their use in NFC communication and TOF localisation. Preference is given to topologies which are flexible, modular, easily matched to real systems, and have favourable group velocity dispersion and propagation loss characteristics.

5.2 Design of loaded transmission lines

Here, we provide a theoretical analysis of waveguide antennas formed by sections of transmission lines (such as coaxial cables) loaded periodically with lumped-element networks. The networks must contain inductors that generate magnetic near fields and can couple to NFC devices placed in their vicinity. We will refer to these networks as sensors and to the entire waveguides as loaded transmission lines (LTLs). Below, we derive the characteristic equations of LTLs and discuss how their properties can be optimised for near field transponder localisation.

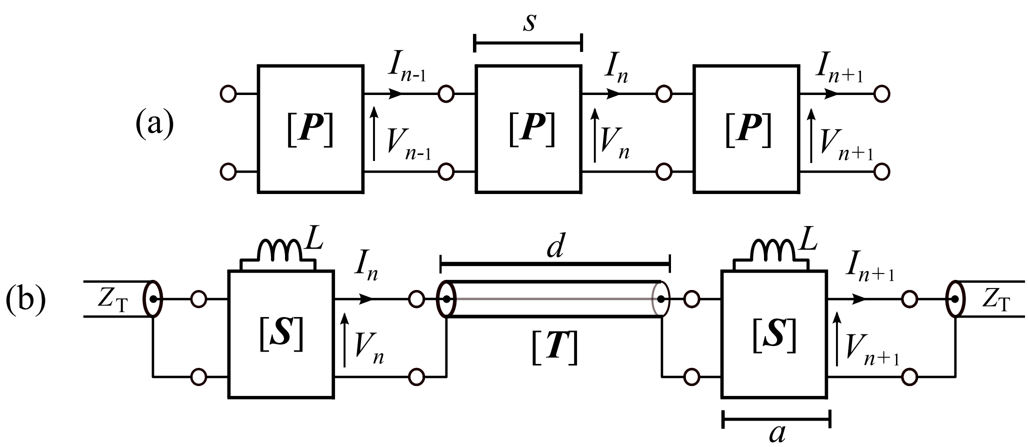

Figure 5.1. Schematic presentation of (a) classical periodic cascade of two-port networks, each described by a transmission matrix $\boldsymbol{P}$ and (b) loaded transmission line (LTL) formed by a periodic cascade of coaxial cable sections and generic two-port networks with transmission matrices $\boldsymbol{T}$ and $\boldsymbol{S}$, respectively.

5.2.1 *Two-port cascades*

First, we briefly discuss some known properties of the periodic two-port network cascades shown in Figure 5.1 (a) [160]. All such networks can be modelled using a two-by-two transmission matrix $\boldsymbol{P} = [A, B; C, D]$. A current I_n at an angular frequency ω flows into the nth network that has a voltage V_n across its left-side terminals. The voltages and currents on either side of the two-port are related by

$$\begin{bmatrix} V_n \\ I_n \end{bmatrix} = \begin{bmatrix} A & B \\ C & D \end{bmatrix} \begin{bmatrix} V_{n+1} \\ I_{n+1} \end{bmatrix}. \tag{5.1}$$

This periodic structure can support waves, with voltages and currents satisfying relationships $V_{n+1} = V_n e^{-jks}$ and $I_{n+1} = I_n e^{-jks}$, where k is the propagation constant, and s is the length of the network. Nontrivial solutions of (5.1) exist when e^{jks} is an eigenvalue of $\boldsymbol{P}$.

$$e^{j2ks} - (A + D)e^{jks} + AD - BC = 0 \tag{5.2}$$

Equation (5.2) is the general dispersion equation for the two-port cascade. If $\boldsymbol{P}$ is reciprocal, then $\det \boldsymbol{P} = 1$, and (5.2) can be simplified to

$$\cos(ks) = \frac{A + D}{2} \tag{5.3}$$

The propagation constant k is generally complex and frequency dependent. However, if $\boldsymbol{P}$ is lossless, A and D are purely real, while B and C are purely imaginary. Propagation may only occur in passbands for which $|\cos(ks)\,| < 1$, so that $\mathrm{Im}(k) = 0$. Propagation is forbidden in stopbands, where k is purely imaginary. If a network contains lossy components, attenuated out-of-band propagation is allowed. If the network is also symmetric, then $A = D$, and (5.3) simplifies to $\cos(ks) = A$.

The voltages and currents at any plane of the cascade are related by a characteristic impedance defined as

$$Z_0 = \frac{V_n}{I_n} = \frac{B}{e^{jks} - A} \tag{5.4}$$

The values of Z_0 are different for forward- and backward-wave propagation. In lossless symmetrical networks, the characteristic impedance is real in the passband and imaginary in the stopbands. In the general case, Z_0 is complex at all frequencies.

5.2.2 *Loaded transmission lines*

We now consider the LTL shown schematically in Figure 5.1 (b). A unit cell is formed by a section of a coaxial cable of length d, followed by a reciprocal two-port network $\boldsymbol{S} = [A_\mathrm{S}, B_\mathrm{S}; C_\mathrm{S}, D_\mathrm{S}]$ of a length a. Together they correspond to the earlier network $\boldsymbol{P}$. Now, the length of each section is $s = d + a$.

The cable can be described as a lossy transmission line with an inductance per unit length L_T and capacitance per unit length C_T, and characteristic impedance Z_T. The cable transmission matrix $\boldsymbol{T}$ is of the form

$$\boldsymbol{T} = \begin{bmatrix} \cos(\gamma d) & jZ_\mathrm{T}\sin(\gamma d) \\ \left(\frac{j}{Z_\mathrm{T}}\right)\sin(\gamma d) & \cos(\gamma d) \end{bmatrix} \tag{5.5}$$

where γ is the cable's complex propagation constant $\gamma = \beta - j\alpha$, with $\beta \approx \omega\sqrt{L_\mathrm{T}C_\mathrm{T}}$ for low-loss cables.

The unit cell of the LTL waveguide can, for example, be described by an asymmetric transmission matrix $\boldsymbol{P} = \boldsymbol{TS}$. Alternatively, a symmetric cell can also be chosen, with $(d/2)$-long cables attached to each sensor port. By substituting the analytic expressions for the elements of $\boldsymbol{P}$ into (5.3), we obtain the LTL dispersion relation.

$$\cos(ks) = \frac{1}{2}\left\{(A_\mathrm{S} + D_\mathrm{S})\cos(\gamma d) + j\left(\frac{B_\mathrm{S}}{Z_\mathrm{T}} + Z_\mathrm{T}C_\mathrm{S}\right)\sin(\gamma d)\right\} \tag{5.6}$$

As before, (5.6) may be simplified if $\boldsymbol{S}$ is symmetric or reciprocal. The characteristic impedance of the LTL may also be obtained using (5.4).

$$Z_0 = \frac{B_\mathrm{S}\cos(\gamma d) + jZ_\mathrm{T}D_\mathrm{S}\sin(\gamma d)}{e^{jks} - [A_\mathrm{S}\cos(\gamma d) + jZ_\mathrm{T}C_\mathrm{S}\sin(\gamma d)]} \tag{5.7}$$

5.2.3 *Sensor network topologies*

Equations (5.6) and (5.7) model generic LTL waveguides, and candidate sensor networks $\boldsymbol{S}$ should now be identified that are suitable for near field communication, identification, and localisation. Requirements are set by communication protocols, and we will again use the ISO/IEC 14443 Type-A specification. If a waveguide antenna is used, the group velocity dispersion should

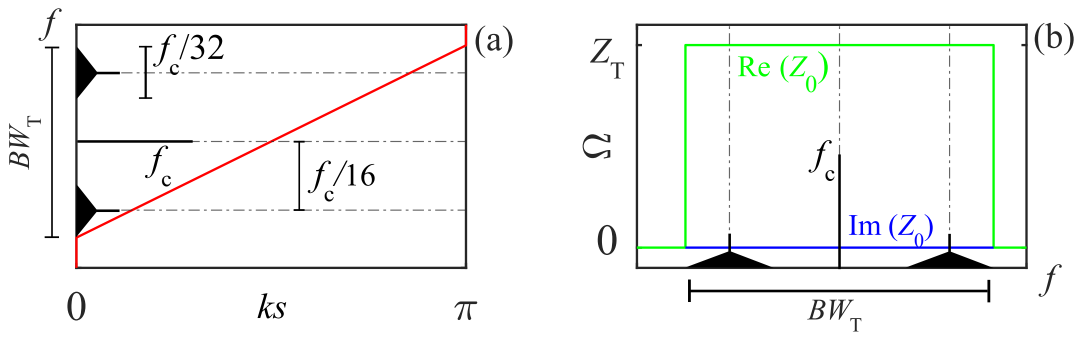

Figure 5.2. (a) Dispersion curve (red) and (b) characteristic impedance (green and blue) of an idealised LTL antenna for transponder tracking and communication. The passband covers the minimum backwards link bandwidth BW_T = 2.12 MHz of the ISO/IEC 14443 Type-A protocol to maximise SWF. The group velocity is constant and minimised. The characteristic impedance is real and constant across the passband.

be minimised over the protocol bandwidth to prevent signal distortion. On the other hand, the TOF localisation method relies on being able to detect the difference in arrival times of transponder signals. To maximise this difference, the slow wave factor of the waveguide should be maximised.

Figure 5.2 shows schematically idealised characteristics of a waveguide antenna optimised for both communication and transponder localisation. The dispersion curve [Figure 5.2 (a)] is linear (to eliminate dispersion), and propagation is band-limited (to minimise the group velocity). The passband is equal to BW_T = 2.12 MHz (the minimum backward-link bandwidth for NFC-A). The group velocity $v_g = (\partial\omega)/(\partial k')$ can be calculated from the idealised dispersion characteristic as $(2\pi \cdot s \cdot BW_T)/\pi = (5/16)f_c \cdot s = 4.24 \cdot 10^6 \cdot s$ m/s. The slow wave factor (SWF $= c/v_g$, where c is the free-space light velocity) is $16c/(5f_c \cdot s) = 70.8/s$, where the numerator is in metres. The characteristic impedance over the passband must be real and equal to Z_T, independently of the cable length, as shown in Figure 5.2 (b). Figure 5.2 shows the characteristics of a right-handed waveguide, but the arguments are equally applicable to a left-handed one.

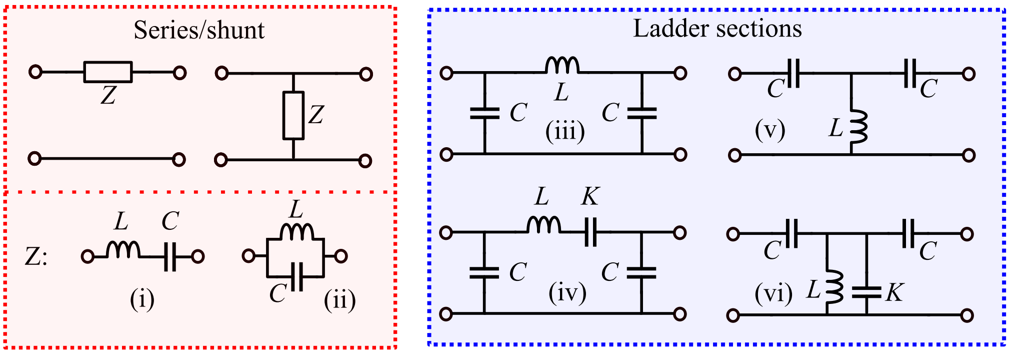

Figure 5.3. Sensor network candidates that include series/shunt impedances (i-)(ii), pi-sections (iii)-(iv), or t-sections (v)-(vi).

Such characteristics are unattainable in practice but can serve to assess practical sensor implementations. Possible candidates are shown in Figure 5.3, in the order of increasing complexity. The simplest LTL topologies comprise a shunt or a series impedance Z. The impedance itself can be either (i) a series or (ii) a parallel LC resonator. Topologies (iii) and (v) are, respectively, the standard lumped-element t- and pi-sections of a right- and a left-handed transmission line. Topologies (iv) and (vi) are constructed from (iii) and (v) by adding another capacitor K as indicated. Analytical calculations presented in this Section will assume lossless wave propagation; effects of loss will be considered in the following Sections.

For LTLs made of coaxial cables loaded with impedances Z in a series or a shunt configuration, we have $A_S = D_S = 1$. Cable sections of non-zero length are required for wave propagation. Equation (5.6) can be simplified as

$$\cos(ks) = \cos(\beta d) + \frac{1}{2} jr \sin(\beta d) \tag{5.8}$$

where $r = Z/Z_T$ for the series and $r = Z_T/Z$ for the shunt configurations.

Figure 5.4 (a) shows the real part of the propagation constant, and Figure 5.4 (b) shows the slow wave factor for (i) series and (ii) parallel LC resonators connected in series and shunt configurations respectively, with $C_T = 92$ pF/m, $L_T = 230$ nH/m, and $Z_T = 50\ \Omega$. In both cases, $L = 2$ µH, and the value of C is chosen to place the resonant frequency at 13.56 MHz. The cable length d is 4 m. Both cases exhibit a bandpass response, and the bandwidth depends on the cable length and the value of L.

For both configurations, increasing the cable length narrows the passband and shifts it down in frequency. The effect is more pronounced at higher frequencies. For the series configuration, a

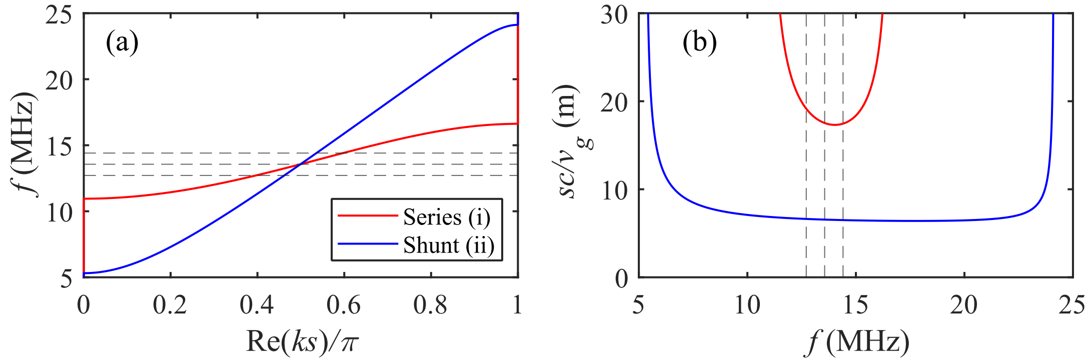

Figure 5.4. Dispersion relation and slow wave factor for LTL waveguide loaded with impedances (i) and (ii) in series and shunt configurations respectively for $L = 2$ µH, $C = 69.9$ pF, and $d = 4$ m. Dashed lines indicate the carrier and subcarrier frequencies.

larger value of L reduces the upper cut-off frequency but has little effect on the lower cut-off. Conversely, a larger value of L increases the upper cut-off frequency for the shunt configuration. The characteristic impedance is $Z_0 = Z_\mathrm{T}$ at f_c for both configurations. Series loading with (i) favours high inductance values, while shunt loading with (ii) requires impractically small L to achieve a similar SWF. Series (ii) and shunt (i) loads are not considered as they cannot satisfy $Z_0 = Z_\mathrm{T}$ within their passband at any frequency.

The LTL becomes a ladder network with cable interconnects when the sensors are formed by a pi- or a t-section shown in Figure 5.3 (iii)-(vi). Denoting k_0 as the propagation constant for a cascade of sensors with no cables, we can express the LTL propagation constant, k, in terms of k_0, and the cable propagation constant, β. For a symmetric pi- or t-section, $\cos(k_0 a) = A_\mathrm{S}$ according to (5.3), $C_\mathrm{S} = (A_\mathrm{S}^2 - 1)/B_\mathrm{S}$ due to reciprocity, and the characteristic impedance is thus given by $Z_\mathrm{S} = B_\mathrm{S}/[j\sin(k_0 a)]$ according to (5.4). Equation (5.6) may then be re-written as

$$\cos(ks) = \cos(k_0 a)\cos(\beta d) - \frac{1}{2}\sin(k_0 a)\left(\frac{Z_\mathrm{S}}{Z_\mathrm{T}} + \frac{Z_\mathrm{T}}{Z_\mathrm{S}}\right)\sin(\beta d) \tag{5.9}$$

Equation (5.9) shows that $k \approx k_0$ for short cables, but long cables affect the value of k owing to the second term on the right-hand side of (5.9). The impedances Z_S and Z_T can always be made equal at a single frequency, for example, f_c. Figure 5.5 (a) shows the dispersion curves and the slow wave factor for cable sections of length $d = 2$ m. The pi-section (iii) has a low-pass response while the t-section (v) has a high-pass one. The presence of cable sections lowers the cut-off frequencies for both topologies. It also converts the high-pass response of a CL section (v) into a

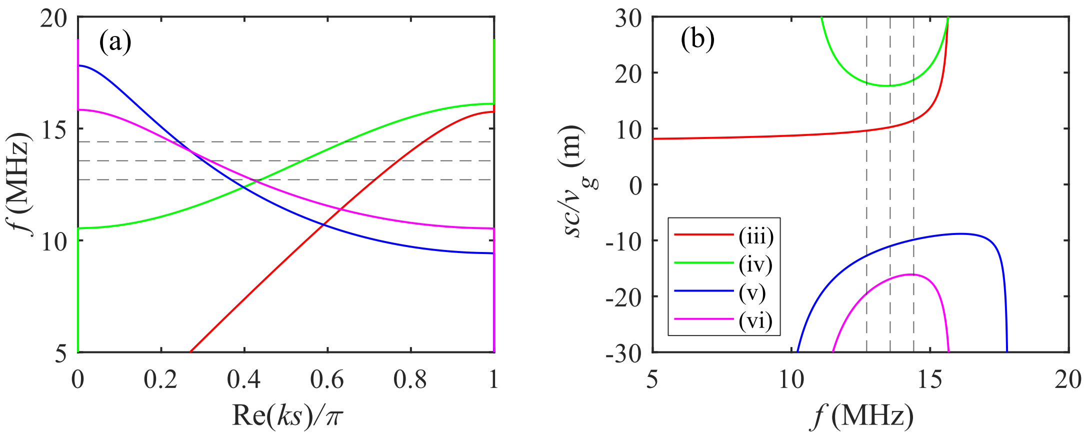

Figure 5.5. (a) Dispersion curves and (b) slow wave factors for LTL antennas with $d = 2$ m loaded with sections (iii)-(vi). For (iii) $L = 0.59$ μH, $C = 250$ pF; (iv) $L = 2$ μH, $C = 140$ pF, $K = 92.8$ pF; (v) $L = 0.59$ μH, $C = 200$ pF; (vi) $L = 0.37$ μH, $C = 190$ pF, $K = 143$ pF. Topology (iv) offers the best match to the ideal requirements of Figure 5.2 (a). Dashed lines indicate the carrier and subcarrier frequencies.

bandpass one. Topology (iii) offers good linearity if the cut-off frequency is sufficiently higher than the upper sideband frequency, but higher slow wave factors may be achievable with (v) owing to its bandpass characteristic. The maximum inductor values of both (iii) and (v) are restricted by the simultaneous need to keep the protocol sidebands within the LTL passband and to impedance match at f_c.

All sensor topologies considered approximate to a different degree the ideal characteristics shown in Figure 5.2. Series loading with (i) offers a bandpass response with good linearity and high SWF. However, this topology leaves little freedom for dispersion engineering since the value of C is restricted by matching requirements. The value of d can be restricted by the geometry of a specific application, and the value of L may be constrained by the minimum magnetic field strength requirements. Topologies (iv) and (vi) have an additional degree of freedom offered by the capacitance K. Both topologies (iv) and (vi) have a band-pass response; topology (vi) supports backward waves and topology (iv) forward waves. Topology (iv), however, favours higher values of L.

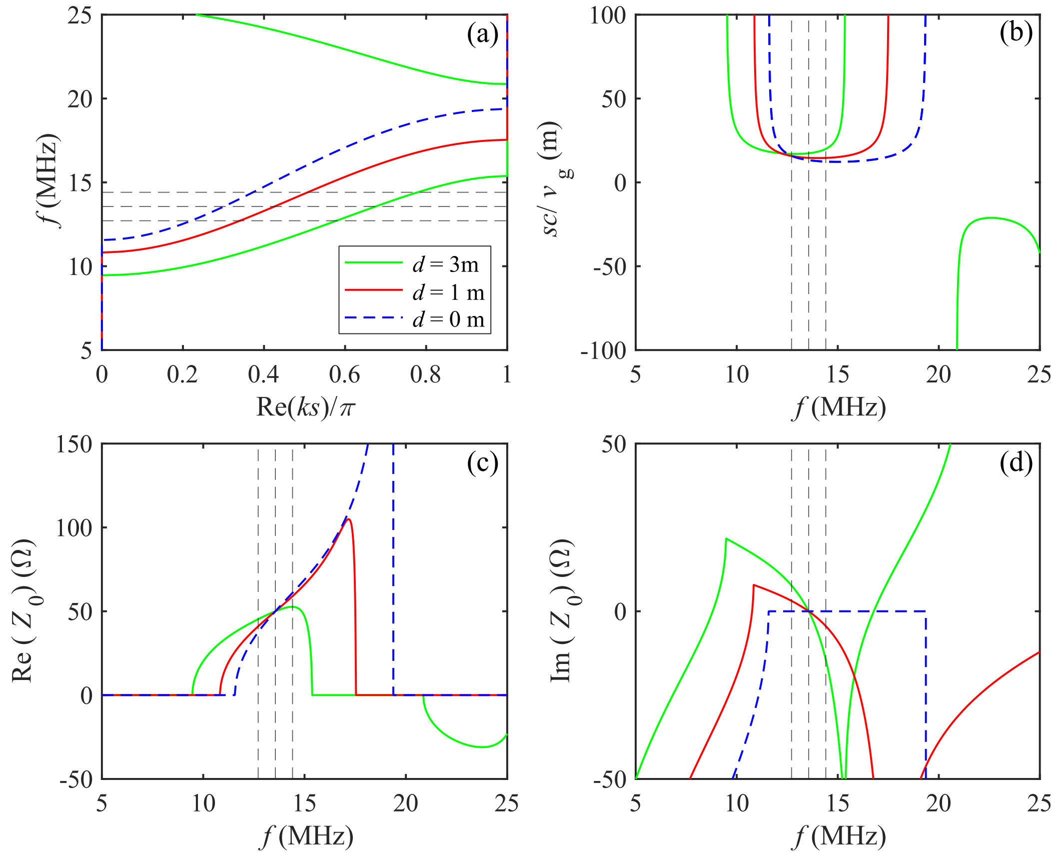

Figure 5.6. Parameters of the LTL antenna with resonant LC pi-section for cable lengths of $d = 0$ m, 1 m, and 3 m: (a) dispersion relation; (b) slow wave factor; (c) real part of the characteristic impedance; (d) imaginary part of the characteristic impedance. Usable cable lengths are limited by the need to accommodate the NFC-A tag bandwidth inside the passband. Dashed lines indicate the carrier and subcarrier frequencies.

5.2.4 *Resonant LC pi-section*

Of all the topologies considered, the pi-section (iv) in Figure 5.3 is the closest match for the communication and localisation requirements of Figure 5.2. It also offers considerable design freedom. Figure 5.6 shows calculated frequency variations of (a) dispersion, (b) slow wave factor, and (c)-(d) real and imaginary parts of the characteristic impedance for several values of cable length d. The LTL is perfectly matched to $Z_\mathrm{S} = Z_\mathrm{T} = 50\ \Omega$ at f_c independently of d. The matching condition at angular frequency f_c is given by

$$K = \frac{1 + \omega_\mathrm{c}^2 C^2 Z_\mathrm{T}^2}{\omega_\mathrm{c}^2 [C Z_\mathrm{T}^2(\omega_\mathrm{c}^2 LC - 2) + L]} \tag{5.10}$$

Capacitance K introduces an additional degree of freedom, allowing L and C to be set independently to tailor dispersion, while retaining matching at f_c if (5.10) is satisfied. The cable length affects the cut-off frequencies and the group velocity. Because longer cables reduce the original passband and shift it to lower frequencies, practical cable lengths are limited by the need to accommodate the NFC-A bandwidth within the first passband.

If $Z_\mathrm{T} = Z_\mathrm{S}$ at f_c, then $ks = \beta d + k_0 a$ according to (5.9), and expressions for the group velocity and slow wave factor can be derived as

$$v_\mathrm{g} = \frac{s}{d\sqrt{L_\mathrm{T} C_\mathrm{T} + \dfrac{2\omega LC}{\sin(k_0 a)}}} \tag{5.11}$$

$$\mathrm{SWF} = \frac{c}{s}\left(d\sqrt{L_\mathrm{T} C_\mathrm{T}} + \frac{2\omega LC}{\sin(k_0 a)}\right) \tag{5.12}$$

Equations (5.11) and (5.12) suggest that in a matched antenna the total slow wave effect is the sum of individual contributions from the cables and the sensors. The equations are exactly correct at f_c and offer good approximations in vicinity.

5.3 Experimental characterisation of LTLs

This section describes fabrication and experimental characterisation of LTL waveguides with resonant LC pi-section sensors. Three waveguides were made by cascading 15 identical sensors with coaxial cables of three different lengths, 0.3, 1.22 (4 ft), and 3 meters. Figure 5.7 shows a schematic of a section of an assembled LTL, together with the equipment (a PC, a custom NFC-A transmitter, an oscilloscope for signal reception, and filter-couplers for signal separation) used in communication and localisation experiments described in the following Sections.

Table 5.1 shows the component values, the equivalent circuit, and the cable parameters. The inductance L was formed by a three-turn square spiral with rounded corners, made from 1/8” soft copper pipe that was bent to shape and held in place using 3D-printed acrylonitrile butadiene styrene (ABS) mounts. The spiral had a width of W = 130 mm and a winding separation of 5 mm. A photograph of a sensor is provided in Figure 5.8. The quality factor was measured as ~ 250 using a vector network analyser (Keysight E5061B) connected to two small inductive probes that coupled to the assembled inductors. In these experiments, the inductors were loaded with capacitors, so that the resonant frequency was equal to f_c.

Table 5.1. Sensor and cable parameters.

Sensors		Cables		
L (μH)	1.73	Type	RG-174	RG-316
C (pF)	120	d (m)	0.30	1.22; 3.00
K (pF)	103	Z_T (Ω)	50	
C_P (pF)	4.12	C_T (pF/m)	105	95
Q	250	v_g/c	66%	69.5%
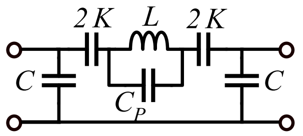		Attenuation at 10 MHz (dB/100m)	9.5	8.86
		Dielectric	PE	Teflon®

A printed circuit board of width 30 mm was inserted laterally into the plastic mount and served to interconnect the three inductive windings and the capacitors forming C and K, as well as to provide SMA connections to coaxial cables (visible at the bottom of Figure 5.8). Capacitance K was implemented using a symmetrical pair of $2K$ capacitors and a small variable capacitor for precision impedance matching at f_c. The parasitic capacitance C_P was found as ~4.1 pF across the inductors. The component values were chosen to optimise the LTL characteristics for a cable length of $d = 1.22$ m. To demonstrate that the waveguide topology offered significant design freedom, shorter and longer cables were also used, without changing the sensors. All three sets of cables had characteristic impedances of 50 Ω, with RG-174 Telegartner used for the short (0.3 m) cables, and RG-316 Cinch Connectors used for the medium-length (1.22 m) and long (3m) cables.

The sensors were individually tuned to minimise reflectivity at f_c as measured by the network analyser. Subsequently, the cable interconnects were introduced, and the scattering parameters of the entire LTL were measured. With 15 sensors, the total waveguide lengths were 5.25 m, 20.0 m, and 48.5 m for the small, medium-length, and long cables, respectively. The number of elements was chosen to be large enough so that effects of dispersion and loss could be observed. Having an odd number of elements provided a convenient midpoint for the localisation experiments described in the following Sections.

Figure 5.9 (a) compares the theoretical propagation constant (dashed lines) with measured data (crosses). Theoretical curves were calculated using the dispersion relation (5.6). Figure 5.9 (b) shows the measured group delay. Figures 5.9 (c)-(h) show the measured (solid lines) and theoretical (dashed lines) scattering parameters. The results for the short cables are shown in blue,

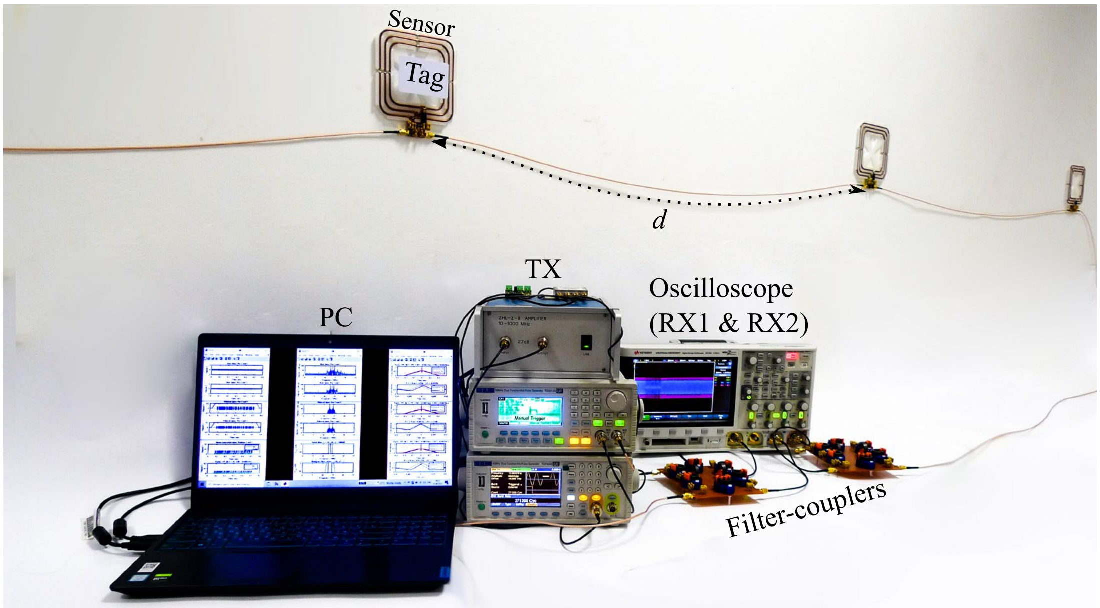

Figure 5.7. Photograph of the complete NFC communication and localisation system including an LTL antenna and a custom reader.

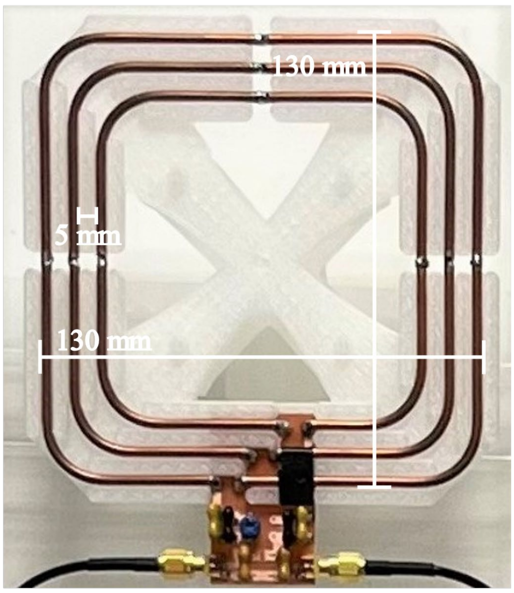

Figure 5.8. A photograph of an experimental sensor with attached cables.

for the medium-long cables in red, and for the long cables in green. The theoretical curves were obtained by first computing the equivalent transmission matrix for each of the three antenna configurations as $\boldsymbol{P}^N\boldsymbol{T}$ with $N = 15$, followed by an S-parameter transformation. Excellent agreement is seen across all figures. The slight deviations in S21 below the lower cut-off for short and medium cables can be attributed to cable effects and have been eliminated for long cables by placing ferrimagnetic rings to impede current flow on the outside surfaces of the shields. As expected, increasing length reduces and shifts the passband lower in frequency. Good matching is retained at f_c regardless of length. The measured group delay is flat between the two sidebands for

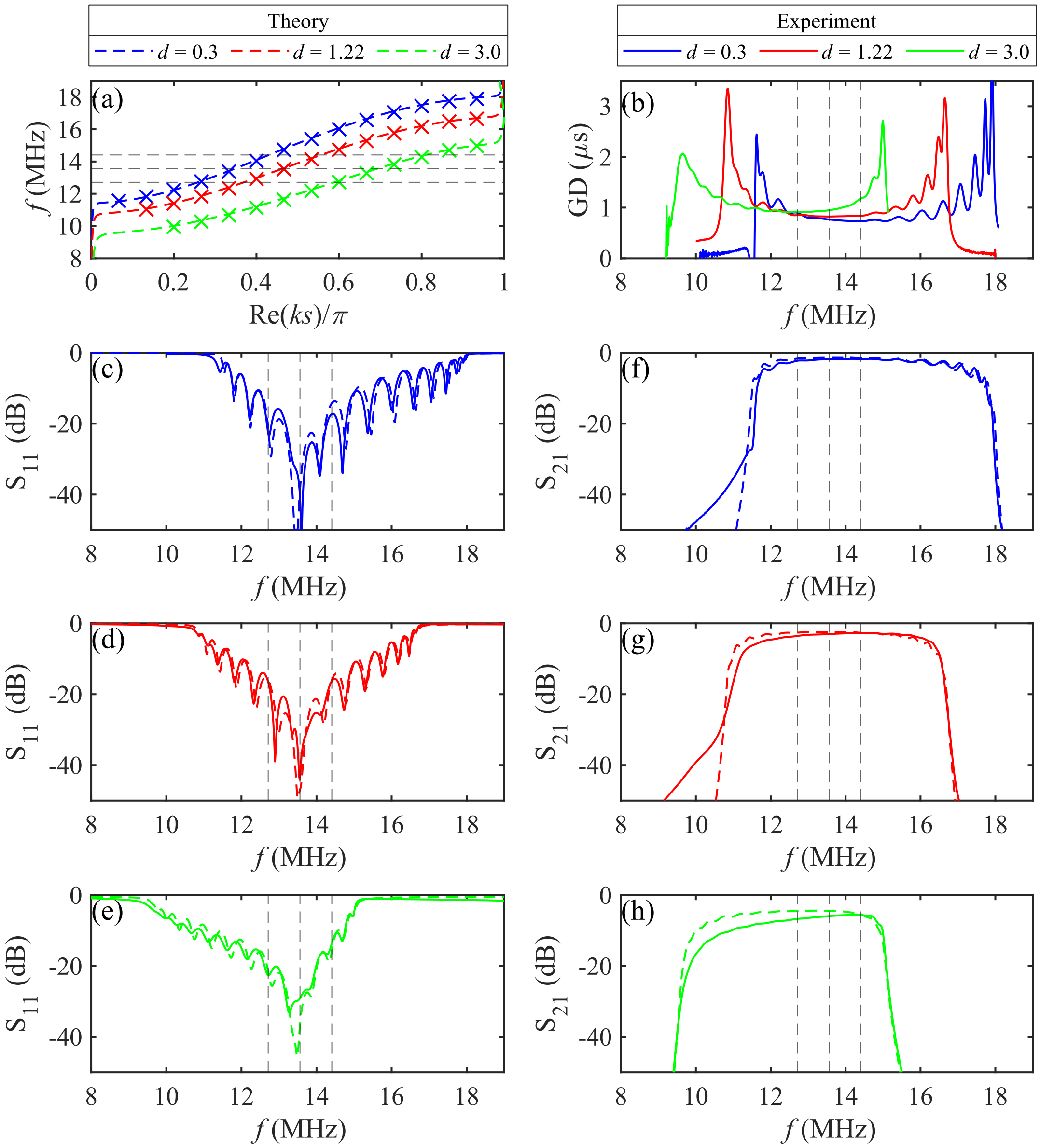

Figure 5.9. Characteristics of LTLs with cable sections of length $d = 0.3$ m (blue), $d = 1.22$ m (red), $d = 3$ m (green): (a) measured (crosses) and theoretical (dashed lines) LTL propagation constant, (b) measured group delay, (c)-(h) measured (solid lines) and simulated (dashed lines) scattering parameters. Agreement between theory and experiment is excellent. The best performing waveguide had a length of $d = 1.22$ m, but the other two waveguides are also suitable for NFC.

the medium-long cables but is sloping for the short and long cables. Despite this performance degradation, all three lengths are suitable for NFC communication and localisation. The loss at f_c is 0.35 dB/m, 0.15 dB/m, and 0.12 dB/m for the short, medium-long, and long cables respectively. The higher value for the short cables is caused by a higher relative contribution of the sensors. The same behaviour can be observed for the group delay, which is dominated by the slow wave effect of the sensors. While the group delay can be improved by reducing the passband, doing so would restrict the range of possible cable lengths.

5.4 Near field localisation with 1-D antennas

This Section discusses experiments on localisation of NFC transponders by time-of-flight difference in tag response. The localisation method was introduced in the previous Chapter. Figure 5.10 shows a functional block diagram of the system; the previous Figure 5.7 shows a photograph. An ISO/IEC 14443 Type-A compliant tag was placed next to one of the sensors along the antenna. A custom reader, capable of transmitting and receiving a subset of compliant signals, injected an HF carrier at one end of the antenna using a single-notch filter-coupler. The carrier propagated along the antenna, and the current circulating in the spiral inductors generated magnetic near fields. The other end of the antenna was connected to a matched filter-coupler.

The reader then sent a UID query, and the tag response propagated towards both ends of the antenna, where the UID signals were received via the filter-couplers. As before, digital out-of-band noise and carrier suppression pre-filters were applied, followed by rectification and low-pass filtering for down-conversion. After a pair-wise cross-correlation on the baseband UID responses, the time-of-arrival difference $\Delta t = t_2 - t_1$ was calculated from the cross-correlation peaks. The theoretical value of the LTL group velocity v_g at the sideband frequencies was then used to convert Δt into a physical tag position estimate $P_{est} = P_m - \Delta t \cdot v_g$, where $P_m = (1 + N)/2$ is the midpoint sensor position, and $N = 15$ is the total number of elements in the LTL.

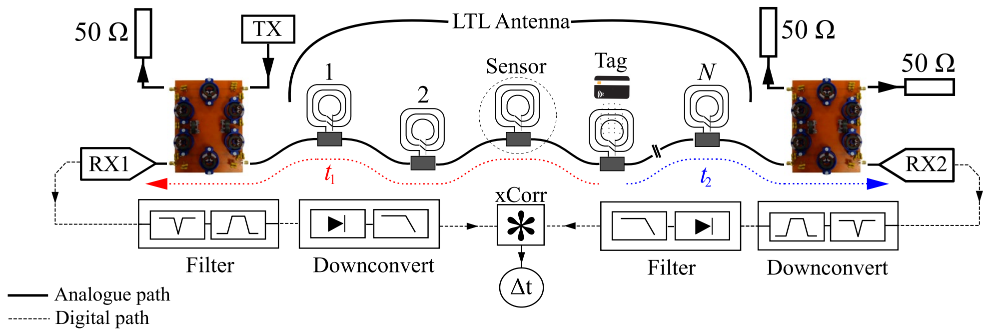

Figure 5.10. Block diagram for NFC system capable of tag localisation along LTL antenna.

The reader transmitter (TX) comprised a pair of phase-locked function generators and an RF switch (Mini-Circuits ZASWA-2-50DRA+). One generator (TTi TG4042) was used for the HF carrier, and the other (TTi TG5012A) was used for the baseband modulation sequences. A 1W amplifier (Mini-Circuits ZHL-32A+) amplified signals before injection into the LTL antenna. The tag responses were acquired with a digital oscilloscope (Keysight InfiniiVision DSOX3024T, sampling rate 1.25 GSa/s), while noise suppression, demodulation, and cross-correlation were done in Matlab using a PC. Tags were placed above the midpoint of a spiral inductor, and tag-to-antenna separation was adjustable by dielectric spacers.

Figure 5.11 shows the positioning error $e = P_{\mathrm{est}} - P$ for each node index P over a range of sensor-tag separation distances using 1W HF carrier power. Figures 5.11 (a), (b), and (c) represent antennas constructed with short, medium-length, and long cables, respectively. Each data point (circle) corresponds to a single time-of-arrival measurement using an ID-1 tag with UID = 0xF38AE495 and dimensions 85 mm x 56 mm. For all waveguides, the tag position was determined correctly ($|e| < 0.5$) over a sensor-tag separation from 1 to 10 cm, so that the correct

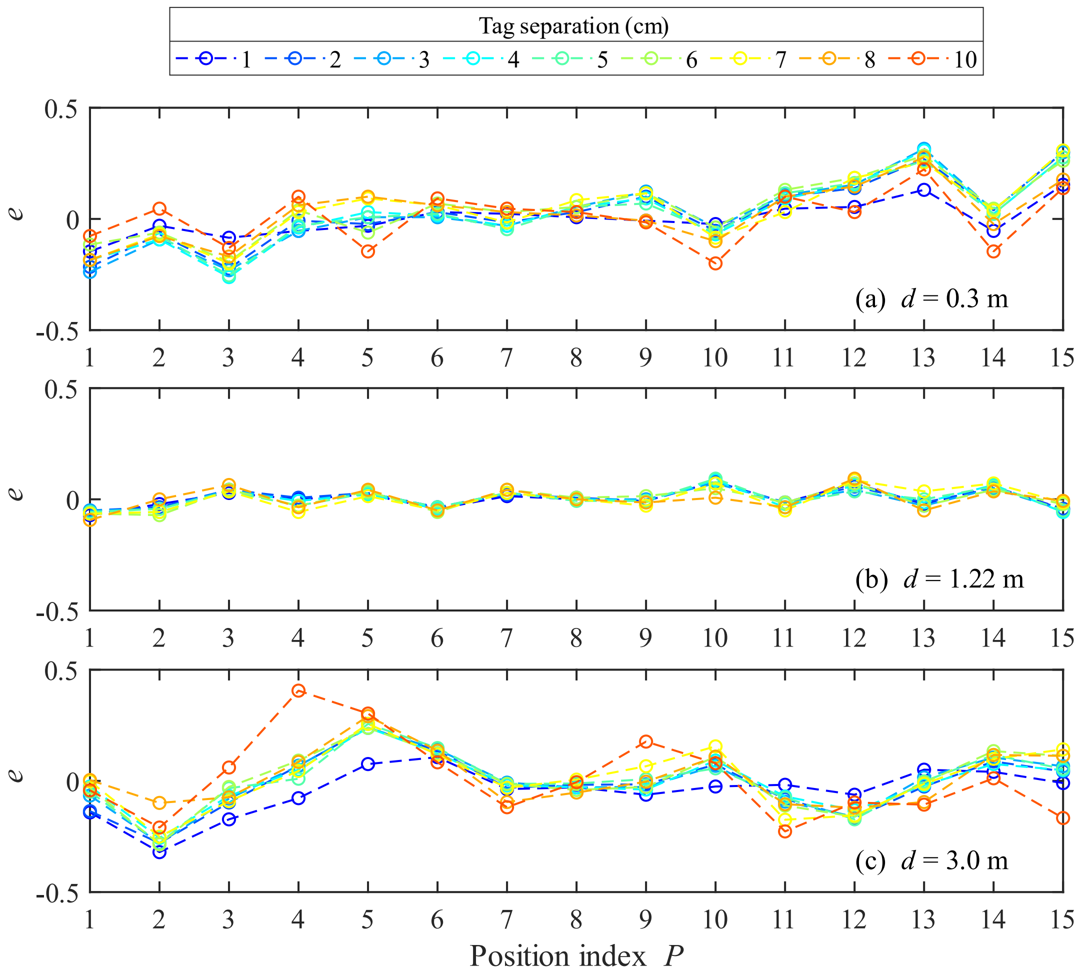

Figure 5.11. Experimental variation of localization error e with tag position index P over a range of sensor-tag separation distances. (a) $d = 0.3$ m; (b) $d = 1.22$ m; (c) $d = 3$ m.

position index could be obtained by rounding P_{est} to the nearest integer. The variation in e is the smallest for the medium-length cables, and largest for the long cables. The results conform to expectations based on the measured antenna dispersion characteristics and scattering parameters (Figure 5.9) and reflect the optimisation of sensors for medium-length cables.

The tag UID could be decoded correctly for separations below 11 cm. Each waveguide demonstrates a consistent error profile, which marginally deteriorates for larger separations. These results suggest that the error variability is inherent to the antennas and not caused by noise. Tags with different UIDs showed comparable error variation. Smaller tags (such as 1-inch diameter fobs) had expectedly shorter detection ranges but produced the same error variability profiles. If multiple transponders were present along the antenna, ISO/IEC 14443 anticollision protocols could be used to sequentially request transponder UIDs for positioning.

Figure 5.12 (a) shows probability density functions (pdf) fitted using normal distributions to 100 samples of P_{est} at each node with the tag placed directly on top of a sensor, using 1W carrier power, and the antenna with the medium-long cables. The position estimates are both highly consistent and resistant to background noise, as is evident from the extremely narrow distributions.

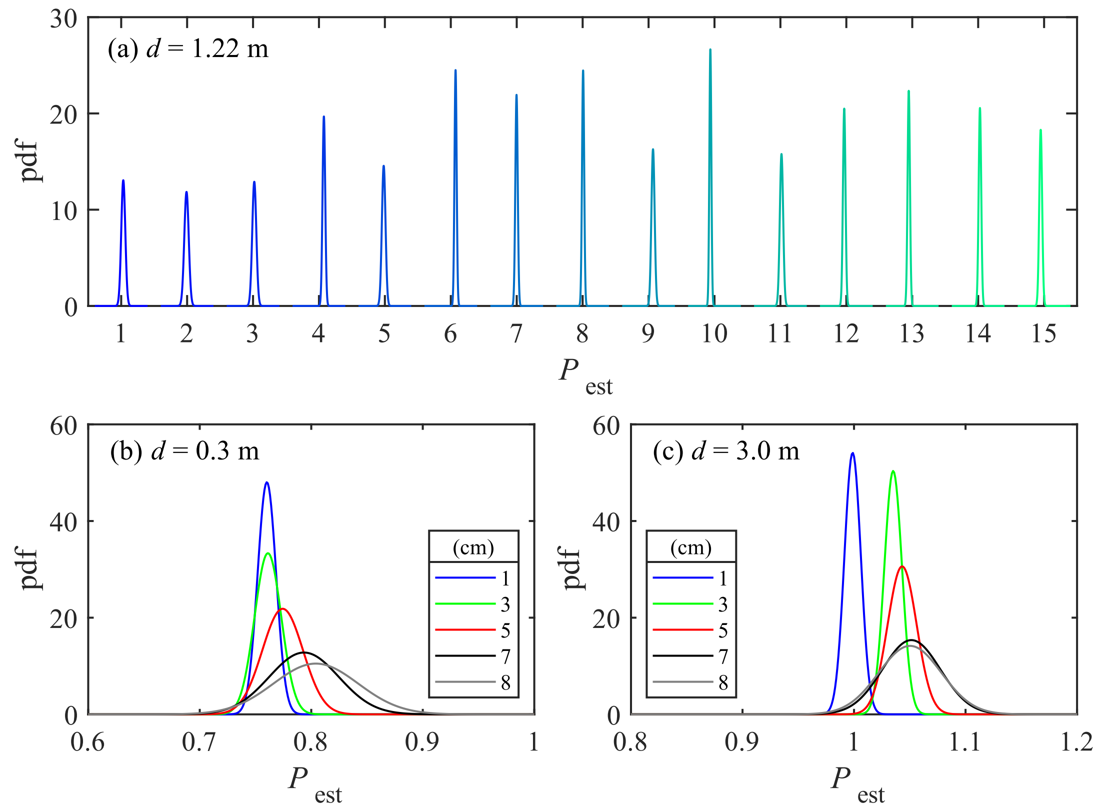

Figure 5.12. Probability density functions fitted to experimental position data using sample size of 100 for each distribution. (a) Tag at 0 cm separation for all 15 sensors with $d = 1.22$ m; (b) tag at varying separation distances at position $P = 1$ with $d = 0.3$ m; (c) tag at varying separation distances at position $P = 1$ with $d = 3$ m. The tag could be located correctly for all measurements.

There was negligible change in mean values and a marginal increase in variances for larger tag separations. Figures 5.12 (b) and (c) show probability density functions fitted using 100 position estimates at the first node ($P = 1$) for the antennas with the short and long cables, respectively, over a range of sensor-tag separations. For both antennas the uncertainty in P_{est} increases with separation, owing to reduced signal-to-noise ratio. A slight upward shift in the pdf mean values can be seen, consistent with Figure 5.11. The shift can be attributed to a slight variation in waveguide group delay caused by weaker antenna loading by a more distant tag. The effects of changing tag-to-antenna separation were more pronounced for antennas with suboptimal cable length. Nevertheless, the variance was still low at all nodes, which guaranteed accurate positioning.

5.5 Near field localisation with quasi-2-D antennas

This Section extends the discussion of tag localisation to quasi two-dimensional antennas. These were formed by re-arranging an LTL into a two-dimensional grid while maintaining sequential cable interconnects. Figure 5.13 (a) shows an LTL forming a planar 4-by-4 grid, in which each row was connected to the next, and the inductor centres are separated by distance h. Coupling coefficients $\kappa = 2M/L$ and $\kappa' = 2M'/L$ were defined, where M was the mutual

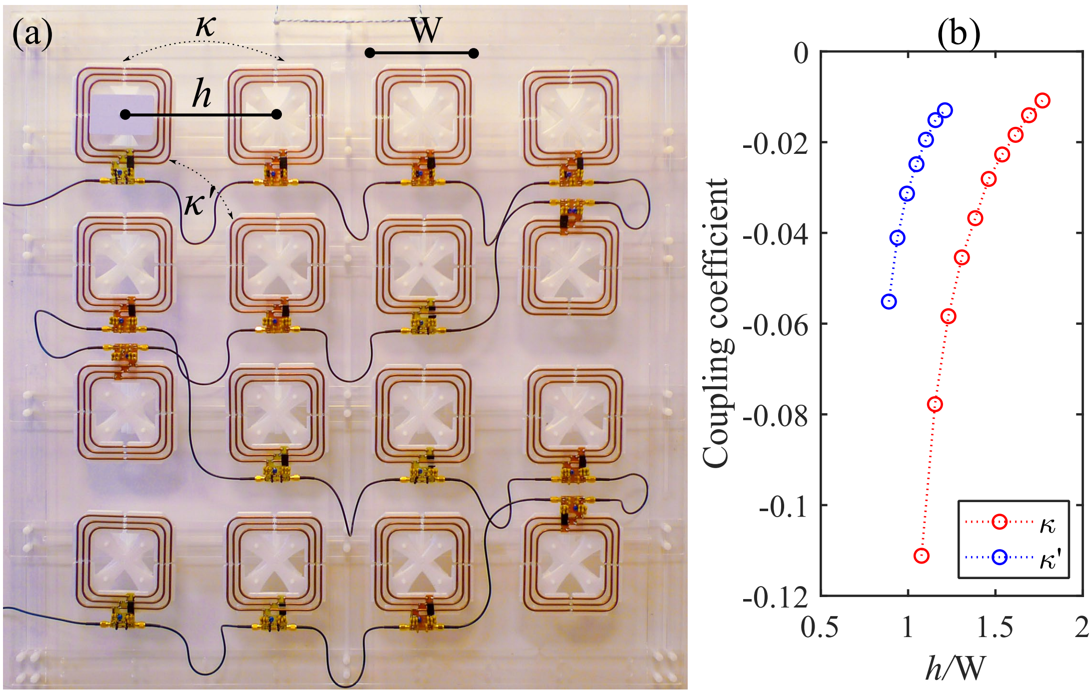

Figure 5.13. (a) Photograph of a quasi-2-D LTL antenna (b) measured magnetic coupling coefficient between nearest neighbours, κ for adjacent elements (red) separated by h/W, and κ' for diagonally adjacent elements (blue).

inductance between a pair of nearest neighbours, and M' was the mutual inductance between a pair of diagonal neighbours. Figure 5.13 (b) shows how the measured values of the coupling coefficients decay with increasing normalised distances h/W. For $h/W > 1.456$, $|\kappa| < 0.03$, and κ' was negligibly small, so that the quasi- two-dimensional antenna can be expected to perform like a one-dimensional one.

Figure 5.14 shows the scattering parameters, per-element group delay, and per-element phase advance of the two-dimensional grid with $d = 1.22$ m. As the element separation h increased from 19 to 26 cm, the value of S11 at the carrier frequency reduced by 10 dB, while the value of S21 increased by 0.8 dB. Similarly, the variation of the group delay between the sideband frequencies reduced as h increased. Further reductions in h resulted in significantly poorer matching and group velocity dispersion, while further increases saw scattering parameters converge to those of the one-dimensional antennas shown in Figure 5.9. Presumably, the effects at small h are caused by non-nearest neighbour coupling.

Figure 5.15 shows the error variation in estimated tag position for the two-dimensional grid with nearest-neighbour separation distance. Figure 5.15 (a) shows e for a card-type tag with UID 0xF38AE495 at 1 cm sensor-tag separation, while Figure 5.15 (b) is for a fob-type tag with UID

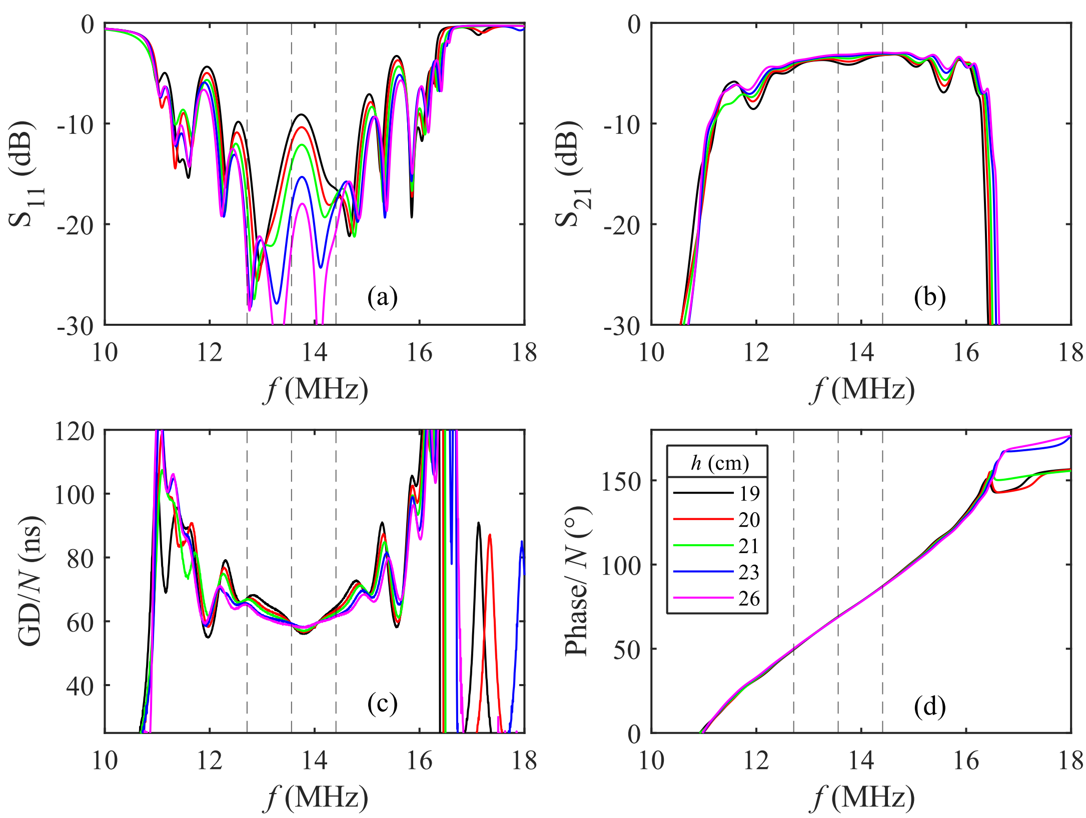

Figure 5.14. (a) Measured scattering parameters of quasi-2D grid for a range of neighbour separation distances h. (a) S_{11} parameters; (b) S_{21} parameters; (c) group delay per element; (d) phase shift per element in degrees.

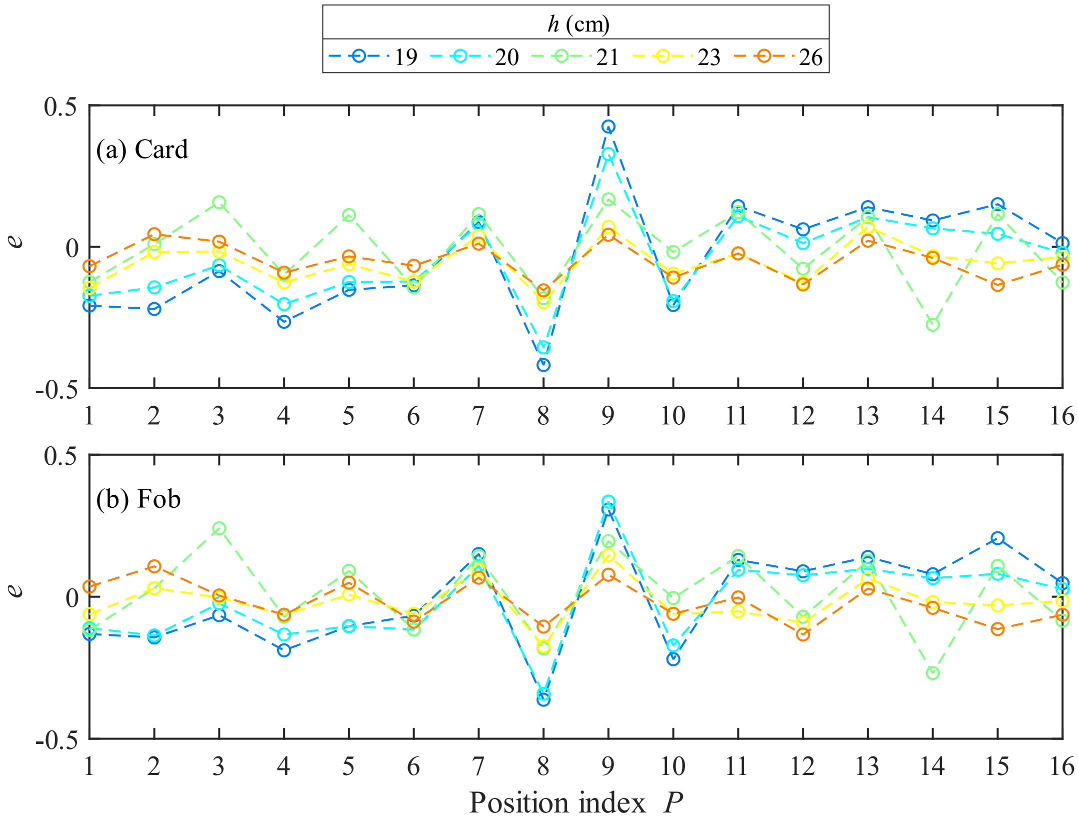

Figure 5.15. Experimental variation of localisation error e with tag position index P over a range of neighbour separation distances h for (a) an ID-1 tag and (b) a fob tag.

0x010D354A placed directly on top of the inductors. Both tags could be correctly located at all elements for $h = 19$ cm. The fob tag on average saw a slight reduction in localisation error compared to the card tag, caused by weaker antenna loading by a smaller fob. Stronger loading may introduce local variations in group delay in the antenna around the contact point owing to asymmetry, thus resulting in higher errors. The shape of the error variation profiles was again nearly identical for the two tags, suggesting the errors were determined by local group velocity variations within the antenna and not by noise. Tags placed between inductors could not be accurately located but could still be read.

5.6 System scalability

The lengths of our waveguide antennas were limited by the constraints of a laboratory experiment. This Section performs an initial investigation of maximum antenna length. A limit will be imposed by waveguide attenuation and dispersion, which corrupt signals generated by tags. The effects were simulated in MATLAB® using the noise models adopted from Chapter 4. A tag injected an amplitude modulated signal $s(t) = \sin(2\pi f_c t)[1 + m(t)]$ into the nth antenna element, where $m(t)$ is the subcarrier-modulated tag UID. The message signal was generated as

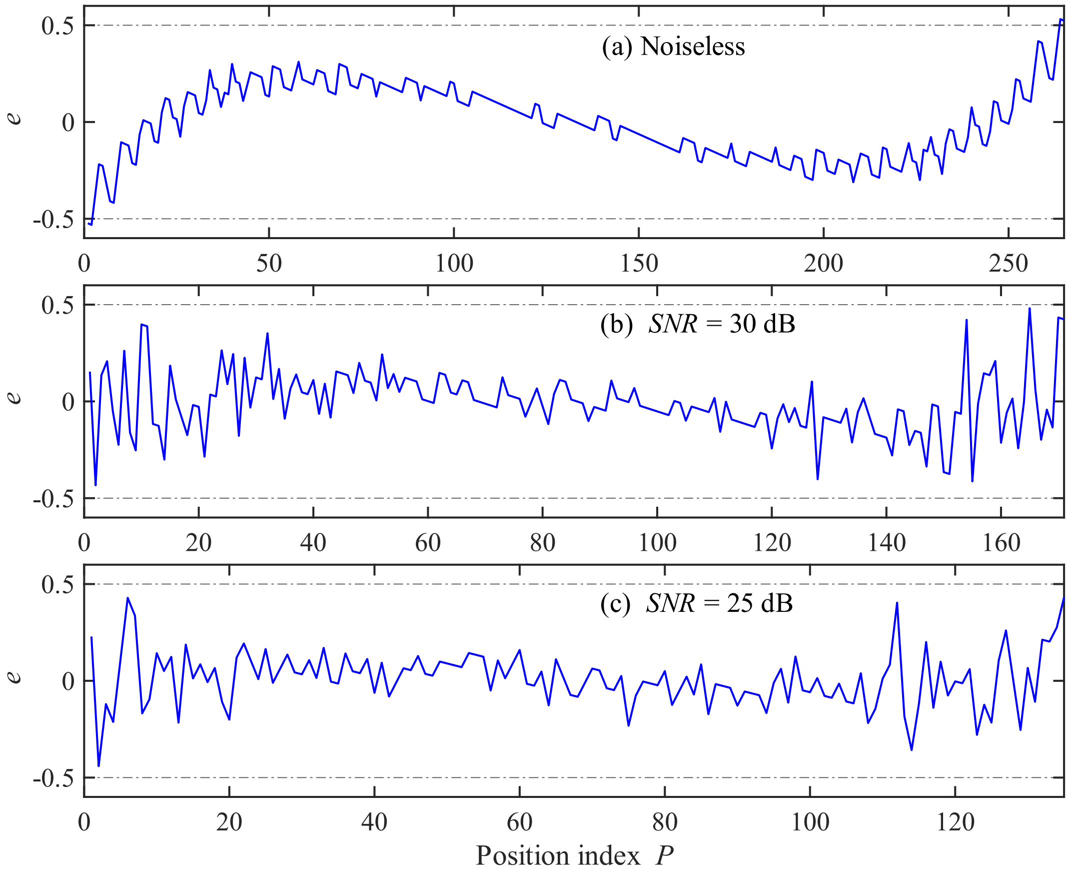

Figure 5.16. Simulated tag positioning using $f_{\mathrm{samp}} = 8f_{\mathrm{c}}$: (a) noiseless antenna with $N = 265$, (b) SNR $= 30$ dB with $N = 171$, (c) SNR $= 25$ dB with $N = 135$.

$m(t) = a_{\mathrm{m}} s_{\mathrm{T}}(t) \sin(2\pi f_{\mathrm{c}} t)$, where s_{T} was the binary UID signal, and a_{m} the message amplitude. The tag signal $s(t)$ was then propagated to both ends of the antenna, taking antenna loss and dispersion into account, and uncorrelated white receiver noise $n_{\mathrm{A}}(t)$ was added to the signals prior to filter-couplers. A sampling rate of $8f_{\mathrm{c}}$ was used, and the tag UID was 0x010D354A. The signal-to-noise ratio (SNR) was defined as

$$\mathrm{SNR} = 10 \log \left(\frac{\sum_{i=1}^{J} |[m(t) \sin(2\pi f_{\mathrm{c}} t)] * f(t)|^2}{\sum_{i=1}^{J} |n_{\mathrm{A}}(t) * f(t)|^2} \right) \tag{5.13}$$

where $f(t)$ is the impulse response of the filter-couplers, J is the number of samples, and the asterisk represents linear convolution. The SNR so defined describes the ratio of the power of the tag signal at the entry to the waveguide to the noise power within the passbands of the filters. The signal power at each end is generally different, and such a definition avoids the need for two SNR values. For antennas with large N, high SNR may be needed to offset propagation losses. The maximum antenna length was determined by requiring that the tag localisation error does not exceed half an element. It is important to note, however, that the model does not account for minimum tag power requirements and assumes the tag responds at all antenna elements.

Figure 5.16 shows the variation of localisation error with tag position for $d = 1.22$ m. Figure 5.16 (a) assumes no noise, and the error profile is anti-symmetric around the midpoint sensor, where the error is zero. The exact shape arises owing to the combined effect of dispersion and smoothing during tag response down-conversion. The error was maximum for tags at antenna extremes because only one of the outputs was affected by dispersion. Figures 5.16 (b)-(c) show localisation error in the presence of receiver noise, with an SNR of 30 dB and 25 dB, respectively. The maximum achievable antenna length became shorter as SNR was reduced, with the error once again being highest at antenna ends. The effect became more pronounced for antennas with higher loss. The maximum number of sensors for each configuration was 265, 171, and 135, respectively. Ambient noise, such as radiofrequency interference picked up by sensors, is not included in the simulation, but its effects have been discussed previously in Chapter 4.

Table 5.2 gives an overview for the other cable lengths used and different values of SNR. As can be expected, the optimised geometry with 1.22-m cables performs the best, and antennas exceeding 100 elements are feasible for the values of SNR above 20 dB. At low SNRs, tags could still be located but their UIDs could no longer be read correctly. This apparent contradiction is explained by higher processing gain in UID cross-correlation, as opposed to the bit-wise correlation required for UID decoding. Achieving high values of SNR as well as being able to power tags via long lossy antennas would require increased carrier powers. It should, however, be noted that localisation performance can be improved by increasing the sampling rate which increases the cross-correlation processing gain.

Table 5.2. Maximum number of sensors for different SNR values

	$d = 0.3$ m	$d = 1.22$ m	$d = 3.0$ m
Noiseless & Lossless	235	281	139
Noiseless & Lossy	195	265	121
SNR = 25 dB	171	135	79
SNR = 20 dB	141	107	63
SNR = 15 dB	93	73	45
SNR = 10 dB	67	51	31
SNR = 5 dB	19	17	13

5.7 Conclusions

Our experiments, simulations, and theoretical analysis suggest that the loaded transmission line antennas considered in this paper can be employed for communication with and localisation of distributed NFC tags and offer significant improvements in both practicality and characteristics over magneto-inductive antenna topologies considered previously. The maximum antenna length realised experimentally was 48 meters, and theoretical estimates show that antennas of several 100s of meters are feasible with favourable SNR. The maximum read node separation demonstrated here was three meters. This separation can be increased to system dimensions by interspersing functional and non-functional nodes, in the process allowing the functional nodes to be irregularly spaced. A simple learning algorithm may then be used to identify the functional nodes. In contrast to multiplexed antenna systems, increasing the number of read nodes carries no hardware overhead. The antennas are flexible and can be arranged in different shapes, as demonstrated by a quasi-two-dimensional grid arrangement. Furthermore, localisation to the nearest node was found to be accurate irrespectively of the range or tag type used, provided the field was strong enough to power the tag.

The localisation method used is based on comparing the time-of-arrival of tag signals reaching both ends of an antenna. The antennas were consequently optimised for low group velocity, with the associated drawback of increased propagation loss. Scenarios that do not require tags to be localised impose less stringent requirements on waveguiding properties of antennas, which could as a result be made longer and rely on simpler topologies. On the other hand, the need to extract signals from both antenna ends limits deployment options by requiring lengthy return cables and two matched receivers. Single-ended localisation systems may offer additional flexibility with sensor layout, reduce reader complexity, and remove the need for return cables. The feasibility of such systems is assessed in the following Chapter, which introduces monostatic tag localisation using slow wave LTL antennas.

Chapter 6:
Monostatic Localisation with Loaded Transmission Line Antennas

The method of tag localisation by differential time-of-flight developed in Chapter 4 is bistatic, requiring tag responses to be extracted from both ends of a slow wave antenna. Despite the significant improvements in antenna design described in Chapter 5, the need for a pair of synchronised receivers may limit deployment options and achievable antenna layouts. Here, we develop a new monostatic localisation method, which estimates tag position from the absolute delay between a reader query and the tag response using a single receiver. The intrinsic variability of the delay was statistically characterised for a selection of off-the-shelf ISO/IEC 14443 compliant Type-A tags over a range of input power and sensor-tag separations, with each tag generating a unique fingerprint. It is shown that despite inter-tag variability, one-dimensional localisation can be achieved provided the per-element group delay of the antenna is sufficiently high. Finally, the localisation method is verified using a 21 metre-long loaded transmission line antenna with eight functional sensor nodes using 1 W input carrier power. The proposed method eliminates the hardware and layout limitations of bistatic localisation and is consequently more practical and deployable.

6.1 Overview

In Chapter 4 we described a bistatic localisation method which estimates tag position from small time-of-flight differences in tag response signals, which are extracted from both antenna ends using a pair of synchronous receivers. Although there exists a significant and variable delay between the end of a reader query and the start of the tag response (as dictated by protocol specifications), this has no effect on localisation accuracy since position is estimated from differential time-of-flight between the two outputs. While highly effective, the method limits deployment options and restricts antenna layout. Specifically, the antenna must form a closed path with both ends connected to a matched receiver pair, meaning meander layouts would require a pair of lengthy return cables. The reader receivers must also be synchronised and equipped with matched filter-couplers, which further inflates hardware cost.

Here, we develop and test a new monostatic localisation method which estimates tag position from absolute time-of-flight differences. The proposed system comprises a single transceiver placed at the input of a flexible loaded transmission line antenna, while the output is terminated with an absorber. The system thus lacks return cables, while a modular antenna structure allows additional sensor nodes to be added on-site. Due to the lack of a second reference signal, tag position is inferred from the delay between the end of a reader query and the start of the unique identifier response frame, using a regenerated UID template in a cross-correlation detection scheme. As opposed to bistatic systems, monostatic localisation is sensitive to differences in response timings between individual tags. Nonetheless, we show that consistently accurate positioning can be achieved for a range of off-the-shelf tag types provided the group delay between functional sensor nodes exceeds the maximum variability of tag response timing.

6.2 LTL antenna design

In the previous Chapter we described several LTL antennas with different sensor topologies. A pi-section with capacitances in the shunt branch and a series LC resonator in the series branch was identified as the optimal candidate for NFC localisation, with the corresponding antenna schematic as shown in Figure 6.1. We briefly discuss the properties this topology, derive topology-specific design equations, and consider antenna parameter selection.

The sensor series impedance is $Z = 1/(j\omega K) + (j\omega L)||(1/(j\omega C_{\mathrm{p}}))$, where "$||$" represents parallel combination and C_{p} is the stray capacitance of the inductor L. The shunt sensor impedance is simply $Z' = 1/(j\omega C_{\mathrm{p}})$. The sensor transmission matrix $\boldsymbol{S}$ may then be written as

$$\boldsymbol{S} = \begin{bmatrix} 1 + \frac{Z}{Z'} & Z \\ \frac{1}{Z}\left(2 + \frac{Z}{Z'}\right) & 1 + \frac{Z}{Z'} \end{bmatrix}. \tag{6.1}$$

The unit cell matrix $\boldsymbol{P} = \boldsymbol{TS}$, where $\boldsymbol{T}$ is as in (5.5), can again be used to compute the dispersion relation for the antenna using (5.3).

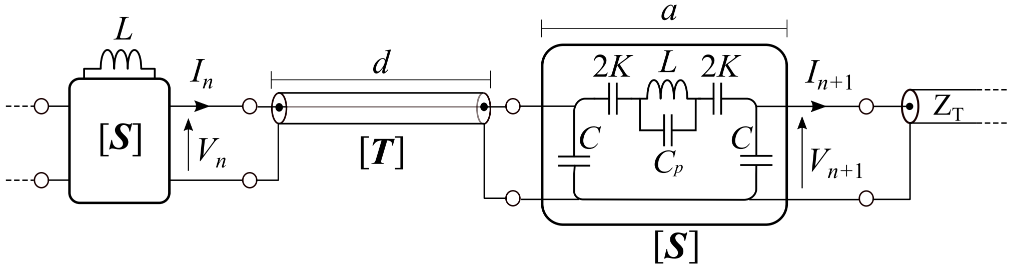

Figure 6.1. Schematic representation of a slow wave loaded transmission line NFC antenna.

$$\cos(ks) = \left(1+\frac{Z}{Z'}\right)\cos(\gamma d) + j\left[\frac{Z}{2Z_\mathrm{T}} + \frac{Z_\mathrm{T}}{Z}\left(1+\frac{Z}{2Z'}\right)\right]\sin(\gamma d) \tag{6.2}$$

As before, γ and k are the cable and antenna complex propagation constants, while d and $s = a + d$ are the cable and antenna unit cell lengths, respectively. The antenna characteristic impedance Z_0 may also be re-written using (5.4).

$$Z_0 = \frac{Z\cos(\gamma d) + jZ_\mathrm{T}\left(1+\frac{Z}{Z'}\right)\sin(\gamma d)}{e^{jks} - \left(1+\frac{Z}{Z'}\right)\cos(\gamma d) - j\frac{Z_\mathrm{T}}{Z'}\left(2+\frac{Z}{Z'}\right)\sin(\gamma d)} \tag{6.3}$$

The characteristic impedance Z_0 can be made equal to Z_T at a particular matching frequency ω_m by tuning capacitance K. Parasitic inductor capacitance, however, may affect matching. We thus re-write (5.10) to include C_p in the matching condition.

$$K = \frac{\left(1-\omega_\mathrm{m}^2 LC_\mathrm{p}\right)\left(1+\omega_\mathrm{m}^2 C^2 Z_\mathrm{T}^2\right)}{\omega_\mathrm{m}^2\left\{CZ_\mathrm{T}^2\left[\omega_\mathrm{m}^2 L\left(C+C_\mathrm{p}\right)-2\right]\right\}} \tag{6.4}$$

When choosing antenna parameters, K should be set such that (6.4) is satisfied at the carrier frequency f_c. The cable parameters (the inductance L_T or capacitance C_T per unit length), as well as the stray inductor capacitance C_p are certainly fixed. Similarly, Z_T is typically limited to 50 Ω or 75 Ω for coaxial cable by manufacturers. The degrees of freedom are thus limited to cable length d, sensor inductance L, and shunt capacitance C, which may be adjusted to shape the dispersion characteristic. Parameter limits are determined by the need to contain the minimum tag response bandwidth BW_T within the first antenna passband.

LTL sensor parameters L and C should ideally be tailored to a particular cable length, with suboptimal values resulting in (as shown in the previous Chapter). Figure 6.2 describe an example of the calibration process, with Figures 6.2 (a) and (b) showing the dispersion characteristic and the per-element group delay $GD_\mathrm{e} = \partial/\partial\omega\big(\mathrm{Re}(ks)\big)$, respectively, for an antenna with a moderate cable length $d = 2$ m, with $L = 1.7$ μH (red) or $L = 3.5$ μH (blue). Capacitance K is set according to (6.4) to achieve 50 Ω at f_c. Capacitance C is used to symmetrically align the antenna passband with the NFC-A spectrum, with higher values acting to lower the passband in frequency. $C =$ 95 pF, for example, results in a symmetric group delay profile around the carrier frequency f_c. The inductance L may then be used to control the passband width and, hence, the group delay. Higher L reduces the width and increases the SWF, but also the group velocity dispersion. For example,

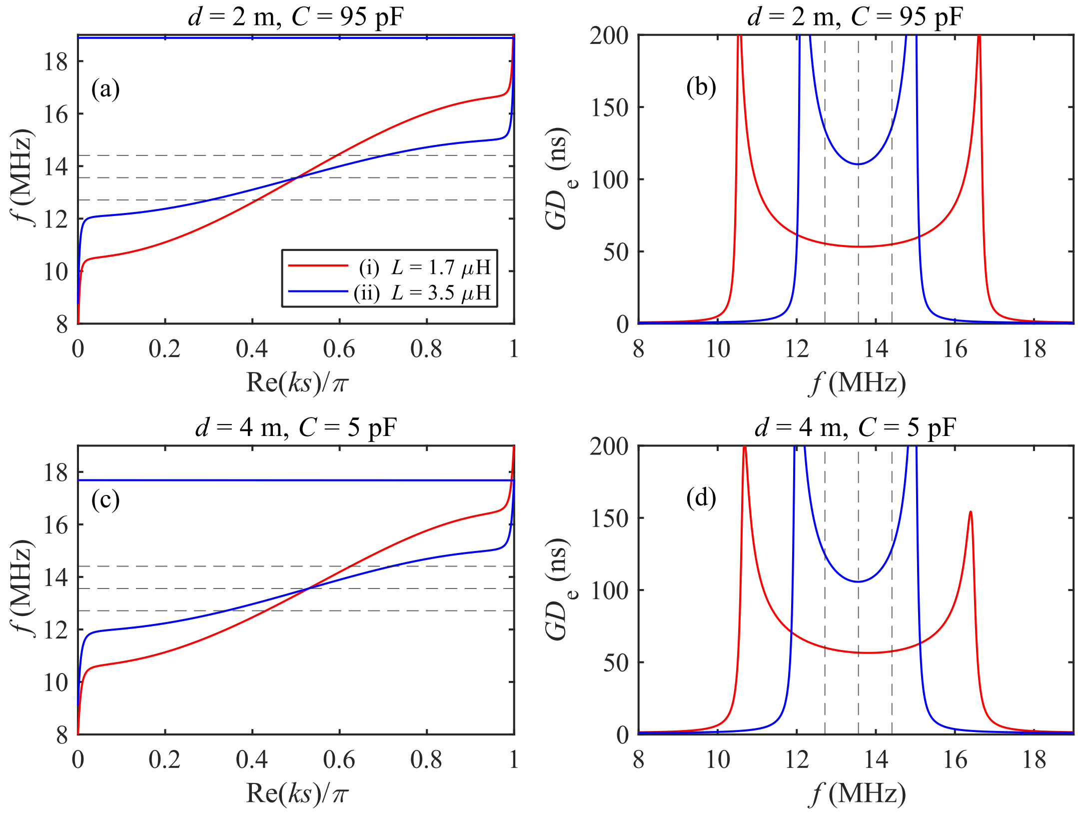

Figure 6.2. Tailoring the characteristics of LTL antenna with $d = 2$ m (a) – (b) and $d = 4$ m (c) – (d). Cables have $C_\mathrm{T} = 95$ pF, $L_\mathrm{T} = 237$ nH, and $Z_\mathrm{T} = 50\ \Omega$. Sensors have $C_\mathrm{p} = 4$ pF and $Q = 300$. Dashed lines indicate the carrier and subcarrier frequencies.

an increase from $L = 1.7$ µH to 3.5 µH raises GD_e from 53 ns to 110 ns at the carrier frequency, but also results in a 22% difference in group delay between the carrier and subcarrier frequencies.

The consequence of increasing the cable length is a reduction in passband width and its downwards shift in frequency. The shift may be compensated for by reducing the value of C, which has the opposite effect. Figures 6.2 (c)-(d) again show dispersion and GD_e but for an antenna with longer cables $d = 4$ m, with C reduced to 5 pF to compensate. Despite the longer cables, the group delay remains the same. Once C reaches zero, no further compensation is possible and maximum cable length has been attained. If longer sensor separation is required, miniature non-functional nodes with ferrite inductors may be employed between each functional node. Cable interconnect length should then be optimised to achieve a satisfactory trade-off between the node-dominated propagation loss, the group delay between functional nodes, and group velocity dispersion.

6.3 Monostatic tag localisation

This Section discusses the monostatic localisation method for distributed NFC tags using a terminated LTL antenna. In contrast to bistatic localisation by differential time-of-arrival, monostatic localisation estimates tag position based on absolute time using a single receiver.

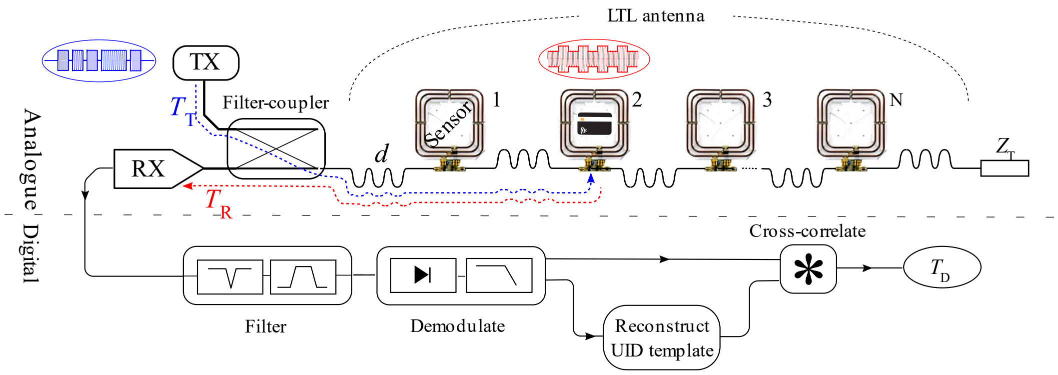

Figure 6.3. System block diagram of a monostatic tag localisation system depicting the hardware setup and digital post-processing method.

Figure 6.3 shows a functional block diagram of the proposed system, consisting of a custom ISO/IEC 14443 Type-A compliant reader, a compliant tag, and an LTL antenna. The reader transmitter (TX) injects an HF carrier at one end of the antenna via a frequency-selective filter-coupler. The carrier propagates along the antenna, generating magnetic near fields at the sensor nodes, powering any tags in the vicinity and placing them into the "idle" state. The reader detects the presence of a Type-A tag by probing the field with the "REQA" command and initialises anticollision with the "SEL" command. Following a pause in communication, the tag responds with its complete unique identifier (UID). The tag response propagates to either end of the antenna. At one end it is absorbed by the matched load Z_T. At the antenna feed end it is detected at the receiver (RX). The delay between the end of the last data bit of the "SEL" frame issued at TX and the start of the first bit of the tag UID received at RX is given by $T_D = T_T + T_R + T_P$, where T_T is the group delay incurred by the transmit signal (blue path), T_R is the group delay incurred by the tag response (red path), and T_P is the frame delay time as seen by the tag. Together, $T_T + T_R$ represent the antenna delay T_A.

Figure 6.4 (a) shows a sample tag response acquired at the receiver, with the time origin aligned to the end of the last data bit of the "SEL" command issued by the transmitter. The delay T_D then corresponds to the first modulation edge of the UID. As in Chapter 5, the baseband response is recovered by applying zero-phase noise and residual carrier suppression filters, followed by rectification and low-pass filtering for demodulation. The UID is then decoded from the filtered tag response (blue), and an idealised UID template is reconstructed (dashed red), as shown in Figure 6.4 (b). Finally, the delay T_D may be estimated by cross-correlating the filtered tag response with the reconstructed UID template, where T_D corresponds to the location of the cross-correlation peak, as shown in Figure 6.4 (c).

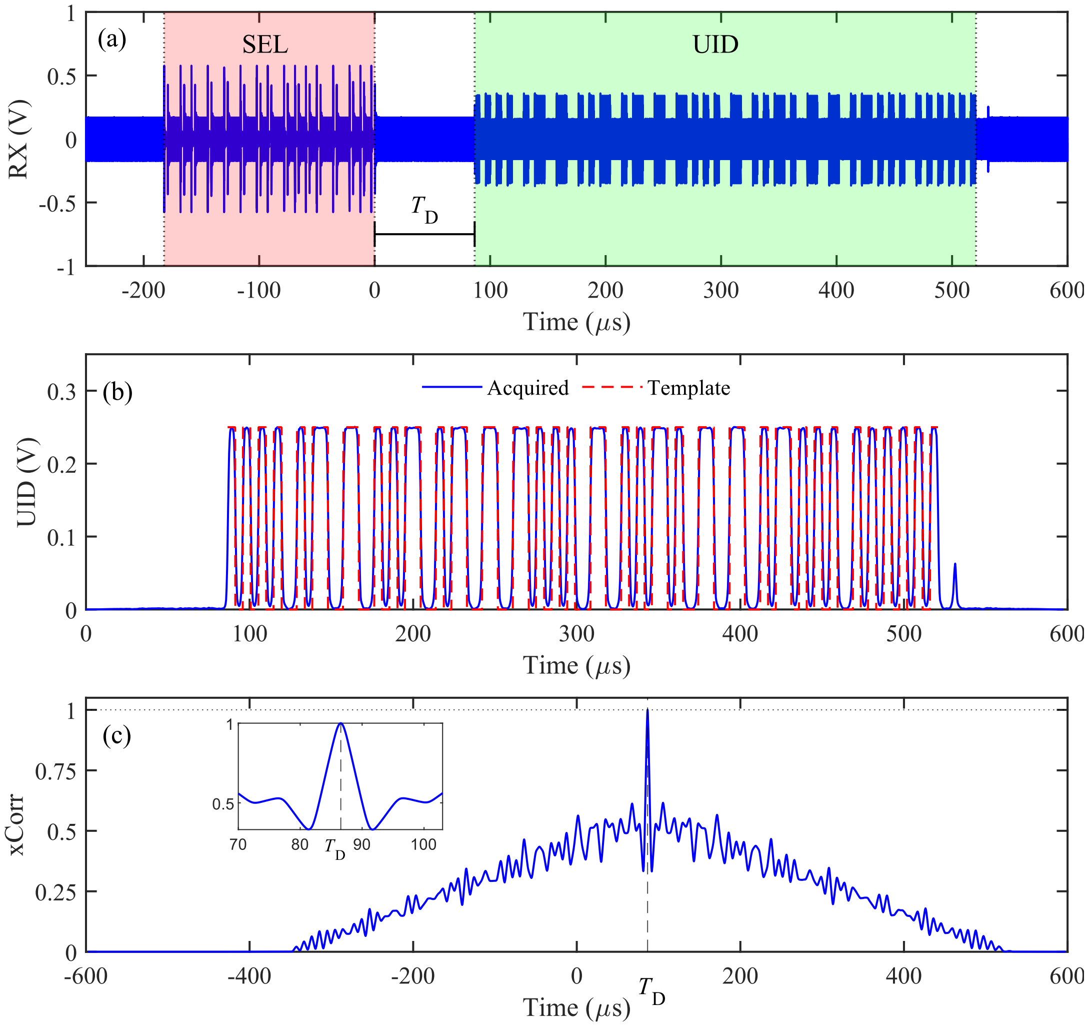

Figure 6.4. Processing steps involved in pause-adjusted delay estimation: (a) digital acquisition of selected tag UID; (b) application of residual carrier and out-of-band noise filters followed by UID template reconstruction; (c) tag delay characterisation by cross-correlation of filtered tag response with the reconstructed UID template.

The duration of the pause in communication T_{P} is regulated by the ISO/IEC 14443 protocol and depends on the reader command type and the value of the last transmitted bit. For the "SEL" command requesting the entire tag UID, $T_{\mathrm{P}} = 1172/f_{\mathrm{c}}$ = 86.431 μs. The per-element group delay of an LTL antenna is typically of the order of 100 ns, as shown in Figures 6.2 (b) and (d), meaning the total delay T_{D} is dominated by the frame delay time T_{P}. For convenience, we define the pause-adjusted delay $t_{\mathrm{D}} = T_{\mathrm{A}} + \Delta T_{\mathrm{P}}$, where $\Delta T_{\mathrm{P}} = T_{\mathrm{P}} - 1172/f_{\mathrm{c}}$ is the frame delay error. The antenna delay T_{A} is position-dependent, such that $T_{\mathrm{A}} = P \cdot t_{\mathrm{A}}$, where P is the node position index, and the delay $t_{\mathrm{A}} \approx 2GD_{\mathrm{e}}(f_{\mathrm{c}})$ is the per-element antenna group delay incurred by the incident reader and reflected tag signals. A mapping between t_{D} and P can thus be established as:

$$t_{\mathrm{D}} = P \cdot t_{\mathrm{A}} + \Delta T_{\mathrm{P}} \tag{6.5}$$

Provided the maximum variation in pause error $e = \max \Delta T_{\mathrm{P}} - \min \Delta T_{\mathrm{P}}$ is such that $e < t_{\mathrm{A}}$, the tag position may be extracted from an estimate of t_{D}. For accurate monostatic localisation, ΔT_{P} must be statistically consistent, and its variability with tag type, sensor-tag separation distance, and input RF power should be characterised.

6.4 Tag delay characterisation

This Section discusses the experimental characterisation of the pause error ΔT_{P} for a selection of off-the-shelf ISO/IEC 14443 compliant Type-A tags. The measurement system architecture was as previously shown in Figure 6.3, but with the LTL antenna shortened to a single sensor node with $d = 30$ cm, so that $t_{\mathrm{D}} \approx \Delta T_{\mathrm{P}}$. The same LTL sensors were employed as in Chapter 5 and a photograph of the end section of the antenna is provided in Figure 6.5 (a).

The reader transmitter (TX) consisted of a pair of function generators, an RF switch (Mini-Circuits ZASWA-50-DRA+), and a power amplifier (Mini-Circuits ZHL-32A+), as shown in Figure 6.5 (b). The first generator (Aim-TTi TGF4042) produced the HF carrier, while the second (Aim-TTi TG5012A) produced the encoded baseband command bits. The generators were synchronised by common trigger signals, allowing the carrier to be phase-locked to the modulation signal edge transitions. The transmitter connected to the antenna via a single-notch filter-coupler

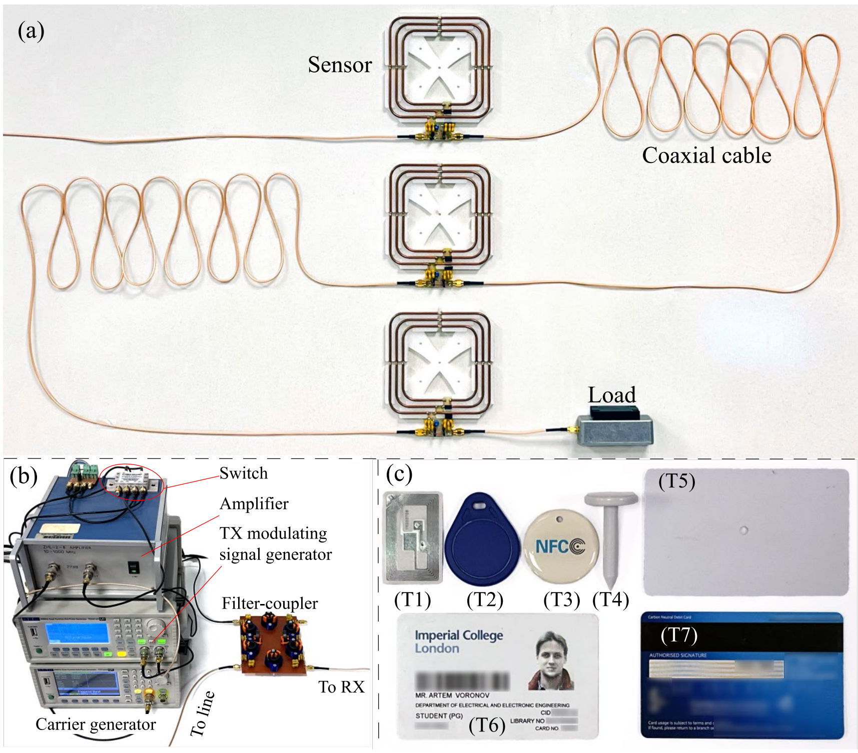

Figure 6.5. (a) Photograph of a terminated LTL antenna section; (b) custom transmitter module and filter-coupler; (c) a selection of NFC tags including a (T1) smart sticker, (T2)-(T3) fobs, (T4) nail, (T5) smart card, (T6) university key card, (T7) debit card.

from Chapter 3. A digital oscilloscope (Keysight InfiniiVision DSOX3024T) was used as the receiver (RX) with a 625 MSa/s sampling rate. The second generator triggered a signal acquisition in the receiver at the end of the "SEL" command as shown in Figure 6.3 (b). For each UID acquisition the HF carrier was switched on for 5 ms prior to the "REQA" command to ensure the tag under test successfully entered the "idle" state.

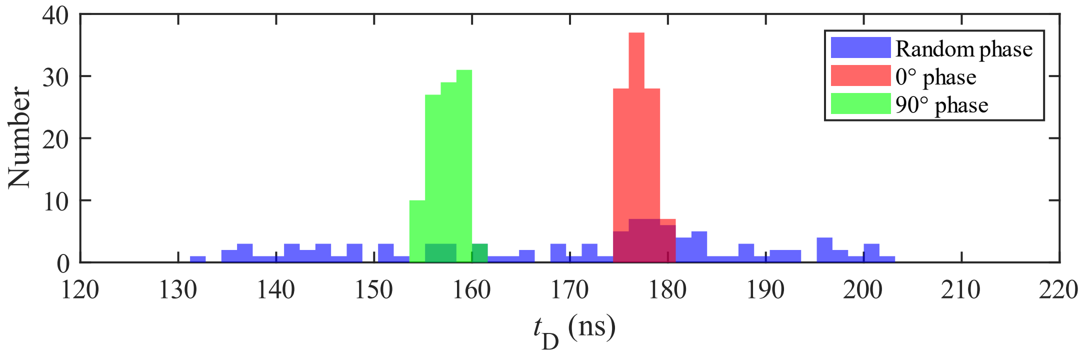

Figure 6.6. Distribution of 100 t_D samples for the smart card (T5), measured at $r = 0$ cm sensor-tag separation using randomised (blue), 0 degree (red), or 90 degree (green) HF carrier phase, respectively.

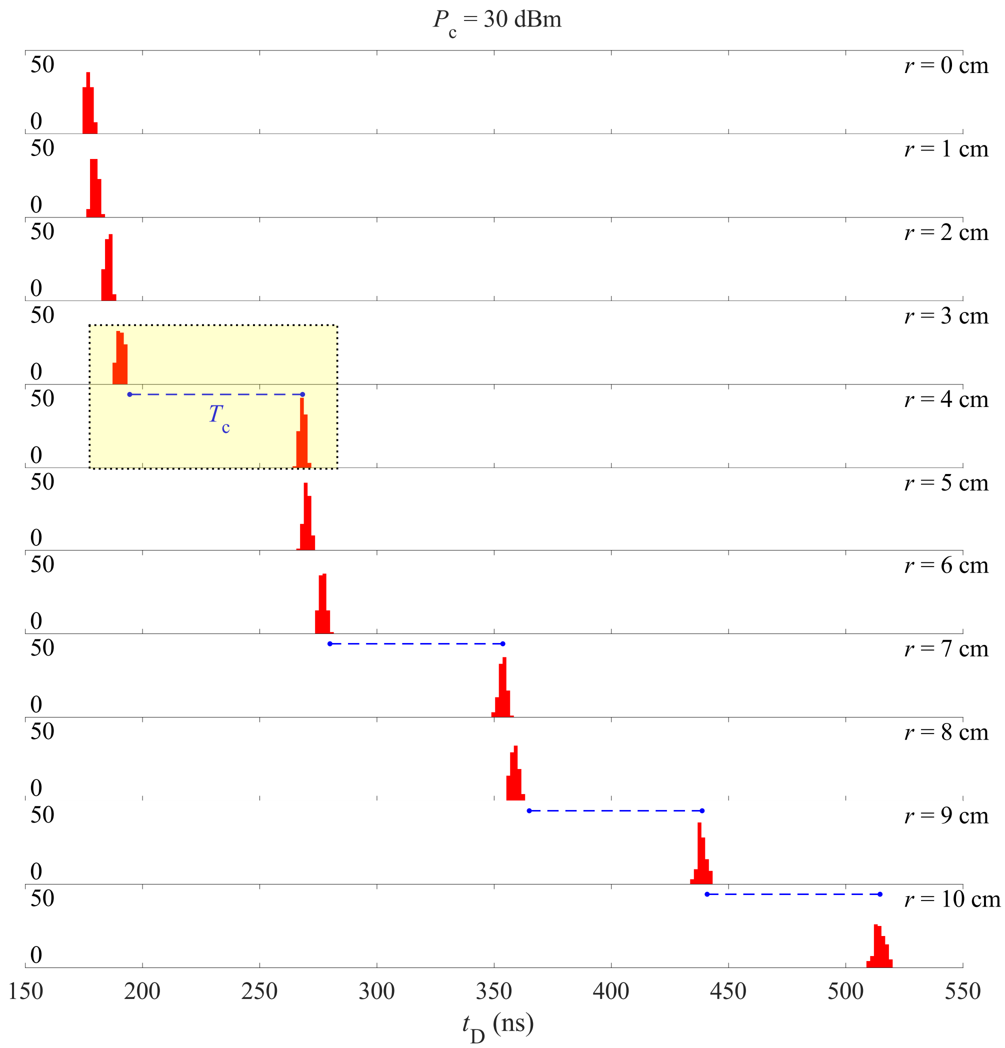

Figure 6.7. Variation of the pause-adjusted frame delay t_D distributions with sensor-to-tag separation r for the smart card (T5). Delay estimates are quantised, with modes separated by carrier cycle periods.

Figure 6.5 (c) shows an assortment of off-the-shelf Type-A tags which were characterised. These include a (T1) flexible smart sticker (DFRobot FIT0313), (T2)-(T3) fobs (MikroElectronika MIKROE-1475, DFRobot FIT0314), (T4) plastic nail (Adafruit Industries 1483), (T5) a generic smart card, (T6) a university access card, and (T7) a debit card. All tags had a single-size UID. To characterise the pause error ΔT_P, the tags were individually centered on top of the sensor node, parallel to the inductor windings. The pause-adjusted delay t_D was then estimated using 100 UID acquisition samples. Since only one sensor node was used in this experiment, the statistical variations in t_D could be directly attributed to ΔT_P. For each measurement, the transverse sensor-to-tag separation r could be adjusted using acrylonitrile butadiene styrene (ABS) dielectric spacers, while the input carrier power P_c could be varied up to 30 dBm.

For all tags, the delay t_D was highly sensitive to the phase of the HF carrier with respect to the bit modulation edges. Figure 6.6 shows histograms of t_D estimates for the smart card (T5) with $r = 0$ cm and $P_\mathrm{c} = 30$ dBm, obtained using random phase (blue), zero-degree phase (red), and 90-degree phase (green). The respective time variation ranges were 70.4 ns, 4.8 ns, and 6.4 ns, quantised by the sampling period of 1.6 ns. Tag microprocessors derive their internal clock signal from the HF carrier field [63], [244], [245], and the random phase estimates were expectedly

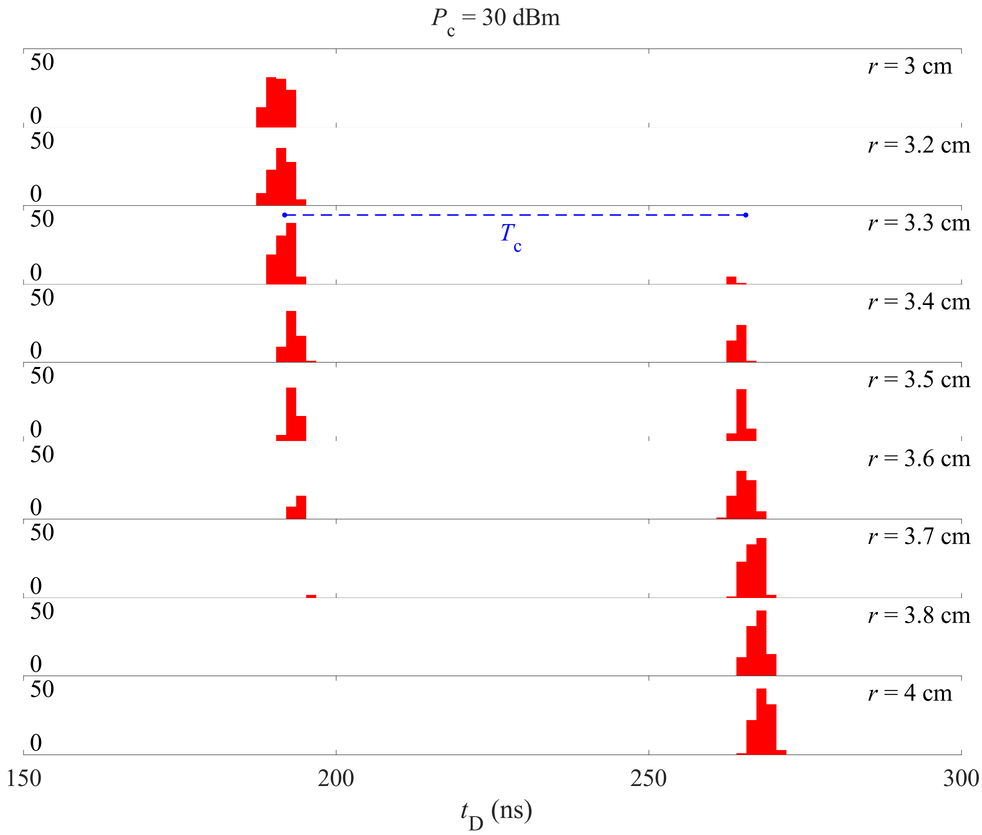

Figure 6.8. A gradual mode transition in the pause-adjusted frame delay t_D was observed at critical sensor-to-tag separation thresholds for the smart card (T5). Distributions became bimodal during the step transition, with lobes separated by a single carrier cycle.

bounded by a carrier cycle period $T_\mathrm{c} = 73.7$ ns. For fixed phase, however, t_D variability fell within four sampling periods, greatly improving consistency.

Figure 6.7 illustrates the effects of sensor-tag separation on the delay estimate t_D for the smart card (T5), with r varied from 0 cm to 10 cm using 30 dBm carrier power. Several observations can be made: 1) the delays were split into narrow response modes; 2) adjacent mode edges were separated by multiples of carrier cycle periods T_c; 3) the steps became more frequent with increasing sensor-to-tag separation. The total variability of t_D for the range shown was 344 ns ($4.66T_\mathrm{c}$), and the largest mode width of 9.6 ns was observed at $r = 10$ cm. The mode transitions, or splitting, occur at certain critical ranges, with a gradual sample redistribution from one mode to the next. The first such transition occurs between $r = 3$ cm and $r = 4$ cm sensor-to-tag separation, as highlighted by the shaded rectangle in Figure 6.7. Figure 6.8 presents a high-resolution snapshot of the transition, with the evolution of t_D updated at 1 mm intervals of sensor-tag-separation r. At $r = 3.2$ cm and 3.8 cm all 100 samples are contained within two distinct modes, with splitting

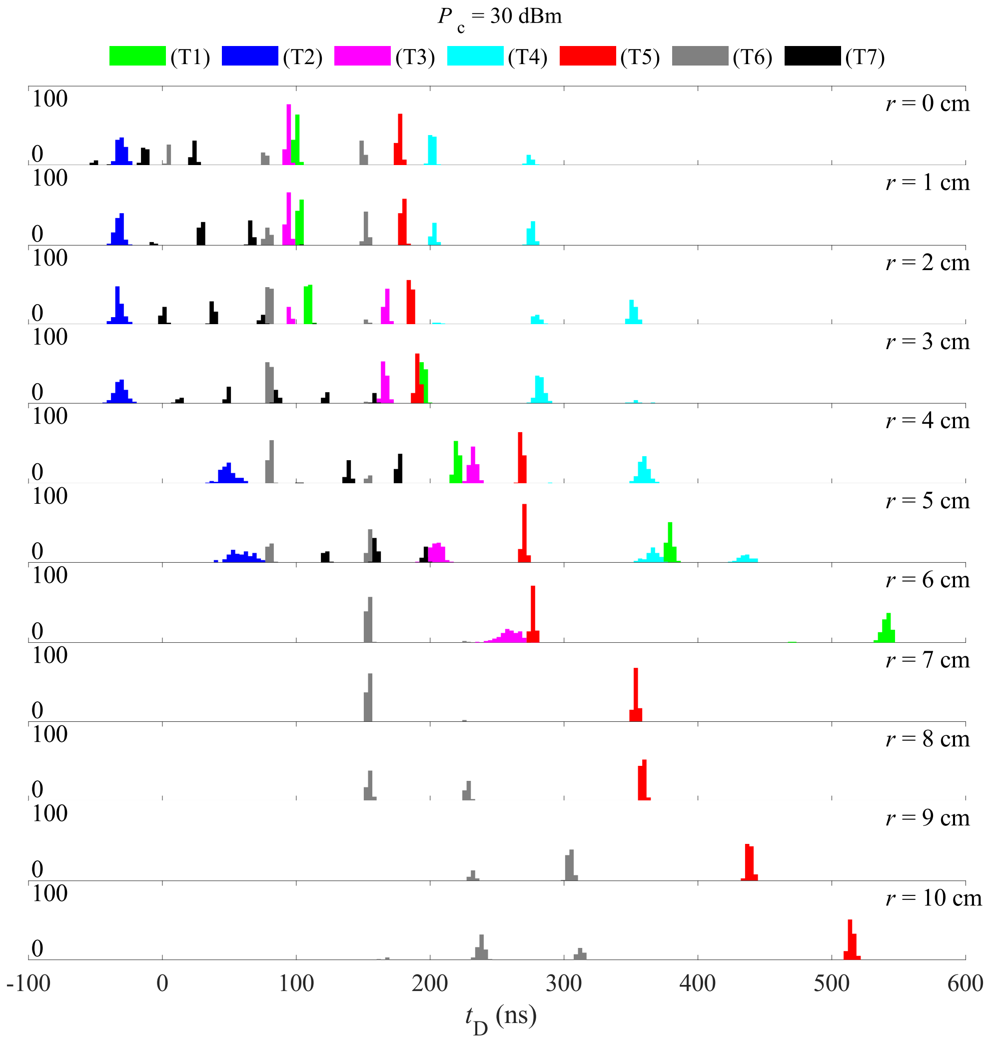

Figure 6.9. Pause adjusted delay distributions for a selection of tags (T1)-(T7) over a range of sensor-to-tag separations, with each distribution containing 100 samples.

occurring between $r = 3.3$ cm and 3.7 cm. The crossover range was $r = 3.5$ cm, with samples distributed evenly across the two modes.

This behaviour appeared universal for all tags tested. Figure 6.9 presents histograms depicting the variation of t_{D} with r for tags (T1) – (T7) using $P_{\mathrm{c}} = 30$ dBm. All tags demonstrated multiple modes, with the mean values becoming more delayed with increasing r. The rate of increase, however, varied with tag type, with the smart sticker (T1) having the largest variation of 449.6 ns. Expectedly, tags with smaller antennas had shorter read ranges. However, the debit card (T7) characteristics differed from other tags, such that the mode edges were spaced by half a carrier cycle, while the maximum range was shortest despite the tag dimensions. The differences can likely be attributed to the higher chip complexity warranted by financial applications. The impact of range on delays was weakest for r between 0 cm and 3 cm, where response modes were stable.

Further investigation showed that mode transitions were not a direct consequence of increased sensor-to-tag separation but were instead caused by an effective reduction in available power.

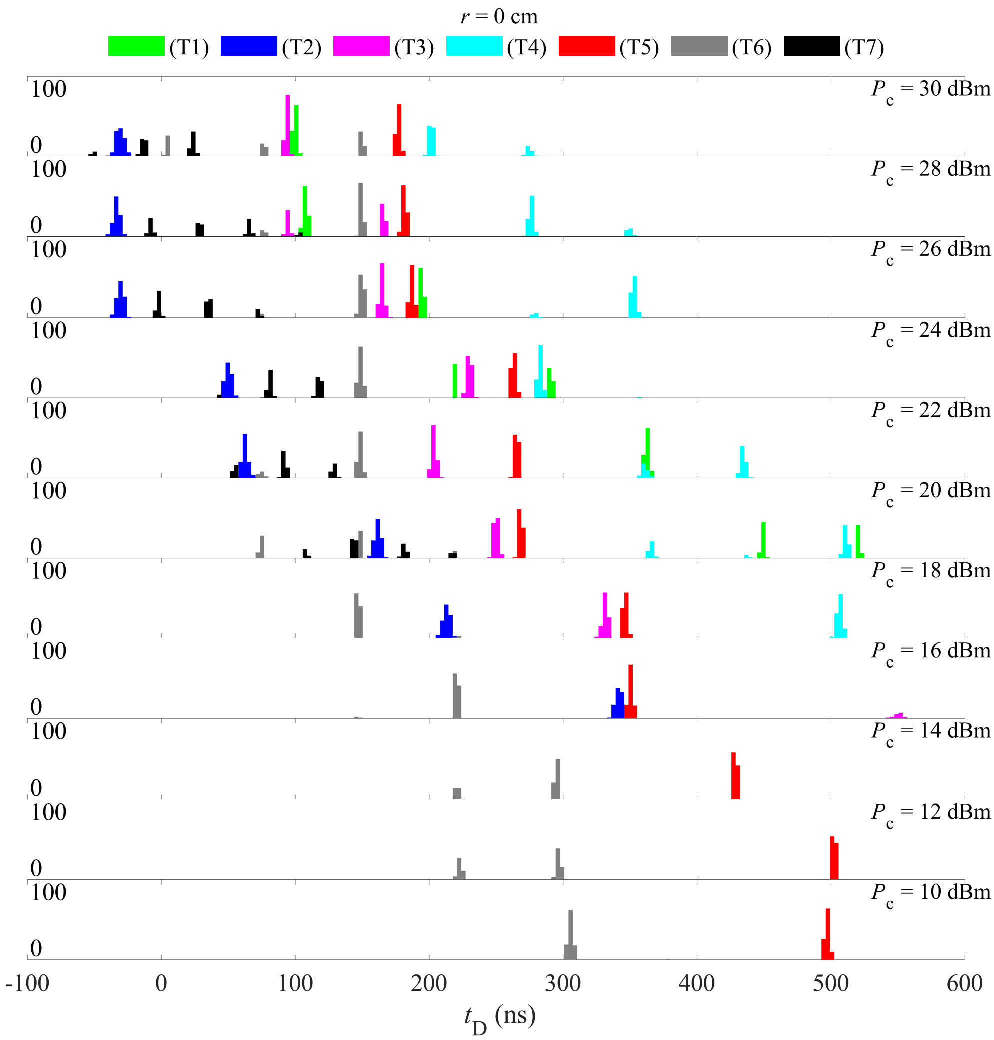

Figure 6.10. Distribution of pause-adjusted delays for tags (T1)-(T7) over a range of input carrier power, with sensor-tag separation fixed at 0 cm.

Figure 6.10 shows t_D histograms for tags (T1) – (T7) as P_c was reduced from 30 dBm to 10 dBm at 2 dBm intervals. The tags were placed directly on top of the sensor node with $r = 0$ cm. Clearly, the effects of increasing sensor-to-tag separation r and reducing reader carrier power P_c are equivalent, as confirmed by Figure 6.9 and Figure 6.10. This is expected, since magnetic near fields decay rapidly with increasing r, resulting in diminishing transmitted power. Monostatic localisation systems should ideally be operated at the smallest possible sensor-tag separation using fixed input carrier power to minimise the effect of range on the delay estimate.

6.5 System verification

This Section discusses the experimental verification of the proposed monostatic tag localisation system. The experimental LTL antenna had 16 sensor nodes and used a cable length of $d = 1.22$ m (optimised antenna with medium-length cables from Chapter 5). A high-power 50 Ω absorber was used to terminate one of the ends, as shown in Figure 6.5 (a). The sensor inductors had $L = 1.73$ μH, Q-factors of 250 at f_c, and a stray capacitance $C_p = 4.13$ pF. Capacitance C was set to 120 pF, while the value of K was tuned to 102 pF according to (6.4). The cable parameters were as in Table 5.1.

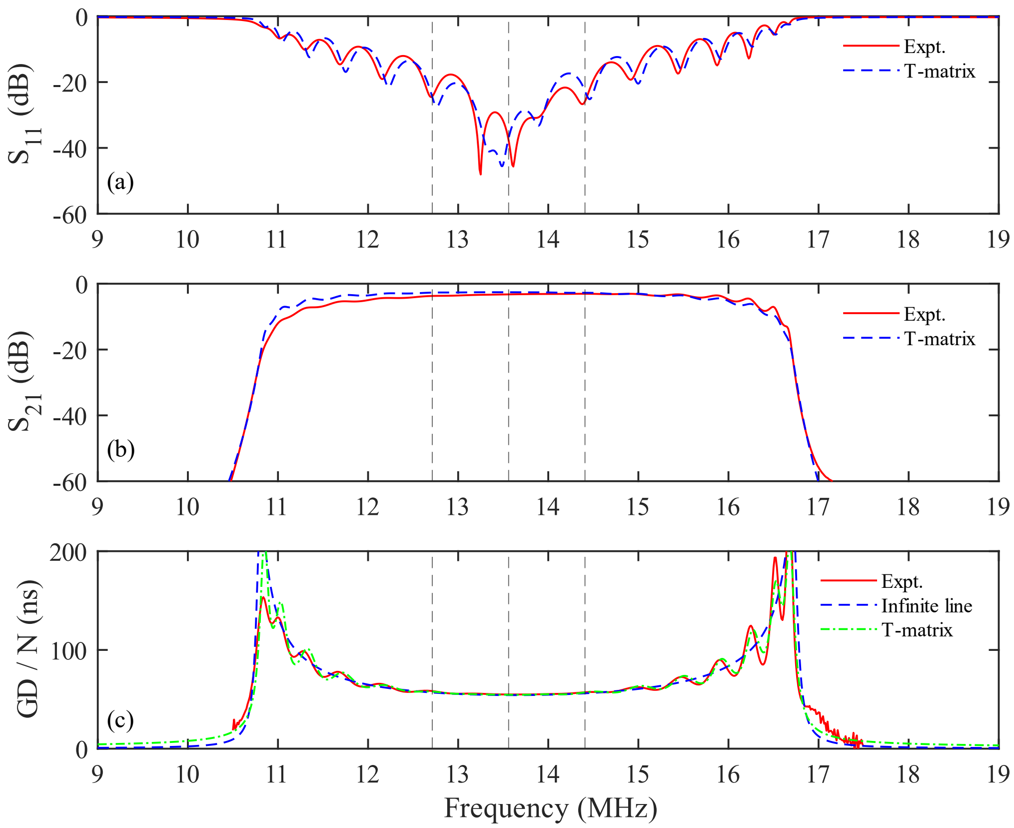

Figure 6.11. Theoretical and measured LTL antenna characteristics: (a)-(b) scattering parameters; (c) per-element group delay. Dashed lines indicate the carrier and subcarrier frequencies.

Figures 6.11 (a) and (b) compare the measured (solid red) scattering parameters of the antenna to theoretical ones (dashed blue), the latter obtained using an S-parameter transformation of the transmission matrix $(\boldsymbol{TS})^N\boldsymbol{T}$ with $N = 16$. Agreement is excellent. Figure 6.11 (c) compares the measured per-element group delay (solid red) with the analytic per-element group delay GD_e of an infinitely long waveguide (dashed blue), and that of a finite 16-element antenna simulated using the equivalent transmission matrix (dashed green). The analytic GD_e assumes perfect matching at all frequencies and thus lacks the ripples around the band edges, which are caused by matching to a real load. Agreement is again excellent. Measurements were made using a vector network analyser (Keysight E5061B). The measured per-element group delay was almost flat, varying from 55 ns at f_c to 58 ns at subcarrier frequencies, confirming that the LTL antenna had minimal dispersion.

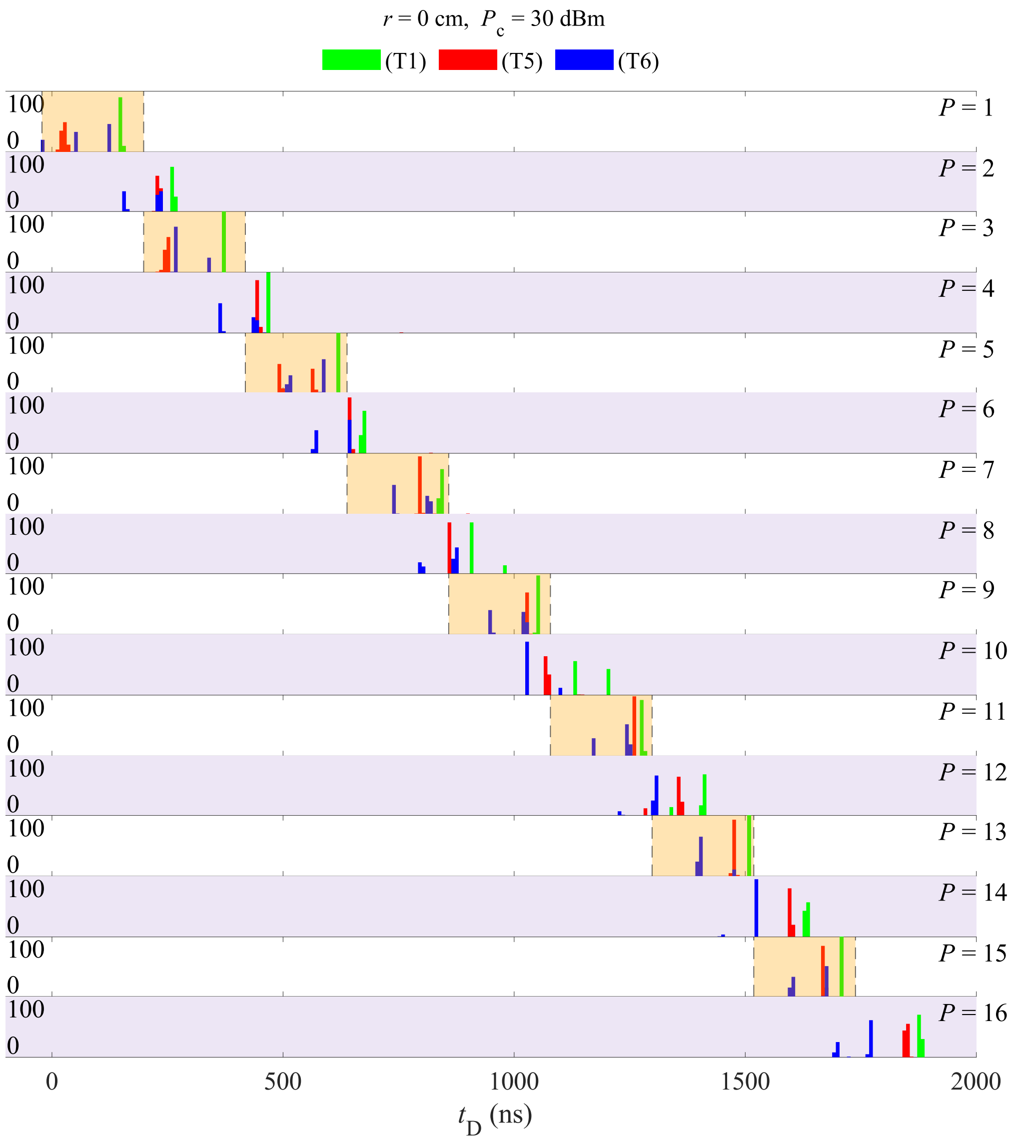

Figure 6.12. Distributions of pause-adjusted frame delays t_D obtained for node indices $P = 1$ to 16 using tags (T1), (T5), and (T6), with $r = 0$ cm and $P_\mathrm{c} = 30$ dBm.

For localisation, tags were sequentially placed at each sensor node, and 100 samples of t_{D} were collected at 0 cm sensor-to-tag separation and 30 dBm input carrier power. Figure 6.12 shows the pause-adjusted frame delay distributions t_{D} obtained for nodes 1 to 16 for the smart sticker (T1), smart card (T5), and a university key card (T6). As expected from (6.5), the response modes were delayed by each node index increment due to the additional antenna group delay t_{A} incurred by the transmitted reader query and the reflected tag response. The distribution shapes differed between node indices, which can be attributed to minor variations in transmitted power between sensors, either due to loss or standing waves. According to Figure 6.9, the variation range of t_{D} for tags (T1), (T5), and (T6) was $e = 174.4$ ns at $r = 0$ cm, while $t_{\mathrm{A}} \approx 110$ ns according to Figure 6.11 (c). Since $t_{\mathrm{A}} < e$, the per-element group delay was insufficiently high for precise localisation at every sensor node. This is confirmed by Figure 6.12 where, for example, the t_{D} estimates at $P = 2$ partially overlap with those at $P = 3$. The per-element group delay could, however, be increased by partitioning the elements into functional and non-functional nodes. The effective per-element delay was defined as $t'_{\mathrm{A}} = m \cdot t_{\mathrm{A}}$, such that every mth node was functional, with the rest used for their slow wave effect. The minimum required value of m was then $m = \lceil e/t_{\mathrm{A}} \rceil$ where "$\lceil . \rceil$" denotes the ceiling function. The current system had $m = 2$ and thus $N' = 8$ functional nodes with position indices $P' = 1 \ldots N'$.

The corresponding node partitioning is shown in Figure 6.12, with delay estimates obtained at non-functional nodes shaded in grey. Functional nodes were each assigned a unique response zone (shaded orange) of width $t'_{\mathrm{A}} = 220$ ns, starting with $P' = 1$. The functional node tag position P' could then be extracted correctly from the t_{D} estimate for all samples using the following mapping:

$$P' = \left\lceil \frac{t_{\mathrm{D}} - \min \Delta T_{\mathrm{P}}}{t'_{\mathrm{A}}} \right\rceil \tag{6.6}$$

Figure 6.13 shows the variation of the reflected UID signal power U measured at the receiver with the node index P for tags (T1), (T2), and (T6), normalised by the reflected tag power at the first sensor node $U_{P=1}$. The overall decay in power with tag position is representative of antenna losses, while the perturbations are indicative of standing waves, likely caused by slight variations in component values between sensor nodes. Such perturbations are most significant at the antenna ends. Expectedly, the recovered tag power was lowest at the last sensor, with total variability limited to 3.88 dB. The variation of reflected power along the antenna would naturally scale with the number of nodes, likely resulting in increased pause error uncertainty. Long antennas may thus

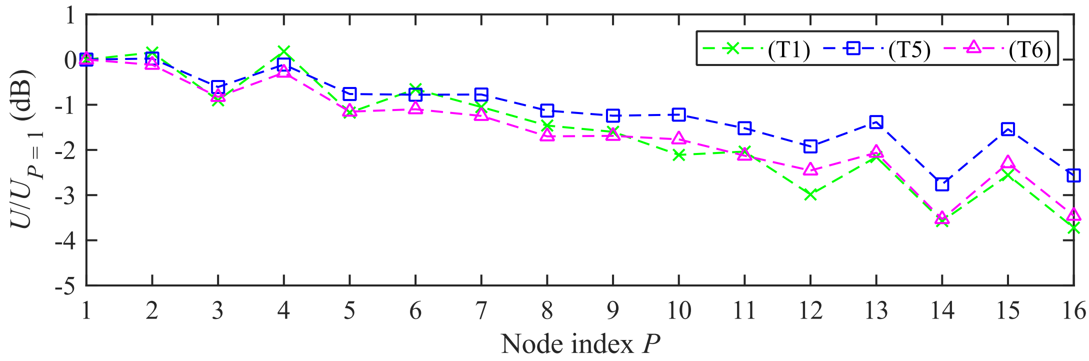

Figure 6.13. Variation of normalised extracted tag signal power with position index for tags (T1), (T5), and (T6) using $P_c = 30$ dBm.

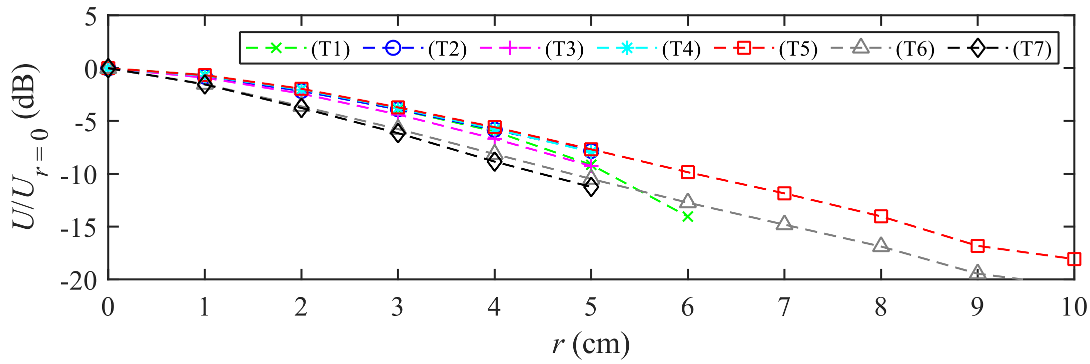

Figure 6.14. Variation of normalised extracted tag signal power with sensor-to-tag separation r for tags (T1) – (T7).

require higher group delay between functional nodes to compensate for increased e, or employ non-uniform response zones to compensate for the positive drift in ΔT_{P} as the carrier power decays at remote nodes.

Accurate monostatic localisation requires sensor-to-tag separation to be both low and equal across all sensor nodes. This requirement may be enforced by discarding t_{D} estimates for UID response samples with atypically low signal powers. Figure 6.14 shows the variation of tag response power U for tags (T1) – (T7) placed at the first sensor node, normalised by the extracted tag signal power at $r = 0$ cm ($U_{r=0}$). Reflected tag powers which diverge from the expected powers at the estimated node index (as in Figure 6.14) would thus indicate unsupported range. For the present system, the worst-case tag power attenuation was -3.7 dB (Figure 6.13), corresponding to the attenuation incurred by an increase in r from 0 cm to 3 cm (Figure 6.14). Samples with greater attenuation were discarded, thus limiting r to 3 cm. The extracted tag power can be cross-referenced with a local database created during an initial system calibration, containing a mapping between P and $U/U_{r=0}$. A mismatch between the extracted tag signal power and the expected tag signal power for the estimated node index would then indicate an invalid sensor-to-tag separation or a misalignment between the sensor and tag.

6.6 Conclusions

A monostatic NFC tag localisation system using an LTL slow wave antenna has been proposed and experimentally verified using a selection of off-the-shelf tags. Compared to bistatic systems, monostatic systems need neither a return signal cable nor a second receiver or filter-coupler. This reduction in complexity renders monostatic systems inherently cheaper, more practical, and deployable. Localisation is achieved by detecting small differences in tag UID response timings attributed to antenna group delay. Because accuracy depends on the variability between tag response fingerprints, all tags should be of the same make and model. The same localisation system can be used for tags with double- or triple-size UIDs by operating with the first four UID bytes obtained at the first cascade level. Accuracy can be improved by partitioning nodes into functional and non-functional nodes, employing the latter for their slow wave effect. Non-functional nodes may be realised using elements with ferrite-core solenoid inductors for field containment and miniaturisation. Alternatively, higher node inductances may be employed to increase the per-element group delay, albeit at the cost of additional signal distortion and increased antenna loss. Longer or shorter cable sections may also be used, based on application requirements.

RF power levels were modest (1W) and fields were well confined, implying inherent safety and low electromagnetic interference. The node separations and antenna lengths already demonstrated suggest potential applications in monitoring building traffic, warehouse management, and animal tracking, but the lack of protection against eavesdropping currently disbars security applications. Enhanced anticollision algorithms would be required to manage card clash at high traffic densities, but localisation merely requires the acquisition of a valid UID. Extension to topologies other than linear (for example, stars) could be achieved by using additional fixed delays to distinguish each branch. Learning algorithms could be used to identify node positions without needing accurate calibration. The localisation method is fundamentally analogous to monostatic radar range-finding over short distance of targets whose scattering involves signal transformation and delay, with the filter coupler acting as a duplexer. Consequently, other developments used to enhance radar performance may be applicable.

Future research may consider the localisation of active NFC-enabled devices such as smartphones, operated in either peer-to-peer or tag emulation modes. Communication between and positioning of battery-less NFC sensors may be of interest for internet-of-things and body-area network applications. Methods for system security enhancement through device fingerprinting can also be considered.

Chapter 7: Conclusions and Outlook

This work saw the development of all aspects of slow wave near field communication and localisation, including complete bistatic and monostatic positioning systems, flexible waveguide antenna topologies with distributed sensor nodes, high-performance RF components for receiver isolation, and power flow modelling methods for periodic waveguides. As far as we are aware, no work of this kind has been performed elsewhere in the world, and many novel component designs and system concepts have resulted. We now reflect on our findings and consider their implications for future work.

In Chapter 1 we reviewed the development history and prominent applications of radio-frequency identification systems, examined the characteristics of available near field communication specifications, and discussed the operating principles and limitations of reader-tag communication. Despite the large number of competing NFC and HF RFID standards, the NFC – A technology based on ISO/IEC 14443 Type–A was identified as the key protocol due to system cross-compatibility and extensive worldwide adoption. The primary limitations of near field communication were determined to be adverse field scaling with transverse range, antenna perimeter and capture volume limitations of individual loops, and the costly hardware overhead of multiplexed antenna array solutions. Recent capture volume enhancement methods employing magneto-inductive travelling-wave antennas were reviewed and found to enable lateral scaling at no detriment to hardware complexity, while simultaneously reducing reader power consumption in multiple-element systems.

In Chapter 2 we developed new magneto-inductive power-wave definitions, which can be used to extract scattering parameters and model internal power flow in waveguides with complex and frequency-dependent characteristic impedance. First, we reviewed the travelling- and power-wave definitions used for the characterisation of conventional transmission lines, highlighting their fundamentally different properties in the presence of propagation loss. Two sets of discrete magneto-inductive power waves were then defined and proven to satisfy the power conservation relations in lossy waveguides. Power-wave analysis was then conducted on multi-port magneto-inductive devices and shown to avoid the physical anomalies of travelling-wave scattering parameters. Finally, we demonstrated how analytic solutions for reflection and transmission coefficients may be converted to power-wave scattering parameters at the junctions between semi-infinite media. This work was inspired by difficulties in modelling MI waveguide NFC systems, the focus of this thesis, but has wider relevance to discrete metamaterials.

In Chapter 3 we designed, manufactured, and experimentally verified a family of frequency-selective filter-couplers based on magneto-inductive waveguides and described their application in high-power NFC readers for receiver isolation and carrier suppression. Analytic design equations were derived using magneto-inductive power-wave definitions and used to develop directional filters with real and complex characteristic impedance. Advanced single-passband filter topologies with infinite rejection using multipath loss compensation and multiple-passband filters with improved rejection were proposed. Three-port devices and filter cascades for frequency-division multiplexing were also discussed. Filters with tuneable transformer-coupled resonators were then fabricated and characterised. Experimental results were shown to be in good agreement with theoretical models, and extremely high performance (very high carrier rejection, combined with low sideband loss) was obtained. Finally, the filter power-handling characteristics were measured using realistic NFC–A signals and found to be linear despite the use of ferrite cores.

In Chapter 4 we introduced and experimentally demonstrated a novel bistatic tag localisation method which employed time-of-flight differences in tag response for accurate one-dimensional positioning using a slow wave magneto-inductive waveguide antenna. We first reviewed existing localisation methods in the high-frequency regime, which were almost entirely limited to multiplexed antenna arrays subject to costly hardware overheads. An improved technique was then proposed whereby reader queries were injected into a slow wave antenna at one end, and the corresponding reflected and transmitted tag identifiers were extracted from both antenna ends via matched filter-couplers. Pair-wise cross correlation of the lengthy tag responses was then used to estimate the time-of-flight difference with high processing gain and converted to a position estimate using the antenna group velocity. The trade-off between slow wave factor and group velocity dispersion was noted and antenna optimisation discussed. A simulation model of the complete system was constructed and used to analyse the effects of system parameters, noise, and tag identifier value on localisation accuracy. The theoretical model was then compared to an experimental system comprising a custom 1 W transceiver module, an 11-element ferrite-coupled magneto-inductive antenna, and off-the-shelf NFC-A transponders. Accurate localisation was demonstrated at all antenna elements up to the tag reading limit.

In Chapter 5 we investigated a new class of flexible slow wave antenna topologies, comprising distributed inductive sensor nodes linked by coaxial transmission lines, developed to address the impracticalities of magneto-inductive waveguide antennas. General characteristic equations for loaded transmission lines were first derived and used to select a suitable sensor configuration. Sensor parameters were then optimised using dispersion engineering for localisation and the effects of cable length analysed. Three experimental loaded transmission line antennas with 15 sensor nodes and cable sections of 0.3 m, 1.22 m, and 3 m were fabricated, resulting in total antenna lengths of 5.25 m, 20.0 m, and 48.5 m, respectively. These dimensions are already compatible with realistic building sizes. Waveguide scattering parameters and dispersion characteristics were measured and excellent agreement with the theoretical model demonstrated. Afterwards, each antenna was integrated with a custom NFC reader and shown to be capable of communication with and localisation of off-the-shelf NFC–A tags with different antenna form factors. Both one- and quasi two-dimensional antenna layouts were tested and accurate localisation up to the tag reading limit demonstrated. Significant improvements over magneto-inductive antennas were observed in terms of system practicality, scalability, signal distortion, and customisability.

In Chapter 6 we developed a novel monostatic tag localisation method using absolute time-of-flight estimates as measured by a single-receiver reader placed at the input of a loaded transmission line antenna. First, we briefly extended our analytic analysis of the waveguide antenna from Chapter 5, deriving topology-specific design equations and discussing parameter selection. We then defined the monostatic system architecture, where a transceiver injects a reader query at one antenna end via a filter-coupler. The delay between the last transmitted reader bit and the first modulation edge of the tag response is then estimated using cross-correlation with a reconstructed tag identifier. Since monostatic positioning is sensitive to tag timing errors, the pause in communication was statistically characterised for a selection of off-the-shelf NFC-A tags and the effects of transverse range, carrier power, and carrier phase investigated. It was then suggested that accurate localisation was possible provided the per-element antenna group delay exceeded the maximum tag delay error. Verification was conducted using the optimised loaded transmission line antenna with 16 sensor nodes and a high-precision custom transceiver. The antenna was then partitioned into functional and non-functional nodes, with the former used for localisation and the latter for the added slow wave effect. The estimated delay range was segmented into response zones and statistically consistent positioning achieved at 8 nodes using a linear mapping. Finally, we measured the variation of response signal power with position and sensor-tag separation.

In this work, we combined radio-frequency identification with metamaterial technology to develop unique slow wave systems for near field communication and localisation. Compared with previously demonstrated HF RFID localisation methods, the radar-like approach demonstrated here provides greatly improved accuracy using simple and scalable hardware. Potential applications include monitoring the transit of goods or people. However, because tag responses at one node may easily be read at another node, there is a significant possibility of eavesdropping. Applications are therefore likely to be limited to closed environments where security is relatively unimportant. Examples include monitoring automated warehouse robotics or providing physical verification of staff attendance at distributed locations for digital timesheets. Given the scope and novelty of the research, there exist numerous avenues for future development. We now discuss prospective research objectives in order of priority.

The reader protypes employed for bistatic and monostatic localisation in Chapters 4 – 6 were implemented using standard RF laboratory equipment. While very effective for proof-of-concept demonstrations, the transceivers were bulky, required a PC for post-processing, and were incapable of addressing tag responses in real time. The development of purpose-built and compact readers is essential for practical system deployment. The readers must also support bit frame anti-collision protocols to enable communication with and localisation of numerous tags simultaneously. Paired- and single-receiver models should be developed for bistatic and monostatic localisation, respectively. Standardised loaded transmission line antenna kits should also be designed. The experimental sensors employed in Chapters 5 – 6 were implemented using copper tubing and 3D-printed frames. Despite their excellent performance and low propagation loss, such designs may be impractical due to high fabrication costs and long assembly times. Sensors implemented entirely using printed circuit boards with a range of inductor dimensions and values should thus be developed. Corresponding non-functional nodes with low-loss ferrite-core inductors should be designed for increasing the group delay and physical separation between functional nodes. The antennas should be modular, easily reconfigurable, and inexpensive. With suitable hardware changes, such systems could be immediately deployed, and there are consequently strong possibilities for commercialisation.

Further experimental tests on monostatic localisation, the most practical embodiment, should be conducted. The variation of tag delay estimates with node index should be characterised for a wider range of tags and the effects of sensor-tag separation, incident carrier power, and antenna length analysed. Relationships between minimum carrier power and antenna length should be established experimentally. The feasibility of active device positioning (such as smartphones) may also be tested. Finally, monostatic localisation with numerous tags distributed along the antenna should be demonstrated, and the effects of tag loading (if any) on delay estimates analysed.

Extending localisation support to other proximity standards (namely NFC-B and NFC-F) is straightforward, requiring minor modifications to reader modulation schemes and bit codes. Adoption of vicinity protocols (NFC-V) is likely to significantly increase the maximum operating range due to reduced tag power requirements. Distributed vicinity localisation systems could be particularly useful in asset management applications. Extension to near field ultra-high frequency RFID is also of interest but may require significant changes to the slow wave antenna topology, reader design, and theoretical models.

Finally, learning algorithms and statistical methods may be developed to enhance positioning accuracy, particularly in the monostatic case, when (in contrast to the bistatic case) variable tag performance introduces uncertainties. Improvements to system security could be realised by tag fingerprinting, enabling (for example) the identification of cloned tags. Theoretical system models could also be improved by including tag loading effects, more sophisticated noise models, and accounting for antenna nonidealities. Such models could be used to develop artificial intelligence methods, increasing system robustness without lengthy hardware trials.

References

[1] C. Hülsmeyer, ‘Verfahren, um entfernte metallische gegenstände mittels elektrischer wellen einem beobachter zu melden’, DE165546C, Nov. 21, 1905.

[2] B. Evenor, ‘Process for radiotelegraphic or radiotelephonic communication’, US1744036A, Jan. 21, 1930.

[3] P. Nikitin, ‘Leon Theremin (Lev Termen)’, *IEEE Antennas Propag. Mag.*, vol. 54, no. 5, pp. 252–257, Oct. 2012.

[4] H. Stockman, ‘Communication by Means of Reflected Power’, *Proc. IRE*, vol. 36, no. 10, pp. 1196–1204, Oct. 1948.

[5] A. J. Minasy, ‘Apparatus for article theft detection’, US3696379A, Oct. 03, 1972.

[6] J. Welsh, R. Vaughan, and L. L. Gordon, ‘Article surveillance method and system’, CA947398A, May 14, 1974.

[7] J. Welsh and R. N. Vaughan, ‘Article surveillance’, US4063229A, Dec. 13, 1977.

[8] G. Lichtblau, ‘Electronic security system’, US3810147A, May 07, 1974.

[9] M. Reiss, H. Inhelder, G. King, and A. Palatnick, ‘Feasibility Study, Automatic Vehicle Identification System’, 1969.

[10] R. A. Hauslen, ‘The promise of automatic vehicle identification’, *IEEE Trans. Veh. Technol.*, vol. 26, no. 1, pp. 30–38, Feb. 1977.

[11] ‘Urban Corridor Demonstration Program Manhattan CBD-New Jersey Corridor. Automatic Bus Identification.’, Tri-State Regional Planning Commission, New York.; Urban Mass Transportation Administration, Washington, D.C.; Federal Highway Administration, Washington, D.C.; Office of the Secretary of Transportation, Washington, D.C.; Port Authority of New York and New Jersey. Tunnels and Bridges Research, PB235061, 1974.

[12] F. Sterzer, ‘Electronic License Plate for Motor Vehicles’, *RCA Rev.*, vol. 35, no. 2, 1974.

[13] A. R. Koelle, S. W. Depp, and R. W. Freyman, ‘Short-range radio-telemetry for electronic identification, using modulated RF backscatter’, *Proc. IEEE*, vol. 63, no. 8, pp. 1260–1261, 1975.

[14] W. Rossing, ‘Animal identification: introduction and history’, *Comput. Electron. Agric.*, vol. 24, no. 1, pp. 1–4, Nov. 1999.

[15] W. W. Bell, ‘Object identification system using an RF roll-call technique’, US3981011A, Sep. 14, 1976.

[16] C. A. Walton, ‘Personal identification and signaling system’, US4236068A, Nov. 25, 1980.

[17] C. A. Walton, ‘Portable radio frequency emitting identifier’, US4384288A, May 17, 1983.

[18] P. Davies, N. Ayland, and C. Hill, ‘Automatic vehicle identification for non-stop toll collection-the Virginia experience’, in *Second International Conference on Road Traffic Monitoring, 1989.*, Feb. 1989, pp. 133–137.

[19] D. J. Reitz, ‘Automatic Vehicle and Container Identification Using Radio Frequency Technology’, presented at the Facing the Challenge: The Intermodal Terminal of the Future: Papers Presented at the Conference on Intermodel Freight Terminal Design, March 2-5, 1986, New Orleans, Louisiana, Transportation Research Board, National Research Council, 1986, p. 123.

[20] L. Kumari, K. Narsaiah, M. K. Grewal, and R. K. Anurag, ‘Application of RFID in agri-food sector’, *Trends Food Sci. Technol.*, vol. 43, no. 2, pp. 144–161, Jun. 2015.

[21] *Radio frequency identification of animals — Technical concept — Technical Corrigendum 1*. ISO 11785:1996/Cor 1:2008, 2008.

[22] S. P. Curtis, ‘Transponder technologies, applications and benefits’, in *IEE Colloquium on Use of Electronic Transponders in Automation*, Feb. 1989, p. 2/1-2/8.

[23] D. R. McKenzie, ‘A step ahead for container tracing’, *Intermodal Age Int.*, Sep. 1988.

[24] D. M. Teller, R. Sheryll, and L. Ong, ‘Inventory control system’, US4961533A, Oct. 09, 1990.

[25] V. D. Hunt, A. Puglia, and M. Puglia, *RFID-A Guide to Radio Frequency Identification*. New York: John Wiley and Sons, 2007.

[26] C. M. Walker and W. K. Brockelsby, ‘Automatic vehicle identification (AVI) technology design considerations for highway applications’, in *[1991 Proceedings] 41st IEEE Vehicular Technology Conference*, May 1991, pp. 805–811.

[27] J. Schurmann and H. Meier, ‘TIRIS–Leader in radio frequency identification technology’, *Tex. Instrum. Tech. J.*, vol. 10, no. 6, 1993.

[28] K. E. Mayes and C. Cid, ‘The MIFARE Classic story’, *Inf. Secur. Tech. Rep.*, vol. 15, no. 1, pp. 8–12, Feb. 2010.

[29] D. McElroy and E. Turban, ‘Smart Cards’, in *Handbook on Electronic Commerce*, M. Shaw, R. Blanning, T. Strader, and A. Whinston, Eds., in International Handbooks on Information Systems. Berlin, Heidelberg: Springer, 2000, pp. 289–311. doi: 10.1007/978-3-642-58327-8_14.

[30] K. M. Shelfer and J. D. Procaccino, ‘Smart card evolution’, *Commun. ACM*, vol. 45, no. 7, pp. 83–88, Jul. 2002.

[31] *Identification cards — Contactless integrated circuit(s) cards*. ISO/IEC 10536, 1992.

[32] *Cards and security devices for personal identification — Contactless proximity objects*. ISO/IEC 14443, 2000.

[33] *Identification cards — Contactless integrated circuit(s) cards — Vicinity cards*. ISO/IEC 15693, 2000.

[34] *EMV Level 1 Specifications for Payment Systems — EMV Contactless Interface Specification*. EMVCo, 2022.

[35] T. Deleruyelle and P. Pannier, ‘Miniaturized HF RFID Antennas for Contactless Payment Devices’, *IEEE J Radio Freq Identif.*, vol. 6, pp. 202–208, 2022.

[36] *Machine Readable Travel Documents – Part 10: Logical Data Structure (LDS) for Storage of Biometrics and Other Data in the Contactless Integrated Circuit (IC)*. International Civil Aviation Organization, 2021.

[37] A. Atanasiu and M. I. Mihailescu, ‘Biometric passports (ePassports)’, in *2010 8th International Conference on Communications*, 2010, pp. 443–446.

[38] P. Rakers, L. Connell, T. Collins, and D. Russell, ‘Secure contactless smartcard ASIC with DPA protection’, *IEEE J Solid-State Circuits*, vol. 36, no. 3, pp. 559–565, 2001.

[39] *CNA Handbook - Calypso Networks Association*. Accessed: Jun. 06, 2023. [Online]. Available: https://calypsonet.org/document/cna-handbook/

[40] S. Sarma, D. L. Brock, and K. Ashton, ‘The networked physical world’, *Auto-ID Cent. White Pap. MIT-AUTOID-WH-001*, pp. 1–16, 2000.

[41] S. Sarma, ‘A History of the EPC’, 2006.

[42] *Information technology — Radio frequency identification for item management — Part 6: Parameters for air interface communications at 860 MHz to 960 MHz*. ISO/IEC 18000-6, 2004.

[43] ‘Sony Global - Press Release - Philips and Sony announce strategic cooperation to define next generation near field radio-frequency communications electronics leaders to jointly establish wireless technology to significantly enhance access to data and services via consumer devices.’ https://www.sony.com/en/SonyInfo/News/Press_Archive/200209/02-0905E/ (accessed Jun. 18, 2023).

[44] *ECMA340—Near Field Communication Interface and Protocol (NFCIP-1)*. European Computer Manufacturers Association, 2002.

[45] *Information technology - Telecommunications and information exchange between systems - Near Field Communication - Interface and Protocol (NFCIP-1)*. ISO/IEC 18092:2004, 2004.

[46] U. Biader Ceipidor, C. Medaglia, A. Moroni, G. Orlandi, and S. Sposato, ‘NFC: Integration between RFID and Mobile, state of the art and future developments’, in *RFIDays 2008-Books of Proceedings*, G. Marrocco, 2008, pp. 76–79.

[47] T. Sanpechuda and L. Kovavisaruch, ‘A review of RFID localization: Applications and techniques’, in *2008 5th International Conference on Electrical Engineering/Electronics, Computer, Telecommunications and Information Technology*, May 2008, pp. 769–772.

[48] C. Li, L. Mo, and D. Zhang, ‘Review on UHF RFID Localization Methods’, *IEEE J. Radio Freq. Identif.*, vol. 3, no. 4, pp. 205–215, Dec. 2019.

[49] A. Decourtye *et al.*, ‘Honeybee tracking with microchips: a new methodology to measure the effects of pesticides’, *Ecotoxicology*, vol. 20, no. 2, pp. 429–437, Mar. 2011.

[50] M. van der Sluis, Y. de Haas, B. de Klerk, T. B. Rodenburg, and E. D. Ellen, ‘Assessing the Activity of Individual Group-Housed Broilers Throughout Life Using a Passive Radio Frequency Identification System—A Validation Study’, *Sensors*, vol. 20, no. 13, Art. no. 13, Jan. 2020.

[51] B. Khoo, ‘RFID- from Tracking to the Internet of Things: A Review of Developments’, in *2010 IEEE/ACM Int’l Conference on Green Computing and Communications & Int’l Conference on Cyber, Physical and Social Computing*, Dec. 2010, pp. 533–538.

[52] A. Lazaro, R. Villarino, and D. Girbau, ‘A Survey of NFC Sensors Based on Energy Harvesting for IoT Applications’, *Sensors*, vol. 18, no. 11, Art. no. 11, Nov. 2018.

[53] S. Olenik, H. S. Lee, and F. Güder, 'The future of near-field communication-based wireless sensing', *Nat. Rev. Mater.*, vol. 6, no. 4, Art. no. 4, Apr. 2021.

[54] J. Kim *et al.*, 'Miniaturized Battery-Free Wireless Systems for Wearable Pulse Oximetry', *Adv. Funct. Mater.*, vol. 27, no. 1, p. 1604373, 2017.

[55] S. P. Lee *et al.*, 'Highly flexible, wearable, and disposable cardiac biosensors for remote and ambulatory monitoring', *Npj Digit. Med.*, vol. 1, no. 1, Art. no. 1, Jan. 2018.

[56] G. Xu *et al.*, 'Smartphone-based battery-free and flexible electrochemical patch for calcium and chloride ions detections in biofluids', *Sens. Actuators B Chem.*, vol. 297, p. 126743, Oct. 2019.

[57] P. Teengam *et al.*, 'NFC-enabling smartphone-based portable amperometric immunosensor for hepatitis B virus detection', *Sens. Actuators B Chem.*, vol. 326, p. 128825, Jan. 2021.

[58] H. Zhang *et al.*, 'Wireless, battery-free optoelectronic systems as subdermal implants for local tissue oximetry', *Sci. Adv.*, vol. 5, no. 3, p. eaaw0873, Mar. 2019.

[59] G. Barandun *et al.*, 'Cellulose Fibers Enable Near-Zero-Cost Electrical Sensing of Water-Soluble Gases', *ACS Sens.*, vol. 4, no. 6, pp. 1662–1669, Jun. 2019.

[60] A. Hajiaghajani, A. H. Afandizadeh Zargari, M. Dautta, A. Jimenez, F. Kurdahi, and P. Tseng, 'Textile-integrated metamaterials for near-field multibody area networks', *Nat. Electron.*, vol. 4, no. 11, Art. no. 11, Nov. 2021.

[61] Y.-S. Chang, C.-L. Chang, Y.-S. Hung, and C.-T. Tsai, 'Ncash: NFC Phone-Enabled Personalized Context Awareness Smart-Home Environment', *Cybern. Syst.*, vol. 41, no. 2, pp. 123–145, Apr. 2010.

[62] *RFID Forecasts, Players and Opportunities 2023-2033*. 2023. Accessed: Jun. 22, 2023. [Online]. Available: https://www.idtechex.com/en/research-report/rfid-forecasts-players-and-opportunities-2023-2033/927

[63] K. Finkenzeller, *Fundamentals and applications in contactless smart cards, radio frequency identification and near-field communication*, 3rd ed. Chichester, West Sussex ; Hoboken, NJ: Wiley, 2010.

[64] V. Coskun, B. Ozdenizci, and K. Ok, 'The Survey on Near Field Communication', *Sensors*, vol. 15, no. 6, Art. no. 6, Jun. 2015.

[65] R. Want, 'Near field communication', *IEEE Pervasive Comput.*, vol. 10, no. 3, pp. 4–7, Jul. 2011.

[66] 'NFC Forum Specifications'. Accessed: Sep. 17, 2023. [Online]. Available: https://nfc-forum.org//build/specifications/

[67] N. S. S. Shobha, K. S. P. Aruna, M. D. P. Bhagyashree, and K. S. J. Sarita, 'NFC and NFC payments: A review', in *2016 International Conference on ICT in Business Industry & Government (ICTBIG)*, Nov. 2016, pp. 1–7.

[68] G. P. Hancke, 'Security of proximity identification systems'. doi: 10.48456/TR-752.

[69] G. P. Hancke, 'Practical eavesdropping and skimming attacks on high-frequency RFID tokens', *J. Comput. Secur.*, vol. 19, no. 2, pp. 259–288, Mar. 2011.

[70] L. Malina, P. Dzurenda, J. Hajny, and Z. Martinasek, 'Assessment of Cryptography Support and Security on Programmable Smart Cards', in *2018 41st International Conference on Telecommunications and Signal Processing (TSP)*, Jul. 2018, pp. 1–5.

[71] P. Nunes-Silva *et al.*, 'Applications of RFID technology on the study of bees', *Insectes Sociaux*, vol. 66, pp. 15–24, Sep. 2018.

[72] K. Zhang, Z. Li, Z. Meng, W. Zhou, N. Gao, and Z. Zhang, 'UHF-HF Integrated RFID Sensor: A Novel Information Interface for Industrial Integration', *IEEE Sens J*, vol. 22, no. 15, pp. 15477–15487, 2022.

[73] *Devices Requirements: High Level Conformance Requirements*, Version 3.1.00. NFC Forum, 2021.

[74] *Cards and security devices for personal identification — Contactless proximity objects — Part 1: Physical characteristics*. ISO/IEC 14443-1:2018, 2018.

[75] *Cards and security devices for personal identification — Contactless proximity objects — Part 2: Radio frequency power and signal interface*. ISO/IEC 14443-2:2020+A1:2021, 2021.

[76] *Cards and security devices for personal — Contactless proximity objects — Part 3: initialisation and anticollision*. ISO/IEC 14443-3:2018+A1:2021, 2021.

[77] *Cards and security devices for personal identification — Contactless proximity objects — Part 4: Transmission protocol*. ISO/IEC 14443-4:2018, 2018.

[78] *Specification of implementation for integrated circuit cards — Part 1: Integrated circuit cards with contacts*. JSA - JIS X 6319-1, 2023.

[79] *Specification of implementation for integrated circuit cards — Part 2: Proximity cards*. JIS X 6319-2, 2023.

[80] *Specification of implementation for integrated circuit(s) cards — Part 3: Common commands for interchange*. JIS X 6319-3, 2023.

[81] *Specification of implementation for integrated circuit(s) cards — Part 4: High speed proximity cards*. JIS X 6319-4, 2020.

[82] *Information technology — Telecommunications and information exchange between systems — Near Field Communication — Interface and Protocol (NFCIP-1) — Technical Corrigendum 1*. ISO/IEC 18092:2013/Cor 1:2015, 2015.

[83] *Cards and security devices for personal identification — Contactless vicinity objects — Part 1: Physical characteristics*. ISO/IEC 15693-1:2018, 2018.

[84] *Cards and security devices for personal identification — Contactless vicinity objects — Part 2: Air interface and initialization*. ISO/IEC 15693-2:2019, 2019.

[85] *Cards and security devices for personal identification — Contactless vicinity objects — Part 3: Anticollision and transmission protocol*. ISO/IEC 15693-3:2019, 2019.

[86] *Analog Technical Specification*, Version 2.0. NFC Forum, 2016.

[87] *Digital Protocol Technical Specification*, Version 2.2. NFC Forum, 2019.

[88] 'PN7120 Antenna Design and Matching Guide', NXP, AN11564, Apr. 2016.

[89] Texas Instruments, 'TRF7970A evaluation module (EVM)', Datasheet SLOU321A, 2011.

[90] Texas Instruments, 'TRF7970A multiprotocol fully integrated 13.56-MHz RFID and near field communication (NFC) transceiver IC', Datasheet SLOS743K, 2011.

[91] I. Kirschenbaum and A. Wool, 'How to build a low-cost, extended-range RFID skimmer', in *Proc. 15th USENIX Security Symp., Vancouver, CA, July 31-Aug 4*, 2006, pp. 43–57.

[92] J. Zirbesegger, M. Gebhart, E. Merlin, and E. Leitgeb, 'Extending the analogue performance of integrated 13.56 MHz proximity reader chips', *E Elektrotechnik Informationstechnik*, vol. 124, no. 11, pp. 369–375, Nov. 2007.

[93] R. Habraken, P. Dolron, E. Poll, and J. de Ruiter, 'An RFID Skimming Gate Using Higher Harmonics', in *Radio Frequency Identification*, S. Mangard and P. Schaumont, Eds., in Lecture Notes in Computer Science. Cham: Springer International Publishing, 2015, pp. 122–137.

[94] R. R. A. Syms, O. Sydoruk, and M. C. K. Wiltshire, 'Magneto-Inductive HF RFID System', *IEEE J. Radio Freq. Identif.*, vol. 5, no. 2, pp. 148–153, Jun. 2021.

[95] 'Mic3-TAG 16 knit', microSensys, Germany.

[96] *Identification cards — Physical characteristics*. ISO/IEC 7810:2019, 2019.

[97] 'Impedance Matching for Near Field Communication Applications', Würth Elektronik, ANP084.

[98] W. Aerts, E. De Mulder, B. Preneel, G. A. E. Vandenbosch, and I. Verbauwhede, 'Dependence of RFID Reader Antenna Design on Read Out Distance', *IEEE Trans. Antennas Propag.*, vol. 56, no. 12, pp. 3829–3837, Dec. 2008.

[99] M. Soma, D. C. Galbraith, and R. L. White, 'Radio-Frequency Coils in Implantable Devices: Misalignment Analysis and Design Procedure', *IEEE Trans. Biomed. Eng.*, vol. BME-34, no. 4, pp. 276–282, Apr. 1987.

[100] M. Misakian, 'Equations for the magnetic field produced by one or more rectangular loops of wire', *J Res Natl Inst Stand Technol*, vol. 105, pp. 557–564, 2000.

[101] E. Weber, *Electromagnetic theory*. New York: Dover, 1965.

[102] F. Pfeiffer, K. Finkenzeller, and E. Biebl, 'Theoretical Limits of ISO/IEC 14443 type A RFID Eavesdropping Attacks', in *Smart SysTech 2012; European Conference on Smart Objects, Systems and Technologies*, Jun. 2012, pp. 1–9.

[103] K. Finkenzeller, F. Pfeiffer, and E. Biebl, 'Range extension of an ISO/IEC 14443 type A RFID system with actively emulating load modulation', in *Proc. RFIDSysTech.'11, Dresden, Germany, May 17-18*, 2011.

[104] M. Engelhardt, F. Pfeiffer, K. Finkenzeller, and E. Biebl, 'Extending ISO/IEC 14443 Type A eavesdropping range using higher harmonics', in *Proc. European Conf. Smart Objects, Systems and Technologies (SmartSysTech), Erlangen, Germany, June 11-12*, 2013, pp. 1–8.

[105] A. Boryssenko and E. Boryssenko, 'Antenna array design for HF RFID smart cabinet', in *2011 IEEE International Conference on Microwaves, Communications, Antennas and Electronic Systems (COMCAS 2011)*, IEEE, 2011, pp. 1–3.

[106] M. Benamara *et al.*, 'A Twisted Loop Antenna to enhance HF RFID detection for different tag positioning', presented at the 2016 10th European Conference on Antennas and Propagation (EuCAP), IEEE, Apr. 2016.

[107] M. Benamara, M. Grzeskowiak, M. Salhi, G. Lissorgues, A. Diet, and Y. Le Bihan, '3D HF RFID reader antenna for tag detection in different angular orientations', in *2016 Loughborough Antennas & Propagation Conference (LAPC)*, 2016, pp. 1–4.

[108] H. Hirayama, Y. Satake, N. Kikuma, and K. Sakakibara, 'Improvement of null zone avoidance capability for HF-band RFID using diversity combining of loop antennas', in *2009 3rd European Conference on Antennas and Propagation*, 2009, pp. 1594–1597.

[109] X. Li, J. Sidén, H. Andersson, and T. Schön, 'A Paper-Based Screen Printed HF RFID Reader Antenna System', *IEEE J Radio Freq Identif. Identif.*, vol. 2, no. 3, pp. 118–126, 2018.

[110] A. C. Alba *et al.*, 'Use of passive radio frequency identification technologies to monitor nest usage in the northern carmine bee-eater (Merops n. nubicus)', *Zoo Biol*, vol. 38, no. 6, pp. 498–507, 2019.

[111] Y. Mehlman, P. Kumar, M. Ozatay, S. Wagner, J. C. Sturm, and N. Verma, 'Large-Area Electronics HF RFID Reader Array for Object-Detecting Smart Surfaces', *IEEE Solid-State Circuits Lett.*, vol. 1, no. 8, pp. 182–185, Aug. 2018.

[112] L. Brillouin, *Wave propagation in periodic structures: electric filters and crystal lattices*, 2. ed. with corr. and Add. in Dover books on engineering and engineering physics. New York: Dover Publications, 1953.

[113] D. R. Smith, W. J. Padilla, D. C. Vier, S. C. Nemat-Nasser, and S. Schultz, 'Composite Medium with Simultaneously Negative Permeability and Permittivity', *Phys. Rev. Lett.*, vol. 84, no. 18, pp. 4184–4187, May 2000.

[114] V. G. Veselago, 'The Electrodynamics of Substances with Simultaneously Negative Values of ε and μ.', *Sov. Phys. Uspekhi*, vol. 10, no. 4, pp. 509–514, Apr. 1968.

[115] E. Shamonina, V. A. Kalinin, K. H. Ringhofer, and L. Solymar, 'Magneto-inductive waveguide', *Electron. Lett.*, vol. 38, no. 8, p. 371, 2002.

[116] R. A. Shelby, D. R. Smith, and S. Schultz, 'Experimental Verification of a Negative Index of Refraction', *Science*, vol. 292, no. 5514, pp. 77–79, Apr. 2001.

[117] E. Shamonina, V. A. Kalinin, K. H. Ringhofer, and L. Solymar, 'Magnetoinductive waves in one, two, and three dimensions', *J Appl Phys*, vol. 92, pp. 6252–6261, 2002.

[118] M. C. K. Wiltshire, E. Shamonina, I. R. Young, and L. Solymar, 'Dispersion characteristics of magneto-inductive waves: comparison between theory and experiment', *Electron. Lett.*, vol. 39, no. 2, p. 215, 2003.

[119] M. J. Freire, R. Marqués, F. Medina, M. A. G. Laso, and F. Martín, 'Planar magnetoinductive wave transducers: Theory and applications', *Appl. Phys. Lett.*, vol. 85, no. 19, pp. 4439–4441, Nov. 2004.

[120] G. Dolling, M. Wegener, A. Schädle, S. Burger, and S. Linden, 'Observation of magnetization waves in negative-index photonic metamaterials', *Appl. Phys. Lett.*, vol. 89, no. 23, Dec. 2006.

[121] I. V. Shadrivov, A. N. Reznik, and Y. S. Kivshar, ‘Magnetoinductive waves in arrays of split-ring resonators’, *Phys. B Condens. Matter*, vol. 394, no. 2, pp. 180–183, May 2007.

[122] N. Liu, S. Kaiser, and H. Giessen, ‘Magnetoinductive and Electroinductive Coupling in Plasmonic Metamaterial Molecules’, *Adv. Mater.*, vol. 20, no. 23, pp. 4521–4525, Dec. 2008.

[123] J. D. Baena, L. Jelinek, R. Marqués, and M. Silveirinha, ‘Unified homogenization theory for magnetoinductive and electromagnetic waves in split-ring metamaterials’, *Phys. Rev. A*, vol. 78, no. 1, Jul. 2008.

[124] H. Liu, Y. M. Liu, T. Li, S. M. Wang, S. N. Zhu, and X. Zhang, ‘Coupled magnetic plasmons in metamaterials’, *Phys. Status Solidi B*, vol. 246, no. 7, pp. 1397–1406, May 2009.

[125] S. Campione, F. Mesa, and F. Capolino, ‘Magnetoinductive Waves and Complex Modes in Two-Dimensional Periodic Arrays of Split Ring Resonators’, *IEEE Trans. Antennas Propag.*, vol. 61, no. 7, pp. 3554–3563, Jul. 2013.

[126] C. J. Stevens, Y. Li, and C. W. T. Chan, ‘Forward magneto-inductive wave propagation in planar magnetically coupled capacitor grids’, *J. Electromagn. Waves Appl.*, vol. 29, no. 6, pp. 753–762, Mar. 2015.

[127] A. Radkovskaya *et al.*, ‘An experimental study of the properties of magnetoinductive waves in the presence of retardation’, *J. Magn. Magn. Mater.*, vol. 300, no. 1, pp. 29–32, May 2006.

[128] O. Zhuromskyy, E. Shamonina, and L. Solymar, ‘Effect of radiation on dispersion of magneto-inductive waves in a metamaterial’, presented at the Congress on Optics and Optoelectronics, SPIE, Sep. 2005.

[129] R. R. A. Syms, O. Sydoruk, E. Shamonina, and L. Solymar, ‘Higher order interactions in magneto-inductive waveguides’, *Metamaterials*, vol. 1, no. 1, pp. 44–51, 2007.

[130] R. R. A. Syms, E. Shamonina, and L. Solymar, ‘Positive and negative refraction of magnetoinductive waves in two dimensions’, *Eur. Phys. J. B*, vol. 46, no. 2, pp. 301–308, Jul. 2005.

[131] S. Chu, M. S. Luloff, J. Yan, P. Petrov, C. J. Stevens, and E. Shamonina, ‘Magnetoinductive waves in attenuating media’, *Sci. Rep.*, vol. 11, no. 1, Art. no. 1, Apr. 2021.

[132] O. Sydoruk, ‘Tailoring the properties of metamaterials for linear and nonlinear applications’, Osnabrück University, 2007.

[133] R. R. A. Syms and L. Solymar, ‘Magneto-inductive phase-shifters and interferometers’, *Metamaterials*, vol. 5, no. 4, pp. 155–161, Dec. 2011.

[134] R. R. A. Syms, E. Shamonina, and L. Solymar, ‘Magneto-inductive waveguide devices’, *IEE Proc. - Microw. Antennas Propag.*, vol. 153, no. 2, p. 111, 2006.

[135] O. Sydoruk, ‘Resistive power divider for magneto-inductive waveguides’, *Electron. Lett.*, vol. 47, no. 9, p. 549, 2011.

[136] F. J. Herraiz-Martinez, F. Paredes, G. Zamora Gonzalez, F. Martin, and J. Bonache, ‘Printed Magnetoinductive-Wave (MIW) Delay Lines for Chipless RFID Applications’, *IEEE Trans. Antennas Propag.*, vol. 60, no. 11, pp. 5075–5082, Nov. 2012.

[137] C. J. Stevens, C. W. T. Chan, K. Stamatis, and D. J. Edwards, 'Magnetic Metamaterials as 1-D Data Transfer Channels: An Application for Magneto-Inductive Waves', *IEEE Trans. Microw. Theory Tech.*, vol. 58, no. 5, pp. 1248–1256, May 2010.

[138] C. W. T. Chan and C. J. Stevens, 'Two-dimensional magneto-inductive wave data structures', in *Proceedings of the EUCAP Conference*, 2011, pp. 1071–1075.

[139] B. Gulbahar and O. B. Akan, 'A Communication Theoretical Modeling and Analysis of Underwater Magneto-Inductive Wireless Channels', *IEEE Trans. Wirel. Commun.*, vol. 11, no. 9, pp. 3326–3334, Sep. 2012.

[140] Z. Sun and I. F. Akyildiz, 'Magnetic induction communications for wireless underground sensor networks', *IEEE Trans Antennas Propag*, vol. 58, no. 7, pp. 2426–2435, 2010.

[141] Z. Sun, I. F. Akyildiz, S. Kisseleff, and W. Gerstacker, 'Increasing the Capacity of Magnetic Induction Communications in RF-Challenged Environments', *IEEE Trans. Commun.*, vol. 61, no. 9, pp. 3943–3952, Sep. 2013.

[142] C. J. Stevens, 'Magnetoinductive Waves and Wireless Power Transfer', *IEEE Trans. Power Electron.*, vol. 30, no. 11, pp. 6182–6190, Nov. 2015.

[143] C. J. Stevens, 'A magneto-inductive wave wireless power transfer device', *Wirel. Power Transf.*, vol. 2, no. 1, pp. 51–59, Mar. 2015.

[144] I. Khromova and C. J. Stevens, 'Harnessing Magneto-inductive Waves for Wireless Power Transfer', presented at the 2018 IEEE Wireless Power Transfer Conference (WPTC), IEEE, Jun. 2018.

[145] W. Zhong, C. K. Lee, and S. Y. R. Hui, 'General Analysis on the Use of Tesla's Resonators in Domino Forms for Wireless Power Transfer', *IEEE Trans. Ind. Electron.*, vol. 60, no. 1, pp. 261–270, Jan. 2013.

[146] G. Puccetti, C. Stevens, U. Reggiani, and L. Sandrolini, 'Experimental and Numerical Investigation of Termination Impedance Effects in Wireless Power Transfer via Metamaterial', *Energies*, vol. 8, no. 3, pp. 1882–1895, Mar. 2015.

[147] M. J. Freire and R. Marqués, 'Planar magnetoinductive lens for three-dimensional subwavelength imaging', *Appl. Phys. Lett.*, vol. 86, no. 18, Apr. 2005.

[148] M. J. Freire and R. Marques, 'Optimizing the magnetoinductive lens: Improvement, limits, and possible applications', *J. Appl. Phys.*, vol. 103, no. 1, 2008.

[149] F. Mesa, M. J. Freire, R. Marqués, and J. D. Baena, 'Three-dimensional superresolution in metamaterial slab lenses: Experiment and theory', *Phys. Rev. B*, vol. 72, no. 23, Dec. 2005.

[150] S. Maslovski, S. Tretyakov, and P. Alitalo, 'Near-field enhancement and imaging in double planar polariton-resonant structures', *J. Appl. Phys.*, vol. 96, no. 3, pp. 1293–1300, Jul. 2004.

[151] M. J. Freire and R. Marques, 'Near-field imaging in the megahertz range by strongly coupled magnetoinductive surfaces: Experiment and ab initio analysis', *J. Appl. Phys.*, vol. 100, no. 6, 2006.

[152] R. R. A. Syms, I. R. Young, M. M. Ahmad, and M. Rea, 'Magnetic resonance imaging using linear magneto-inductive waveguides', *J. Appl. Phys.*, vol. 112, no. 11, Dec. 2012.

[153] M. C. K. Wiltshire, J. B. Pendry, I. R. Young, D. J. Larkman, D. J. Gilderdale, and J. V. Hajnal, ‘Microstructured Magnetic Materials for RF Flux Guides in Magnetic Resonance Imaging’, *Science*, vol. 291, no. 5505, pp. 849–851, Feb. 2001.

[154] R. R. A. Syms, T. Floume, I. R. Young, L. Solymar, and M. Rea, ‘Flexible magnetoinductive ring MRI detector: Design for invariant nearest-neighbour coupling’, *Metamaterials*, vol. 4, no. 1, pp. 1–14, May 2010.

[155] R. Syms, I. Young, and L. Solymar, ‘Flexible Magneto-Inductive Resonators and Waveguides’, 2008.

[156] R. R. A. Syms, I. R. Young, M. M. Ahmad, S. D. Taylor-Robinson, and M. Rea, ‘Magneto-Inductive Catheter Receiver for Magnetic Resonance Imaging’, *IEEE Trans. Biomed. Eng.*, vol. 60, no. 9, pp. 2421–2431, Sep. 2013.

[157] R. R. A. Syms *et al.*, ‘Magneto-Inductive Magnetic Resonance Imaging Duodenoscope’, *Prog. Electromagn. Res.*, vol. 159, pp. 125–138, 2017.

[158] R. R. A. Syms, E. Kardoulaki, and I. R. Young, ‘Thin-Film Catheter-Based Receivers for Internal MRI’, in *Micro and Nano Scale NMR*, John Wiley & Sons, Ltd, 2018, pp. 237–263. doi: 10.1002/9783527697281.ch9.

[159] R. R. A. Syms, L. Solymar, I. R. Young, and T. Floume, ‘Thin-film magneto-inductive cables’, *J. Phys. Appl. Phys.*, vol. 43, no. 5, p. 055102, Jan. 2010.

[160] F. Martín, *Artificial transmission lines for RF and microwave applications*. in Wiley series in microwave and optical engineering. Hoboken: John Wiley and Sons, Inc, 2015.

[161] R. R. A. Syms, L. Solymar, and I. R. Young, ‘Broadband coupling transducers for magneto-inductive cables’, *J Phys Appl Phys*, vol. 43, no. 28, p. 285003, 2010.

[162] O. Sydoruk, ‘Coupling transducers for magnetoinductive waveguides: Minimising reflection over the whole pass band’, *Metamaterials*, vol. 5, no. 1, pp. 42–48, Apr. 2011.

[163] V. Mishra and A. Kiourti, ‘Wearable magnetoinductive waveguide for low-loss wireless body area networks’, *IEEE Trans Antennas Propag*, vol. 69, no. 5, pp. 2864–2876, 2020.

[164] ‘Metaboards - Seamless Charging Experience’, *Metaboards*. https://www.metaboards.com/ (accessed Sep. 19, 2023).

[165] S. J. Orfanidis, ‘Chapter 14: S-Parameters’, in *Electromagnetic Waves and Antennas*, Rutgers University, 2016.

[166] D. M. Pozar, ‘Microwave Network Analysis’, in *Microwave engineering*, 4th ed.Hoboken, NJ: Wiley, 2012.

[167] E. W. Matthews, ‘The Use of Scattering Matrices in Microwave Circuits’, *IEEE Trans. Microw. Theory Tech.*, vol. 3, no. 3, pp. 21–26, Apr. 1955.

[168] D. C. Youla, ‘On scattering matrices normalized to complex port numbers.’, in *Proc IRE*, 1961, p. 1221.

[169] P. Penfield, ‘Noise in Negative-Resistance Amplifiers’, *IRE Trans. Circuit Theory*, vol. 7, no. 2, pp. 166–170, 1960.

[170] S. Llorente-Romano, A. Garca-Lamperez, T. K. Sarkar, and M. Salazar-Palma, ‘An Exposition on the Choice of the Proper S Parameters in Characterizing Devices Including Transmission Lines with Complex Reference Impedances and a General Methodology for Computing Them’, *IEEE Antennas Propag. Mag.*, vol. 55, no. 4, pp. 94–112, Aug. 2013.

[171] S. C. Dutta Roy, ‘Some Little-Known Facts About Transmission Lines and Some New Results’, *IEEE Trans. Educ.*, vol. 53, no. 4, pp. 556–561, Nov. 2010.

[172] K. Kurokawa, ‘Power Waves and the Scattering Matrix’, *IEEE Trans. Microw. Theory Tech.*, vol. 13, no. 2, pp. 194–202, Mar. 1965.

[173] G. E. Stannard, ‘Calculation of power on a transmission line’, *Proc. IEEE*, vol. 55, no. 1, pp. 132–132, 1967.

[174] R. J. Vernon and S. R. Seshadri, ‘Reflection coefficient and reflected power on a lossy transmission line’, *Proc. IEEE*, vol. 57, no. 1, pp. 101–102, 1969.

[175] J. Rahola, ‘Power Waves and Conjugate Matching’, *IEEE Trans. Circuits Syst. II Express Briefs*, vol. 55, no. 1, pp. 92–96, Jan. 2008.

[176] S. Cohn and F. Coale, ‘Directional Channel-Separation Filters’, *Proc. IRE*, vol. 44, no. 8, pp. 1018–1024, Aug. 1956.

[177] F. S. Coale, ‘A Traveling-Wave Directional Filter’, *IEEE Trans. Microw. Theory Tech.*, vol. 4, no. 4, pp. 256–260, Oct. 1956.

[178] J. L. B. Walker, ‘Exact and Approximate Synthesis of TEM-Mode Transmission-Type Directional Filters’, *IEEE Trans. Microw. Theory Tech.*, vol. 26, no. 3, pp. 186–192, Mar. 1978.

[179] G. L. Matthaei, L. Young, and E. M. T. Jones, *Microwave filters, impedance-matching networks, and coupling structures*, Reprint of the ed. publ. by MacGraw-Hill 1964. in The Artech House microwave library. Norwood, Mass: Artech House, 1985.

[180] F. S. Coale, ‘Applications of Directional Filters for Multiplexing Systems’, *IEEE Trans. Microw. Theory Tech.*, vol. 6, no. 4, pp. 450–453, Oct. 1958.

[181] O. Wing, ‘Cascade Directional Filter’, *IEEE Trans. Microw. Theory Tech.*, vol. 7, no. 2, pp. 197–201, Apr. 1959.

[182] R. Cameron and M. Yu, ‘Design of manifold-coupled multiplexers’, *IEEE Microw. Mag.*, vol. 8, no. 5, pp. 46–59, Oct. 2007.

[183] L. P. Tuttle and R. D. Wanselow, ‘Practical Design of Strip-Transmission-Line Half-Wavelength Resonator Directional Filters’, *IEEE Trans. Microw. Theory Tech.*, vol. 7, no. 1, pp. 168–173, Jan. 1959.

[184] B. D. Moore and J. R. Cogdell, ‘A Millimeter-Wave Directional Filter Cavity’, *IEEE Trans. Microw. Theory Tech.*, vol. 24, no. 11, pp. 843–847, Nov. 1976.

[185] S. Uysal, ‘Microstrip loop directional filter’, *Electron. Lett.*, vol. 33, no. 6, p. 475, 1997.

[186] S. Rosloniec and T. Habib, ‘Novel microstrip-line directional filters’, *IEEE Trans. Microw. Theory Tech.*, vol. 45, no. 9, pp. 1633–1637, 1997.

[187] Y. Cheng, W. Hong, and K. Wu, ‘Half Mode Substrate Integrated Waveguide (HMSIW) Directional Filter’, *IEEE Microw. Wirel. Compon. Lett.*, vol. 17, no. 7, pp. 504–506, Jul. 2007.

[188] J. P. Kim, ‘Improved Design of Single-Section and Cascaded Planar Directional Filters’, *IEEE Trans. Microw. Theory Tech.*, vol. 59, no. 9, pp. 2206–2213, Sep. 2011.

[189] Y.-B. Zhang, B. Chen, and C.-Z. Ran, ‘An X-band single-layer waveguide directional filter with compact size and low insertion loss’, *IEICE Electron. Express*, vol. 15, no. 21, pp. 20180826–20180826, 2018.

[190] Y. Zhang, S. Shi, R. D. Martin, and D. W. Prather, ‘Slot-Coupled Directional Filters in Multilayer LCP Substrates at 95 GHz’, *IEEE Trans. Microw. Theory Tech.*, vol. 65, no. 2, pp. 476–483, Feb. 2017.

[191] A. M. Stone and J. L. Lawson, ‘Infinite-Rejection Filters’, *J. Appl. Phys.*, vol. 18, no. 8, pp. 691–703, Aug. 1947.

[192] D. Parthasarathy and R. Harjani, ‘Novel integratable notch filter implementation for 100 dB image rejection’, in *Proceedings of the 2003 International Symposium on Circuits and Systems*, IEEE, 2003.

[193] D. R. Jachowski, ‘Passive enhancement of resonator Q in microwave notch filters’, presented at the 2004 IEEE MTT-S International Microwave Symposium Digest (IEEE Cat. No.04CH37535), IEEE.

[194] D. R. Jachowski, ‘Compact, frequency-agile, absorptive bandstop filters’, presented at the IEEE MTT-S International Microwave Symposium Digest, 2005., IEEE, 2005.

[195] A. Ghaffari, E. A. M. Klumperink, and B. Nauta, ‘Tunable N-Path Notch Filters for Blocker Suppression: Modeling and Verification’, *IEEE J. Solid-State Circuits*, vol. 48, no. 6, pp. 1370–1382, Jun. 2013.

[196] R. Lababidi *et al.*, ‘Compact highly selective passive notch filter for 3.1–5 GHz UWB receiver system’, presented at the 2015 IEEE International Conference on Electronics, Circuits, and Systems (ICECS), IEEE, Dec. 2015.

[197] M. A. Morgan and T. A. Boyd, ‘Theoretical and Experimental Study of a New Class of Reflectionless Filter’, *IEEE Trans. Microw. Theory Tech.*, vol. 59, no. 5, pp. 1214–1221, May 2011.

[198] R. D. Standley, ‘A Time-Delay Equalizer Using Directional Filter Cascades (Correspondence)’, *IEEE Trans. Microw. Theory Tech.*, vol. 19, no. 5, pp. 497–498, May 1971.

[199] N. R. Erickson, ‘A Directional Filter Diplexer Using Optical Techniques for Millimeter to Submillimeter Wavelengths’, *IEEE Trans. Microw. Theory Tech.*, vol. 25, no. 10, pp. 865–866, Oct. 1977.

[200] I. Hunter, E. Musonda, R. Parry, M. Guess, and M. Meng, ‘Transversal directional filters for channel combining’, presented at the 2013 IEEE MTT-S International Microwave Symposium Digest (MTT), IEEE, Jun. 2013.

[201] J. Sorocki, I. Piekarz, S. Gruszczynski, and K. Wincza, ‘Miniaturized directional filter multiplexer for band separation in UWB antenna systems.’, in *2015 International Symposium on Antennas and Propagation (ISAP)*, Hobart, Australia, 2015, pp. 1–4.

[202] K. Wincza and S. Gruszczynski, ‘Frequency-Selective Feeding Network Based on Directional Filter for Constant-Beamwidth Scalable Antenna Arrays’, *IEEE Trans. Antennas Propag.*, vol. 65, no. 8, pp. 4346–4350, Aug. 2017.

[203] J. S. Sun, H. Lobato-Morales, J. H. Choi, A. Corona-Chavez, and T. Itoh, ‘Multistage Directional Filter Based on Band-Reject Filter With Isolation Improvement Using Composite Right-/Left-Handed Transmission Lines’, *IEEE Trans. Microw. Theory Tech.*, vol. 60, no. 12, pp. 3950–3958, Dec. 2012.

[204] J. L. Snoek, ‘Dispersion and absorption in magnetic ferrites at frequencies above one Mc/s’, *Physica*, vol. 14, no. 4, pp. 207–217, May 1948.

[205] M. Kazimierczuk, *High-Frequency Magnetic Components*. Wiley, 2013. doi: 10.1002/9781118717806.

[206] A. Motroni, A. Buffi, and P. Nepa, ‘A Survey on Indoor Vehicle Localization Through RFID Technology’, *IEEE Access*, vol. 9, pp. 17921–17942, 2021.

[207] L. Ni, D. Zhang, and M. Souryal, ‘RFID-based localization and tracking technologies’, *IEEE Wirel. Commun.*, vol. 18, no. 2, pp. 45–51, Apr. 2011.

[208] H. Liu, H. Darabi, P. Banerjee, and J. Liu, ‘Survey of Wireless Indoor Positioning Techniques and Systems’, *IEEE Trans. Syst. Man Cybern. Part C Appl. Rev.*, vol. 37, no. 6, pp. 1067–1080, Nov. 2007.

[209] P. V. Nikitin, R. Martinez, S. Ramamurthy, H. Leland, G. Spiess, and K. V. S. Rao, ‘Phase based spatial identification of UHF RFID tags’, in *2010 IEEE International Conference on RFID (IEEE RFID 2010)*, Apr. 2010, pp. 102–109.

[210] M. Scherhaufl, M. Pichler, and A. Stelzer, ‘UHF RFID Localization Based on Phase Evaluation of Passive Tag Arrays’, *IEEE Trans. Instrum. Meas.*, vol. 64, no. 4, pp. 913–922, Apr. 2015.

[211] L. M. Ni, Y. Liu, Y. C. Lau, and A. P. Patil, ‘LANDMARC: indoor location sensing using active RFID’, in *Proceedings of the First IEEE International Conference on Pervasive Computing and Communications, 2003. (PerCom 2003).*, Mar. 2003, pp. 407–415.

[212] Y. Zhang, M. G. Amin, and S. Kaushik, ‘Localization and Tracking of Passive RFID Tags Based on Direction Estimation’, *Int. J. Antennas Propag.*, vol. 2007, pp. 1–9, 2007.

[213] Youngsu Park, Je Won Lee, and SangWoo Kim, ‘Improving position estimation on RFID tag floor localization using RFID reader transmission power control’, presented at the 2008 IEEE International Conference on Robotics and Biomimetics, IEEE, Feb. 2009.

[214] C. Hekimian-Williams, B. Grant, Xiuwen Liu, Zhenghao Zhang, and P. Kumar, ‘Accurate localization of RFID tags using phase difference’, presented at the 2010 IEEE International Conference on RFID (IEEE RFID 2010), IEEE, Apr. 2010.

[215] J. Wang and D. Katabi, ‘Dude, where’s my card?’, *ACM SIGCOMM Comput. Commun. Rev.*, vol. 43, no. 4, pp. 51–62, Aug. 2013.

[216] H. Wu, B. Tao, Z. Gong, Z. Yin, and H. Ding, ‘A Fast UHF RFID Localization Method Using Unwrapped Phase-Position Model’, *IEEE Trans. Autom. Sci. Eng.*, vol. 16, no. 4, pp. 1698–1707, Oct. 2019.

[217] A. Raptopoulos Chatzistefanou, A. Tzitzis, S. Megalou, G. Sergiadis, and A. G. Dimitriou, 'Trajectory-Tracking of UHF RFID Tags, Exploiting Phase Measurements Collected From Fixed Antennas', *IEEE J. Radio Freq. Identif.*, vol. 5, no. 2, pp. 191–206, Jun. 2021.

[218] I. Ehrenberg, C. Floerkemeier, and S. Sarma, 'Inventory Management with an RFID-equipped Mobile Robot', presented at the 2007 IEEE International Conference on Automation Science and Engineering, IEEE, Sep. 2007.

[219] L. Xu, J. Liu, X. Wang, H. Gong, Y. Wang, and L. Chen, 'HF RFID-based Book Localization via Mobile Scanning', presented at the 2020 17th Annual IEEE International Conference on Sensing, Communication, and Networking (SECON), IEEE, Jun. 2020.

[220] W. Shi and V. W. S. Wong, 'MDS-Based Localization Algorithm for RFID Systems', in *2011 IEEE International Conference on Communications (ICC)*, Jun. 2011, pp. 1–6.

[221] E. L. Berz, D. A. Tesch, and F. P. Hessel, 'RFID indoor localization based on support vector regression and k-means', in *2015 IEEE 24th International Symposium on Industrial Electronics (ISIE)*, Jun. 2015, pp. 1418–1423.

[222] K. Yamano, K. Tanaka, M. Hirayama, E. Kondo, Y. Kimuro, and M. Matsumoto, 'Self-localization of mobile robots with RFID system by using support vector machine', in *2004 IEEE/RSJ International Conference on Intelligent Robots and Systems (IROS) (IEEE Cat. No.04CH37566)*, 2004, pp. 3756–3761 vol.4.

[223] S. Park and S. Hashimoto, 'Indoor localization for autonomous mobile robot based on passive RFID', in *2008 IEEE International Conference on Robotics and Biomimetics*, 2009, pp. 1856–1861.

[224] K. Kodaka, H. Niwa, Y. Sakamoto, M. Otake, Y. Kanemori, and S. Sugano, 'Pose estimation of a mobile robot on a lattice of RFID tags', presented at the 2008 IEEE/RSJ International Conference on Intelligent Robots and Systems, IEEE, Sep. 2008.

[225] S. Han, H. Lim, and J. Lee, 'An Efficient Localization Scheme for a Differential-Driving Mobile Robot Based on RFID System', *IEEE Trans Ind Electron*, vol. 54, no. 6, pp. 3362–3369, 2007.

[226] M. Y. Ahmad and A. S. Mohan, 'Novel Bridge-Loop Reader for Positioning With HF RFID Under Sparse Tag Grid', *IEEE Trans. Ind. Electron.*, vol. 61, no. 1, pp. 555–566, Jan. 2014.

[227] J. Mi and Y. Takahashi, 'Low cost design of HF-band RFID system for mobile robot self-localization based on multiple readers and tags', in *2015 IEEE International Conference on Robotics and Biomimetics (ROBIO)*, 2015, pp. 194–199.

[228] C. Röhrig, D. Heß, and F. Künemund, 'Constrained Kalman filtering for indoor localization of transport vehicles using floor-installed HF RFID transponders', in *2015 IEEE International Conference on RFID (RFID)*, 2015, pp. 113–120.

[229] P. Yang, W. Wu, M. Moniri, and C. C. Chibelushi, 'Efficient Object Localization Using Sparsely Distributed Passive RFID Tags', *IEEE Trans. Ind. Electron.*, vol. 60, no. 12, pp. 5914–5924, Dec. 2013.

[230] A. A. Nazari Shirehjini and S. Shirmohammadi, ‘Improving Accuracy and Robustness in HF-RFID-Based Indoor Positioning With Kalman Filtering and Tukey Smoothing’, *IEEE Trans. Instrum. Meas.*, vol. 69, no. 11, pp. 9190–9202, Nov. 2020.
[231] B. Ozdenizci, V. Coskun, and K. Ok, ‘NFC Internal: An Indoor Navigation System’, *Sensors*, vol. 15, no. 4, pp. 7571–7595, 2015.
[232] R.-S. Cheng, W.-J. Hong, J.-S. Wang, and K. W. Lin, ‘Seamless Guidance System Combining GPS, BLE Beacon, and NFC Technologies’, *Mob Inf Syst*, vol. 2016, p. 5032365, Jan. 2016.
[233] P. Sedighi, M. H. Norouzi, and M. Delrobaei, ‘An RFID-Based Assistive Glove to Help the Visually Impaired’, *IEEE Trans Instrum Meas*, vol. 70, pp. 1–9, 2021.
[234] J. Yan, C. J. Stevens, and E. Shamonina, ‘A Metamaterial Position Sensor Based on Magnetoinductive Waves’, *IEEE Open J. Antennas Propag.*, vol. 2, pp. 259–268, 2021.
[235] T. Trivedi, Y. Chen, I. A. D. Williamson, P. Pasupathy, and D. P. Neikirk, ‘Group Velocity Estimation and Defect Localization in Magneto-Inductive Waveguides’, *IEEE Trans. Microw. Theory Tech.*, vol. 69, no. 4, pp. 2072–2077, Apr. 2021.
[236] I. Khromova, C. Stevens, and E. Chatziantoniou, ‘Load Localisation’, WO 2020/128520 A1, Jun. 2020.
[237] T. Kailath, ‘Correlation detection of signals perturbed by a random channel’, *IEEE Trans. Inf. Theory*, vol. 6, no. 3, pp. 361–366, Jun. 1960.
[238] L. A. Pflug, G. E. Ioup, J. W. Ioup, and R. L. Field, ‘Prefiltering for improved correlation detection of bandlimited transient signals’, *J. Acoust. Soc. Am.*, vol. 95, no. 3, pp. 1459–1473, Mar. 1994.
[239] E. Cummins, S. Jaurggui, and W. Vincent, ‘Time-and Frequency-Domain Characteristics of Man-Made Radio Noise Affecting HF-Communications Sites’, *IEEE Trans. Electromagn. Compat.*, vol. EMC-21, no. 3, pp. 182–189, Aug. 1979.
[240] T. W. H. Fockens, A. P. M. Zwamborn, and F. Leferink, ‘Measurement Methodology and Results of Measurements of the Man-Made Noise Floor on HF in The Netherlands’, *IEEE Trans. Electromagn. Compat.*, vol. 61, no. 2, pp. 337–343, Apr. 2019.
[241] T. Itoh and C. Caloz, *Electromagnetic metamaterials: transmission line theory and microwave applications*. Hoboken N. J.: John Wiley & Sons Inc., 2005.
[242] G. V. Eleftheriades and K. G. Balmain, *Negative-refraction metamaterials: fundamental principles and applications*. Hoboken N. J.: John Wiley & Sons Inc., 2005.
[243] L. Solymar and E. Shamonina, *Waves in Metamaterials*. Oxford, UK: Oxford University Press, 2009.
[244] S. Prouet and S. Brennsteiner, ‘Phase Alignment of a Controller Clock to Field’, EP3703269, 2022.
[245] T. Pichler, ‘Clock Recovery in an RFID transponder’, EP3809329, 2019.